# Numerical Simulation of Intense Ultrafast Quantum Phenomena

By

Joshua Tree Karpel

A dissertation submitted in partial fulfillment of

the requirements for the degree of

Doctor of Philosophy

(Physics)

at the

UNIVERSITY OF WISCONSIN–MADISON

2019

Date of final oral examination: December 2, 2019

The dissertation is approved by the following members of the Final Oral Committee:

Deniz D. Yavuz, Professor, Physics

James E. Lawler, Professor, Physics

Thad G. Walker, Professor, Physics

Daniel van der Weide, Professor, Electrical and Computer Engineering

For Frodo

## Acknowledgments

Huge thanks to...

Deniz Yavuz, my advisor, who kept me sane and encouraged me to pursue my own interests. Without Deniz's gentle and endless support, I would certainly not be here today.

Jim Reardon, who fielded my endless agonizing over teaching responsibilities with unbelievable grace. I also deeply appreciate the opportunity to work on the radio project with him.

Brett Unks, whose presence was a cool, dry breeze on the swampy days of running unending teaching labs. Without him, I would have looked like an idiot in front of even more undergraduates than I actually did.

Jeff Schmidt, whose brain and heart are both the size of mountains. There are many derivations in this thesis that are adapted from other works that Jeff helped me understand, especially those where the original authors were... less than clear.

Christina Koch, Lauren Michael, Jason Patton, and Todd Tannenbaum at the Center for High Throughput Computing. Christina and Lauren opened my eyes, and Jason and Todd gave me wings.

Ben Lemberger, David Gold, Dipto Das, Shay Inbar, and Eli Mueller, for all of those long lunches full of good conversation and occasionally-insane arguments.

Steven Casper, Chris Yip, Patrick Vanmeter, and Sam Neyens. I literally cannot believe how many times we ate at Mirch Masala. We probably should have gone to Maharani more often, at least.

Adrian Fraser, from whom all good things flow. I'll always be your vice president in spirit, if not in practice. Sail on, my friend.

Zach Buckholtz, my office mate and partner-in-crime (especially chair theft). My endless thanks to you for being my physics rubber duck. It has been an honor serving with you.

Taylor Russi: there is a penguin hidden somewhere in this thesis. Good luck!

My parents, Darcie and Lenny, whose 27-year-long scheme has finally come to fruition.

# Contents

# List of Figures

# List of Tables

# Abstract


## Numerical Simulation of Intense Ultrafast Quantum Phenomena

*Joshua Tree Karpel*

*Under the supervision of Professor Deniz D. Yavuz*

*at the University of Wisconsin–Madison*

Lasers are the basis of many of the most recent exciting advances in physics, like the ever-improving atomic clocks, the detection of gravitational waves by LIGO, or the generation of incredibly intense pulses of light. They are useful as a foundational tool because of their incredible flexibility. On one end of the spectrum, they can be made so accurate that their actual waveform, oscillating more than a million billion times per second, will be predictable for minutes. On the other end, a laser pulse can be made so intense that it rivals the entire world's power output, if only for a few millionths of a billionth of a second.

This enormous range of possibilities is surely hiding a great number of possible applications. In this work, we investigate two such possibilities. The first project is about the modeling of an optical modulator, a device which can shift the frequency of light. Optical modulators are a foundational technology in both commercial telecommunications and optical physics. Our design would beat the state-of-the-art continuous-wave modulation frequency by two orders of magnitude, a significant improvement for an important kind of device.

The second project is more exploratory. We investigate what happens when a laser pulse is used to ionize hydrogen, but the pulse is of a comparable length to the classical orbit time of hydrogen's electron. We find that very counterintuitive behavior emerges at these timescales, and develop a simple model which is able to describe this counterintuitive behavior.

These two projects are united by common techniques: we use simple, robust numerical models of the coupled electromagnetic-quantum phenomena we are investigating. We run these models at huge scale using high-throughput computing to explore the vast parameter spaces inherent in these problems and find new insight.

# Chapter 0

# Introduction

When one thinks about computational techniques in physics, they are often drawn to the extreme limits of high-performance computing. Supercomputers are becoming incredibly powerful, and much useful physics is done on them: simulations of particle interactions in detectors like the LHC, of the motion of fluids and plasmas, or of the evolution of the entire universe from scratch. However, this kind of computing has not found much use in atomic, molecular, and optical (AMO) physics, where the problems generally have few enough interacting pieces to not need the enormous, focused computational power of a supercomputer.

And yet, computational power is still needed. Although AMO physics problems don't often need supercomputers, there are still plenty of problems whose solutions cannot be found by hand. We often need to computationally explore how a system behaves when the initial conditions are different, or when some parameter of the experiment design changes. Doing this exploration densely over large parameter spaces is still a project in extreme computing, although in our case it is *high-throughput*, not *high-performance*.

This thesis discusses two separate (but philosophically similar) projects in the field of ultrafast intense optics. In both projects we used simple, robust electromagnetic and quantum models. Both projects took advantage of high-throughput computing to perform wide, dense parameter scans to characterize the behavior of the simulated systems in different regimes. The computational power required for any given simulation could usually be provided by a fraction of a laptop: one CPU and a few gigabytes of memory. By keeping these requirements low, we were able to run thousands of simulations simultaneously on resources provided locally by the Center for High-Throughput Computing at the University of Wisconsin-Madison.

The first project is about the design of an ultrafast high-efficiency optical modulator based

on four-wave mixing. Although conceptually similar to a standard electro-optical modulator, we predict that this device would have a modulation frequency of roughly 10 THz, with an efficiency exceeding 1%. The key to the extraordinary efficiency at such a large modulation frequency is that this modulator is implemented in a high-quality microresonator. The tiny mode volume and high quality factor of a microresonator lead to enormous electric field intensities, which drives a nonlinear four-wave mixing process that produces the modulated light. Chapter 1 discusses this project.

The second project was sparked by a simple question: if you try to ionize a hydrogen atom with a pulse shorter than the classical orbital period of the electron, what happens? Classically, one might expect that the electron cannot ionize, because it needs to interact with the nucleus to gain enough momentum to break free. Although we only saw hints that a similar process might be occuring quantum-mechanically, we found another equally-interesting avenue to explore: how could pulses with smaller peak intensity possible ionize **more** than pulses with higher peak intensity? Chapter 2 discusses this project.

Each chapter can be read independently. The content in the appendices is a mixture from both projects; each appendix is referenced in the relevant section of the main text. Chronologically, the Ionization project actually happened first, followed by the Modulation project (the order was reversed to enhance the overall flow of this thesis).

All of the software written for these projects is home-grown and open-source:

- Modulation – Modulation simulations for the first project.
- Ionization – Ionization simulations for the second project.
- Simulacra – Support package for running simulations and creating visualizations, used by both Modulation and Ionization.
- IDESolver – Specialized integro-differential equation solver, used by Ionization but published separately as [1].

The material product of this thesis is largely composed of these packages. They are designed to be reusable and extensible for future work.

All of these projects depend heavily on Python's scientific computing ecosystem, a collection of packages for handling numerical computation and scientific visualization [2]. We have found Python to be an effective programming language for scientific computing due to it being a fully general-purpose language while still allowing access to efficient numerical routines through free, open-source packages maintained by the community.

As mentioned above, our simulations were designed to be run on the Center for High Throughput Computing's local HTCondor high-throughput computing cluster. Starting with the Modulation project, we accomplished this using HTMap[1], a Python package that helps run Python code on HTCondor clusters.

[1] Which happens to be developed by the author, in his alter-ego as a CHTC project assistant.

# Chapter 1

# Molecular Modulation in Microresonators

Optical modulators are powerful tools that have found a wide variety of uses, ranging from encoding information to synthesizing ultrafast waveforms. Acousto-optical and electro-optical modulators (AOMs and EOMs) provide frequency shifts limited to the electrical frequencies that drive them, with a maximum of a few hundred GHz. Although new techniques continue to incrementally improve electrically-driven modulators [3–7], there is little prospect for pushing them to significantly higher modulation frequencies. Optical modulators with THz-scale modulation frequencies need to be driven by optical processes [8–10].

Over the past decade The Yavuz group developed a 90 THz continuous-wave (CW) optical modulator based on a technique called molecular modulation, a kind of driven four-wave mixing based on CW Raman lasing [11–20]. Molecular modulation was originally developed using pulsed pump lasers [21–32], but these systems suffer from large linewidths and low repetition rates [33]. Using CW driving beams for our modulator avoided these problems, but required the use of an optical cavity to reach the high intensities necessary for molecular modulation to occur. Using a large gas-filled cavity ultimately limited the usefulness of the modulator due to its complexity of operation and sensitivity to mechanical and thermal fluctuations, all of which negatively impacted the steady-state modulation efficiency $\epsilon$.

In this project we investigated the possibility of extending our CW molecular modulation technique to solid-state Raman-active microresonators and discuss the prospective characteristics of such a device, which we call a Microresonator-based Molecular Modulator (MMM).

Why pursue this route? Microresonator modes have small volumes and high quality factors over a wide range of wavelengths, which make them ideal platforms for building nonlinear optical devices like molecular modulators [34, 35]. For example, Grudinin et al. demonstrated an ultra-

low-threshold Raman laser in a $CaF_2$ microresonator which required just 15 µW of launched pump power [36, 37]. Other groups have used microresonators to create high-quality stabilized optical frequency combs or explore more exotic nonlinear behavior such as soliton formation [38–40]. As an added benefit, the smaller overall system size and better mechanical and thermal stability offered by microresonators will help mitigate the issues that limited the efficiency of our previous device. Microresonators could also be integrated into complex optical systems much more readily. Overall, microresonators are a much more promising platform for continuing to improve the efficiency and usability of our molecular modulation technique.

The main product of this investigation was numerical simulations that indicate that an MMM based on a silica microsphere could achieve a frequency shift of $\sim 12\,\mathrm{THz}$ with modulation efficiencies of $\epsilon \approx 1\%$ at any optical wavelength. We also investigated how the performance of the modulator varies with respect to a number of parameters, and considered how that variations would influence the design of the device. These results were published in [41]. In the following sections, we will introduce the theory of Raman processes in optical resonators (Section 1.2), use it to describe driven four-wave mixing in a microresonator (Sections 1.3 and 1.4), and discuss the numerical simulations we ran using that result (Section 1.5).

## 1.1 Electromagnetic Waves in a Medium

The MMM will be implemented in a electromagnetically-active medium, so we need a wave equation that clearly shows how the electromagnetic field couples to a medium. In our particular case we will be interested in the polarization of the material: how it responds to incident electric fields. This derivation follows the one laid out in [42], but with emphasis on the elements that we'll need for modeling the MMM.

We begin with from the differential form of Maxwell's equations [43].

$$\boldsymbol{\nabla} \cdot \mathbf{D} = \rho \tag{1.1.1a}$$

$$\boldsymbol{\nabla} \cdot \boldsymbol{\mathcal{B}} = 0 \tag{1.1.1b}$$

$$\boldsymbol{\nabla} \times \mathbf{H} = \mathbf{J} + \frac{\partial \mathbf{D}}{\partial t} \tag{1.1.1c}$$

$$\boldsymbol{\nabla} \times \boldsymbol{\mathcal{E}} = -\frac{\partial \boldsymbol{\mathcal{B}}}{\partial t} \tag{1.1.1d}$$

where $\boldsymbol{\mathcal{E}}$ is the electric field, $\mathbf{D} = \epsilon_0 \boldsymbol{\mathcal{E}} + \mathbf{P}$ is the **electric displacement field**, $\mathbf{P}$ is the **electric polarization field**, $\boldsymbol{\mathcal{B}}$ is the **magnetic induction**, $\mathbf{H}$ is the **magnetic field**, $\rho$ is the **charge density**, and $\mathbf{J}$ is the **current density**.

For simple materials we have a linear relationship between $\mathbf{D}$ and $\boldsymbol{\mathcal{E}}$: $\mathbf{P} = \epsilon_0 \chi_e \boldsymbol{\mathcal{E}}$, where $\chi_e$ is the **electric susceptibility**. Using this we write $\mathbf{D} = \epsilon \boldsymbol{\mathcal{E}}$, where $\epsilon = \epsilon_0(1 + \chi_e)$ is the **electric permittivity**.

From this relatively-macroscopic perspective (length scales smaller than the whole experiment but still much larger than a single atom), we can cause the frequency of light to change by causing the polarization field to change in a time or space-dependent way. Any such dependence will couple into the resulting $\boldsymbol{\mathcal{E}}$ and $\boldsymbol{\mathcal{B}}$ fields via Maxwell's equations and end up producing an electromagnetic wave at a different frequency than the input wave. Both time and space-dependent polarization fields will end up causing a frequency shift, because the propagation equations couple the time-dependent and space-dependent properties of the wave together (intuitively, we know that because the speed of light is fixed, its wavelength and frequency are coupled). Our goal is to capture this dependence for a propagating electromagnetic wave, so we want to write down a wave equation for the electric field that depends explicitly on the polarization of the medium.

We will assume that we're working in a medium that is macroscopically neutral (no free charges or currents) and has no particular magnetic response ($\mu = \mu_0$). Then we have $\rho = 0$, $\mathbf{J} = 0$, and

$\boldsymbol{\mathcal{B}} = \mu_0 \mathbf{H}$. Maxwell's equations become

$$\boldsymbol{\nabla} \cdot \mathbf{D} = 0 \tag{1.1.2a}$$

$$\boldsymbol{\nabla} \cdot \boldsymbol{\mathcal{B}} = 0 \tag{1.1.2b}$$

$$\boldsymbol{\nabla} \times \boldsymbol{\mathcal{B}} = \mu_0 \frac{\partial \mathbf{D}}{\partial t} \tag{1.1.2c}$$

$$\boldsymbol{\nabla} \times \boldsymbol{\mathcal{A}} = -\frac{\partial \boldsymbol{\mathcal{B}}}{\partial t} \tag{1.1.2d}$$

We now follow the standard steps: take the curl of the last equation, swap the time and space derivatives, and use the third equation to simplify.

$$\begin{aligned}
\boldsymbol{\nabla} \times \boldsymbol{\mathcal{E}} &= -\frac{\partial \boldsymbol{\mathcal{B}}}{\partial t} \\
\boldsymbol{\nabla} \times \boldsymbol{\nabla} \times \boldsymbol{\mathcal{E}} &= -\boldsymbol{\nabla} \times \frac{\partial \boldsymbol{\mathcal{B}}}{\partial t} \\
\boldsymbol{\nabla} \times \boldsymbol{\nabla} \times \boldsymbol{\mathcal{E}} &= -\frac{\partial}{\partial t}(\boldsymbol{\nabla} \times \boldsymbol{\mathcal{B}}) \\
\boldsymbol{\nabla} \times \boldsymbol{\nabla} \times \boldsymbol{\mathcal{E}} &= -\frac{\partial}{\partial t}\left(\mu_0 \frac{\partial \mathbf{D}}{\partial t}\right) \\
\boldsymbol{\nabla} \times \boldsymbol{\nabla} \times \boldsymbol{\mathcal{E}} + \mu_0 \frac{\partial^2 \mathbf{D}}{\partial t^2} &= 0
\end{aligned} \tag{1.1.3}$$

If we were in a linear medium we would have $\boldsymbol{\mathcal{E}} = \epsilon_0 \epsilon \mathbf{D}$ and we would be done ($\epsilon$ is the relative permittivity of the material). In a general medium we can't do that, so instead we'll split $\mathbf{D}$ into the electric field and the polarization, yielding

$$\begin{aligned}
\boldsymbol{\nabla} \times \boldsymbol{\nabla} \times \boldsymbol{\mathcal{E}} + \mu_0 \epsilon_0 \frac{\partial^2 \boldsymbol{\mathcal{E}}}{\partial t^2} + \mu_0 \frac{\partial^2 \mathbf{P}}{\partial t^2} &= 0 \\
\boldsymbol{\nabla} \times \boldsymbol{\nabla} \times \boldsymbol{\mathcal{E}} + \frac{1}{c^2} \frac{\partial^2 \boldsymbol{\mathcal{E}}}{\partial t^2} &= -\frac{1}{\epsilon_0 c^2} \frac{\partial^2 \mathbf{P}}{\partial t^2}
\end{aligned} \tag{1.1.4}$$

where $c = 1/\sqrt{\epsilon_0 \mu_0}$ is the speed of light in vacuum. Next we use the vector calculus identity for the curl of the curl ($\boldsymbol{\nabla} \times \boldsymbol{\nabla} \times \mathbf{A} = \boldsymbol{\nabla}(\boldsymbol{\nabla} \cdot \mathbf{A}) - \nabla^2 \mathbf{A}$) to rewrite the left hand side:

$$\boldsymbol{\nabla}(\boldsymbol{\nabla} \cdot \boldsymbol{\mathcal{E}}) - \nabla^2 \boldsymbol{\mathcal{E}} + \frac{1}{c^2} \frac{\partial^2 \boldsymbol{\mathcal{E}}}{\partial t^2} = -\frac{1}{\epsilon_0 c^2} \frac{\partial^2 \mathbf{P}}{\partial t^2} \tag{1.1.5}$$

Typically we would be able to remove the first term because, in a linear medium, the first Maxwell

equation would tell us that $\boldsymbol{\nabla} \cdot \boldsymbol{\mathcal{E}}$ is zero if there are no free charges. However, this is no longer true: $\mathbf{D}$ is indeed divergence-less, but $\boldsymbol{\mathcal{E}}$ is not necessarily a linear function of $\mathbf{D}$, so there is no guarantee that it is also divergence-less.

Luckily, there are other conditions that lead to $\boldsymbol{\nabla} \cdot \boldsymbol{\mathcal{E}}$ being negligible. For example, we often work with infinite plane waves, where $\boldsymbol{\nabla} \cdot \boldsymbol{\mathcal{E}}$ is zero. In fact, as long as the wavefront curvature is not too large and the electric field envelope varies slowly, the entire first term $\boldsymbol{\nabla}(\boldsymbol{\nabla} \cdot \boldsymbol{\mathcal{E}})$ is negligible, and we can drop it. We'll do that now so that we can write

$$\nabla^2 \boldsymbol{\mathcal{E}} - \frac{1}{c^2} \frac{\partial^2 \boldsymbol{\mathcal{E}}}{\partial t^2} = \frac{1}{\epsilon_0 c^2} \frac{\partial^2 \mathbf{P}}{\partial t^2} \tag{1.1.6}$$

This is the familiar electromagnetic wave equation, but with a source term on the right. In a linear medium the source term combines with the second term on the left to cause a change in the index of refraction. The nonlinear parts of the polarization can act as sources of electric field at new polarizations or frequencies.

## 1.2 Generalized Coupled-Mode Model of Molecular Modulation in an Optical Resonator

There are two main approaches to studying the nonlinear dynamics of electromagnetic fields in an optical cavity. Each has their own advantages and disadvantages.

The first approach is **finite element modeling**. In a finite element model, the physical resonator is decomposed into many small pieces that are each easy to analyze, and the propagation equations are stitched together along the boundaries. Finite element techniques are therefore capable of propagating the electric field in time and space for any cavity geometry without understanding the resonator modes beforehand.

The second approach, which we use, is **coupled mode theory**. In coupled mode theory, we decompose the electromagnetic field into the eigenmodes of the resonator. Although this decomposition requires some up-front knowledge about the resonator's modes, it leads to differential equations that are more compact and intuitive than the ones provided by a finite element model. This is a critical advantage for our purposes: it gives us a chance of interpreting the results of our

parameter scans.

For that and other reasons, we chose to use a coupled mode theory. First, we simply have more institutional familiarity with it inside the Yavuz group, having used it for the analysis of previous resonators designed for the molecular modulation project [44]. Second, it leads to simpler code with fewer external dependencies (we do not have to rely on an external finite element library). Third (as we will see), the behavior of the model is less dependent of the physical resonator under consideration, because only certain properties of the modes enter into the calculation. The conclusions drawn from this model, and the code used to simulate it, are therefore much more widely-applicable and flexible.

In this section, we will derive a set of coupled ordinary nonlinear differential equations that describe the evolution of the electric field amplitude prefactor of each resonator eigenmode in time. The theory will be fully general, making no assumptions whatsoever about the physical resonator that we are modeling (besides the fact that it has eigenmodes and supports four-wave mixing, of course).

Given a Hamiltonian for the Raman system and the initial electric field, it would technically be possible to simply begin carrying out the entire calculation numerically via brute force. The electric field tells us how the wavefunction evolves in time, and the wavefunction tells us what the total polarization field is, and that tells us how the electric field evolves in time. Unfortunately, such a calculation would perform extremely poorly in both time and space due to the number of intermediate steps and transitions between different quantities. Instead, we will try to attack the quantum problem enough that we can arrive at a propagation equation for the electric field modes *in terms of the electric field modes themselves.* This will cut out the middle step of the calculation, which is where the incredible complexity of the quantum system will kill us numerically. If we can do that part on paper, we'll be able to make a much more efficient final calculation.

Through the rest of this section we will follow the general technique of [44] to analyze the Raman process in a resonator, but without the restriction that the relevant resonator modes form a Raman sideband ladder. This will complicate the derivation somewhat, but not terribly, and the final result is reasonably elegant.

### 1.2.1 Hamiltonian for the Ro-Vibrational Quantum System

The Hamiltonian for the ro-vibrational Raman system is a sum of two parts, an unperturbed Hamiltonian $\widehat{\mathcal{H}}_0$ and a perturbing Hamiltonian $\widehat{\mathcal{H}}_I$: $\widehat{\mathcal{H}} = \widehat{\mathcal{H}}_0 + \widehat{\mathcal{H}}_I$. The unperturbed Hamiltonian accounts for everything but the external electric fields, and the perturbing Hamiltonian account for those external fields.

We will expand the wavefunction for a single molecule in terms of the orthonormal eigenstates of the unperturbed Hamiltonian:

$$|\Psi(\mathbf{r},t)\rangle = c_a(\mathbf{r},t)\, e^{-i\omega_a t}\,|a\rangle + c_b(\mathbf{r},t)\, e^{-i\omega_b t}\,|b\rangle + \sum_i c_i(\mathbf{r},t)\, e^{-i\omega_i t}\,|i\rangle \tag{1.2.1}$$

where $|a\rangle$ and $|b\rangle$ are the two ro-vibrational states we are targeting and $|i\rangle$ are the electronic states. The position $\mathbf{r}$ refers to the nominal position of the molecule in space macroscopically, *not* to any internal degrees of freedom. Those are entirely captured by the expansion coefficients.

In this basis, the Hamiltonians are

$$\widehat{\mathcal{H}}_0 = \hbar\left[\omega_a\,|a\rangle\langle a| + \omega_b\,|b\rangle\langle b| + \sum_i \omega_i\,|i\rangle\langle i|\right] \tag{1.2.2a}$$

$$\begin{aligned}\widehat{\mathcal{H}}_I &= -\boldsymbol{\mathcal{E}}(\mathbf{r},t)\cdot\widehat{\mathbf{P}} \\ &= -\sum_i \boldsymbol{\mathcal{E}}(\mathbf{r},t)\cdot\boldsymbol{\mu}_{ai}\,|a\rangle\langle i| - \sum_i \boldsymbol{\mathcal{E}}(\mathbf{r},t)\cdot\boldsymbol{\mu}_{bi}\,|b\rangle\langle i| \\ &\quad - \sum_i \boldsymbol{\mathcal{E}}^*(\mathbf{r},t)\cdot\boldsymbol{\mu}^*_{ai}\,|i\rangle\langle a| - \sum_i \boldsymbol{\mathcal{E}}^*(\mathbf{r},t)\cdot\boldsymbol{\mu}^*_{bi}\,|i\rangle\langle b|\end{aligned} \tag{1.2.2b}$$

where we have made the dipole approximation for the interaction Hamiltonian. Note that the direct dipole transition between $|a\rangle$ and $|b\rangle$ is not allowed (i.e., $\boldsymbol{\mu}_{ab} = \mathbf{0}$). We also ignore any possible transitions among the electron states $|i\rangle$, because we don't actually expect any significant population to be in them at any time.

This Hamiltonian is a pain to work with because it has a lot of states in it. Luckily, we don't actually care about the populations of the $|i\rangle$ states. We can eliminate them by decomposing the electric field into a sum of orthogonal (*not orthonormal*, we aren't going to normalize them) cavity

modes, indexed by $q$:

$$\boldsymbol{\mathcal{E}}(\mathbf{r},t) = \frac{1}{2}\sum_q \left[\mathcal{E}_q(t)\, e^{-i\omega_q t}\, \mathbf{u}_q(\mathbf{r}) + \mathcal{E}_q^*(t)\, e^{i\omega_q t}\, \mathbf{u}_q^*(\mathbf{r})\right] \tag{1.2.3}$$

Note that this is a spatial decomposition, not a frequency decomposition. We have additionally pulled out a mode frequency $\omega_q$, but that's incidental. By pulling that out, we get a slowly-varying complex amplitude coefficient $\mathcal{E}_q(t)$. In particular, we're going to assume that all of the slowly varying quantities (the $c_n(t)$ and the $\mathcal{E}_q(t)$) vary much slower than the single-photon detuning from the electron $|i\rangle$ states). Note that this decomposition is not a basis for any function, but just for functions that satisfy the wave equation and the boundary conditions of the cavity.

### 1.2.2 Evolution of the Wavefunction in Time

Our first major goal is to determine the time evolution of the wavefunction. The Schrödinger equation says that

$$\begin{aligned} i\hbar\frac{\partial}{\partial t}\,|\Psi(\mathbf{r},t)\rangle &= \widehat{\mathcal{H}}\,|\Psi(\mathbf{r},t)\rangle \\ &= \widehat{\mathcal{H}}_0\,|\Psi(\mathbf{r},t)\rangle + \widehat{\mathcal{H}}_I\,|\Psi(\mathbf{r},t)\rangle \end{aligned} \tag{1.2.4}$$

The left-hand side is the time derivative of (1.2.1):

$$\begin{aligned} i\hbar\frac{\partial}{\partial t}\,|\Psi(\mathbf{r},t)\rangle = {} & [i\hbar\,\dot{c}_a(\mathbf{r},t) + \hbar\,\omega_a\,c_a(\mathbf{r},t)]e^{-i\omega_a t}\,|a\rangle \\ & + [i\hbar\,\dot{c}_b(\mathbf{r},t) + \hbar\,\omega_b\,c_b(\mathbf{r},t)]e^{-i\omega_b t}\,|b\rangle \\ & + \sum_i [i\hbar\,\dot{c}_i(\mathbf{r},t) + \hbar\,\omega_i\,c_i(\mathbf{r},t)]e^{-i\omega_i t}\,|i\rangle \end{aligned} \tag{1.2.5}$$

The first term on the right-hand side is

$$\begin{aligned}
\widehat{\mathcal{H}}_0 \left|\Psi(\mathbf{r},t)\right\rangle &= \hbar\Big[\omega_a \left|a\right\rangle\!\left\langle a\right| + \omega_b \left|b\right\rangle\!\left\langle b\right| + \sum_i \omega_i \left|i\right\rangle\!\left\langle i\right| + i\gamma_{ba} \left|a\right\rangle\!\left\langle b\right| - i\gamma_{ba} \left|b\right\rangle\!\left\langle a\right|\Big] \\
&\quad \times \left[c_a(\mathbf{r},t)\, e^{-i\omega_a t} \left|a\right\rangle + c_b(\mathbf{r},t)\, e^{-i\omega_b t} \left|b\right\rangle + \sum_j c_j(\mathbf{r},t)\, e^{-i\omega_j t} \left|j\right\rangle\right] \\
&= \hbar\,\omega_a\, c_a(\mathbf{r},t)\, e^{-i\omega_a t} \left|a\right\rangle \\
&\quad + \hbar\,\omega_b\, c_b(\mathbf{r},t)\, e^{-i\omega_b t} \left|b\right\rangle \\
&\quad + \sum_i \hbar\,\omega_i\, c_i(\mathbf{r},t)\, e^{-i\omega_i t} \left|i\right\rangle
\end{aligned} \tag{1.2.6}$$

The second term is

$$\begin{aligned}
\widehat{\mathcal{H}}_I \left|\Psi(\mathbf{r},t)\right\rangle &= \Big[-\sum_i \boldsymbol{\mathcal{E}}(\mathbf{r},t)\cdot\boldsymbol{\mu}_{ai} \left|a\right\rangle\!\left\langle i\right| - \sum_i \boldsymbol{\mathcal{E}}(\mathbf{r},t)\cdot\boldsymbol{\mu}_{bi} \left|b\right\rangle\!\left\langle i\right| \\
&\qquad - \sum_i \boldsymbol{\mathcal{E}}^*(\mathbf{r},t)\cdot\boldsymbol{\mu}^*_{ai} \left|i\right\rangle\!\left\langle a\right| - \sum_i \boldsymbol{\mathcal{E}}^*(\mathbf{r},t)\cdot\boldsymbol{\mu}^*_{bi} \left|i\right\rangle\!\left\langle b\right|\Big] \\
&\quad \times \left[c_a(\mathbf{r},t)\, e^{-i\omega_a t} \left|a\right\rangle + c_b(\mathbf{r},t)\, e^{-i\omega_b t} \left|b\right\rangle + \sum_j c_i(\mathbf{r},t)\, e^{-i\omega_j t} \left|j\right\rangle\right] \\
&= -\sum_i \boldsymbol{\mathcal{E}}(\mathbf{r},t)\cdot\boldsymbol{\mu}_{ai}\, c_i(\mathbf{r},t)\, e^{-i\omega_i t} \left|a\right\rangle - \sum_i \boldsymbol{\mathcal{E}}(\mathbf{r},t)\cdot\boldsymbol{\mu}_{bi}\, c_i(\mathbf{r},t)\, e^{-i\omega_i t} \left|b\right\rangle \\
&\quad - \sum_i \boldsymbol{\mathcal{E}}^*(\mathbf{r},t)\cdot\boldsymbol{\mu}^*_{ai}\, c_a(\mathbf{r},t)\, e^{-i\omega_a t} \left|i\right\rangle - \sum_i \boldsymbol{\mathcal{E}}^*(\mathbf{r},t)\cdot\boldsymbol{\mu}^*_{bi}\, c_b(\mathbf{r},t)\, e^{-i\omega_b t} \left|i\right\rangle
\end{aligned} \tag{1.2.7}$$

If we sum the two parts of the right-hand side and match state kets with the left-hand side (1.2.5), we get two plus infinity ($a$, $b$, and the infinitely many $i$) coupled differential equations for the state coefficients:

$$\dot{c}_a(\mathbf{r},t) = \frac{i}{\hbar}\sum_i \boldsymbol{\mathcal{E}}(\mathbf{r},t)\cdot\boldsymbol{\mu}_{ai}\, c_i(\mathbf{r},t)\, e^{-i(\omega_i-\omega_a)t} \tag{1.2.8a}$$

$$\dot{c}_b(\mathbf{r},t) = \frac{i}{\hbar}\sum_i \boldsymbol{\mathcal{E}}(\mathbf{r},t)\cdot\boldsymbol{\mu}_{bi}\, c_i(\mathbf{r},t)\, e^{-i(\omega_i-\omega_b)t} \tag{1.2.8b}$$

$$\dot{c}_i(\mathbf{r},t) = \frac{i}{\hbar}\,\boldsymbol{\mathcal{E}}^*(\mathbf{r},t)\cdot\Big[\boldsymbol{\mu}^*_{ai}\, c_a(\mathbf{r},t)\, e^{i(\omega_i-\omega_a)t} + \boldsymbol{\mu}^*_{bi}\, c_b(\mathbf{r},t)\, e^{i(\omega_i-\omega_b)t}\Big] \tag{1.2.8c}$$

These expressions are still exact, but there isn't much we can do with them.

### 1.2.3 Eliminating the Electronic States

Our next step will be to eliminate the equations for the $c_i(t)$ by assuming that we cannot access the electronic states via single-photon resonant transitions. To see that dependence, we need to insert the decomposition of the electric field into cavity modes (1.2.3) into the coupled differential equation for $c_i(t)$ (1.2.8c) (noting that $\boldsymbol{\mathcal{E}}^* = \boldsymbol{\mathcal{E}}$, because it is purely real).

$$\begin{aligned}
\dot{c}_i(\mathbf{r},t) &= \frac{i}{\hbar}\frac{1}{2}\sum_q \left[\mathcal{E}_q(t)\, e^{-i\omega_q t}\,\mathbf{u}_q(\mathbf{r}) + \mathcal{E}_q^*(t)\, e^{i\omega_q t}\,\mathbf{u}_q^*(\mathbf{r})\right] \\
&\qquad \times \left[\boldsymbol{\mu}_{ai}^*\, c_a(\mathbf{r},t)\, e^{i(\omega_i-\omega_a)t} + \boldsymbol{\mu}_{bi}^*\, c_b(\mathbf{r},t)\, e^{i(\omega_i-\omega_b)t}\right] \\
&= \frac{i}{2\hbar}\sum_q \Big[\mathcal{E}_q(t)\, e^{-i\omega_q t}\,\mathbf{u}_q(\mathbf{r})\cdot\boldsymbol{\mu}_{ai}^*\, c_a(\mathbf{r},t)\, e^{i(\omega_i-\omega_a)t} \\
&\qquad\qquad + \mathcal{E}_q^*(t)\, e^{i\omega_q t}\,\mathbf{u}_q^*(\mathbf{r})\cdot\boldsymbol{\mu}_{ai}^*\, c_a(\mathbf{r},t)\, e^{i(\omega_i-\omega_a)t} \\
&\qquad\qquad + \mathcal{E}_q(t)\, e^{-i\omega_q t}\,\mathbf{u}_q(\mathbf{r})\cdot\boldsymbol{\mu}_{bi}^*\, c_b(\mathbf{r},t)\, e^{i(\omega_i-\omega_b)t} \\
&\qquad\qquad + \mathcal{E}_q^*(t)\, e^{i\omega_q t}\,\mathbf{u}_q^*(\mathbf{r})\cdot\boldsymbol{\mu}_{bi}^*\, c_b(\mathbf{r},t)\, e^{i(\omega_i-\omega_b)t}\Big] \\
&= \frac{i}{2\hbar}\sum_q \Big[\mathcal{E}_q(t)\,\mathbf{u}_q(\mathbf{r})\cdot\boldsymbol{\mu}_{ai}^*\, c_a(\mathbf{r},t)\, e^{i(\omega_i-\omega_a-\omega_q)t} \\
&\qquad\qquad + \mathcal{E}_q^*(t)\,\mathbf{u}_q^*(\mathbf{r})\cdot\boldsymbol{\mu}_{ai}^*\, c_a(\mathbf{r},t)\, e^{i(\omega_i-\omega_a+\omega_q)t} \\
&\qquad\qquad + \mathcal{E}_q(t)\,\mathbf{u}_q(\mathbf{r})\cdot\boldsymbol{\mu}_{bi}^*\, c_b(\mathbf{r},t)\, e^{i(\omega_i-\omega_b-\omega_q)t} \\
&\qquad\qquad + \mathcal{E}_q^*(t)\,\mathbf{u}_q^*(\mathbf{r})\cdot\boldsymbol{\mu}_{bi}^*\, c_b(\mathbf{r},t)\, e^{i(\omega_i-\omega_b+\omega_q)t}\Big]
\end{aligned} \tag{1.2.9}$$

Because we aren't near any single-photon resonances, all of the frequency differences in the exponentials are large, and are much faster than the variation in $c_a(t)$, $c_b(t)$, or $\mathcal{E}_q$, which are all slowly-varying envelopes. We are therefore justified in treating them as constants and formally

integrating this equation in time, using $\int e^{\alpha t} = e^{\alpha t}/\alpha$:

$$\begin{aligned} c_i(\mathbf{r},t) = \frac{1}{2\hbar}\sum_q \Bigg[ & \frac{\mathcal{E}_q(t)\,\mathbf{u}_q(\mathbf{r})\cdot\boldsymbol{\mu}^*_{ai}\,c_a(\mathbf{r},t)}{\omega_i-\omega_a-\omega_q}\,e^{i(\omega_i-\omega_a-\omega_q)t} \\ & + \frac{\mathcal{E}^*_q(t)\mathbf{u}^*_q(\mathbf{r})\cdot\boldsymbol{\mu}^*_{ai}\,c_a(\mathbf{r},t)}{\omega_i-\omega_a+\omega_q}\,e^{i(\omega_i-\omega_a+\omega_q)t} \\ & + \frac{\mathcal{E}_q(t)\,\mathbf{u}_q(\mathbf{r})\cdot\boldsymbol{\mu}^*_{bi}\,c_b(\mathbf{r},t)}{\omega_i-\omega_b-\omega_q}\,e^{i(\omega_i-\omega_b-\omega_q)t} \\ & + \frac{\mathcal{E}^*_q(t)\mathbf{u}^*_q(\mathbf{r})\cdot\boldsymbol{\mu}^*_{bi}\,c_b(\mathbf{r},t)}{\omega_i-\omega_b+\omega_q}\,e^{i(\omega_i-\omega_b+\omega_q)t}\Bigg] \end{aligned} \tag{1.2.10}$$

If we plug in the electric field decomposition into $c_b(\mathbf{r},t)$, we find that

$$\begin{aligned} \dot{c}_b(\mathbf{r},t) &= \frac{i}{\hbar}\sum_i \frac{1}{2}\sum_q \left[\mathcal{E}_q(t)\,e^{-i\omega_q t}\,\mathbf{u}_q(\mathbf{r}) + \mathcal{E}^*_q(t)\,e^{i\omega_q t}\,\mathbf{u}^*_q(\mathbf{r})\right]\cdot\boldsymbol{\mu}_{bi}\,c_i(\mathbf{r},t)\,e^{-i(\omega_i-\omega_b)t} \\ &= \frac{i}{2\hbar}\sum_i\sum_q \left[\mathcal{E}_q(t)\,\mathbf{u}_q(\mathbf{r})\cdot\boldsymbol{\mu}_{bi}\,e^{-i(\omega_i-\omega_b+\omega_q)t} + \mathcal{E}^*_q(t)\,\mathbf{u}^*_q(\mathbf{r})\cdot\boldsymbol{\mu}_{bi}\,e^{-i(\omega_i-\omega_b-\omega_q)t}\right]\,c_i(\mathbf{r},t) \end{aligned} \tag{1.2.11}$$

Now we plug in $c_i(t)$ from (1.2.10):

$$\begin{aligned} \dot{c}_b(\mathbf{r},t) = \frac{i}{4\hbar^2}\sum_i\sum_q & \left[\mathcal{E}_q(t)\,\mathbf{u}_q(\mathbf{r})\cdot\boldsymbol{\mu}_{bi}\,e^{-i(\omega_i-\omega_b+\omega_q)t} + \mathcal{E}^*_q(t)\,\mathbf{u}^*_q(\mathbf{r})\cdot\boldsymbol{\mu}_{bi}\,e^{-i(\omega_i-\omega_b-\omega_q)t}\right] \\ \times\sum_r \Bigg[ & \frac{\mathcal{E}_r(t)\,\mathbf{u}_r(\mathbf{r})\cdot\boldsymbol{\mu}^*_{ai}\,c_a(\mathbf{r},t)}{\omega_i-\omega_a-\omega_r}\,e^{i(\omega_i-\omega_a-\omega_r)t} \\ & + \frac{\mathcal{E}^*_r(t)\mathbf{u}^*_r(\mathbf{r})\cdot\boldsymbol{\mu}^*_{ai}\,c_a(\mathbf{r},t)}{\omega_i-\omega_a+\omega_r}\,e^{i(\omega_i-\omega_a+\omega_r)t} \\ & + \frac{\mathcal{E}_r(t)\,\mathbf{u}_r(\mathbf{r})\cdot\boldsymbol{\mu}^*_{bi}\,c_b(\mathbf{r},t)}{\omega_i-\omega_b-\omega_r}\,e^{i(\omega_i-\omega_b-\omega_r)t} \\ & + \frac{\mathcal{E}^*_r(t)\mathbf{u}^*_r(\mathbf{r})\cdot\boldsymbol{\mu}^*_{bi}\,c_b(\mathbf{r},t)}{\omega_i-\omega_b+\omega_r}\,e^{i(\omega_i-\omega_b+\omega_r)t}\Bigg] \end{aligned} \tag{1.2.12}$$

This product results in eight terms:

$$\begin{aligned}
\dot{c}_b(\mathbf{r},t) = \frac{i}{4\hbar^2}\sum_i\sum_q\sum_r\Bigg[ & \\
& \frac{\mathcal{E}_q(t)\,\mathcal{E}_r(t)\,[\mathbf{u}_q(\mathbf{r})\cdot\boldsymbol{\mu}_{bi}][\mathbf{u}_r(\mathbf{r})\cdot\boldsymbol{\mu}^*_{ai}]}{\omega_i-\omega_a-\omega_r}\,e^{-i(\omega_a-\omega_b+\omega_q+\omega_r)t}\,c_a(\mathbf{r},t) \\
& + \frac{\mathcal{E}_q(t)\,\mathcal{E}^*_r(t)\,[\mathbf{u}_q(\mathbf{r})\cdot\boldsymbol{\mu}_{bi}][\mathbf{u}^*_r(\mathbf{r})\cdot\boldsymbol{\mu}^*_{ai}]}{\omega_i-\omega_a+\omega_r}\,e^{-i(\omega_a-\omega_b+\omega_q-\omega_r)t}\,c_a(\mathbf{r},t) \\
& + \frac{\mathcal{E}_q(t)\,\mathcal{E}_r(t)\,[\mathbf{u}_q(\mathbf{r})\cdot\boldsymbol{\mu}_{bi}][\mathbf{u}_r(\mathbf{r})\cdot\boldsymbol{\mu}^*_{bi}]}{\omega_i-\omega_b-\omega_r}\,e^{-i(\omega_q+\omega_r)t}\,c_b(\mathbf{r},t) \\
& + \frac{\mathcal{E}_q(t)\,\mathcal{E}^*_r(t)\,[\mathbf{u}_q(\mathbf{r})\cdot\boldsymbol{\mu}_{bi}][\mathbf{u}^*_r(\mathbf{r})\cdot\boldsymbol{\mu}^*_{bi}]}{\omega_i-\omega_b+\omega_r}\,e^{-i(\omega_q-\omega_r)t}\,c_b(\mathbf{r},t) \\
& + \frac{\mathcal{E}^*_q(t)\,\mathcal{E}_r(t)\,\left[\mathbf{u}^*_q(\mathbf{r})\cdot\boldsymbol{\mu}_{bi}\right][\mathbf{u}_r(\mathbf{r})\cdot\boldsymbol{\mu}^*_{ai}]}{\omega_i-\omega_a-\omega_r}\,e^{-i(\omega_a-\omega_b-\omega_q+\omega_r)t}\,c_a(\mathbf{r},t) \\
& + \frac{\mathcal{E}^*_q(t)\,\mathcal{E}^*_r(t)\,\left[\mathbf{u}^*_q(\mathbf{r})\cdot\boldsymbol{\mu}_{bi}\right][\mathbf{u}^*_r(\mathbf{r})\cdot\boldsymbol{\mu}^*_{ai}]}{\omega_i-\omega_a+\omega_r}\,e^{-i(\omega_a-\omega_b-\omega_q-\omega_r)t}\,c_a(\mathbf{r},t) \\
& + \frac{\mathcal{E}^*_q(t)\,\mathcal{E}_r(t)\,\left[\mathbf{u}^*_q(\mathbf{r})\cdot\boldsymbol{\mu}_{bi}\right][\mathbf{u}_r(\mathbf{r})\cdot\boldsymbol{\mu}^*_{bi}]}{\omega_i-\omega_b-\omega_r}\,e^{-i(-\omega_q+\omega_r)t}\,c_b(\mathbf{r},t) \\
& + \frac{\mathcal{E}^*_q(t)\,\mathcal{E}^*_r(t)\,\left[\mathbf{u}^*_q(\mathbf{r})\cdot\boldsymbol{\mu}_{bi}\right][\mathbf{u}^*_r(\mathbf{r})\cdot\boldsymbol{\mu}^*_{bi}]}{\omega_i-\omega_b+\omega_r}\,e^{-i(-\omega_q-\omega_r)t}\,c_b(\mathbf{r},t)\Bigg]
\end{aligned} \tag{1.2.13}$$

Note that there was a great deal of cancellation in the frequency and decay terms. Be careful with the "product of dot products" - there is *no dot product between the two cavity modes*!

At this point we'll make a big assumption: that the system is almost always in the ground state, so that $c_a(t) \approx 1$ for all times $t$. Additionally, $c_b(\mathbf{r},t)$ is slowly-varying in time, so we can neglect any terms where the exponential cannot cancel down to near-zero frequency. The only terms where this can happen are ones where we have the same number of positive and negative frequencies in the exponents. Equivalently, they are the only terms where the two electric field mode expansion coefficients are not both conjugated or un-conjugated. Those are the second, fourth, fifth, and

seventh terms, which leaves us with

$$\dot{c}_b(\mathbf{r},t) = \frac{i}{4\hbar^2}\sum_i\sum_q\sum_r\Bigg[ \frac{\mathcal{E}_q(t)\,\mathcal{E}_r^*(t)\,[\mathbf{u}_q(\mathbf{r})\cdot\boldsymbol{\mu}_{bi}][\mathbf{u}_r^*(\mathbf{r})\cdot\boldsymbol{\mu}_{ai}^*]}{\omega_i-\omega_a+\omega_r}\,e^{-i(\omega_a-\omega_b+\omega_q-\omega_r)t} + \frac{\mathcal{E}_q(t)\,\mathcal{E}_r^*(t)\,[\mathbf{u}_q(\mathbf{r})\cdot\boldsymbol{\mu}_{bi}][\mathbf{u}_r^*(\mathbf{r})\cdot\boldsymbol{\mu}_{bi}^*]}{\omega_i-\omega_b+\omega_r}\,e^{-i(\omega_q-\omega_r)t}\,c_b(\mathbf{r},t) + \frac{\mathcal{E}_q^*(t)\,\mathcal{E}_r(t)\,\left[\mathbf{u}_q^*(\mathbf{r})\cdot\boldsymbol{\mu}_{bi}\right][\mathbf{u}_r(\mathbf{r})\cdot\boldsymbol{\mu}_{ai}^*]}{\omega_i-\omega_a-\omega_r}\,e^{-i(\omega_a-\omega_b-\omega_q+\omega_r)t} + \frac{\mathcal{E}_q^*(t)\,\mathcal{E}_r(t)\,\left[\mathbf{u}_q^*(\mathbf{r})\cdot\boldsymbol{\mu}_{bi}\right][\mathbf{u}_r(\mathbf{r})\cdot\boldsymbol{\mu}_{bi}^*]}{\omega_i-\omega_b-\omega_r}\,e^{-i(-\omega_q+\omega_r)t}\,c_b(\mathbf{r},t)\Bigg] \tag{1.2.14}$$

Note that we cannot set $q = r$ in the first and third lines of the result because the cavity modes may be degenerate in frequency. We have also replaced $c_a(\mathbf{r},t)$ with 1.

Now, since we know that all of exponents are still oscillating faster than any of the expansion coefficients, we integrate these equations in time to determine $c_b(\mathbf{r},t)$:

$$c_b(\mathbf{r},t) = \frac{1}{4\hbar^2}\sum_i\sum_q\sum_r\Bigg[ \frac{\mathcal{E}_q(t)\,\mathcal{E}_r^*(t)\,[\mathbf{u}_q(\mathbf{r})\cdot\boldsymbol{\mu}_{bi}][\mathbf{u}_r^*(\mathbf{r})\cdot\boldsymbol{\mu}_{ai}^*]}{(\omega_i-\omega_a+\omega_r)(\omega_a-\omega_b+\omega_q-\omega_r)}\,e^{-i(\omega_a-\omega_b+\omega_q-\omega_r)t} + \frac{\mathcal{E}_q(t)\,\mathcal{E}_r^*(t)\,[\mathbf{u}_q(\mathbf{r})\cdot\boldsymbol{\mu}_{bi}][\mathbf{u}_r^*(\mathbf{r})\cdot\boldsymbol{\mu}_{bi}^*]}{(\omega_i-\omega_b+\omega_r)(\omega_q-\omega_r)}\,e^{-i(\omega_q-\omega_r)t}\,c_b(\mathbf{r},t) + \frac{\mathcal{E}_q^*(t)\,\mathcal{E}_r(t)\,\left[\mathbf{u}_q^*(\mathbf{r})\cdot\boldsymbol{\mu}_{bi}\right][\mathbf{u}_r(\mathbf{r})\cdot\boldsymbol{\mu}_{ai}^*]}{(\omega_i-\omega_a-\omega_r)(\omega_a-\omega_b-\omega_q+\omega_r)}\,e^{-i(\omega_a-\omega_b-\omega_q+\omega_r)t} + \frac{\mathcal{E}_q^*(t)\,\mathcal{E}_r(t)\,\left[\mathbf{u}_q^*(\mathbf{r})\cdot\boldsymbol{\mu}_{bi}\right][\mathbf{u}_r(\mathbf{r})\cdot\boldsymbol{\mu}_{bi}^*]}{(\omega_i-\omega_b-\omega_r)(-\omega_q+\omega_r)}\,e^{-i(-\omega_q+\omega_r)t}\,c_b(\mathbf{r},t)\Bigg] \tag{1.2.15}$$

Solving for $c_b(\mathbf{r},t)$ yields

$$c_b(\mathbf{r},t) = \frac{\frac{1}{4\hbar^2}\sum_{i,q,r}[A+B]}{1-\frac{1}{4\hbar^2}\sum_{i,q,r}[C+D]} \tag{1.2.16}$$

where

$$A = \frac{\mathcal{E}_q^*(t)\,\mathcal{E}_r(t)\,\left[\mathbf{u}_q^*(\mathbf{r})\cdot\boldsymbol{\mu}_{bi}\right]\left[\mathbf{u}_r(\mathbf{r})\cdot\boldsymbol{\mu}_{ai}^*\right]}{(\omega_i-\omega_a-\omega_r)(\omega_a-\omega_b-\omega_q+\omega_r)}\,e^{-i(\omega_a-\omega_b-\omega_q+\omega_r)t} \tag{1.2.17a}$$

$$B = \frac{\mathcal{E}_q^*(t)\,\mathcal{E}_r(t)\,\left[\mathbf{u}_q^*(\mathbf{r})\cdot\boldsymbol{\mu}_{bi}\right]\left[\mathbf{u}_r(\mathbf{r})\cdot\boldsymbol{\mu}_{ai}^*\right]}{(\omega_i-\omega_a-\omega_r)(\omega_a-\omega_b-\omega_q+\omega_r)}\,e^{-i(\omega_a-\omega_b-\omega_q+\omega_r)t} \tag{1.2.17b}$$

$$C = \frac{\mathcal{E}_q(t)\,\mathcal{E}_r^*(t)\,[\mathbf{u}_q(\mathbf{r})\cdot\boldsymbol{\mu}_{bi}][\mathbf{u}_r^*(\mathbf{r})\cdot\boldsymbol{\mu}_{bi}^*]}{(\omega_i-\omega_b+\omega_r)(\omega_q-\omega_r)}\,e^{-i(\omega_q-\omega_r)t} \tag{1.2.17c}$$

$$D = \frac{\mathcal{E}_q^*(t)\,\mathcal{E}_r(t)\,\left[\mathbf{u}_q^*(\mathbf{r})\cdot\boldsymbol{\mu}_{bi}\right]\left[\mathbf{u}_r(\mathbf{r})\cdot\boldsymbol{\mu}_{bi}^*\right]}{(\omega_i-\omega_b-\omega_r)(-\omega_q+\omega_r)}\,e^{-i(-\omega_q+\omega_r)t} \tag{1.2.17d}$$

We will assume that the last two terms in the denominator are small enough that the denominator is always approximately equal to 1. Then we have

$$c_b(\mathbf{r},t) = \frac{1}{4\hbar^2}\sum_{i,q,r}\left[\frac{\mathcal{E}_q(t)\,\mathcal{E}_r^*(t)\,[\mathbf{u}_q(\mathbf{r})\cdot\boldsymbol{\mu}_{bi}][\mathbf{u}_r^*(\mathbf{r})\cdot\boldsymbol{\mu}_{ai}^*]}{(\omega_i-\omega_a+\omega_r)\Delta_{qr}}\,e^{-i\Delta_{qr}t}\right.$$
$$\left.+\frac{\mathcal{E}_q^*(t)\,\mathcal{E}_r(t)\,\left[\mathbf{u}_q^*(\mathbf{r})\cdot\boldsymbol{\mu}_{bi}\right]\left[\mathbf{u}_r(\mathbf{r})\cdot\boldsymbol{\mu}_{ai}^*\right]}{(\omega_i-\omega_a-\omega_r)\Delta_{rq}}\,e^{-i\Delta_{rq}t}\right] \tag{1.2.18}$$

where

$$\Delta_{xy} = (\omega_x-\omega_y)-\omega_m = (\omega_x-\omega_y)-(\omega_b-\omega_a) \tag{1.2.19}$$

is a two-photon detuning from the modulation frequency $\omega_m = \omega_b - \omega_a$. Note that $\Delta_{qr} \neq -\Delta_{rq}$.

### 1.2.4 Assuming an Isotropic Medium

If the medium is isotropic, we have $\mathbf{u}_q(\mathbf{r})\cdot\boldsymbol{\mu} = u_q(\mathbf{r})\,\bar{\mu}$, where $u_q(\mathbf{r})$ is the magnitude of the mode shape function at position $\mathbf{r}$, and $\bar{\mu}$ is the magnitude of the ensemble-average dipole moment of the medium. We don't really know how to calculate $\bar{\mu}$ from the actual microscopic quantum dipole moments, so this will essentially end up being a free parameter that we need to set based on

experimental measurements of the medium. Now we have

$$c_b(\mathbf{r},t) = \frac{1}{4\hbar^2}\sum_{q,r}\left[\left[\sum_i \frac{\bar{\mu}_{ai}\bar{\mu}_{bi}}{\omega_i-\omega_a+\omega_r}\right]\frac{\mathcal{E}_q(t)\,\mathcal{E}_r^*(t)\,u_q(\mathbf{r})\,u_r(\mathbf{r})}{\Delta_{qr}}\,e^{-i\Delta_{qr}t} + \left[\sum_i \frac{\bar{\mu}_{ai}\bar{\mu}_{bi}}{\omega_i-\omega_a-\omega_r}\right]\frac{\mathcal{E}_q^*(t)\,\mathcal{E}_r(t)\,u_q(\mathbf{r})\,u_r(\mathbf{r})}{\Delta_{rq}}\,e^{-i\Delta_{rq}t}\right] \tag{1.2.20}$$

Define

$$\mathcal{E}_{qr} = \mathcal{E}_q(t)\,\mathcal{E}_r^*(t) = (\mathcal{E}_{rq})^* \tag{1.2.21a}$$

$$u_{qr} = u_q(\mathbf{r})\,u_r(\mathbf{r}) = (u_{qr})^* \tag{1.2.21b}$$

$$\theta_{qr} = e^{-i(\omega_q-\omega_r)t} \tag{1.2.21c}$$

$$\omega_{abc\cdots}^{xyz\cdots} = \omega_a+\omega_b+\omega_c+\cdots-\omega_x-\omega_y-\omega_z-\cdots \tag{1.2.21d}$$

Then we can compact the above expression down to

$$c_b(\mathbf{r},t) = \frac{1}{4\hbar^2}\sum_{q,r} u_{qr}\left[\left[\sum_i \frac{\bar{\mu}_{ai}\bar{\mu}_{bi}}{\omega_{ir}^a}\right]\frac{\mathcal{E}_{qr}}{\Delta_{qr}}\,\theta_{qr}\,\theta_{ab} + \left[\sum_i \frac{\bar{\mu}_{ai}\bar{\mu}_{bi}}{\omega_i^{ar}}\right]\frac{\mathcal{E}_{rq}}{\Delta_{rq}}\,\theta_{rq}\,\theta_{ab}\right] \tag{1.2.22}$$

### 1.2.5 The Macroscopic Nonlinear Polarization

Now that we know the quantum state of the microsystems that compose the medium, we can determine the polarization of a single microsystem $\mathbf{P}(\mathbf{r},t)$. The polarization will then tell us how the electric field propagates through the medium through a wave equation derived from Maxwell's equations. Note that this is only the nonlinear part of the polarization. The linear part should be included post-facto using a measured index of refraction.

By definition, the macroscopic polarization is the expectation value of the polarization operator:

$$\mathbf{P}(\mathbf{r},t) = \langle\Psi(t)|\widehat{\mathbf{P}}|\Psi(t)\rangle \tag{1.2.23}$$

where

$$\widehat{\mathbf{P}} = -\sum_i \boldsymbol{\mu}_{ai}\,|a\rangle\langle i| - \sum_i \boldsymbol{\mu}_{bi}\,|b\rangle\langle i| - \sum_i \boldsymbol{\mu}_{ai}^*\,|i\rangle\langle a| - \sum_i \boldsymbol{\mu}_{bi}^*\,|i\rangle\langle b| \tag{1.2.24}$$

Let's calculate $\widehat{\mathbf{P}}\,|\Psi(t)\rangle$ first, using the wavefunction expansion (1.2.1):

$$\begin{aligned}
\widehat{\mathbf{P}}\,|\Psi(t)\rangle &= \left(\sum_i \boldsymbol{\mu}_{ai}\,|a\rangle\langle i| + \sum_i \boldsymbol{\mu}_{bi}\,|b\rangle\langle i| + \sum_i \boldsymbol{\mu}^*_{ai}\,|i\rangle\langle a| + \sum_i \boldsymbol{\mu}^*_{bi}\,|i\rangle\langle b|\right) \\
&\qquad \times \left(c_a(\mathbf{r},t)\,e^{-i\omega_a t}\,|a\rangle + c_b(\mathbf{r},t)\,e^{-i\omega_b t}\,|b\rangle + \sum_i c_i(\mathbf{r},t)\,e^{-i\omega_i t}\,|i\rangle\right) \\
&= \sum_i \boldsymbol{\mu}_{ai}\,c_i(\mathbf{r},t)\,e^{-i\omega_i t}\,|a\rangle + \sum_i \boldsymbol{\mu}_{bi}\,c_i(\mathbf{r},t)\,e^{-i\omega_i t}\,|b\rangle \\
&\quad + \sum_i \boldsymbol{\mu}^*_{ai}\,c_a(\mathbf{r},t)\,e^{-i\omega_a t}\,|i\rangle + \sum_i \boldsymbol{\mu}^*_{bi}\,c_b(\mathbf{r},t)\,e^{-i\omega_b t}\,|i\rangle
\end{aligned} \tag{1.2.25}$$

Now act on that from the left with $\langle\Psi(\mathbf{r},t)|$:

$$\begin{aligned}
\mathbf{P}(\mathbf{r},t) &= \langle\Psi(t)|\widehat{\mathbf{P}}|\Psi(t)\rangle \\
&= \left(c^*_a(\mathbf{r},t)\,e^{i\omega_a t}\,\langle a| + c^*_b(\mathbf{r},t)\,e^{i\omega_b t}\,\langle b| + \sum_i c^*_i(\mathbf{r},t)\,e^{i\omega_i t}\,\langle i|\right) \\
&\qquad \times \left(\sum_i \boldsymbol{\mu}_{ai}\,c_i(\mathbf{r},t)\,e^{-i\omega_i t}\,|a\rangle + \sum_i \boldsymbol{\mu}_{bi}\,c_i(\mathbf{r},t)\,e^{-i\omega_i t}\,|b\rangle\right. \\
&\qquad\quad \left. + \sum_i \boldsymbol{\mu}^*_{ai}\,c_a(\mathbf{r},t)\,e^{-i\omega_a t}\,|i\rangle + \sum_i \boldsymbol{\mu}^*_{bi}\,c_b(\mathbf{r},t)\,e^{-i\omega_b t}\,|i\rangle)\right) \\
&= \sum_i \boldsymbol{\mu}_{ai}\,c^*_a(\mathbf{r},t)\,c_i(\mathbf{r},t)\,e^{i(\omega_a-\omega_i)t} + \sum_i \boldsymbol{\mu}_{bi}\,c^*_b(\mathbf{r},t)\,c_i(\mathbf{r},t)\,e^{i(\omega_b-\omega_i)t} \\
&\quad + \sum_i \boldsymbol{\mu}^*_{ai}\,c_a(\mathbf{r},t)\,c^*_i(\mathbf{r},t)\,e^{i(\omega_i-\omega_a)t} + \sum_i \boldsymbol{\mu}^*_{bi}\,c_b(\mathbf{r},t)\,c^*_i(\mathbf{r},t)\,e^{i(\omega_i-\omega_b)t}
\end{aligned} \tag{1.2.26}$$

Unfortunately, we now need to plug in $c_i(\mathbf{r},t)$ from (1.2.10). Take it term-by-term. The first is

$$\begin{aligned}
\sum_i \boldsymbol{\mu}_{ai}\, c_a^*(\mathbf{r},t)\, c_i(\mathbf{r},t)\, e^{i(\omega_a-\omega_i)t} &= \sum_i \boldsymbol{\mu}_{ai}\, c_a^*(\mathbf{r},t)\, e^{i(\omega_a-\omega_i)t} \\
&\quad \times \frac{1}{2\hbar}\sum_q \left[ \frac{\mathcal{E}_q(t)\, \mathbf{u}_q(\mathbf{r})\cdot\boldsymbol{\mu}_{ai}^*\, c_a(\mathbf{r},t)}{\omega_i-\omega_a-\omega_q}\, e^{i(\omega_i-\omega_a-\omega_q)t} \right. \\
&\qquad + \frac{\mathcal{E}_q^*(t)\mathbf{u}_q^*(\mathbf{r})\cdot\boldsymbol{\mu}_{ai}^*\, c_a(\mathbf{r},t)}{\omega_i-\omega_a+\omega_q}\, e^{i(\omega_i-\omega_a+\omega_q)t} \\
&\qquad + \frac{\mathcal{E}_q(t)\, \mathbf{u}_q(\mathbf{r})\cdot\boldsymbol{\mu}_{bi}^*\, c_b(\mathbf{r},t)}{\omega_i-\omega_b-\omega_q}\, e^{i(\omega_i-\omega_b-\omega_q)t} \\
&\qquad \left. + \frac{\mathcal{E}_q^*(t)\mathbf{u}_q^*(\mathbf{r})\cdot\boldsymbol{\mu}_{bi}^*\, c_b(\mathbf{r},t)}{\omega_i-\omega_b+\omega_q}\, e^{i(\omega_i-\omega_b+\omega_q)t} \right] \\
&= \frac{1}{2\hbar}\sum_i\sum_q \frac{\mathcal{E}_q(t)\, \boldsymbol{\mu}_{ai}\big[\mathbf{u}_q(\mathbf{r})\cdot\boldsymbol{\mu}_{ai}^*\big]}{\omega_i-\omega_a-\omega_q}\, |c_a(\mathbf{r},t)|^2\, e^{-i\omega_q t} \\
&\quad + \frac{1}{2\hbar}\sum_i\sum_q \frac{\mathcal{E}_q^*(t)\, \boldsymbol{\mu}_{ai}\big[\mathbf{u}_q^*(\mathbf{r})\cdot\boldsymbol{\mu}_{ai}^*\big]}{\omega_i-\omega_a+\omega_q}\, |c_a(\mathbf{r},t)|^2\, e^{i\omega_q t} \\
&\quad + \frac{1}{2\hbar}\sum_i\sum_q \frac{\mathcal{E}_q(t)\, \boldsymbol{\mu}_{ai}\big[\mathbf{u}_q(\mathbf{r})\cdot\boldsymbol{\mu}_{bi}^*\big]}{\omega_i-\omega_b-\omega_q}\, c_a^*(\mathbf{r},t)\, c_b(\mathbf{r},t)\, e^{i(\omega_a-\omega_b-\omega_q)t} \\
&\quad + \frac{1}{2\hbar}\sum_i\sum_q \frac{\mathcal{E}_q^*(t)\, \boldsymbol{\mu}_{ai}\big[\mathbf{u}_q^*(\mathbf{r})\cdot\boldsymbol{\mu}_{bi}^*\big]}{\omega_i-\omega_b+\omega_q}\, c_a^*(\mathbf{r},t)\, c_b(\mathbf{r},t)\, e^{i(\omega_a-\omega_b+\omega_q)t}
\end{aligned} \tag{1.2.27}$$

The second term is

$$\begin{aligned}
\sum_i \boldsymbol{\mu}_{bi}\, c_b^*(\mathbf{r},t)\, c_i(\mathbf{r},t)\, e^{i(\omega_b-\omega_i)t} &= \sum_i \boldsymbol{\mu}_{bi}\, c_b^*(\mathbf{r},t)\, e^{i(\omega_b-\omega_i)t} \\
&\quad \times \frac{1}{2\hbar}\sum_q \left[ \frac{\mathcal{E}_q(t)\, \mathbf{u}_q(\mathbf{r})\cdot\boldsymbol{\mu}_{ai}^*\, c_a(\mathbf{r},t)}{\omega_i-\omega_a-\omega_q}\, e^{i(\omega_i-\omega_a-\omega_q)t} \right. \\
&\qquad + \frac{\mathcal{E}_q^*(t)\mathbf{u}_q^*(\mathbf{r})\cdot\boldsymbol{\mu}_{ai}^*\, c_a(\mathbf{r},t)}{\omega_i-\omega_a+\omega_q}\, e^{i(\omega_i-\omega_a+\omega_q)t} \\
&\qquad + \frac{\mathcal{E}_q(t)\, \mathbf{u}_q(\mathbf{r})\cdot\boldsymbol{\mu}_{bi}^*\, c_b(\mathbf{r},t)}{\omega_i-\omega_b-\omega_q}\, e^{i(\omega_i-\omega_b-\omega_q)t} \\
&\qquad \left. + \frac{\mathcal{E}_q^*(t)\mathbf{u}_q^*(\mathbf{r})\cdot\boldsymbol{\mu}_{bi}^*\, c_b(\mathbf{r},t)}{\omega_i-\omega_b+\omega_q}\, e^{i(\omega_i-\omega_b+\omega_q)t} \right] \\
&= \frac{1}{2\hbar}\sum_i\sum_q \frac{\mathcal{E}_q(t)\, \boldsymbol{\mu}_{bi}\left[\mathbf{u}_q(\mathbf{r})\cdot\boldsymbol{\mu}_{ai}^*\right]}{\omega_i-\omega_a-\omega_q}\, c_a(\mathbf{r},t)\, c_b^*(\mathbf{r},t)\, e^{i(\omega_b-\omega_a-\omega_q)t} \\
&\quad + \frac{1}{2\hbar}\sum_i\sum_q \frac{\mathcal{E}_q^*(t)\, \boldsymbol{\mu}_{bi}\left[\mathbf{u}_q^*(\mathbf{r})\cdot\boldsymbol{\mu}_{ai}^*\right]}{\omega_i-\omega_a+\omega_q}\, c_a(\mathbf{r},t)\, c_b^*(\mathbf{r},t)\, e^{i(\omega_b-\omega_a+\omega_q)t} \\
&\quad + \frac{1}{2\hbar}\sum_i\sum_q \frac{\mathcal{E}_q(t)\, \boldsymbol{\mu}_{bi}\left[\mathbf{u}_q(\mathbf{r})\cdot\boldsymbol{\mu}_{bi}^*\right]}{\omega_i-\omega_b-\omega_q}\, |c_b(\mathbf{r},t)|^2\, e^{-i\omega_q t} \\
&\quad + \frac{1}{2\hbar}\sum_i\sum_q \frac{\mathcal{E}_q^*(t)\, \boldsymbol{\mu}_{bi}\left[\mathbf{u}_q^*(\mathbf{r})\cdot\boldsymbol{\mu}_{bi}^*\right]}{\omega_i-\omega_b+\omega_q}\, |c_b(\mathbf{r},t)|^2\, e^{i\omega_q t} \qquad (1.2.28)
\end{aligned}$$

Because of the symmetry in the product, the third and fourth terms are the complex conjugates of the first and second terms, respectively. The products of states coefficients are density matrix elements. Grouping by frequency and density matrix element, the entire sum of sixteen terms can

be written as

$$\begin{aligned}\mathbf{P}(\mathbf{r},t) = \frac{1}{2\hbar}\sum_i\sum_q\Bigg[&\left(\frac{\mathcal{E}_q(t)\,\boldsymbol{\mu}_{ai}\big[\mathbf{u}_q(\mathbf{r})\cdot\boldsymbol{\mu}^*_{ai}\big]}{\omega_i-\omega_a-\omega_q}+\frac{\mathcal{E}_q(t)\,\boldsymbol{\mu}^*_{ai}\big[\mathbf{u}_q(\mathbf{r})\cdot\boldsymbol{\mu}_{ai}\big]}{\omega_i-\omega_a+\omega_q}\right)|c_a(\mathbf{r},t)|^2\,e^{-i\omega_q t}\\
&+\left(\frac{\mathcal{E}^*_q(t)\,\boldsymbol{\mu}_{ai}\big[\mathbf{u}^*_q(\mathbf{r})\cdot\boldsymbol{\mu}^*_{ai}\big]}{\omega_i-\omega_a+\omega_q}+\frac{\mathcal{E}^*_q(t)\,\boldsymbol{\mu}^*_{ai}\big[\mathbf{u}^*_q(\mathbf{r})\cdot\boldsymbol{\mu}_{ai}\big]}{\omega_i-\omega_a-\omega_q}\right)|c_a(\mathbf{r},t)|^2\,e^{i\omega_q t}\\
&+\left(\frac{\mathcal{E}_q(t)\boldsymbol{\mu}_{bi}\big[\mathbf{u}_q(\mathbf{r})\cdot\boldsymbol{\mu}^*_{ai}\big]}{\omega_i-\omega_a-\omega_q}+\frac{\mathcal{E}_q(t)\boldsymbol{\mu}^*_{ai}\big[\mathbf{u}_q(\mathbf{r})\cdot\boldsymbol{\mu}_{bi}\big]}{\omega_i-\omega_b+\omega_q}\right)c_a(\mathbf{r},t)c^*_b(\mathbf{r},t)e^{i(\omega_b-\omega_a)t}e^{-i\omega_q t}\\
&+\left(\frac{\mathcal{E}^*_q(t)\boldsymbol{\mu}_{bi}\big[\mathbf{u}^*_q(\mathbf{r})\cdot\boldsymbol{\mu}^*_{ai}\big]}{\omega_i-\omega_a+\omega_q}+\frac{\mathcal{E}^*_q(t)\boldsymbol{\mu}^*_{ai}\big[\mathbf{u}^*_q(\mathbf{r})\cdot\boldsymbol{\mu}_{bi}\big]}{\omega_i-\omega_b-\omega_q}\right)c_a(\mathbf{r},t)c^*_b(\mathbf{r},t)e^{i(\omega_b-\omega_a)t}e^{i\omega_q t}\\
&+\left(\frac{\mathcal{E}_q(t)\boldsymbol{\mu}_{ai}\big[\mathbf{u}_q(\mathbf{r})\cdot\boldsymbol{\mu}^*_{bi}\big]}{\omega_i-\omega_b-\omega_q}+\frac{\mathcal{E}_q(t)\boldsymbol{\mu}^*_{bi}\big[\mathbf{u}_q(\mathbf{r})\cdot\boldsymbol{\mu}_{ai}\big]}{\omega_i-\omega_a+\omega_q}\right)c^*_a(\mathbf{r},t)c_b(\mathbf{r},t)e^{-i(\omega_b-\omega_a)t}e^{-i\omega_q t}\\
&+\left(\frac{\mathcal{E}^*_q(t)\boldsymbol{\mu}_{ai}\big[\mathbf{u}^*_q(\mathbf{r})\cdot\boldsymbol{\mu}^*_{bi}\big]}{\omega_i-\omega_b+\omega_q}+\frac{\mathcal{E}^*_q(t)\boldsymbol{\mu}^*_{bi}\big[\mathbf{u}^*_q(\mathbf{r})\cdot\boldsymbol{\mu}_{ai}\big]}{\omega_i-\omega_a-\omega_q}\right)c^*_a(\mathbf{r},t)c_b(\mathbf{r},t)e^{-i(\omega_b-\omega_a)t}e^{i\omega_q t}\\
&+\left(\frac{\mathcal{E}_q(t)\boldsymbol{\mu}_{bi}\big[\mathbf{u}_q(\mathbf{r})\cdot\boldsymbol{\mu}^*_{bi}\big]}{\omega_i-\omega_b-\omega_q}+\frac{\mathcal{E}_q(t)\boldsymbol{\mu}^*_{bi}\big[\mathbf{u}_q(\mathbf{r})\cdot\boldsymbol{\mu}_{bi}\big]}{\omega_i-\omega_b+\omega_q}\right)|c_b(\mathbf{r},t)|^2e^{-i\omega_q t}\\
&+\left(\frac{\mathcal{E}^*_q(t)\boldsymbol{\mu}_{bi}\big[\mathbf{u}^*_q(\mathbf{r})\cdot\boldsymbol{\mu}^*_{bi}\big]}{\omega_i-\omega_b+\omega_q}+\frac{\mathcal{E}^*_q(t)\boldsymbol{\mu}^*_{bi}\big[\mathbf{u}^*_q(\mathbf{r})\cdot\boldsymbol{\mu}_{bi}\big]}{\omega_i-\omega_b-\omega_q}\right)|c_b(\mathbf{r},t)|^2e^{i\omega_q t}\Bigg]\end{aligned}\tag{1.2.29}$$

Recall that we are assuming that $c_a(\mathbf{r},t)\approx 1$ and that $c_b(\mathbf{r},t)$ is therefore small enough that $|c_b(\mathbf{r},t)|^2\approx 0$. Then we have

$$\begin{aligned}\mathbf{P}(\mathbf{r},t) = \frac{1}{2\hbar}\sum_i\sum_q\Bigg[&\left(\frac{\mathcal{E}_q(t)\,\boldsymbol{\mu}_{ai}\big[\mathbf{u}_q(\mathbf{r})\cdot\boldsymbol{\mu}^*_{ai}\big]}{\omega_i-\omega_a-\omega_q}+\frac{\mathcal{E}_q(t)\,\boldsymbol{\mu}^*_{ai}\big[\mathbf{u}_q(\mathbf{r})\cdot\boldsymbol{\mu}_{ai}\big]}{\omega_i-\omega_a+\omega_q}\right)e^{-i\omega_q t}\\
&+\left(\frac{\mathcal{E}^*_q(t)\,\boldsymbol{\mu}_{ai}\big[\mathbf{u}^*_q(\mathbf{r})\cdot\boldsymbol{\mu}^*_{ai}\big]}{\omega_i-\omega_a+\omega_q}+\frac{\mathcal{E}^*_q(t)\,\boldsymbol{\mu}^*_{ai}\big[\mathbf{u}^*_q(\mathbf{r})\cdot\boldsymbol{\mu}_{ai}\big]}{\omega_i-\omega_a-\omega_q}\right)e^{i\omega_q t}\\
&+\left(\frac{\mathcal{E}_q(t)\,\boldsymbol{\mu}_{bi}\big[\mathbf{u}_q(\mathbf{r})\cdot\boldsymbol{\mu}^*_{ai}\big]}{\omega_i-\omega_a-\omega_q}+\frac{\mathcal{E}_q(t)\,\boldsymbol{\mu}^*_{ai}\big[\mathbf{u}_q(\mathbf{r})\cdot\boldsymbol{\mu}_{bi}\big]}{\omega_i-\omega_b+\omega_q}\right)c^*_b(\mathbf{r},t)\,e^{i(\omega_b-\omega_a)t}\,e^{-i\omega_q t}\\
&+\left(\frac{\mathcal{E}^*_q(t)\,\boldsymbol{\mu}_{bi}\big[\mathbf{u}^*_q(\mathbf{r})\cdot\boldsymbol{\mu}^*_{ai}\big]}{\omega_i-\omega_a+\omega_q}+\frac{\mathcal{E}^*_q(t)\,\boldsymbol{\mu}^*_{ai}\big[\mathbf{u}^*_q(\mathbf{r})\cdot\boldsymbol{\mu}_{bi}\big]}{\omega_i-\omega_b-\omega_q}\right)c^*_b(\mathbf{r},t)\,e^{i(\omega_b-\omega_a)t}\,e^{i\omega_q t}\\
&+\left(\frac{\mathcal{E}_q(t)\,\boldsymbol{\mu}_{ai}\big[\mathbf{u}_q(\mathbf{r})\cdot\boldsymbol{\mu}^*_{bi}\big]}{\omega_i-\omega_b-\omega_q}+\frac{\mathcal{E}_q(t)\,\boldsymbol{\mu}^*_{bi}\big[\mathbf{u}_q(\mathbf{r})\cdot\boldsymbol{\mu}_{ai}\big]}{\omega_i-\omega_a+\omega_q}\right)c_b(\mathbf{r},t)\,e^{-i(\omega_b-\omega_a)t}\,e^{-i\omega_q t}\\
&+\left(\frac{\mathcal{E}^*_q(t)\,\boldsymbol{\mu}_{ai}\big[\mathbf{u}^*_q(\mathbf{r})\cdot\boldsymbol{\mu}^*_{bi}\big]}{\omega_i-\omega_b+\omega_q}+\frac{\mathcal{E}^*_q(t)\,\boldsymbol{\mu}^*_{bi}\big[\mathbf{u}^*_q(\mathbf{r})\cdot\boldsymbol{\mu}_{ai}\big]}{\omega_i-\omega_a-\omega_q}\right)c_b(\mathbf{r},t)\,e^{-i(\omega_b-\omega_a)t}\,e^{i\omega_q t}\Bigg]\end{aligned}\tag{1.2.30}$$

Compactify:

$$\begin{aligned}\mathbf{P}(\mathbf{r},t) = \frac{1}{2\hbar}\sum_q \Bigg[ &\left[\sum_i \left( \frac{\boldsymbol{\mu}_{ai}\big[\mathbf{u}_q(\mathbf{r})\cdot\boldsymbol{\mu}^*_{ai}\big]}{\omega_i^{aq}} + \frac{\boldsymbol{\mu}^*_{ai}\big[\mathbf{u}_q(\mathbf{r})\cdot\boldsymbol{\mu}_{ai}\big]}{\omega_{ia}^{q}} \right)\right] \mathcal{E}_q(t)\, e^{-i\omega_q t} \\ &+ \left[\sum_i \left( \frac{\boldsymbol{\mu}_{ai}\big[\mathbf{u}^*_q(\mathbf{r})\cdot\boldsymbol{\mu}^*_{ai}\big]}{\omega_{iq}^{a}} + \frac{\boldsymbol{\mu}^*_{ai}\big[\mathbf{u}^*_q(\mathbf{r})\cdot\boldsymbol{\mu}_{ai}\big]}{\omega_i^{aq}} \right)\right] \mathcal{E}^*_q(t)\, e^{i\omega_q t} \\ &+ \left[\sum_i \left( \frac{\boldsymbol{\mu}_{bi}\big[\mathbf{u}_q(\mathbf{r})\cdot\boldsymbol{\mu}^*_{ai}\big]}{\omega_i^{aq}} + \frac{\boldsymbol{\mu}^*_{ai}\big[\mathbf{u}_q(\mathbf{r})\cdot\boldsymbol{\mu}_{bi}\big]}{\omega_{iq}^{b}} \right)\right] \mathcal{E}_q(t)\, c^*_b(\mathbf{r},t)\,\theta_{ab}\, e^{-i\omega_q t} \\ &+ \left[\sum_i \left( \frac{\boldsymbol{\mu}_{bi}\big[\mathbf{u}^*_q(\mathbf{r})\cdot\boldsymbol{\mu}^*_{ai}\big]}{\omega_{iq}^{a}} + \frac{\boldsymbol{\mu}^*_{ai}\big[\mathbf{u}^*_q(\mathbf{r})\cdot\boldsymbol{\mu}_{bi}\big]}{\omega_i^{bq}} \right)\right] \mathcal{E}^*_q(t)\, c^*_b(\mathbf{r},t)\,\theta_{ab}\, e^{i\omega_q t} \\ &+ \left[\sum_i \left( \frac{\boldsymbol{\mu}_{ai}\big[\mathbf{u}_q(\mathbf{r})\cdot\boldsymbol{\mu}^*_{bi}\big]}{\omega_i^{bq}} + \frac{\boldsymbol{\mu}^*_{bi}\big[\mathbf{u}_q(\mathbf{r})\cdot\boldsymbol{\mu}_{ai}\big]}{\omega_{iq}^{a}} \right)\right] \mathcal{E}_q(t)\, c_b(\mathbf{r},t)\,\theta_{ba}\, e^{-i\omega_q t} \\ &+ \left[\sum_i \left( \frac{\boldsymbol{\mu}_{ai}\big[\mathbf{u}^*_q(\mathbf{r})\cdot\boldsymbol{\mu}^*_{bi}\big]}{\omega_{iq}^{b}} + \frac{\boldsymbol{\mu}^*_{bi}\big[\mathbf{u}^*_q(\mathbf{r})\cdot\boldsymbol{\mu}_{ai}\big]}{\omega_i^{aq}} \right)\right] \mathcal{E}^*_q(t)\, c_b(\mathbf{r},t)\,\theta_{ba}\, e^{i\omega_q t}\Bigg] \end{aligned} \tag{1.2.31}$$

Next we'll insert $c_b$ from (1.2.22). Also, we'll allow the two-photon detuning to be complex to

account for the decay of the excited state $|b\rangle$ (i.e., $\omega_b \to \omega_b + i\gamma_b$).

$$
\begin{aligned}
\mathbf{P}(\mathbf{r},t) =& \frac{1}{8\hbar^3}\sum_q \left[ 4\hbar^2 \left[ \sum_i \left( \frac{\boldsymbol{\mu}_{ai}\big[\mathbf{u}_q(\mathbf{r})\cdot\boldsymbol{\mu}^*_{ai}\big]}{\omega_i^{aq}} + \frac{\boldsymbol{\mu}^*_{ai}\big[\mathbf{u}_q(\mathbf{r})\cdot\boldsymbol{\mu}_{ai}\big]}{\omega_{ia}^{q}} \right) \right] \mathcal{E}_q\, e^{-i\omega_q t} \right. \\
&+4\hbar^2 \left[ \sum_i \left( \frac{\boldsymbol{\mu}_{ai}\big[\mathbf{u}^*_q(\mathbf{r})\cdot\boldsymbol{\mu}^*_{ai}\big]}{\omega_{iq}^{a}} + \frac{\boldsymbol{\mu}^*_{ai}\big[\mathbf{u}^*_q(\mathbf{r})\cdot\boldsymbol{\mu}_{ai}\big]}{\omega_i^{aq}} \right) \right] \mathcal{E}^*_q\, e^{i\omega_q t} \\
&+\left[ \sum_i \left( \frac{\boldsymbol{\mu}_{bi}\big[\mathbf{u}_q(\mathbf{r})\cdot\boldsymbol{\mu}^*_{ai}\big]}{\omega_i^{aq}} + \frac{\boldsymbol{\mu}^*_{ai}\big[\mathbf{u}_q(\mathbf{r})\cdot\boldsymbol{\mu}_{bi}\big]}{\omega_{iq}^{b}} \right) \right] \mathcal{E}_q \sum_{s,t} \left[ \sum_j \frac{\bar{\mu}_{aj}\bar{\mu}_{bj}}{\omega_{jt}^{a}} \right] \frac{\mathcal{E}_{ts}\, u_{st}}{\Delta^*_{st}}\, \theta_{ts}\, \theta_{ba}\, \theta_{ab}\, e^{-i\omega_q t} \\
&+\left[ \sum_i \left( \frac{\boldsymbol{\mu}_{bi}\big[\mathbf{u}_q(\mathbf{r})\cdot\boldsymbol{\mu}^*_{ai}\big]}{\omega_i^{aq}} + \frac{\boldsymbol{\mu}^*_{ai}\big[\mathbf{u}_q(\mathbf{r})\cdot\boldsymbol{\mu}_{bi}\big]}{\omega_{iq}^{b}} \right) \right] \mathcal{E}_q \sum_{s,t} \left[ \sum_j \frac{\bar{\mu}_{aj}\bar{\mu}_{bj}}{\omega_{j}^{at}} \right] \frac{\mathcal{E}_{st}\, u_{st}}{\Delta^*_{ts}}\, \theta_{st}\, \theta_{ba}\, \theta_{ab}\, e^{-i\omega_q t} \\
&+\left[ \sum_i \left( \frac{\boldsymbol{\mu}_{bi}\big[\mathbf{u}^*_q(\mathbf{r})\cdot\boldsymbol{\mu}^*_{ai}\big]}{\omega_{iq}^{a}} + \frac{\boldsymbol{\mu}^*_{ai}\big[\mathbf{u}^*_q(\mathbf{r})\cdot\boldsymbol{\mu}_{bi}\big]}{\omega_i^{bq}} \right) \right] \mathcal{E}^*_q \sum_{s,t} \left[ \sum_j \frac{\bar{\mu}_{aj}\bar{\mu}_{bj}}{\omega_{jt}^{a}} \right] \frac{\mathcal{E}_{ts}\, u_{st}}{\Delta^*_{st}}\, \theta_{ts}\, \theta_{ba}\, \theta_{ab}\, e^{i\omega_q t} \\
&+\left[ \sum_i \left( \frac{\boldsymbol{\mu}_{bi}\big[\mathbf{u}^*_q(\mathbf{r})\cdot\boldsymbol{\mu}^*_{ai}\big]}{\omega_{iq}^{a}} + \frac{\boldsymbol{\mu}^*_{ai}\big[\mathbf{u}^*_q(\mathbf{r})\cdot\boldsymbol{\mu}_{bi}\big]}{\omega_i^{bq}} \right) \right] \mathcal{E}^*_q \sum_{s,t} \left[ \sum_j \frac{\bar{\mu}_{aj}\bar{\mu}_{bj}}{\omega_{j}^{at}} \right] \frac{\mathcal{E}_{st}\, u_{st}}{\Delta^*_{ts}}\, \theta_{st}\, \theta_{ba}\, \theta_{ab}\, e^{i\omega_q t} \\
&+\left[ \sum_i \left( \frac{\boldsymbol{\mu}_{ai}\big[\mathbf{u}_q(\mathbf{r})\cdot\boldsymbol{\mu}^*_{bi}\big]}{\omega_i^{bq}} + \frac{\boldsymbol{\mu}^*_{bi}\big[\mathbf{u}_q(\mathbf{r})\cdot\boldsymbol{\mu}_{ai}\big]}{\omega_{iq}^{a}} \right) \right] \mathcal{E}_q \sum_{s,t} \left[ \sum_j \frac{\bar{\mu}_{aj}\bar{\mu}_{bj}}{\omega_{jt}^{a}} \right] \frac{\mathcal{E}_{st}\, u_{st}}{\Delta_{st}}\, \theta_{st}\, \theta_{ab}\, \theta_{ba}\, e^{-i\omega_q t} \\
&+\left[ \sum_i \left( \frac{\boldsymbol{\mu}_{ai}\big[\mathbf{u}_q(\mathbf{r})\cdot\boldsymbol{\mu}^*_{bi}\big]}{\omega_i^{bq}} + \frac{\boldsymbol{\mu}^*_{bi}\big[\mathbf{u}_q(\mathbf{r})\cdot\boldsymbol{\mu}_{ai}\big]}{\omega_{iq}^{a}} \right) \right] \mathcal{E}_q \sum_{s,t} \left[ \sum_j \frac{\bar{\mu}_{aj}\bar{\mu}_{bj}}{\omega_{j}^{at}} \right] \frac{\mathcal{E}_{ts}\, u_{st}}{\Delta_{ts}}\, \theta_{ts}\, \theta_{ab}\, \theta_{ba}\, e^{-i\omega_q t} \\
&+\left[ \sum_i \left( \frac{\boldsymbol{\mu}_{ai}\big[\mathbf{u}^*_q(\mathbf{r})\cdot\boldsymbol{\mu}^*_{bi}\big]}{\omega_{iq}^{b}} + \frac{\boldsymbol{\mu}^*_{bi}\big[\mathbf{u}^*_q(\mathbf{r})\cdot\boldsymbol{\mu}_{ai}\big]}{\omega_i^{aq}} \right) \right] \mathcal{E}^*_q \sum_{s,t} \left[ \sum_j \frac{\bar{\mu}_{aj}\bar{\mu}_{bj}}{\omega_{jt}^{a}} \right] \frac{\mathcal{E}_{st}\, u_{st}}{\Delta_{st}}\, \theta_{st}\, \theta_{ab}\, \theta_{ba}\, e^{i\omega_q t} \\
&+\left. \left[ \sum_i \left( \frac{\boldsymbol{\mu}_{ai}\big[\mathbf{u}^*_q(\mathbf{r})\cdot\boldsymbol{\mu}^*_{bi}\big]}{\omega_{iq}^{b}} + \frac{\boldsymbol{\mu}^*_{bi}\big[\mathbf{u}^*_q(\mathbf{r})\cdot\boldsymbol{\mu}_{ai}\big]}{\omega_i^{aq}} \right) \right] \mathcal{E}^*_q \sum_{s,t} \left[ \sum_j \frac{\bar{\mu}_{aj}\bar{\mu}_{bj}}{\omega_{j}^{at}} \right] \frac{\mathcal{E}_{ts}\, u_{st}}{\Delta_{ts}}\, \theta_{ts}\, \theta_{ab}\, \theta_{ba}\, e^{i\omega_q t} \right]
\end{aligned}
\tag{1.2.32}
$$

Simplify:

$$
\begin{aligned}
\mathbf{P}(\mathbf{r},t) = \frac{1}{8\hbar^3}\Bigg[ & 4\hbar^2 \sum_q \left[ \sum_i \left( \frac{\boldsymbol{\mu}_{ai}\left[\mathbf{u}_q(\mathbf{r})\cdot\boldsymbol{\mu}_{ai}^*\right]}{\omega_i^{aq}} + \frac{\boldsymbol{\mu}_{ai}^*\left[\mathbf{u}_q(\mathbf{r})\cdot\boldsymbol{\mu}_{ai}\right]}{\omega_{ia}^{q}} \right) \right] \mathcal{E}_q\, e^{-i\omega_q t} \\
& + 4\hbar^2 \sum_q \left[ \sum_i \left( \frac{\boldsymbol{\mu}_{ai}\left[\mathbf{u}_q^*(\mathbf{r})\cdot\boldsymbol{\mu}_{ai}^*\right]}{\omega_{iq}^{a}} + \frac{\boldsymbol{\mu}_{ai}^*\left[\mathbf{u}_q^*(\mathbf{r})\cdot\boldsymbol{\mu}_{ai}\right]}{\omega_i^{aq}} \right) \right] \mathcal{E}_q^*\, e^{i\omega_q t} \\
& + \sum_{q,s,t} \left[ \sum_{i,j} \left( \frac{\boldsymbol{\mu}_{bi}\left[\mathbf{u}_q(\mathbf{r})\cdot\boldsymbol{\mu}_{ai}^*\right]}{\omega_i^{aq}} + \frac{\boldsymbol{\mu}_{ai}^*\left[\mathbf{u}_q(\mathbf{r})\cdot\boldsymbol{\mu}_{bi}\right]}{\omega_{iq}^{b}} \right) \frac{\bar{\mu}_{aj}\bar{\mu}_{bj}}{\omega_{jt}^{a}} \right] \frac{\mathcal{E}_q\mathcal{E}_t\mathcal{E}_s^*\, u_{st}}{\Delta_{st}^*}\, e^{-i(\omega_t-\omega_s+\omega_q)t} \\
& + \sum_{q,s,t} \left[ \sum_{i,j} \left( \frac{\boldsymbol{\mu}_{bi}\left[\mathbf{u}_q(\mathbf{r})\cdot\boldsymbol{\mu}_{ai}^*\right]}{\omega_i^{aq}} + \frac{\boldsymbol{\mu}_{ai}^*\left[\mathbf{u}_q(\mathbf{r})\cdot\boldsymbol{\mu}_{bi}\right]}{\omega_{iq}^{b}} \right) \frac{\bar{\mu}_{aj}\bar{\mu}_{bj}}{\omega_{j}^{at}} \right] \frac{\mathcal{E}_q\mathcal{E}_s\mathcal{E}_t^*\, u_{st}}{\Delta_{ts}^*}\, e^{-i(\omega_s-\omega_t+\omega_q)t} \\
& + \sum_{q,s,t} \left[ \sum_{i,j} \left( \frac{\boldsymbol{\mu}_{bi}\left[\mathbf{u}_q^*(\mathbf{r})\cdot\boldsymbol{\mu}_{ai}^*\right]}{\omega_{iq}^{a}} + \frac{\boldsymbol{\mu}_{ai}^*\left[\mathbf{u}_q^*(\mathbf{r})\cdot\boldsymbol{\mu}_{bi}\right]}{\omega_{i}^{bq}} \right) \frac{\bar{\mu}_{aj}\bar{\mu}_{bj}}{\omega_{jt}^{a}} \right] \frac{\mathcal{E}_q^*\mathcal{E}_t\mathcal{E}_s^*\, u_{st}}{\Delta_{st}^*}\, e^{-i(\omega_t-\omega_s-\omega_q)t} \\
& + \sum_{q,s,t} \left[ \sum_{i,j} \left( \frac{\boldsymbol{\mu}_{bi}\left[\mathbf{u}_q^*(\mathbf{r})\cdot\boldsymbol{\mu}_{ai}^*\right]}{\omega_{iq}^{a}} + \frac{\boldsymbol{\mu}_{ai}^*\left[\mathbf{u}_q^*(\mathbf{r})\cdot\boldsymbol{\mu}_{bi}\right]}{\omega_{i}^{bq}} \right) \frac{\bar{\mu}_{aj}\bar{\mu}_{bj}}{\omega_{j}^{at}} \right] \frac{\mathcal{E}_q^*\mathcal{E}_s\mathcal{E}_t^*\, u_{st}}{\Delta_{ts}^*}\, e^{-i(\omega_s-\omega_t-\omega_q)t} \\
& + \sum_{q,s,t} \left[ \sum_{i,j} \left( \frac{\boldsymbol{\mu}_{ai}\left[\mathbf{u}_q(\mathbf{r})\cdot\boldsymbol{\mu}_{bi}^*\right]}{\omega_i^{bq}} + \frac{\boldsymbol{\mu}_{bi}^*\left[\mathbf{u}_q(\mathbf{r})\cdot\boldsymbol{\mu}_{ai}\right]}{\omega_{iq}^{a}} \right) \frac{\bar{\mu}_{aj}\bar{\mu}_{bj}}{\omega_{jt}^{a}} \right] \frac{\mathcal{E}_q\mathcal{E}_s\mathcal{E}_t^*\, u_{st}}{\Delta_{st}}\, e^{-i(\omega_s-\omega_t+\omega_q)t} \\
& + \sum_{q,s,t} \left[ \sum_{i,j} \left( \frac{\boldsymbol{\mu}_{ai}\left[\mathbf{u}_q(\mathbf{r})\cdot\boldsymbol{\mu}_{bi}^*\right]}{\omega_i^{bq}} + \frac{\boldsymbol{\mu}_{bi}^*\left[\mathbf{u}_q(\mathbf{r})\cdot\boldsymbol{\mu}_{ai}\right]}{\omega_{iq}^{a}} \right) \frac{\bar{\mu}_{aj}\bar{\mu}_{bj}}{\omega_{j}^{at}} \right] \frac{\mathcal{E}_q\mathcal{E}_t\mathcal{E}_s^*\, u_{st}}{\Delta_{ts}}\, e^{-i(\omega_t-\omega_s+\omega_q)t} \\
& + \sum_{q,s,t} \left[ \sum_{i,j} \left( \frac{\boldsymbol{\mu}_{ai}\left[\mathbf{u}_q^*(\mathbf{r})\cdot\boldsymbol{\mu}_{bi}^*\right]}{\omega_{iq}^{b}} + \frac{\boldsymbol{\mu}_{bi}^*\left[\mathbf{u}_q^*(\mathbf{r})\cdot\boldsymbol{\mu}_{ai}\right]}{\omega_{i}^{aq}} \right) \frac{\bar{\mu}_{aj}\bar{\mu}_{bj}}{\omega_{jt}^{a}} \right] \frac{\mathcal{E}_q^*\mathcal{E}_s\mathcal{E}_t^*\, u_{st}}{\Delta_{st}}\, e^{-i(\omega_s-\omega_t-\omega_q)t} \\
& + \sum_{q,s,t} \left[ \sum_{i,j} \left( \frac{\boldsymbol{\mu}_{ai}\left[\mathbf{u}_q^*(\mathbf{r})\cdot\boldsymbol{\mu}_{bi}^*\right]}{\omega_{iq}^{b}} + \frac{\boldsymbol{\mu}_{bi}^*\left[\mathbf{u}_q^*(\mathbf{r})\cdot\boldsymbol{\mu}_{ai}\right]}{\omega_{i}^{aq}} \right) \frac{\bar{\mu}_{aj}\bar{\mu}_{bj}}{\omega_{j}^{at}} \right] \frac{\mathcal{E}_q^*\mathcal{E}_t\mathcal{E}_s^*\, u_{st}}{\Delta_{ts}}\, e^{-i(\omega_t-\omega_s-\omega_q)t} \Bigg]
\end{aligned}
\tag{1.2.33}
$$

### 1.2.6 Decomposition of the Polarization into Cavity Modes

We decompose the polarization into cavity modes:

$$
\mathbf{P}(\mathbf{r},t) = \frac{1}{2}\sum_r \left[ P_r(t)\,\mathbf{u}_r(\mathbf{r})\, e^{-i\omega_r t} + P_r^*(t)\,\mathbf{u}_r^*(\mathbf{r})\, e^{i\omega_r t} \right] \tag{1.2.34}
$$

This decomposition is reasonable to use because the propagation equation for the cavity modes in terms of the nonlinear polarization is

$$\frac{\partial \mathcal{E}_r(t)}{\partial t} = i\,\frac{N}{2}\frac{\omega_r}{\epsilon_0\,\epsilon^{(1)}(\omega_r)}P_r(t) \tag{1.2.35}$$

which is linear in the polarization. $N$ is the number density of polarizable particles. Therefore, although the polarization in mode $r$ is *produced* nonlinearly, it couples to the electric field mode $r$ linearly. Note that the first term of (1.2.29) is actually linear, not nonlinear. We will thus ignore it in further calculations; it would contribute to the index of refraction, which we already know we are going to deal with post-facto.

Now compare Equation (1.2.29) to (1.2.35). The two expressions for $\mathbf{P}(\mathbf{r},t)$ must agree, so any terms that have a $e^{-i\omega_r t}$ in them must belong to the first term in the decomposition (1.2.34), because we have explicitly extracted that term and know that no other terms inside can contribute that frequency [45]. Unfortunately, there are still many terms in (1.2.33) with that frequency. However, some of the terms simply cannot agree: the second term has a single frequency with the wrong sign, so that will never work. We can also assume that over the range of frequencies we care about, we won't be able to match frequencies if two of the three frequencies are negative. Therefore, we save only the first, third, fourth, seventh, and eighth terms. Also, choose a single cavity mode

$R$ with frequency $\omega_R$ and multiply both sides by the complex conjugate of that spatial mode:

$$\begin{aligned}
&\sum_r P_r(t)\,\mathbf{u}_r(\mathbf{r})\cdot\mathbf{u}_R^*(\mathbf{r})\,e^{-i\omega_r t}\\
&= \frac{1}{4\hbar^3}\Bigg[\sum_{q,s,t}\Bigg[\sum_{i,j}\left(\frac{[\mathbf{u}_R^*(\mathbf{r})\cdot\boldsymbol{\mu}_{bi}]\big[\mathbf{u}_q(\mathbf{r})\cdot\boldsymbol{\mu}_{ai}^*\big]}{\omega_i^{aq}}+\frac{[\mathbf{u}_R^*(\mathbf{r})\cdot\boldsymbol{\mu}_{ai}^*]\big[\mathbf{u}_q(\mathbf{r})\cdot\boldsymbol{\mu}_{bi}\big]}{\omega_{iq}^{b}}\right)\frac{\bar{\mu}_{aj}\bar{\mu}_{bj}}{\omega_{jt}^{a}}\Bigg]\\
&\qquad\times\frac{\mathcal{E}_q\mathcal{E}_t\mathcal{E}_s^*\,u_t u_s}{\Delta_{st}^*}e^{-i(\omega_q-\omega_s+\omega_t)t}\\
&\quad+\sum_{q,s,t}\Bigg[\sum_{i,j}\left(\frac{[\mathbf{u}_R^*(\mathbf{r})\cdot\boldsymbol{\mu}_{bi}]\big[\mathbf{u}_q(\mathbf{r})\cdot\boldsymbol{\mu}_{ai}^*\big]}{\omega_i^{aq}}+\frac{[\mathbf{u}_R^*(\mathbf{r})\cdot\boldsymbol{\mu}_{ai}^*]\big[\mathbf{u}_q(\mathbf{r})\cdot\boldsymbol{\mu}_{bi}\big]}{\omega_{iq}^{b}}\right)\frac{\bar{\mu}_{aj}\bar{\mu}_{bj}}{\omega_{j}^{at}}\Bigg]\\
&\qquad\times\frac{\mathcal{E}_q\mathcal{E}_t^*\mathcal{E}_s\,u_t u_s}{\Delta_{ts}^*}e^{-i(\omega_s-\omega_t+\omega_q)t}\\
&\quad+\sum_{q,s,t}\Bigg[\sum_{i,j}\left(\frac{[\mathbf{u}_R^*(\mathbf{r})\cdot\boldsymbol{\mu}_{ai}]\big[\mathbf{u}_q(\mathbf{r})\cdot\boldsymbol{\mu}_{bi}^*\big]}{\omega_i^{bq}}+\frac{[\mathbf{u}_R^*(\mathbf{r})\cdot\boldsymbol{\mu}_{bi}^*]\big[\mathbf{u}_q(\mathbf{r})\cdot\boldsymbol{\mu}_{ai}\big]}{\omega_{iq}^{a}}\right)\frac{\bar{\mu}_{aj}\bar{\mu}_{bj}}{\omega_{jt}^{a}}\Bigg]\\
&\qquad\times\frac{\mathcal{E}_q\mathcal{E}_t^*\mathcal{E}_s\,u_s u_t}{\Delta_{st}}e^{-i(\omega_s-\omega_t+\omega_q)t}\\
&\quad+\sum_{q,s,t}\Bigg[\sum_{i,j}\left(\frac{[\mathbf{u}_R^*(\mathbf{r})\cdot\boldsymbol{\mu}_{ai}]\big[\mathbf{u}_q(\mathbf{r})\cdot\boldsymbol{\mu}_{bi}^*\big]}{\omega_i^{bq}}+\frac{[\mathbf{u}_R^*(\mathbf{r})\cdot\boldsymbol{\mu}_{bi}^*]\big[\mathbf{u}_q(\mathbf{r})\cdot\boldsymbol{\mu}_{ai}\big]}{\omega_{iq}^{a}}\right)\frac{\bar{\mu}_{aj}\bar{\mu}_{bj}}{\omega_{j}^{at}}\Bigg]\\
&\qquad\times\frac{\mathcal{E}_q\mathcal{E}_t\mathcal{E}_s^*\,u_s u_t}{\Delta_{ts}}e^{-i(\omega_t-\omega_s+\omega_q)t}\Bigg]
\end{aligned}\tag{1.2.36}$$

Use the assumption that the medium is isotropic to simplify the quantum coupling factors on the right:

$$\begin{aligned}
&\sum_r P_r(t)\,\mathbf{u}_r(\mathbf{r})\cdot\mathbf{u}_R^*(\mathbf{r})\,e^{-i\omega_r t}\\
&= \frac{1}{4\hbar^3}\Bigg[\sum_{q,s,t}\Bigg[\sum_{i,j}\bar{\mu}_{bi}\bar{\mu}_{ai}\bar{\mu}_{aj}\bar{\mu}_{bj}\left(\frac{1}{\omega_i^{aq}}+\frac{1}{\omega_{iq}^{b}}\right)\frac{1}{\omega_{jt}^{a}}\Bigg]\frac{\mathcal{E}_q\mathcal{E}_t\mathcal{E}_s^*\,u_R u_q u_t u_s}{\Delta_{st}^*}e^{-i(\omega_q-\omega_s+\omega_t)t}\\
&\quad+\sum_{q,s,t}\Bigg[\sum_{i,j}\bar{\mu}_{bi}\bar{\mu}_{ai}\bar{\mu}_{aj}\bar{\mu}_{bj}\left(\frac{1}{\omega_i^{aq}}+\frac{1}{\omega_{iq}^{b}}\right)\frac{1}{\omega_{j}^{at}}\Bigg]\frac{\mathcal{E}_q\mathcal{E}_t^*\mathcal{E}_s\,u_R u_q u_t u_s}{\Delta_{ts}^*}e^{-i(\omega_s-\omega_t+\omega_q)t}\\
&\quad+\sum_{q,s,t}\Bigg[\sum_{i,j}\bar{\mu}_{bi}\bar{\mu}_{ai}\bar{\mu}_{aj}\bar{\mu}_{bj}\left(\frac{1}{\omega_i^{bq}}+\frac{1}{\omega_{iq}^{a}}\right)\frac{1}{\omega_{jt}^{a}}\Bigg]\frac{\mathcal{E}_q\mathcal{E}_t^*\mathcal{E}_s\,u_R u_q u_t u_s}{\Delta_{st}}e^{-i(\omega_s-\omega_t+\omega_q)t}\\
&\quad+\sum_{q,s,t}\Bigg[\sum_{i,j}\bar{\mu}_{bi}\bar{\mu}_{ai}\bar{\mu}_{aj}\bar{\mu}_{bj}\left(\frac{1}{\omega_i^{bq}}+\frac{1}{\omega_{iq}^{a}}\right)\frac{1}{\omega_{j}^{at}}\Bigg]\frac{\mathcal{E}_q\mathcal{E}_t\mathcal{E}_s^*\,u_R u_q u_t u_s}{\Delta_{ts}}e^{-i(\omega_t-\omega_s+\omega_q)t}\Bigg]
\end{aligned}\tag{1.2.37}$$

Now we will integrate over all of space. On the left, this collapses the sum, yielding just the mode volume of mode $R$ times the polarization expansion coefficient $P_R(t)$. On the right, we'll get volume integrals of products of modes, but only over the volume of the sphere, because outside the sphere the dipole moments $\mu$ are zero. Define the multi-mode volume

$$V_{ab\cdots}(v) = \int_v \mathrm{d}^3 r \, u_a u_b \cdots , \tag{1.2.38}$$

where $v$ represents the volume to be integrated over. It is either $v$, which represents the cavity volume, or $\infty$, for all of space. The standard "mode volume" of a mode $q$ is then given by $V_{qq}(\infty)$. Because the mode volume outside of the resonator are negligible for good modes, we will generally drop the volume-specification part of the notation and only perform the integral over the resonator volume. The ordering of the indices doesn't matter.

$$\begin{aligned} P_R(t)\, V_{RR}\, e^{-i\omega_R t} = \frac{V_{Rqts}}{4\hbar^3} \Bigg[ & \sum_{q,s,t} \left[ \sum_{i,j} \bar{\mu}_{bi}\bar{\mu}_{ai}\bar{\mu}_{aj}\bar{\mu}_{bj} \left( \frac{1}{\omega_i^{aq}} + \frac{1}{\omega_{iq}^{b}} \right) \frac{1}{\omega_{jt}^{a}} \right] \frac{\mathcal{E}_q \mathcal{E}_t \mathcal{E}_s^*}{\Delta_{st}^*} e^{-i(\omega_q - \omega_s + \omega_t)t} \\ & + \sum_{q,s,t} \left[ \sum_{i,j} \bar{\mu}_{bi}\bar{\mu}_{ai}\bar{\mu}_{aj}\bar{\mu}_{bj} \left( \frac{1}{\omega_i^{aq}} + \frac{1}{\omega_{iq}^{b}} \right) \frac{1}{\omega_{j}^{at}} \right] \frac{\mathcal{E}_q \mathcal{E}_t^* \mathcal{E}_s}{\Delta_{ts}^*} e^{-i(\omega_s - \omega_t + \omega_q)t} \\ & + \sum_{q,s,t} \left[ \sum_{i,j} \bar{\mu}_{bi}\bar{\mu}_{ai}\bar{\mu}_{aj}\bar{\mu}_{bj} \left( \frac{1}{\omega_i^{bq}} + \frac{1}{\omega_{iq}^{a}} \right) \frac{1}{\omega_{jt}^{a}} \right] \frac{\mathcal{E}_q \mathcal{E}_t^* \mathcal{E}_s}{\Delta_{st}} e^{-i(\omega_s - \omega_t + \omega_q)t} \\ & + \sum_{q,s,t} \left[ \sum_{i,j} \bar{\mu}_{bi}\bar{\mu}_{ai}\bar{\mu}_{aj}\bar{\mu}_{bj} \left( \frac{1}{\omega_i^{bq}} + \frac{1}{\omega_{iq}^{a}} \right) \frac{1}{\omega_{j}^{at}} \right] \frac{\mathcal{E}_q \mathcal{E}_t \mathcal{E}_s^*}{\Delta_{ts}} e^{-i(\omega_t - \omega_s + \omega_q)t} \Bigg] \end{aligned} \tag{1.2.39}$$

Technically, we're done, because we could move everything but $P_R(t)$ to the right and write down a propagation equation for the electric field modes in time purely in terms of the electric field modes using (1.2.35). However, as we will discuss in the next section, this is not practical.

### 1.2.7 Simplifications to Reduce Computational Complexity

Unfortunately, (1.2.39) would be quite expensive to compute numerically, and would require detailed knowledge of a huge number of dipole moments. It also isn't very easy to work with by hand. Therefore, we will make some further assumptions which will let us dramatically simplify it into a

form that we (and the computer) can wrap our heads around.

They key assumption to simplifying (1.2.39) is to try to collapse it into a single term inside the sum. As a first step, swap the indices $t$ and $s$ in the second and third lines, then join them to the first and fourth lines respectively:

$$\begin{aligned} &P_R(t)\, V_{RR}\, e^{-i\omega_R t} \\ &\quad = \frac{V_{Rqts}}{4\hbar^3}\left[\sum_{q,s,t}\left[\sum_{i,j}\bar{\mu}_{bi}\bar{\mu}_{ai}\bar{\mu}_{aj}\bar{\mu}_{bj}\left(\frac{1}{\omega_i^{aq}}+\frac{1}{\omega_{iq}^{b}}\right)\left(\frac{1}{\omega_{jt}^{a}}+\frac{1}{\omega_j^{at}}\right)\right]\frac{\mathcal{E}_q\mathcal{E}_t\mathcal{E}_s^*\, u_R u_q u_t u_s}{\Delta_{st}^*}e^{-i(\omega_q-\omega_s+\omega_t)t}\right. \\ &\qquad \left.+\sum_{q,s,t}\left[\sum_{i,j}\bar{\mu}_{bi}\bar{\mu}_{ai}\bar{\mu}_{aj}\bar{\mu}_{bj}\left(\frac{1}{\omega_i^{bq}}+\frac{1}{\omega_{iq}^{a}}\right)\left(\frac{1}{\omega_{jt}^{a}}+\frac{1}{\omega_j^{at}}\right)\right]\frac{\mathcal{E}_q\mathcal{E}_t^*\mathcal{E}_s}{\Delta_{st}}e^{-i(\omega_s-\omega_t+\omega_q)t}\right] \end{aligned} \tag{1.2.40}$$

Now we will make as assumption: the sum over $i, j$ in each of the two terms is the same quantity, $C^2$, with

$$C^2 = \frac{\mu^4}{\delta^2} \tag{1.2.41}$$

where $\mu$ and $\delta$ are a representative dipole moment and frequency (which we need not ever actually specify, if we have some other way of determining $C^2$). Now we can join those two terms together, leaving us with a single term on the right:

$$P_R(t)\, V_{RR}\, e^{-i\omega_R t} = \frac{C^2 V_{Rqts}}{4\hbar^3}\sum_{q,s,t}\mathcal{E}_q\mathcal{E}_t\mathcal{E}_s^*\left(\frac{1}{\Delta_{st}^*}+\frac{1}{\Delta_{ts}}\right)e^{-i(\omega_q-\omega_s+\omega_t)t} \tag{1.2.42}$$

Move the other factors on the left to the right:

$$P_R(t) = \frac{C^2}{4\hbar^3}\sum_{q,s,t}\mathcal{E}_q\mathcal{E}_t\mathcal{E}_s^*\,\frac{V_{Rqts}}{V_{RR}}\left(\frac{1}{\Delta_{st}^*}+\frac{1}{\Delta_{ts}}\right)e^{-i(\omega_q-\omega_s+\omega_t-\omega_R)t} \tag{1.2.43}$$

And finally, switch around the indices to get to a nice representation:

$$P_q(t) = \frac{C^2}{4\hbar^3}\sum_{r,s,t}\mathcal{E}_r\mathcal{E}_s^*\mathcal{E}_t\,\frac{V_{rstq}}{V_{qq}}\left(\frac{1}{\Delta_{st}^*}+\frac{1}{\Delta_{ts}}\right)e^{-i(\omega_r-\omega_s+\omega_t-\omega_q)t} \tag{1.2.44}$$

### 1.2.8 Mode Amplitude Propagation Equation

We can plug (1.2.44) into (1.2.35) to get a propagation equation for the mode amplitude of mode $q$ in terms of all of the mode amplitudes:

$$\dot{\mathcal{E}}_q = i\,\frac{N}{2}\,\frac{\omega_q}{\epsilon_0\,\epsilon^{(1)}(\omega_q)}\,\frac{C^2}{4\hbar^3}\sum_{r,s,t}\mathcal{E}_r\mathcal{E}_s^*\mathcal{E}_t\,\frac{V_{rstq}}{V_{qq}}\left(\frac{1}{\Delta_{st}^*}+\frac{1}{\Delta_{ts}}\right)e^{-i\Delta_{rstq}t} \tag{1.2.45}$$

where $\Delta_{rsqt} = \omega_r - \omega_s + \omega_t - \omega_q$.

However, this is only the part of the propagation equation that involves the polarization. There are two more terms: one to account for the decay of light from the resonator, and another to account for any input light which couples to the resonator. Therefore, we won't be able to write down the complete propagation equation until we describe the properties of the resonator we are working in. This is the subject of the next section.

As a sanity check, one might wonder whether this is actually a super-model of the more typical sideband model. We show that this is indeed the case in Appendix B.

## 1.3 Coupling Light to Microresonators

The next thing we need to understand is how to couple light into and out of the resonator. There are many ways to do this for a microresonator. One of the first ways researchers developed was to simply blast microspheres with a focused laser beam [34]. This turns out to be terribly inefficient for the same reason that the mode have excellent quality factors: they simply don't couple well to external propagating electromagnetic waves. A better but much more technically challenging technique involves coupling to the microsphere via frustrated evanescent waves. It turns out that this process can be extremely efficient, reaching coupling efficiencies of more than 99% with excellent mode selectivity [46, 47].

This is very much unlike how mode-matching works in Fabry-Perot cavity, where (depending on the cavity geometry) it may be impossible to separate the even-$m$ modes from each other, and the coupling may never go above a few tens of percent. The key difference is that the evanescent coupling is essentially a tunneling process, and we know from the equivalent quantum mechanics problem that the tunneling probability through a barrier can approach 100% when certain conditions are

met.

There are several ways to implement the evanescent coupling in a more controlled way One of the first was to bounce a laser off the back surface of a prism at the prism's critical angle, creating an evanescent wave emanating from the back surface [48, 49]. Unfortunately, this doesn't give much control over the coupling properties, and leads to very non-ideal coupling (in the technical sense, not the colloquial). A better way, and what is commonly used in modern setups, is to couple light to the microsphere using a "tapered fiber", a normal fiber-optic cable that has been heated and stretched to form a thin (a few µm) waveguide. Such a waveguide has a long evanescent tail, and if it can be maneuvered to within a few wavelengths of the microsphere, the evanescent wave will become frustrated. Effectively, photons will tunnel from the tapered fiber (sometimes just referred to as a "taper" in the literature) directly into the microsphere [47]. We need to understand how to model these kinds of processes at the level of the electric field amplitude in the resonator modes.

Because our goal is a full time-dependent model of the cavity modes, we need to understand how energy leaks out of the modes, and how to give energy to the modes from an external source, like a laser beam. However, we don't want to get too specific about the details of the coupling scheme yet, just like we didn't get too specific about the actual physical resonator in the previous section. Thus, we will need to start with a theoretical model of a resonator coupled to an energy source or sink that is independent of any specific physical system.

A useful conceptual model of an optical cavity without nonlinear coupling between the modes is to relate each resonator mode to an independent resonant electrical circuit (an $RLC$ circuit) [50]. We will start from this analogy, using it to build a model of a resonator that is independent of the underlying components and only refers to generalized quantities like the mode energy, the pump power, and the dissipation timescale, which can be defined for any resonant system. We will then simply add these terms to the nonlinear terms we derived in the previous section, based on the reasonable assumption that these processes aren't directly coupled to each other.

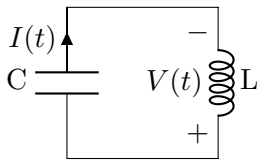


Figure 1.1: An $LC$ circuit, as a reasonable model of a cavity mode.

We'll start with an $LC$ circuit, as shown in Figure 1.1. The coupled differential equations that govern this circuit are

$$V = L\frac{\mathrm{d}I}{\mathrm{d}t} \tag{1.3.1a}$$

$$I = -C\frac{\mathrm{d}V}{\mathrm{d}t} \tag{1.3.1b}$$

These equations can be combined into a single second-order differential equation by plugging the derivative of the second equation into the first:

$$\begin{aligned} \frac{\mathrm{d}I}{\mathrm{d}t} &= -C\frac{\mathrm{d}^2V}{\mathrm{d}t^2} \\ \implies V &= -LC\frac{\mathrm{d}^2V}{\mathrm{d}t^2} \\ \frac{\mathrm{d}^2V}{\mathrm{d}t^2} + \frac{1}{LC}V &= 0 \\ \frac{\mathrm{d}^2V}{\mathrm{d}t^2} + \omega_0^2 V &= 0 \end{aligned} \tag{1.3.2}$$

where $\omega_0 \equiv \sqrt{1/LC}$ is the angular resonant frequency. This is the route we would typically take if we were doing pure circuit analysis, but it won't work as well when we couple this system to external sources and sinks that aren't ideal. Instead, we will turn (1.3.1) into two *decoupled* first-order *complex* differential equations by introducing a new quantity $a_\pm$, defined by

$$a_\pm = \sqrt{\frac{C}{2}}\left(V \pm i\sqrt{\frac{L}{C}}\, I\right) \tag{1.3.3}$$

Note that $a_+$ and $a_-$ are complex conjugates of each other. Manipulating (1.3.1), we find that

$$\begin{aligned}
\sqrt{\frac{C}{2}}V \pm i\sqrt{\frac{L}{2}}\,I &= \sqrt{\frac{C}{2}}L\frac{\mathrm{d}I}{\mathrm{d}t} \mp i\sqrt{\frac{L}{2}}C\frac{\mathrm{d}V}{\mathrm{d}t} \\
\sqrt{\frac{C}{2}}\left(V \pm i\sqrt{\frac{L}{C}}\,I\right) &= \sqrt{\frac{C}{2}}\left(L\frac{\mathrm{d}I}{\mathrm{d}t} \mp i\sqrt{LC}\,\frac{\mathrm{d}V}{\mathrm{d}t}\right) \\
a_\pm &= \sqrt{\frac{C}{2}}\left(L\frac{\mathrm{d}I}{\mathrm{d}t} \mp i\sqrt{LC}\,\frac{\mathrm{d}V}{\mathrm{d}t}\right) \\
i\omega_0 a_\pm &= \sqrt{\frac{C}{2}}\left(i\sqrt{\frac{L}{C}}\frac{\mathrm{d}I}{\mathrm{d}t} \pm \frac{\mathrm{d}V}{\mathrm{d}t}\right) \\
i\omega_0 a_\pm &= \pm\sqrt{\frac{C}{2}}\left(\frac{\mathrm{d}V}{\mathrm{d}t} \pm i\sqrt{\frac{L}{C}}\frac{\mathrm{d}I}{\mathrm{d}t}\right) \\
\pm\, i\omega_0\, a_\pm &= \sqrt{\frac{C}{2}}\left(\frac{\mathrm{d}V}{\mathrm{d}t} \pm i\sqrt{\frac{L}{C}}\frac{\mathrm{d}I}{\mathrm{d}t}\right) \\
\implies \frac{\mathrm{d}a_\pm}{\mathrm{d}t} &= \pm\, i\omega_0\, a_\pm
\end{aligned} \tag{1.3.4}$$

Either of these two equations alone is a complete description of the (complex) voltage and current (the real part of which are the real voltage and current). Using the known solutions to (1.3.1),

$$V(t) = |V|\cos\omega_0 t + \phi \tag{1.3.5a}$$

$$I(t) = \sqrt{\frac{C}{L}}|V|\sin\omega_0 t + \phi \tag{1.3.5b}$$

we find that

$$\begin{aligned}
a_\pm &= \sqrt{\frac{C}{2}}|V|(\cos(\omega_0 t + \phi) + i\sin(\omega_0 t + \phi)) \\
a_\pm &= \sqrt{\frac{C}{2}}Ve^{\pm\, i\omega_0 t}
\end{aligned} \tag{1.3.6}$$

where any phase has been absorbed into the now-complex voltage $V$.

The important thing about this version of the calculation is that $a_\pm$ is neither a voltage nor a current. What is it? Note that

$$|a_\pm|^2 = a_\pm\, a_\pm^* = a_+\, a_- = \frac{C}{2}|V|^2 \tag{1.3.7}$$

which is the peak energy in the capacitor, which is necessarily the total energy in the circuit $U$. So the quantity $a_\pm$ is the "square root of the energy" (literally units $\sqrt{\text{J}}$), but keeping track of the underlying phase. This is the trick to building a model of the cavity that doesn't care about the actual physical structure comprising it without sacrificing the ability to talk about mode amplitudes.

From here, we can introduce energy loss to the cavity, described by a timescale $\tau_0/2$. In particular, we want the total energy $U$ to decay like $U_0 \exp(-2t/\tau_0)$, so that the decay timescale of $a \sim \sqrt{U}$ is $\tau_0$. This loss is represented by adding an extra term to (1.3.4). For simplicity, we'll proceed with $a_+$ alone and drop the subscript.

$$\frac{\mathrm{d}a}{\mathrm{d}t} = i\omega_0\, a - \frac{a}{\tau_0} \tag{1.3.8}$$

This is a reasonable approximation as long as the decay rate is small (i.e., it takes many cycles for the energy to decay), because otherwise we would need to take into account how the losses change the resonant frequency of the cavity (see [50] for more details). This is like adding a resistor to the LC circuit.

Proceeding with this assumption, we can determine how much energy leaks out of the cavity from (1.3.8) to check that we did it right:

$$\begin{aligned}
\frac{\mathrm{d}U}{\mathrm{d}t} &= \frac{\mathrm{d}|a|^2}{\mathrm{d}t} = a\frac{\mathrm{d}a^*}{\mathrm{d}t} + a^*\frac{\mathrm{d}a}{\mathrm{d}t} \\
\frac{\mathrm{d}U}{\mathrm{d}t} &= a\left(i\omega_0\, a - \frac{a}{\tau_0}\right) + a^*\left(-i\omega_0\, a - \frac{a}{\tau_0}\right) \\
\frac{\mathrm{d}U}{\mathrm{d}t} &= i\omega_0\,|a|^2 - \frac{|a|^2}{\tau_0} - i\omega_0\,|a|^2 - \frac{|a|^2}{\tau_0} \\
\frac{\mathrm{d}U}{\mathrm{d}t} &= -2\frac{|a|^2}{\tau_0} \\
\frac{\mathrm{d}U}{\mathrm{d}t} &= -2\frac{U}{\tau_0} = -P_d
\end{aligned} \tag{1.3.9}$$

where $P_d$ is the power dissipated by the loss mechanism (in the circuit model, it would be a resistor).

We define the **intrinsic quality factor**[1] of the cavity mode as the unitless ratio

$$Q^I = \omega_0 \frac{U}{P_d} = \frac{\omega_0 \tau_0}{2} \tag{1.3.10}$$

which (roughly) measures the number of cycles necessary to reduce the initial energy by a factor of $e$.

Now that we understand how the isolated resonator behaves, we can add sources and sinks. This will essentially be done phenomenologically, by adding terms with what we suspect is the correct form directly to (1.3.8). As usual, the motivation is that we have found this description to work in practice.

To add an external sink of energy, such as a waveguide that is coupled to our cavity mode, we just add an additional type of loss to the differential equation (1.3.8):

$$\frac{\mathrm{d}a}{\mathrm{d}t} = i\omega_0\, a - \left(\frac{1}{\tau_0} + \frac{1}{\tau_e}\right) a \tag{1.3.11}$$

where $\tau_e$ is the timescale for coupling to the external source. The total power loss is now

$$\frac{\mathrm{d}U}{\mathrm{d}t} = -2\left(\frac{1}{\tau_0} + \frac{1}{\tau_e}\right) U \tag{1.3.12}$$

which is not terribly surprising. The *output power* that is coupled to the external sink is just the second term, $P_e = 2U/\tau_e$.

To match the notation of the previous section, we define a **coupling quality factor**

$$Q^C = \frac{\omega_0\, U}{P_e} = \frac{\omega_0\, \tau_e}{2} \tag{1.3.13}$$

and a **total quality factor**[2]

$$\frac{1}{Q} = \frac{1}{Q^I} + \frac{1}{Q^C} \tag{1.3.14}$$

[1] The intrinsic quality factor is sometimes called the "unloaded" quality factor because the cavity doesn't have a "load" yet, in the electronics sense of the term.

[2] Or "loaded" quality factor, in contrast to the unloaded quality factor.

for the cavity, and similarly a **total decay rate**

$$\frac{1}{\tau} = \frac{1}{\tau_0} + \frac{1}{\tau_e} \tag{1.3.15}$$

That takes care of sinks, but what about sources? Suppose that the waveguide carries some **launched input power** given by

$$P_{\text{in}} = |s_{\text{in}}(t)|^2 \tag{1.3.16}$$

where $s_{\text{in}}(t)$ is the "square root of a power", with time-dependent phase (units $\sqrt{\text{J/s}}$). We insert a term into (1.3.11) for this input power:

$$\frac{\mathrm{d}a}{\mathrm{d}t} = i\omega_0\, a - \left(\frac{1}{\tau_0} + \frac{1}{\tau_e}\right) a + \kappa s_{\text{in}} \tag{1.3.17}$$

where $\kappa$ has units of $\sqrt{1/\text{s}}$ so that the overall term carries the correct units ($\sqrt{\text{J}}/\text{s}$, as can be seen from the units of $a/\tau$ and the other terms). $\kappa$ describes the coupling between the input power and the cavity energy in a similar fashion to the timescales $\tau$. In fact, one can use time reversal symmetry to show that

$$\kappa = \sqrt{\frac{2}{\tau_e}} \tag{1.3.18}$$

A complete derivation is given in [50]. It can also be shown that the output field $s_{\text{out}}$ is [51]

$$s_{\text{out}}(t) = -s_{\text{in}}(t) + \sqrt{\frac{2}{\tau_e}}\, a \tag{1.3.19}$$

Calculating $Q^C$ is not trivial. It depends strongly on the material properties and coupling scheme that are chosen. However, it is possible to get a compact solution for some common schemes; see [49] for some useful results, particularly for the coupling between a spherical microresonator and a tapered fiber, which we will use later.

### 1.3.1 Full Mode Amplitude Propagation Equation

Now that we understand both how light decays out of the resonator and how light can be injected into the resonator, we can write the full propagation equation for the electric field amplitude coefficient of a resonator mode:

$$\begin{aligned}\dot{\mathcal{E}}_q(t) = &-\frac{\omega_q}{2Q_q}\mathcal{E}_q + \frac{1}{2}\sqrt{\frac{\omega_q}{Q_q^C\, E_q}}\sum_l \sqrt{S_l}\, e^{-i(\omega_q-\omega_l)t} \\ &+ i\frac{N}{2}\frac{\omega_q}{\epsilon_0\,\epsilon^{(1)}(\omega_q)}\frac{C^2}{4\hbar^3}\sum_{r,s,t}\omega_q\,\mathcal{E}_r\,\mathcal{E}_s^*\,\mathcal{E}_t\,\frac{V_{rstq}}{V_{qq}}\left(\frac{1}{\delta_{st}^*}+\frac{1}{\delta_{ts}}\right)e^{i\,\Delta_{rstq}\,t}\end{aligned} \tag{1.3.20}$$

where $U_q = E_q|\mathcal{E}_q|^2$, and $\mathcal{S}_l$ and $\omega_l$ are the power and angular frequency of each launched beam. A summary of all of the notation used in this equation is shown in Table 1.1.

Equation (1.3.20) is our master equation for describing any driven Raman nonlinear process inside the resonator. Note, however, that it does not account for the *spontaneous* Raman process. In the numerical simulation, it may be necessary to provide a tiny initial amplitude to all of the modes to get it to start properly. We typically use an initial amplitude that corresponds to much less than a single photon worth of energy for the mode for this purpose.

| Symbol | Meaning |
|---|---|
| $q, r, s, t$ | Mode indices. |
| $\mathcal{E}_q$ | The complex electric field amplitude coefficient for mode $q$ as a function of time. |
| $\omega_q$ | The mode frequency of mode $q$. |
| $Q_q$ | The total quality factor of mode $q$. |
| $Q_q^I$ | The intrinsic quality factor of mode $q$. |
| $Q_q^C$ | The coupling quality factor of mode $q$. |
| $U_q$ | The energy stored in mode $q$. |
| $E_q$ | The "mode energy prefactor" for mode $q$ ($U_q = E_q\|\mathcal{E}_q\|^2$). |
| $l$ | Launched beam index. |
| $S_l$ | The power of launched beam $l$. |
| $\omega_l$ | The angular frequency of launched beam $l$. |
| $V_{abcd}$ | The four-mode volume coupling factor for modes $a$, $b$, $c$, and $d$. |
| $V_{aa}$ | The mode volume of mode $a$. |
| $\delta_{ab}$ | The two-mode Raman detuning for modes $a$ and $b$. |
| $\Delta_{abcd}$ | The four-mode detuning for modes $a$, $b$, $c$, and $d$. |
| $C^2$ | The quantum coupling factor for the ro-vibrational and electronic states. |
| $\epsilon^{(1)}$ | The first-order permittivity of the material (the index of refraction is $n = \sqrt{\epsilon^{(1)}}$). |

Table 1.1: Notation for the master mode amplitude propagation equation (1.3.20).

## 1.4 The Microresonator-based Molecular Modulator

The theoretical analysis described in the previous sections is essentially independent of the optical resonator used. In this section, we will begin thinking about an actual resonator design: the Microresonator-based Molecular Modulator (MMM). The simulations described in this section and the next indicate that an MMM based on a silica microsphere could achieve a frequency shift of $\sim 12\,\mathrm{THz}$ with modulation efficiencies of $\epsilon \approx 1\%$ at any optical wavelength.

Figure 1.2 shows a cartoon of an MMM based on a silica microsphere. A pump laser is evanescently coupled to one of the whispering gallery modes of the microsphere using a tapered fiber [51]. This **pump mode** builds up to high intensity. The pump mode then generates a high-intensity **Stokes mode** through stimulated Raman scattering (SRS). Once the pump and Stokes modes have both built up to high intensities, molecular modulation can occur: a separate low-power **mixing beam** is coupled to the resonator and is modulated via driven four-wave mixing to produce light

at the **target** frequency.

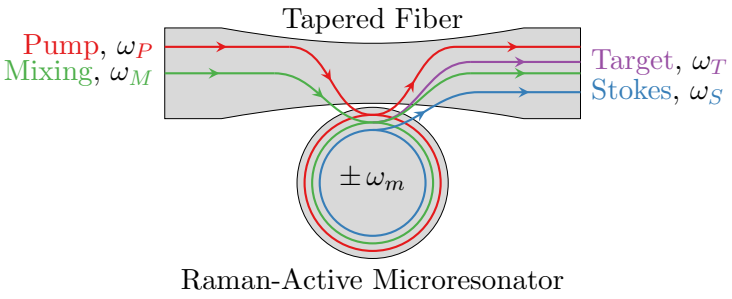


Figure 1.2: A cartoon of our molecular modulation scheme implemented using a microsphere made of Raman-active material with frequency shift $\omega_m$ coupled to a tapered fiber. The launched pump beam at frequency $\omega_P$ drives a Stokes mode at frequency $\omega_S = \omega_P - \omega_m$ via Raman lasing. Then a launched "mixing" beam at frequency $\omega_M$ is modulated by the intense pump and Stokes modes via four-wave mixing to produce light at the "target" frequency $\omega_T = \omega_M + \omega_m$.

This system is exactly the one we have built up the theory for in the previous sections. The MMM is an optical resonator in a Raman-active medium, coupled to a source and to a sink (both of which happen to be the same tapered fiber).

### 1.4.1 The Mode Propagation Equation in an MMM

Let's try to understand the mode propagation equation for the MMM at a high level. For convenience, we consolidate the various prefactors of each term in (1.3.20) to get the following form:

$$\dot{\mathcal{E}}_q = -\,\mathcal{D}_q\,\mathcal{E}_q + \mathcal{P}_q \sum_l \sqrt{S_l}\,e^{-i(\omega_q-\omega_l)t} + i\sum_{r,s,t} \mathcal{G}_{rstq}\,\mathcal{E}_r\,\mathcal{E}_s^*\,\mathcal{E}_t\,e^{i\,\Delta_{rstq}\,t} \tag{1.4.1}$$

The most important terms in the sum for a given mode $q$ can be identified in advance by a simple graphical algorithm using the energy level diagram in Figure 1.3. We label the terms by the four modes they involve, so the term $i\,\mathcal{G}_{MSPT}\,\mathcal{E}_M\mathcal{E}_S^*\mathcal{E}_T\,\exp(i\,\Delta_{MSPT}\,t)$ is labeled $MSP \to T$. The notation indicates that this term is the one where modes $M$, $S$, and $P$ contribute to the derivative of $T$.

The arrows on the diagram must form a closed loop (their directions may need to be reversed) to have small $\Delta_{rstq}$ (see Section 1.5.2), so important terms must be either of the form $qrr \to q$ (two pairs of modes) or $rst \to q$ (all four modes different). Additionally, arrows that do not touch the same energy level must not appear next to each other (e.g., $T$ cannot appear next to $S$). Finally,

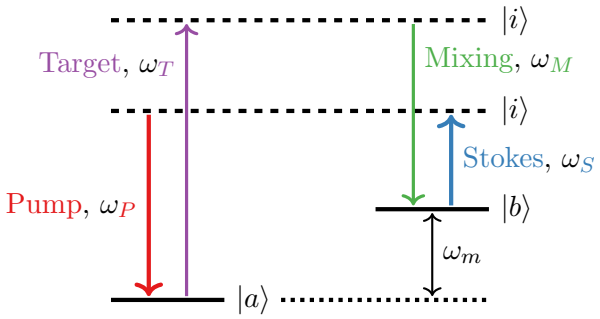


Figure 1.3: The energy level diagram for molecular modulation. Two stable molecular ro-vibrational states $|a\rangle$ and $|b\rangle$ interact with four photons via two intermediate virtual states (both labeled $|i\rangle$). The Raman frequency shift $\omega_m$ is the frequency difference between the molecular states. The arrows are in the correct direction for term $MSP \rightarrow T$.

the last mode's arrow must point upward (this corresponds to an arbitrary sign convention in the derivation and has no physical significance; if the sign choice were reversed, the term with the last arrow pointing downward would be the important one).

For example, the most relevant terms for the target mode $T$ must be of the forms $Trr \rightarrow T$ or $rst \rightarrow T$. For the first form, $rr$ could be either $MM$, $PP$, or $SS$. These correspond to the possibility of stimulated Raman scattering (SRS) between the target and mixing, pump, or Stokes modes. For the second form, the $T$ arrow must point upward, so we are forced to go around the diagram in an order that gives us the term $MSP \rightarrow T$. This term corresponds to molecular modulation: it says that energy can be delivered to the target mode from the other three modes via four-wave mixing.

### 1.4.2 Numerical Simulations of the MMM

We evolve the mode amplitudes in time using a simple Runge-Kutta scheme with a time step of a few picoseconds, which is enough to resolve frequency detunings of up to a few hundred GHz (more than large enough to resolve all of the important terms in Equation (1.4.1)). For consistency, four-wave mixing terms in Equation (1.4.1) that have a $\Delta_{qrst}$ larger than the Nyquist frequency for the chosen time step are not included in the calculation. The simulations are converged with respect to the time step and always reach a steady-state with constant energy in each mode. The final energies do not depend on the relative timing of the launched pump and mixing beams being turned on, so we turn both beams on at the beginning of the simulation.

We take the resonator to be a silica microsphere with radius $R = 50\,\mu\text{m}$. We model the silica Raman shift as a Lorentzian with $\omega_m = 2\pi \times 12\,\text{THz}$ and a linewidth of 2 THz, and the $\mathcal{G}_{rstq}$ are calculated from the bulk Raman coefficient [52]. We take the intrinsic quality factors of all of the modes to be $10^8$ (quality factors this high have been regularly achieved in practice [51]), except in Section 1.5.4 where we look at how the modulation efficiency depends on it.

Light is coupled to and from the resonator using a tapered fiber. We generally either calculate the coupling quality factors from Eq. (35) of [49] with a 1 µm taper radius and the pump mode critically coupled to the launched pump beam ("pump-critical"), or we take all of the modes to be critically coupled ("all-critical"). The pump-critical case does not give the highest modulation efficiency, but it does have the lowest threshold (this will be addressed in Section 1.5.5).

The all-critical case is roughly equivalent to adding a second tapered fiber to the system, with coupling optimized for the mixing mode instead of the pump mode. This kind of coupling scheme is common for communications applications [53, 54], and could be re-purposed for the MMM. It would be necessary to prevent the secondary fiber from disturbing the coupling between the first fiber and the microsphere, perhaps by suppressing any propagating fiber modes near that wavelength using an engineered stopband [55]. However, the purpose of this case is just to approximate the maximum possible theoretical efficiency of the system, and in our simulations we simply assume it might be possible without implementing a model of how it would work in practice. As we will see in Section 1.5.5, even this is not the most ideal coupling scheme.

For better control over the parameters of the simulation, we use representative modes instead of real cavity modes. The mode volumes and four-mode shape overlaps of the representative modes are given values calculated from averages over real cavity modes, while we set the modes frequencies and intrinsic quality factors arbitrarily. It is important to control the mode frequencies exactly because the modulation efficiency is quite sensitive to the four-mode detuning $\Delta_{rstq}$, which is a measure of the timescale over which the modulation process conserves energy. We will generally set the four-mode detuning for the molecular modulation path to zero. A possible method for control of the four-mode detuning will be discussed in Section 1.5.2.

We did initially use real cavity modes, and the simulation package is capable of working with them. See Appendix A for some notes on numerical techniques for calculating these modes, and Appendix C for notes on numerically evaluating the vector spherical harmonics which form the

angular part of the whispering gallery mode eigenbasis.

As mentioned above, the mode volumes $V_{qq}$ and four-mode shape overlaps $V_{rstq}$ are given uniform values for all modes that are representative of the average volumes and overlaps calculated from real cavity modes [51, 56]. The actual mode volumes and four-mode shape overlaps vary up and down somewhat-independently from mode to mode over the range of mode wavelengths we use by approximately an order of magnitude, depending on the wavelengths of the modes, their angular momentum and radial quantization numbers, and their polarizations. Since the four-wave mixing terms in Equation (1.4.1) depend only on the ratio between a four-mode overlap and a mode volume, we expect the real modulation efficiencies to be within an order of magnitude of those calculated with the representative values.

For simplicity, we assume that cascaded SRS has been suppressed. This could perhaps be achieved in practice [57], but actually turns out to be irrelevant. We have run the same simulations with enough higher-order Stokes modes to capture the full cascade at the highest launched pump powers that we show below, and there is no significant difference in the modulation efficiency compared to simulations without the cascaded modes (this surprising result will be discussed in Section 1.5.1). The launched mixing power is always $S_M = 1\,\mu\text{W}$, which is below the threshold for the mixing mode to create its own Stokes mode.

Our simulations do not take into account other nonlinear processes, such as generation of parametric sidebands through self-phase modulation, which is due to the Kerr nonlinearity [58]. The Kerr and Raman nonlinearities are both third order, so one would expect their thresholds to be comparable. In a real experiment, there will likely be additional modes excited near the pump mode due to Kerr mixing. However, there is good reason to believe that the existence of these additional excited modes will not significantly change our results.

First, the primary effect of these modes will be to deplete the energy of the pump mode. However, in Raman lasing, the pump energy inside the resonator is clamped once it reaches the Stokes lasing threshold [59]. When a Raman laser is pumped far above threshold, a large fraction of the incident pump power does not couple into the resonator. This excess incident pump power can overcome any additional depletion of the pump beam due to the presence of other nonlinear optical processes. Second, the additional four-wave mixing pathways made available by these extra excitations will not, in general, produce a target frequency that is aligned with a resonator mode

frequency (i.e., these terms will have large four-mode detunings). As we will see in Section 1.5.2, this should suppress any additional modulation of the mixing beam. However, a detailed analysis of all of these additional nonlinear processes in addition to Raman generation is beyond the scope of this work, and possibly too computationally expensive to explore with the mode-based simulations we use.

## 1.5 Characterization of the MMM

In this section, we discuss the dependence of the modulation efficiency $\epsilon$ on a variety of parameters. Our goal is to elucidate some of the design criteria of the MMM. There are clearly an enormous set of possible parameters, so we have chosen to focus on ones that establish the maximum theoretical performance of a single device, as well as some details of the coupling scheme and operational characteristics. We do not consider the possibility of using a different resonator or coupling scheme entirely, and we focus on a single pump wavelength $\lambda_P = 1064\,\text{nm}$. The launched mixing beam power is always low enough that without the launched pump power, it would cause no nonlinear effects.

### 1.5.1 Dependence of Modulation Efficiency on Launched Pump Power

An important metric for a modulator is the modulation efficiency $\epsilon$, which we define to be the output power of the target mode $P_T$ divided by the launched mixing power $S_M$ ($\epsilon = P_T/S_M$). Since the molecular modulation process only relies on establishing coherence between the molecular states through SRS, we should only expect non-zero modulation efficiency as soon as the pump mode energy goes above the threshold to produce a Stokes mode. Figure 1.4 shows that this is indeed the case.

The modulation efficiency curves are quite unlike what we expected based on the behavior of our previous device. In that system the mixing and target frequencies were not resonant in the cavity, so the target light was produced in a single pass of the mixing beam through the system. The modulation efficiency was very low, so the pump mode, Stokes mode, and mixing beam were essentially unperturbed by the molecular modulation process. This allowed the modulation efficiency to scale roughly like the Stokes mode energy in the ideal case. In contrast, the situation

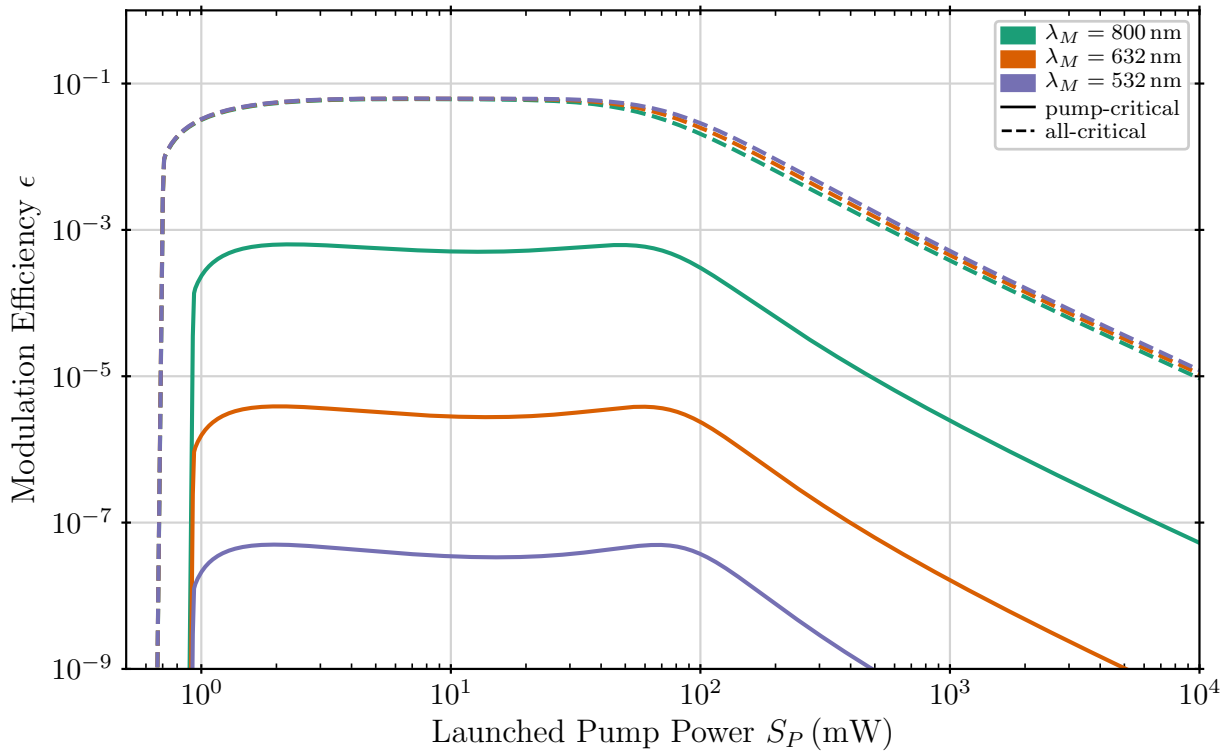


Figure 1.4: The modulation efficiency $\epsilon$ as a function of launched pump power $S_P$ for three different mixing wavelengths $\lambda_M$. The modulation efficiency is $\epsilon = P_T/S_M$, where $P_T$ is the target mode output power and $S_M$ is the launched mixing power. The pump mode wavelength is $\lambda_P = 1064\,\mathrm{nm}$, and it is critically coupled to the launched pump beam.

in the MMM is shown in Figure 1.5. The mixing mode energy decreases after an initial plateau, corresponding to the decrease in the modulation efficiency.

To investigate this counterintuitive decrease, we start by noting that the complex mixing mode amplitude $\mathcal{E}_M$ is constant at steady-state (not just the mode energy $U_M$) because it is externally pumped. Therefore, we can set the derivative of $\mathcal{E}_M$ to zero at steady-state, assume that it is too far detuned from the launched pump beam to interact with it, and write

$$\begin{aligned}\dot{\mathcal{E}}_M = 0 &= -\mathcal{D}_M \mathcal{E}_M + \mathcal{P}_M \sqrt{S_M} + i \sum_{r,s,t} \mathcal{G}_{rstM}\, \mathcal{E}_r\, \mathcal{E}_s^*\, \mathcal{E}_t\, e^{i\,\Delta_{rstM}\,t} \\ \mathcal{E}_M &= \frac{\mathcal{P}_M}{\mathcal{D}_M} \sqrt{S_M} + i \sum_{r,s,t} \frac{G_{rstM}}{\mathcal{D}_M}\, \mathcal{E}_r\, \mathcal{E}_s^*\, \mathcal{E}_t\, e^{i\,\Delta_{rstM}\,t} \end{aligned} \tag{1.5.1}$$

This equation does not let us determine $\mathcal{E}_M$ from the initial conditions, but it does let us explain why $\mathcal{E}_M$ has the steady-state value it does phenomenologically. The most important terms in

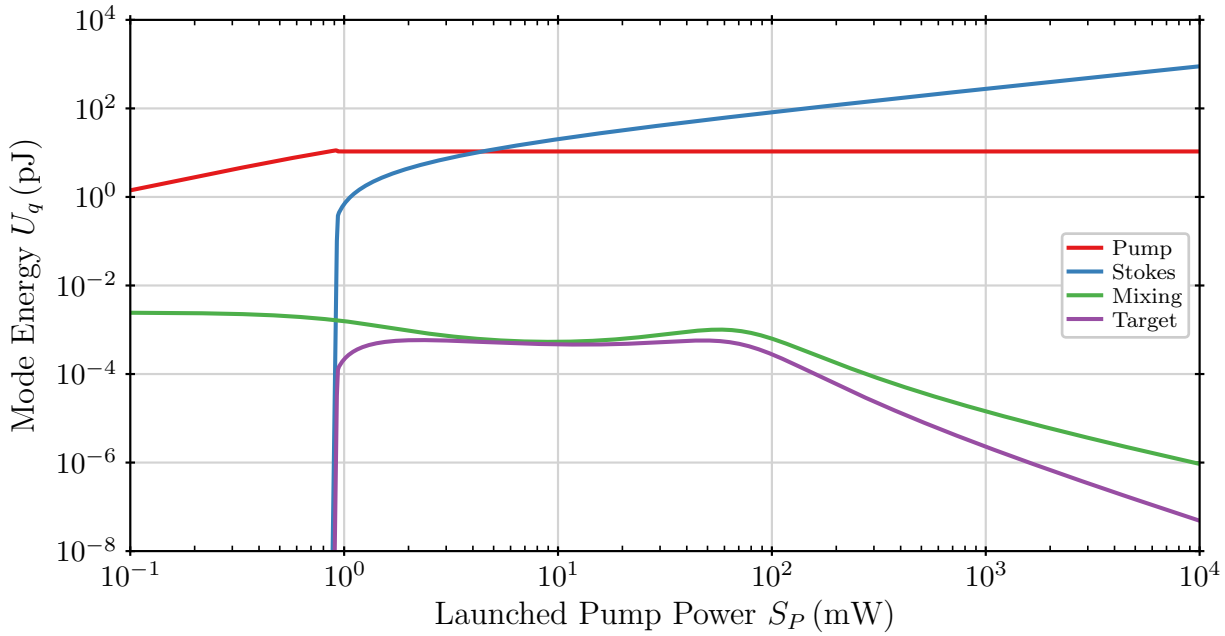


Figure 1.5: The energy stored in each resonator mode $U_q$ as a function of launched pump power $S_P$. After threshold, $U_P$ is clamped and $U_S$ grows like the square root of the launched pump power. After an initial plateau following threshold, $U_M$ and $U_T$ begin to decrease, which reduces the modulation efficiency.

Equation (1.5.1) are shown in Figure 1.6 for one of the curves from Figure 1.4. Note that all of these terms have a four-mode detuning of zero in these simulations, so they do not have time-dependent phases that do not arise from the mode amplitudes themselves. As expected, the launched mixing beam and the four wave mixing are both important. However, another term is also important: $MSS \rightarrow M$, which corresponds to SRS between the mixing mode and the Stokes modes (the next most important is $MPP \rightarrow M$, not shown).

SRS would normally be suppressed between these modes because they are not on Raman-resonance. However, the Raman linewidth of silica is several THz, so the frequency difference is not enough to suppress this term when the Stokes mode energy is large. Although the simulations we present here only include one Stokes mode, we have performed similar simulations with enough higher-order Stokes modes to model the entire cascade out to $S_P = 10\,\mathrm{W}$, and there is no significant difference in the behavior of the modulator. The combined effect of all of the cascaded Stokes modes together is similar to the single large un-cascaded Stokes mode. This effect is why there is no significant difference in modulation efficiency between simulations run with and without cascaded

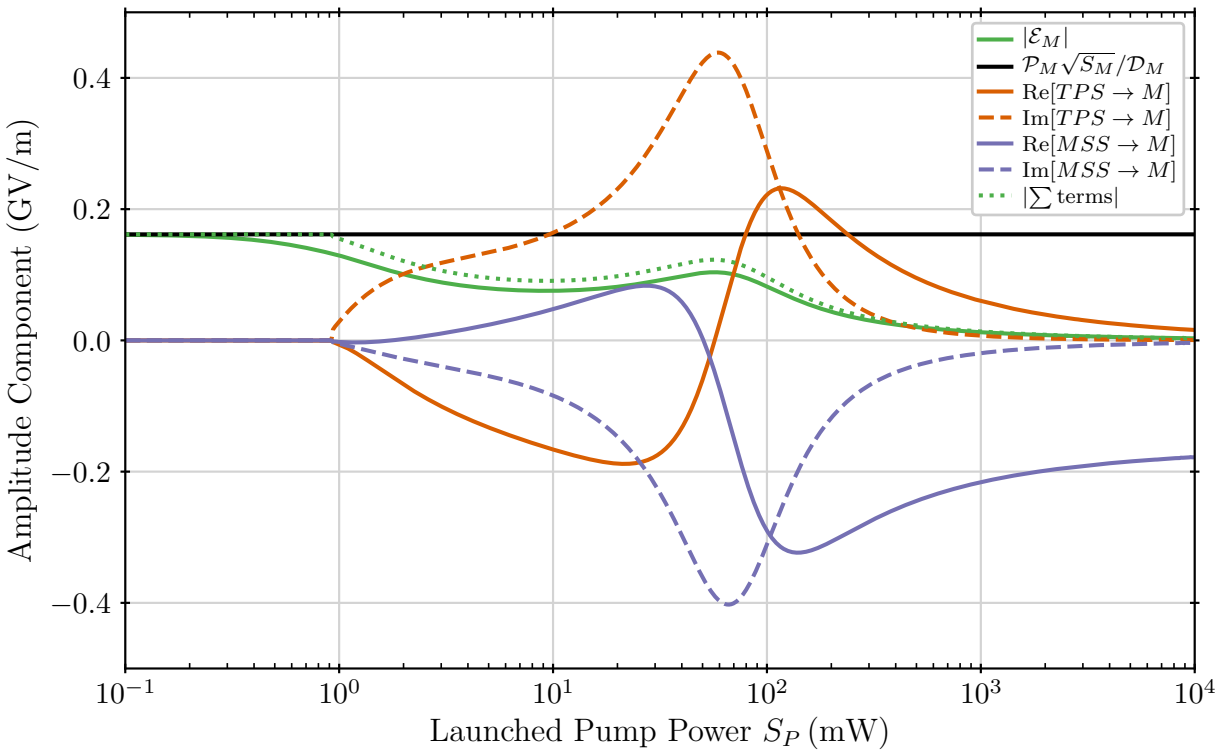


Figure 1.6: The real and imaginary contributions of the three most important terms in Equation (1.5.1) to the mixing mode amplitude (magnitude plotted as $|\mathcal{E}_M|$): the launched mixing beam, the molecular modulation term $TPS \to M$, and the SRS term $MSS \to M$. These three terms together almost entirely compose the steady-state mixing mode amplitude (the magnitude of their sum is plotted in dotted green).

Stokes modes.

Remarkably, this off-resonant SRS actually supports the mixing mode, causing the plateau. We ran a set of simulations with the Raman linewidth reduced by a factor of $10^3$ (i.e., it is a few GHz instead of a few THz) while keeping everything else constant. This suppresses the off-resonant SRS between the mixing mode and pump or Stokes modes. The mode energies and mixing mode amplitude composition for these simulations are shown in the left and right panels of Figure 1.7 respectively. With no SRS from the mixing mode to the pump or Stokes modes, the mixing and target mode energies begin to decrease immediately after threshold with no plateau. Now the only important terms in the mixing mode amplitude are the external beam and the molecular modulation term, as originally expected.

Now that the off-resonant SRS has been suppressed, all four modes have nearly-constant complex amplitude at steady state. If we approximate them as constant, we can solve for the amplitudes

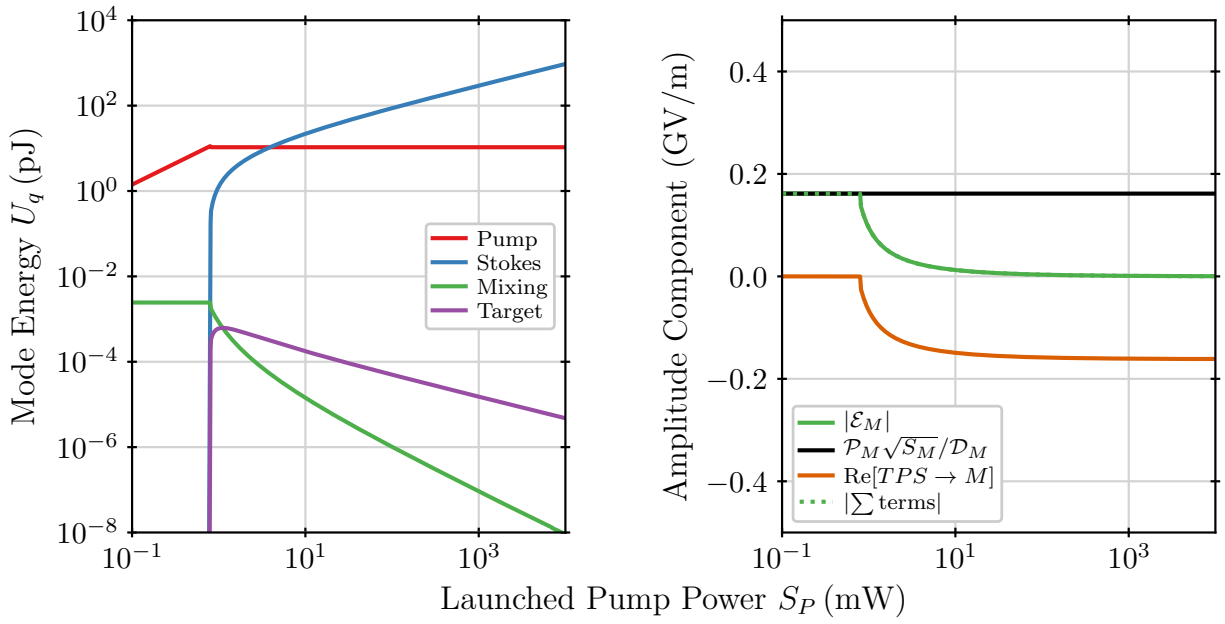


Figure 1.7: Mode energies (left) and mixing mode amplitude composition (right) when the Raman linewidth has been artificially reduced by a factor of $10^3$. The mixing and target mode energies now drop off without a plateau. There are only two important contributions to the mixing mode amplitude: the launched mixing beam and the molecular modulation term $TPS \to M$ (which is now purely real). These two terms together entirely compose the mixing mode amplitude at steady-state (the two green curves overlap). The reduction of the Raman linewidth has removed the off-resonant SRS between the mixing mode and other modes that was present in Figure 1.6.

of the target and mixing modes in terms of the pump and Stokes mode amplitudes. Using the graphical algorithm for determining relevant terms described above, we can solve for the target mode amplitude:

$$\begin{aligned} \dot{\mathcal{E}}_T = 0 &= -\mathcal{D}_T\,\mathcal{E}_T + i\,\mathcal{G}_{MSPT}\,\mathcal{E}_M\,\mathcal{E}_S^*\,\mathcal{E}_P \\ \mathcal{E}_T &= i\,\frac{\mathcal{G}_{MSPT}}{\mathcal{D}_T}\,\mathcal{E}_M\,\mathcal{E}_S^*\,\mathcal{E}_P \end{aligned} \tag{1.5.2}$$

We can use Equation (1.5.2) to solve for $\mathcal{E}_M$, arriving at a form that only depends on $\mathcal{E}_P$ and $\mathcal{E}_S$:

$$\begin{aligned} \dot{\mathcal{E}}_M = 0 &= -\mathcal{D}_M\,\mathcal{E}_M + \mathcal{P}_M\sqrt{S_M} + i\,\mathcal{G}_{TPSM}\,\mathcal{E}_T\,\mathcal{E}_P^*\,\mathcal{E}_S \\ 0 &= -\mathcal{D}_M\,\mathcal{E}_M + \mathcal{P}_M\sqrt{S_M} + i^2\,\mathcal{G}_{TPSM}\,\frac{\mathcal{G}_{MSPT}}{\mathcal{D}_T}\,\mathcal{E}_M\,\mathcal{E}_S^*\,\mathcal{E}_P\,\mathcal{E}_P^*\,\mathcal{E}_S \\ \mathcal{E}_M &= \frac{\mathcal{P}_M\sqrt{S_M}}{\mathcal{D}_M + \mathcal{G}_{TPSM}\,\mathcal{G}_{MSPT}\,|\mathcal{E}_P|^2\,|\mathcal{E}_S|^2/\mathcal{D}_T} \end{aligned} \tag{1.5.3}$$

When $|\mathcal{E}_S|^2$, which is proportional to the Stokes mode energy, becomes large, the second term in the denominator dominates the first and $\mathcal{E}_M$ begins to decrease. This is the root cause of the decrease in modulation efficiency: the mixing mode amplitude decreases like $|\mathcal{E}_S|^2$, which causes the target mode amplitude to go like $\mathcal{E}_T \sim \mathcal{E}_M \mathcal{E}_S^* \sim \mathcal{E}_S^*/|\mathcal{E}_S|^2 \sim 1/\mathcal{E}_S$ (from Equation (1.5.2)).

This behavior is similar to pump mode clamping in cascaded SRS, where the behavior of a mode that is not being externally pumped causes a change in the form of the evolution equation for another mode that changes its qualitative dynamics [59, 60]. The off-resonant SRS terms, despite their apparently-detrimental behavior in Figure 1.6, provide extra paths for energy flow that limit the effect of the clamping-like behavior described by Equation (1.5.3) until the Stokes mode reaches much higher energy. This causes the plateau that we observe in the modulation efficiency in Figure 1.4. An observer in the lab would see the launched mixing beam have higher transmission through the fiber as the launched pump power increases, much like the launched pump beam itself begins to have higher transmission due to traditional SRS clamping.

Although this clamping-like effect prevents the modulation efficiency from scaling like the Stokes amplitude as we initially expected, the modulation efficiencies in the plateau region are still very high. Even the simple single-fiber coupling setup gives an efficiency of approximately 0.1% at $\lambda_M = 800\,\text{nm}$, several orders of magnitude higher than our previous modulator. Critical coupling could boost the efficiency to nearly 10%. The existence of the plateau means that the modulation efficiency should be quite stable to fluctuations in the launched pump power. The MMM will also never need much more launched pump power than the threshold power.

### 1.5.2 Dependence of Modulation Efficiency on Four-Mode Detuning

Bringing the four-mode detuning $\Delta_{MSPT}$ down to less than a mode linewidth $\Gamma_q = \omega_q/Q_q$ (a few MHz for optical frequencies if $Q_q \approx 10^8$) is necessary for high-efficiency operation. Figure 1.8 shows what happens when $\Delta_{MSPT}$ (which is equal to the target mode detuning $\delta_T$ in that figure) becomes larger than the target mode linewidth $\Gamma_T$. As $\Delta_{MSPT}$ grows, the exponential phase in the relevant terms in Equation (1.4.1) becomes too fast to effectively drive the target mode, and the target mode energy (and therefore output power) begins to decrease like $1/(\Delta_{MSPT}/\Gamma_T)^2$. Equivalently, when this process fails to conserve energy (i.e., when $\hbar\Delta_{MSPT}$ is non-zero), the steady-state efficiency decreases. However, as long as $\Delta_{MSPT} < \Gamma_T$, there is no significant change in $\epsilon$ from perfect

four-mode resonance.

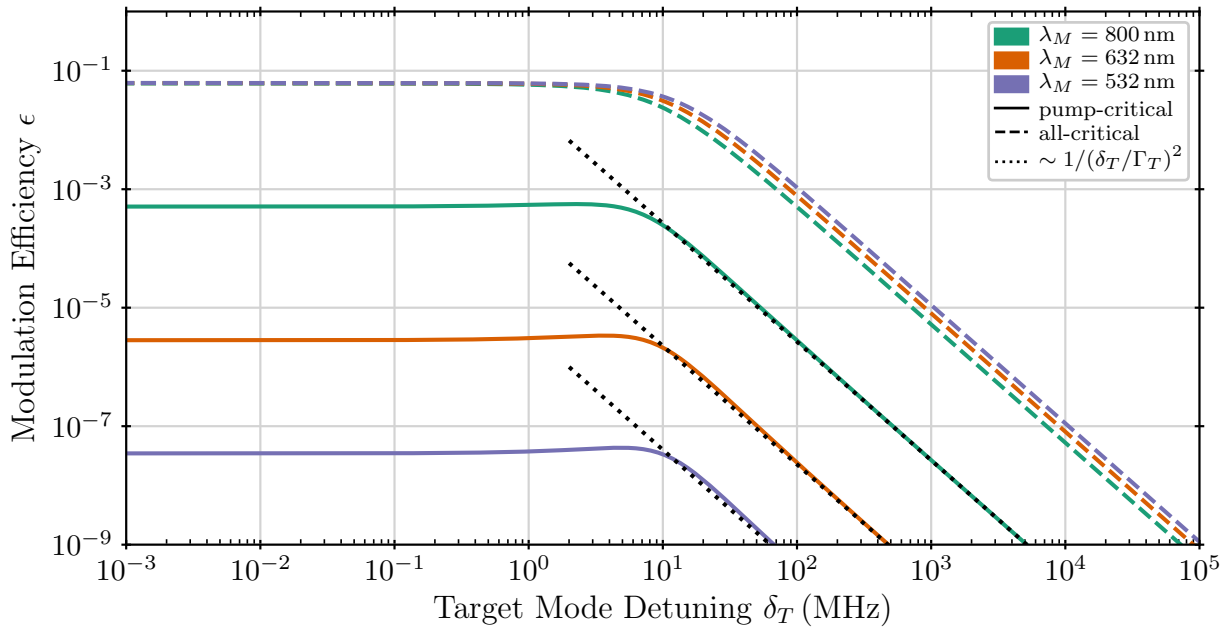


Figure 1.8: The modulation efficiency as the target mode frequency $\omega_T$ is detuned from perfect four-mode resonance. Since the other mode frequencies are constant, $\delta_T = \Delta_{MSPT}$, which appears in the molecular modulation terms in Equation (1.4.1). As the detuning becomes larger than the target mode linewidth $\Gamma_T$ (a few MHz for each $\lambda_M$), the modulation efficiency begins to decrease.

Because the mode structure in a microresonator is generally quite irregular, it is important to consider how we could achieve low four-mode detuning in an actual device. One possible method is that the resonator's mode frequencies could be tuned via the material's thermo-optic response (the change in index of refraction $n(\omega, T)$ with temperature $T$). The first-order thermo-optic coefficient in silica is $\alpha_n = 1.09 \times 10^{-5}\,\mathrm{K}^{-1}$ [61]. For small changes in the index of refraction, the resonator's mode frequencies will change by the same fraction that the index of refraction at that frequency changes [51]:

$$\frac{\partial \omega}{\partial T} \approx \frac{\omega}{n(\omega, T)} \frac{\partial n(\omega, T)}{\partial T} = \frac{\omega}{n(\omega, T)} \alpha_n \,. \tag{1.5.4}$$

Thus we have

$$\frac{\partial \Delta_{MSPT}}{\partial T} \approx \alpha_n \left( \frac{\omega_M}{n(\omega_M, T)} - \frac{\omega_S}{n(\omega_S, T)} + \frac{\omega_P}{n(\omega_P, T)} - \frac{\omega_T}{n(\omega_T, T)} \right) . \tag{1.5.5}$$

If we use $\lambda_P = 1064\,\text{nm}$ and $\lambda_M = 800\,\text{nm}$, assume that $\omega_T \approx \omega_M + 2\pi \times 12\,\text{THz}$ and $\omega_S \approx \omega_P - 2\pi \times 12\,\text{THz}$, and use the Sellmeier coefficients for silica at 20 °C [62], we find that $\frac{\partial \Delta_{MSPT}}{\partial T} \approx 2.0\,\text{MHz}\,\text{K}^{-1}$. With $\lambda_M = 532\,\text{nm}$, $\frac{\partial \Delta_{MSPT}}{\partial T} = 9.1\,\text{MHz}\,\text{K}^{-1}$.

This calculation indicates that the four-mode detuning could be adjusted by at least a few tens of MHz by a standard thermoelectric controller for any mixing wavelength in the optical region of the spectrum. Although the free spectral range in microresonators is generally at least a few GHz, the actual mode spacing (i.e., the distance to the mode with the closest frequency, not the next mode in the same family) in a non-ideal device can be much denser. For example, by giving a spherical microresonator a small eccentricity to lift the degeneracy of the whispering gallery modes, the actual spacing between adjacent modes could be reduced to a few tens of MHz [63], meaning the four-mode detuning should never be off by more than a few tens of MHz to begin with. However, one may still need to try many different four-mode sets to find a set with high modulation efficiency (due to the mode-dependent coupling factors).

### 1.5.3 Dependence of Modulation Efficiency on Mixing Wavelength

One of the key advantages of the MMM is that, depending on the size, geometry, and material of the microresonator, modes could be available over a wide range of wavelengths. Figure 1.9 shows how the modulation efficiency varies with the wavelength of the mixing mode. From the left panel we see that in the pump-critical case the modulation efficiency decreases dramatically as the separation between the pump and mixing wavelengths increases because the mixing and target modes become poorly coupled to the fiber (i.e., $Q_M^I$ is not close to $Q_M^C$). However, if we can critically couple all of the modes, $\epsilon$ becomes largely independent of $\lambda_M$ throughout the optical spectrum, as illustrated in the right panel.

In reality, we would still expect some variation with $\lambda_M$ because the mixing and target mode volumes and four-mode overlaps will vary, as discussed earlier. Nevertheless, as long as the MMM is built with the capability to adjust the coupling scheme and resonator temperature appropriately, the same device should be able to modulate efficiently over a large, continuous range of mixing beam wavelengths.

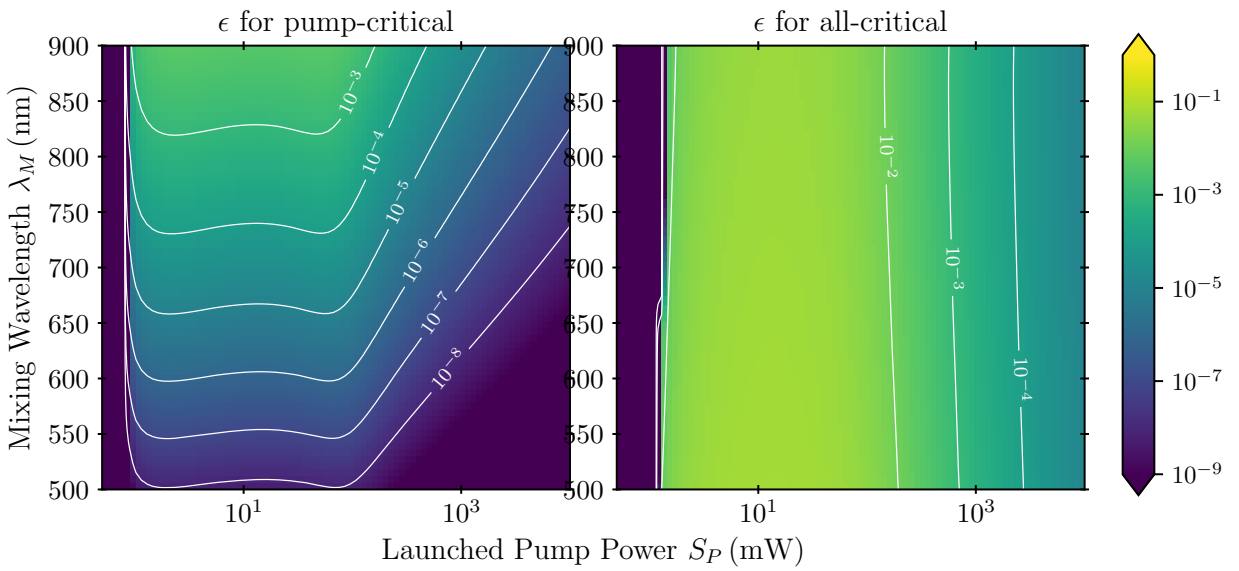


Figure 1.9: The modulation efficiency $\epsilon = P_T/S_M$ as a function of the launched pump power $S_P$ and the mixing mode wavelength $\lambda_M$, with the pump mode critically coupled (left) or all modes critically coupled (right). The dominant factor in the decreasing modulation efficiency on the left is the increasingly-non-critical coupling between the fiber and the mixing mode as $\lambda_M$ is moved further from the pump wavelength $\lambda_P = 1064\,\text{nm}$. On the right, where all modes are critically coupled, $\epsilon$ is essentially independent of $\lambda_M$.

### 1.5.4 Dependence of Modulation Efficiency on Intrinsic Quality Factor

Another factor that we could control is the intrinsic quality factor of the microsphere. So far, we have assumed that it is fixed at $Q^I = 10^8$. However, microspheres could be produced with either smaller or larger intrinsic quality factors than that. The results of simulations where we vary the intrinsic quality factor are shown in Figure 1.10.

When the intrinsic quality factor is increased at fixed launched pump power the modulation efficiency decreases. Increasing the intrinsic quality factor is essentially the same as shifting the curves in Figure 1.4 to lower pump power: threshold decreases, but since we are at fixed launched pump power, we are now further out on the curve, where we already know the modulation efficiency begins to decrease.

### 1.5.5 Dependence of Modulation Efficiency on fiber separation

So far, we have been working with two coupling schemes: either there is a single fiber critically coupled to the pump mode, or all of the modes are critically coupled. In this section, we will use

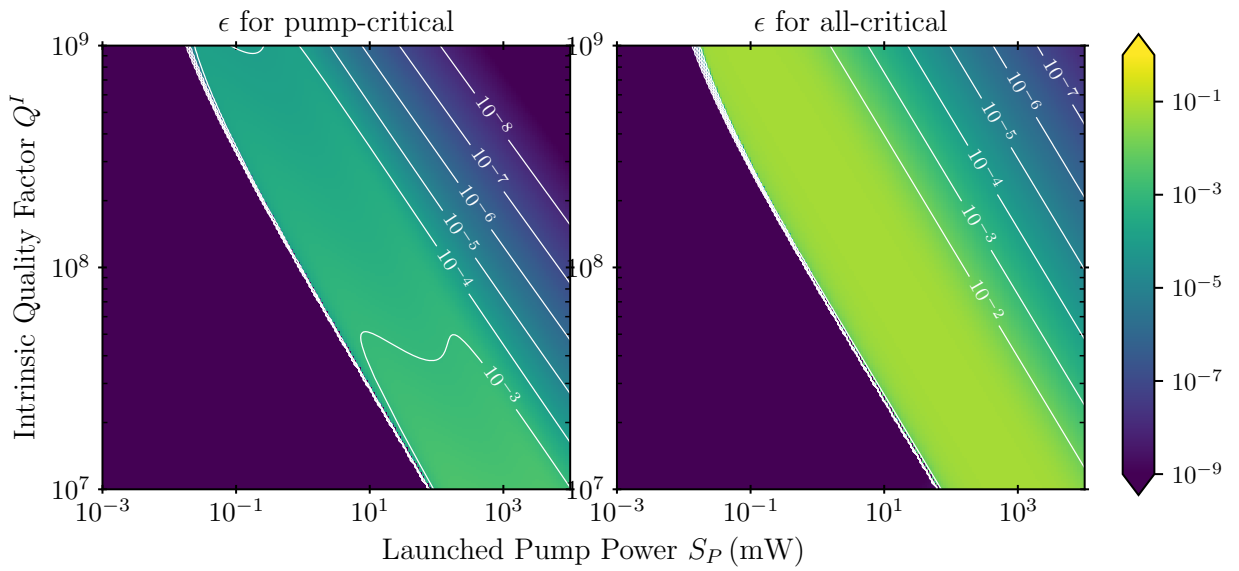


Figure 1.10: The modulation efficiency $\epsilon = P_T/S_M$ as a function of the launched pump power $S_P$ and the intrinsic quality factor $Q^I$, with the pump mode critically coupled (left) or all modes critically coupled (right). The pump and mixing wavelengths are $\lambda_P = 1064\,\text{nm}$ and $\lambda_M = 800\,\text{nm}$. When the intrinsic quality factor increases, threshold is decreased, but modulation efficiency also decreases, and vice-versa.

a single fiber as in the first case, but we will change its distance from the microsphere (the fiber separation $s$). As $s$ decreases, the coupling quality factor $Q^C$ decreases at all wavelengths, meaning that light can more easily move between the fiber and the microsphere. This scheme is the easiest to achieve experimentally, requiring no special modifications of the fiber or microsphere.

The results, shown in Figure 1.11, show that the modulation efficiency tends to increase as $Q^C$ decreases, with no special behavior near the critical separations. This is a result of the target mode not being directly pumped: we do not need to balance input and output power to get critical coupling, we just need to maximize the output power. Decreasing $Q^C$ lets more light leave the target mode and go to the fiber. Simultaneously, the threshold pump power is increasing, but this is not necessarily detrimental, because we know from Section 1.5.1 that there is no reason to go far beyond threshold. So we have an indirect route to increasing the modulation efficiency by increasing the launched pump power (which eluded us in Section 1.5.1): if we have spare pump power, we can move the fiber closer to the microsphere to get higher efficiency.

These results also indicate that the all-critical coupling scheme is not the coupling scheme that maximizes the modulation efficiency. Determining the ideal scheme will depend on a variety

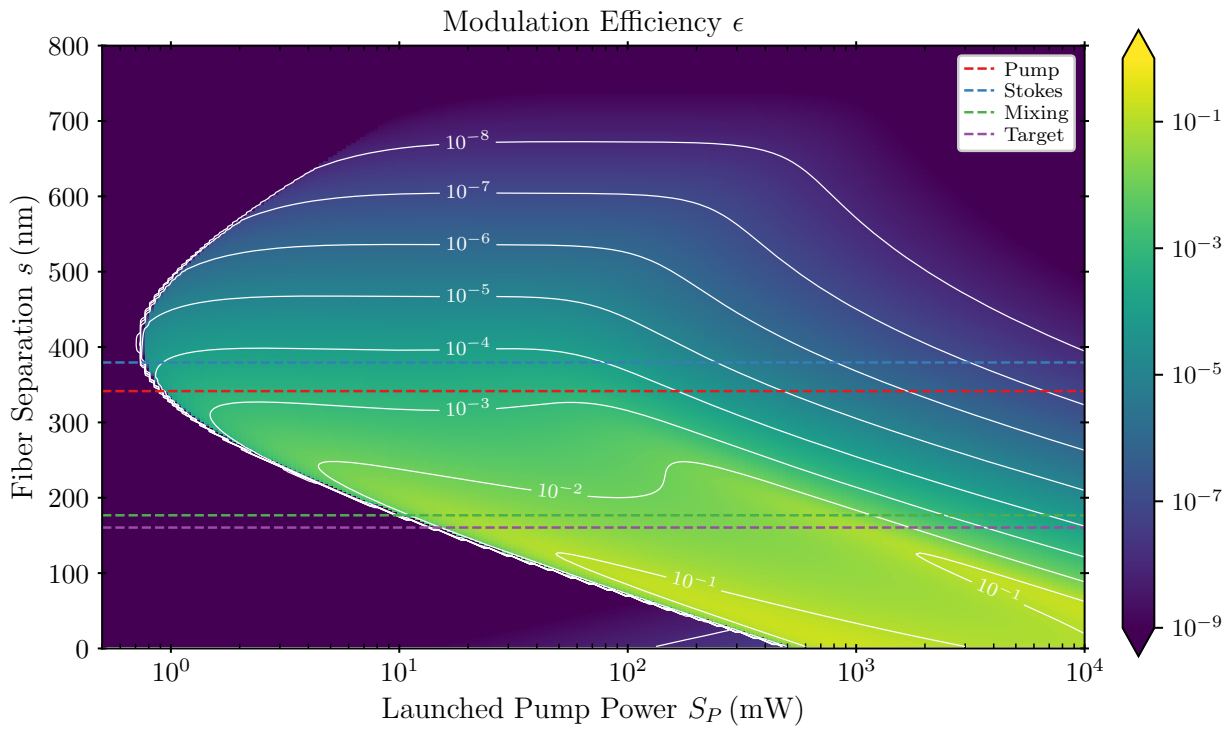


Figure 1.11: The modulation efficiency $\epsilon = P_T/S_M$ as a function of the launched pump power $S_P$ and the fiber separation $s$. Horizontal dashed lines are the fiber separations where each mode is critically coupled (but note that there is no special behavior at these separations). The pump and mixing wavelengths are $\lambda_P = 1064\,\text{nm}$ and $\lambda_M = 800\,\text{nm}$, and the fiber taper radius is $1\,\mu\text{m}$. The coupling quality factors $Q_q^C$ decrease for all modes as the fiber separation decreases.

of other design parameters and will involve a detailed search through the coupling and intrinsic quality factor parameter space for each mode (in addition to determining how to achieve those quality factors in practice).

## 1.6 Conclusions and Future Work

In this chapter, we have laid out the necessary theory to analyze a novel device: the Microresonator-based Molecular Modulator, or MMM. We have used this theory to simulate the behavior of the MMM over a significant set of design parameters for the device. We predict that it can achieve high efficiency (on the level of 1%) at THz-scale modulation frequencies for any mixing beam in the optical region of the spectrum.

Now that we have a basic idea of how to produce an MMM and what the design parameters should be, the next step is to fabricate one. We imagine that as this process continues, more

simulations will need to be run to answer design questions as they arise. Additionally, more physics might need to be added to the model to accurately describe the behavior of the physical modulator.

If an MMM can be produced, it would represent a significant improvement to the state-of-the-art in optical modulation, opening the doors to new techniques and applications in both research and industry. Below, we discuss some of these possibilities.

Synthesizing ever-shorter pulses requires ever-wider spectra. Optical modulators could be used to produce these spectra: if an optical modulator has sufficiently high efficiency, it can produce multiple modulation orders. This broad spectrum could be used to synthesize optical waveforms with a temporal resolution not currently achievable in the optical domain [64]. For example, if the modulation frequency is 100 THz and we can generate five modulated sidebands on each side of the mixing beam, the total bandwidth would be 1000 THz. This is large enough to produce ultrashort pulses with a duration less than 1 femtosecond. The MMM could finally provide a platform for achieving the necessary efficiency and modulation frequency.

Currently such short pulses can only be synthesized in the soft-X-ray region of the spectrum. Synthesizing these pulses in the more-accessible optical region may allow unprecedented access to these time scales in atoms and molecules. In the second chapter of this thesis, we explore one possible path of investigation that could be unlocked by this kind of waveform synthesizer.

Because the modulator works in the CW domain, the absolute frequency of the modulator can be set to a specific value with high precision. If a frequency-stabilized carrier is modulated, the generated sideband frequencies will also be known to very high precision, and their linewidths will be similar to the linewidth of the carrier [33]. These sidebands could then be used for precision spectroscopy of atoms and molecules at different wavelengths. This technique would also allow for the construction of optical clocks in new regions of the spectrum.

An optical modulator with a THz-scale modulation frequency could also be used to produce lasers in regions of the spectrum that are difficult to access, such as the far-infrared and the THz region [65]. For example, to generate THz radiation efficiently, one can use an infrared carrier beam and frequency down-shift it with the optical modulator [66]. A key advantage of a THz source based on modulation would be its tunability. Even a modest tuning of the carrier beam would generate a unique source that is tunable over the full THz region (1–10 THz). THz radiation sources have become increasingly important due to their applications in a wide range of fields, such as remote

sensing of chemicals.

Together, these applications form a compelling reason to continue improving our continuous-wave molecular modulation technique, and microresonators present a clear path for implementing those improvements.

# Chapter 2

# Ionization by Intense Ultrashort Pulses

There is great interest in producing ever-shorter and more-intense laser pulses. For example, the Extreme Light Infrastructure project has received nearly a billion dollars in funding to produce petawatt-scale lasers. Separately, researchers have been able to produce X-ray laser pulses only a few dozen attoseconds in duration [67].

Understandably, these researches are focused on the clearest technical challenges: the intensity and duration of the pulses. However, the intensity and duration of a pulse do not fully characterize it: the **shape** of the pulse is also important. The intensity, duration, and shape of a laser pulse are all interesting knobs that can be adjusted to produce different effects on the target. In the quest for maximum intensity and minimum duration, control over the shape is often sacrificed, or simply not considered important in the first place. Understanding and controlling all aspects of an ultrafast pulse is important for implementing what Krausz calls "ultrafast control" [68, 69].

In the previous chapter we investigated the possibility of producing an optical modulator that could, in principle, be used as the basis of an optical waveform generator [70, 71]. An ideal optical waveform generator could produce an arbitrary Fourier spectrum of light, which would allow it to synthesize exotic optical pulses, such as square waves [64]. Although utterly normal in electronics, the bandwidth and control required to generate a well-structured square wave optical pulse is far beyond current techniques.

But in the meantime, we can dream. In this chapter we investigate what happens when you crank all the knobs up: a pulse with an electric field amplitude comparable to the electric field in a hydrogen atom, with a duration comparable to the classical orbital period of the electron in a hydrogen atom, and with a shape that can be controlled on sub-cycle timescales. No existing laser systems can reach all three of these regimes simultaneously, but we can investigate the effects of

such a pulse by solving the time-dependent Schrödinger equation numerically.

As atomic physicists, our interest lies in what effect this pulse might have on a target atom. Our system of choice is the humble hydrogen atom. We chose hydrogen, despite it's short classical orbital period and huge electric field (which are what push this question past the bounds of current techniques), because the unperturbed problem is analytically solvable. This gives us a solid foundation that we can reproduce numerically to prove that our simulation is behaving as expected. The lack of multi-electron effects that would surely come in to play with a larger atom or a molecule also provides for easier intuition and visualization of the resulting quantum state.

The presence of only a single electron also provides a clear research question. As will be elaborated on later, a free electron cannot gain any energy or momentum from an electromagnetic wave (in the dipole approximation), while bound electrons can [72]. This raises a question: how does the electron "know" that it is bound? By analogy with classical orbital systems, it seems that this "knowledge" must come from the wavefunction exploring the potential energy landscape that it lives on. The timescale for this exploration should be on the order of the **classical orbital period** of the bound state: the time it would take the electron to orbit the proton in the Bohr model.

Thus, the question we originally aimed to answer with this research: what happens when the laser pulse is shorter than the classical orbital period? Does the electron begin to behave as if it was effectively free, and refuse to ionize no matter how large the applied electric field is?

Unfortunately, we were unable to arrive at a satisfactory answer to this question. The incredibly short timescales below the classical orbital period lead to laser pulses that are simply too intense to treat with the techniques we used. However, along the way, we did find another interesting question, with a clearer and more straightforward answer: under what conditions can a laser pulse with *smaller* peak intensity cause *more* ionization than a pulse with *larger* peak intensity? Surprisingly, we found that such conditions do indeed exist, and we devised a simple model that predicts this ionization probability reversal. These results were published in [73].

The first few sections in this chapter are intended to provide a bootstrap to understanding the computational techniques laid out in Section 2.3 and the results described in Section 2.4. Section 2.5 then discuses the details of the model that we devised, and Section 2.6 discusses more properties and possible future applications of that model.

## 2.1 Electromagnetic Waves

### 2.1.1 Maxwell's Equations and the Electromagnetic Wave Equations

The first step toward modeling the interaction of a laser field with an electron is to model the laser field independent of any interactions. Because we do not quantize the electromagnetic field in our simulations, we will need to deal with the electromagnetic wave equations. We begin with the differential form of Maxwell's equations for the electric field $\boldsymbol{\mathcal{E}}$ and the magnetic field $\boldsymbol{\mathcal{B}}$ [43]:

$$\boldsymbol{\nabla} \cdot \boldsymbol{\mathcal{E}} = \frac{\rho_e}{\epsilon_0} \tag{2.1.1a}$$

$$\boldsymbol{\nabla} \cdot \boldsymbol{\mathcal{B}} = 0 \tag{2.1.1b}$$

$$\boldsymbol{\nabla} \times \boldsymbol{\mathcal{E}} = -\frac{\partial \boldsymbol{\mathcal{B}}}{\partial t} \tag{2.1.1c}$$

$$\boldsymbol{\nabla} \times \boldsymbol{\mathcal{B}} = \mu_0 \left( \mathbf{J} + \epsilon_0 \frac{\partial \boldsymbol{\mathcal{E}}}{\partial t} \right), \tag{2.1.1d}$$

where $\rho_e$ is the volume density of electric charges, $\mathbf{J}$ is the volume density of electric currents, and $\epsilon_0$ and $\mu_0$ are the vacuum permittivity and permeability respectively. If we work in vacuum so that $\rho_e = 0$ and $\mathbf{J} = \mathbf{0}$, the equations become symmetric:

$$\boldsymbol{\nabla} \cdot \boldsymbol{\mathcal{E}} = 0 \tag{2.1.2a}$$

$$\boldsymbol{\nabla} \cdot \boldsymbol{\mathcal{B}} = 0 \tag{2.1.2b}$$

$$\boldsymbol{\nabla} \times \boldsymbol{\mathcal{E}} = -\frac{\partial \boldsymbol{\mathcal{B}}}{\partial t} \tag{2.1.2c}$$

$$\boldsymbol{\nabla} \times \boldsymbol{\mathcal{B}} = \mu_0 \, \epsilon_0 \frac{\partial \boldsymbol{\mathcal{E}}}{\partial t} \tag{2.1.2d}$$

If we take the curl of the two curl equations (2.1.2c) and (2.1.2d) we get, on the right hand side,

$$\boldsymbol{\nabla} \times \boldsymbol{\nabla} \times \boldsymbol{\mathcal{E}} = \boldsymbol{\nabla} \times \left( -\frac{\partial \boldsymbol{\mathcal{B}}}{\partial t} \right) = -\frac{\partial}{\partial t} \boldsymbol{\nabla} \times (\boldsymbol{\mathcal{B}}) = -\mu_0 \, \epsilon_0 \frac{\partial^2 \boldsymbol{\mathcal{E}}}{\partial t^2} \tag{2.1.3a}$$

$$\boldsymbol{\nabla} \times \boldsymbol{\nabla} \times \boldsymbol{\mathcal{B}} = \boldsymbol{\nabla} \times \left( \mu_0 \, \epsilon_0 \frac{\partial \boldsymbol{\mathcal{E}}}{\partial t} \right) = \mu_0 \, \epsilon_0 \, \frac{\partial}{\partial t} \boldsymbol{\nabla} \times (\boldsymbol{\mathcal{E}}) = -\mu_0 \, \epsilon_0 \frac{\partial^2 \boldsymbol{\mathcal{B}}}{\partial t^2} \tag{2.1.3b}$$

and on the left,

$$\boldsymbol{\nabla} \times \boldsymbol{\nabla} \times \boldsymbol{\mathcal{E}} = \boldsymbol{\nabla}(\boldsymbol{\nabla} \cdot \boldsymbol{\mathcal{E}}) - \nabla^2 \boldsymbol{\mathcal{E}} = -\nabla^2 \boldsymbol{\mathcal{E}} \tag{2.1.4a}$$

$$\boldsymbol{\nabla} \times \boldsymbol{\nabla} \times \boldsymbol{\mathcal{B}} = \boldsymbol{\nabla}(\boldsymbol{\nabla} \cdot \boldsymbol{\mathcal{B}}) - \nabla^2 \boldsymbol{\mathcal{B}} = -\nabla^2 \boldsymbol{\mathcal{B}} \tag{2.1.4b}$$

Combining, we find that

$$\mu_0 \, \epsilon_0 \frac{\partial^2 \boldsymbol{\mathcal{E}}}{\partial t^2} - \nabla^2 \boldsymbol{\mathcal{E}} = 0 \tag{2.1.5a}$$

$$\mu_0 \, \epsilon_0 \frac{\partial^2 \boldsymbol{\mathcal{B}}}{\partial t^2} - \nabla^2 \boldsymbol{\mathcal{B}} = 0 \tag{2.1.5b}$$

This pair of partial differential equations describes a propagating electromagnetic wave with speed $c = 1/\sqrt{\mu_0 \, \epsilon_0}$. It's not immediately apparent from (2.1.5) how $\boldsymbol{\mathcal{E}}$ and $\boldsymbol{\mathcal{B}}$ are related, but they are still coupled via (2.1.2).

### 2.1.2 Power Density

One of the measures we will use to classify a laser pulse is how much energy it contains. The key to performing that calculation is to determine the power density (units $\mathrm{J\,m^{-2}\,s^{-1}}$) of the electromagnetic wave. The tool for looking at this is the **Poynting vector**, which can be defined for any electromagnetic field as

$$\mathbf{S}(\mathbf{r}, t) = \frac{1}{\mu_0} \boldsymbol{\mathcal{E}}(\mathbf{r}, t) \times \boldsymbol{\mathcal{B}}(\mathbf{r}, t) = \epsilon_0 \, c^2 \, \boldsymbol{\mathcal{E}}(\mathbf{r}, t) \times \boldsymbol{\mathcal{B}}(\mathbf{r}, t) \tag{2.1.6}$$

The magnitude of the Poynting vector field is the instantaneous power density field.

For an electromagnetic wave in vacuum, (2.1.6) reduces to

$$\mathbf{S} = \epsilon_0 \, c^2 \, \mathcal{E}(\mathbf{r}, t) \, \mathcal{B}(\mathbf{r}, t) \, \mathbf{k} \tag{2.1.7}$$

where $|\mathbf{k}| = 2\pi/\lambda$, and (in vacuum) $\mathbf{k}$ points in the direction of propagation of the electromagnetic wave.

Now note that, via (2.1.2) (and thus only for an electromagnetic wave), we have

$$\begin{aligned} k\,\mathcal{E}(\mathbf{r},t) &= \omega\,\mathcal{B}(\mathbf{r},t) \\ \frac{k}{\omega}\,\mathcal{E}(\mathbf{r},t) &= \mathcal{B}(\mathbf{r},t) \\ \frac{\mathcal{E}(\mathbf{r},t)}{c} &= \mathcal{B}(\mathbf{r},t) \end{aligned} \tag{2.1.8}$$

Inserting (2.1.8) into (2.1.7) the magnitude of the Poynting vector becomes

$$\begin{aligned} \mathbf{S}(\mathbf{r},t) &= \epsilon_0\,c^2\,\mathcal{E}(\mathbf{r},t)\,\frac{\mathcal{E}(\mathbf{r},t)}{c}\,\mathbf{k} \\ \mathbf{S}(\mathbf{r},t) &= \epsilon_0\,c\,|\mathcal{E}(\mathbf{r},t)|^2\,\mathbf{k} \\ |\mathbf{S}(\mathbf{r},t)| &= \epsilon_0\,c\,|\mathcal{E}(\mathbf{r},t)|^2 \end{aligned} \tag{2.1.9}$$

The purely electric or purely magnetic power density are both half of (2.1.9): the electric and magnetic fields share the power of the electromagnetic wave equally.

Although the power densities of the two fields are equal, the magnitude of their effect on particles is generally not similar. For example, the expectation value of the speed of the electron in the ground state of a hydrogen atom is $\alpha c \approx c/137$. This reduces the magnetic force felt by the electron in the wave by a factor of $\alpha$ compared to the electric force, because the magnetic force cares about the speed of whatever it acts on.

This is quite relevant for the discussion to follow. Despite the high intensity of the laser pulses we will consider, we will entirely neglect the magnetic component of the electromagnetic field. This is the primary reason why we had difficulty looking for ionization suppression below the classical orbit time: when the pulses become that short, the intensities becomes so high that we always leave the regime where neglecting the magnetic component is reasonable [74–78].

### 2.1.3 Electromagnetic Potentials and Gauge Invariance

Although the physical fields $\boldsymbol{\mathcal{E}}$ and $\boldsymbol{\mathcal{B}}$ are what ultimately cause the physical effects that we see in nature, they are often inconvenient to perform calculations with. By using vector calculus identities we can generate a smaller system of coupled second-order differential equations from the first-order Maxwell equations.

In particular, note that since the divergence of $\boldsymbol{\mathcal{B}}$ is zero, it must be the curl of some vector field that we call $\boldsymbol{\mathcal{A}}$:

$$\boldsymbol{\nabla} \times \boldsymbol{\mathcal{A}} \equiv \boldsymbol{\mathcal{B}} \tag{2.1.10}$$

Now we can rewrite the third equation as

$$\begin{aligned} \boldsymbol{\nabla} \times \boldsymbol{\mathcal{E}} &= -\frac{\partial \boldsymbol{\mathcal{B}}}{\partial t} \\ \boldsymbol{\nabla} \times \boldsymbol{\mathcal{E}} &= -\frac{\partial}{\partial t} \boldsymbol{\nabla} \times \boldsymbol{\mathcal{A}} \\ \boldsymbol{\nabla} \times \left( \boldsymbol{\mathcal{E}} + \frac{\partial \boldsymbol{\mathcal{A}}}{\partial t} \right) &= \mathbf{0} \end{aligned} \tag{2.1.11}$$

Since the curl of $\boldsymbol{\mathcal{E}} + \partial_t \boldsymbol{\mathcal{A}}$ is $\mathbf{0}$, it must be the gradient of a scalar field which we call $\Phi$:

$$\begin{aligned} -\boldsymbol{\nabla}\Phi &\equiv \boldsymbol{\mathcal{E}} + \frac{\partial \boldsymbol{\mathcal{A}}}{\partial t} \\ \boldsymbol{\mathcal{E}} &= -\boldsymbol{\nabla}\Phi - \frac{\partial \boldsymbol{\mathcal{A}}}{\partial t} \end{aligned} \tag{2.1.12}$$

If we plug these back into the other two Maxwell equations we arrive at a pair of coupled second-order differential equations, which unfortunately include many mixed (i.e., both space and time) derivatives.

$$\begin{aligned} \boldsymbol{\nabla} \cdot \boldsymbol{\mathcal{E}} &= \frac{\rho_e}{\epsilon_0} \\ \boldsymbol{\nabla} \cdot -\boldsymbol{\nabla}\Phi - \frac{\partial \boldsymbol{\mathcal{A}}}{\partial t} &= \frac{\rho_e}{\epsilon_0} \\ \nabla^2 \Phi + \frac{\partial}{\partial t}(\boldsymbol{\nabla} \cdot \boldsymbol{\mathcal{A}}) &= -\frac{\rho_e}{\epsilon_0} \end{aligned} \tag{2.1.13}$$

and

$$\begin{aligned} \boldsymbol{\nabla} \times (\boldsymbol{\nabla} \times \boldsymbol{\mathcal{A}}) &= \mu_0 \left( \mathbf{J} + \epsilon_0 \frac{\partial}{\partial t} \left[ -\boldsymbol{\nabla}\Phi - \frac{\partial \boldsymbol{\mathcal{A}}}{\partial t} \right] \right) \\ \boldsymbol{\nabla}(\boldsymbol{\nabla} \cdot \boldsymbol{\mathcal{A}}) - \nabla^2 \boldsymbol{\mathcal{A}} &= \mu_0 \left( \mathbf{J} + \epsilon_0 \frac{\partial}{\partial t} \left[ -\boldsymbol{\nabla}\Phi - \frac{\partial \boldsymbol{\mathcal{A}}}{\partial t} \right] \right) \end{aligned} \tag{2.1.14}$$

These equations are not particularly pleasant to work with, but luckily we haven't used all of

our degrees of freedom yet. Since $\boldsymbol{\mathcal{B}}$ is the curl of $\boldsymbol{\mathcal{A}}$ and the curl of the gradient of any vector field is zero, we can add an arbitrary gradient to $\boldsymbol{\mathcal{A}}$ without changing the physical field $\boldsymbol{\mathcal{B}}$. To make sure the electric field is also unchanged we must balance the addition of the new gradient to $\boldsymbol{\mathcal{A}}$ by subtracting the time derivative of that field from $\Phi$. If we make both transformations simultaneously, we get a new pair of potentials $\boldsymbol{\mathcal{A}}'$ and $\Phi'$ that produce the same physical fields $\boldsymbol{\mathcal{E}}$ and $\boldsymbol{\mathcal{B}}$:

$$\boldsymbol{\mathcal{A}} \to \boldsymbol{\mathcal{A}}' = \boldsymbol{\mathcal{A}} + \boldsymbol{\nabla}\Lambda \tag{2.1.15}$$

$$\Phi \to \Phi' = \Phi - \frac{\partial \Lambda}{\partial t}, \tag{2.1.16}$$

where $\Lambda$ can be an arbitrary smooth function of space and time. This kind of transformation, which preserves the physical fields while modifying the potentials, is called a **gauge transformation**. These extra degrees of freedom let us pick $\boldsymbol{\mathcal{A}}$ and $\Phi$ in special ways to reduce the complexity of the second-order equations above.

### 2.1.4 Laser Pulses

Now that we have the general tools for understanding how an electromagnetic wave, we will use them to analyze a particular kind of wave: a pulse. A pulse is a short, isolated, and often intense excitation of the electromagnetic field, generally produced by a laser (hence, laser pulses).

We will assume that the pulse is uniform in space, which lets us drop position dependence throughout. This is a reasonable assumption as long as the region of interest is smaller than the wavelength of the electromagnetic wave. We also assume that the electromagnetic wave is **polarized** along the $\hat{z}$ direction, which means that the electric field vector always points along $\hat{z}$. Together, we have $\boldsymbol{\mathcal{E}}(r,t) = \mathcal{E}(t)\,\hat{\mathbf{z}}$.

Such a laser pulse is necessarily composed of a large number of individual frequency components, called its **spectrum**. In our research we generally assume that the pulses are constructed out of continuous spectra (as opposed to discrete). Thus, we will be doing a lot of work with Fourier transforms in this section to go back and forth between the pulse's temporal profile and its spectral properties. The function that describes the (complex) electric field amplitude of each frequency component is called the **amplitude spectrum**.

The electric field of a transform-limited laser pulse (i.e., the phase across the pulse's frequency spectrum varies very slowly) at a given position can be put into **carrier-envelope form**

$$\mathcal{E}(t) = \mathcal{E}_t \, F(t) \, \cos(\omega_c \, t + \varphi) \tag{2.1.17}$$

where $\omega_c$ is the **carrier angular frequency**, $F(t)$ is an **envelope function**, and $\varphi$ is the **carrier-envelope phase** (a constant in our work, but possibly varying in time on its own in other work, as in a chirped pulse). Such a pulse has an amplitude spectrum that is symmetric around $\omega_c$. We only work with transform-limited pulses due to their simplicity.

We define the **pulse fluence** $H$ (the total energy density, units $\mathrm{J\,m^{-2}}$) by integrating the pulse power density (2.1.9) over time at some position:

$$\begin{aligned} H &= \int_{-\infty}^{\infty} |\mathbf{S}(t)| \, \mathrm{d}t \\ H &= \epsilon_0 \, c \int_{-\infty}^{\infty} |\mathcal{E}(t)|^2 \, \mathrm{d}t \end{aligned} \tag{2.1.18}$$

The quantity $|\mathbf{S}(t)| = \epsilon_0 \, c |\mathcal{E}(t)|^2$ is the **instantaneous intensity** of the laser. We can also determine the fluence via the Plancherel theorem, which in this context tells us that

$$\int_{-\infty}^{\infty} |\mathcal{E}(t)|^2 \, \mathrm{d}t = \int_{-\infty}^{\infty} \left| \widehat{\mathcal{E}}(\omega) \right|^2 \mathrm{d}\omega \tag{2.1.19}$$

Therefore,

$$H = \epsilon_0 \, c \int_{-\infty}^{\infty} |\mathcal{E}(t)|^2 \, \mathrm{d}t = \epsilon_0 \, c \int_{-\infty}^{\infty} \left| \widehat{\mathcal{E}}(\omega) \right|^2 \mathrm{d}\omega = \epsilon_0 \, c \int_{-\infty}^{\infty} \left| \widehat{\mathcal{E}}(f) \right|^2 \mathrm{d}f \tag{2.1.20}$$

Note that this definition only makes sense for pulses with continuous spectra: real, physical pulses might be part of a pulse train, with a discontinuous spectra, and the above definition would need to be modified.

Since the electric field $\mathcal{E}(t)$ is always real its Fourier transform $\widehat{\mathcal{E}}(\omega)$ is Hermitian (i.e., $\widehat{\mathcal{E}}(-\omega) = \widehat{\mathcal{E}}^*(\omega)$). The frequency information at negative frequency is therefore superfluous. To facilitate calculations we will sometimes consider only the positive frequency components. In this case, when

we perform the inverse Fourier transform we really produce the complex electric field $\widetilde{\mathcal{E}}(t)$:

$$\frac{1}{\sqrt{2\pi}} \int_0^\infty \widehat{\mathcal{E}}(\omega)\, \mathrm{d}\omega = \widetilde{\mathcal{E}}(t) \tag{2.1.21a}$$

$$\mathcal{E}(t) = \mathrm{Re}\Big\{\widetilde{\mathcal{E}}(t)\Big\} \tag{2.1.21b}$$

The complex electric field contains some useful information that is somewhat harder to get from $\mathcal{E}(t)$. For example, its absolute value is the envelope of the electric field:

$$|\mathcal{E}(t)| \leq \Big|\widetilde{\mathcal{E}}(t)\Big| \tag{2.1.22}$$

For simplicity, all calculations are performed with a pulse centered at $t = 0$. To get a pulse centered at $t = t_0$, replace $t$ with $t - t_0$ in $\mathcal{E}(t)$ and replace $\widehat{\mathcal{E}}(\omega)$ with $e^{-2\pi i\, t_0\, \omega}\, \widehat{\mathcal{E}}(\omega)$.

| Symbol | Units | Meaning |
|---|---|---|
| $\mathcal{E}(t)$ | $\mathrm{V\,m^{-1}}$ | The physical electric field as a function of time |
| $\widetilde{\mathcal{E}}(t)$ | $\mathrm{V\,m^{-1}}$ | The complex electric field as a function of time |
| $\widehat{\mathcal{E}}(\omega)$ | $\mathrm{V\,m^{-1}\,s}$ | The electric field amplitude density in the angular frequency domain |
| $\widehat{\mathcal{E}}(f)$ | $\mathrm{V\,m^{-1}\,Hz^{-1}}$ | The electric field amplitude density in the frequency domain |
| $F(t)$ | - | The envelope function in the time domain |
| $\widehat{F}(\omega)$ | - | The envelope function in the angular frequency domain |
| $\widehat{F}(f)$ | - | The envelope function in the frequency domain |
| $\mathcal{E}_t$ | $\mathrm{V\,m^{-1}}$ | The peak electric field amplitude in the time domain |
| $\mathcal{E}_\omega$ | $\mathrm{V\,m^{-1}\,s}$ | The peak electric field amplitude density in the angular frequency domain |
| $\mathcal{E}_f$ | $\mathrm{V\,m^{-1}\,Hz^{-1}}$ | The peak electric field amplitude density in the frequency domain |
| $\Delta_t$ | s | The full-width at half-max (FWHM) of the electric field amplitude in the time domain |
| $\Delta_\omega$ | $\mathrm{s^{-1}}$ | The "bandwidth" (typically FWHM) of the electric field amplitude density in the angular frequency domain |
| $\Delta_f$ | Hz | The "bandwidth" (typically FWHM) of the electric field amplitude density in the frequency domain |
| $\tau$ | s | The "pulse width" in the time domain, typically the inverse of the bandwidth $\Delta_f$ |
| $\omega_c$ | $\mathrm{s^{-1}}$ | The carrier or center angular frequency of the pulse |
| $f_c$ | Hz | The carrier or center frequency of the pulse |
| $\varphi$ | - | The global phase difference between the carrier frequency and the envelope function, often called the carrier-envelope phase (CEP) |
| $H$ | $\mathrm{J\,m^{-2}}$ | The fluence of the electromagnetic pulse |
| $I_p$ | $\mathrm{W\,m^{-2}}$ | The peak intensity of the electromagnetic pulse |

Table 2.1: Notation for laser pulses.

#### 2.1.4.1 Sinc Pulses

A sinc pulse is produced from a rectangular power spectrum. A transform-limited sinc pulse has an amplitude spectrum that looks like

$$\widehat{\mathcal{E}}(\omega) = \begin{cases} \mathcal{E}_\omega\, e^{i\varphi} & \omega_{\min} < \omega < \omega_{\max} \\ \mathcal{E}_\omega\, e^{-i\varphi} & \omega_{\min} < -\omega < \omega_{\max} \\ 0 & \text{else} \end{cases} \tag{2.1.23}$$

For this spectrum we define the bandwidth $\Delta_\omega$ to be $\omega_{\max} - \omega_{\min}$.

The fluence is easy to determine via Parseval's theorem:

$$\begin{aligned} H &= \epsilon_0\, c \int_{-\infty}^{\infty} \left|\widehat{\mathcal{E}}(\omega)\right|^2 \mathrm{d}\omega \\ &= 2\epsilon_0\, c\, (\omega_{\max} - \omega_{\min}) |\mathcal{E}_\omega|^2 \\ H &= 2\,\epsilon_0\, c\, \Delta_\omega\, \mathcal{E}_\omega^2 \\ \mathcal{E}_\omega &= \sqrt{\frac{H}{2\,\epsilon_0\, c\, \Delta_\omega}} \end{aligned} \tag{2.1.24}$$

We can calculate $\mathcal{E}(t)$ by inverse Fourier transforming $\widehat{\mathcal{E}}(\omega)$:

$$\begin{aligned} \mathcal{E}(t) &= \frac{1}{\sqrt{2\pi}} \int_{-\infty}^{\infty} \widehat{\mathcal{E}}(\omega)\, e^{i\omega t}\, \mathrm{d}\omega \\ &= \frac{1}{\sqrt{2\pi}} \left[ \int_{-\omega_{\max}}^{-\omega_{\min}} \mathcal{E}_\omega\, e^{-i\varphi}\, e^{i\omega t}\, \mathrm{d}\omega + \int_{\omega_{\min}}^{\omega_{\max}} \mathcal{E}_\omega\, e^{i\varphi}\, \mathrm{d}\omega \right] \\ &= \frac{\mathcal{E}_\omega}{\sqrt{2\pi}} \left[ e^{-i\varphi} \int_{-\omega_{\max}}^{-\omega_{\min}} e^{i\omega t}\, \mathrm{d}\omega + e^{i\varphi} \int_{\omega_{\min}}^{\omega_{\max}} e^{i\omega t}\, \mathrm{d}\omega \right] \\ &= \frac{\mathcal{E}_\omega}{\sqrt{2\pi}} \left[ e^{-i\varphi}\, \frac{e^{i\omega t}}{it}\bigg|_{-\omega_{\max}}^{-\omega_{\min}} + e^{i\varphi}\, \frac{e^{i\omega t}}{it}\bigg|_{\omega_{\min}}^{\omega_{\max}} \right] \\ &= \frac{\mathcal{E}_\omega}{\sqrt{2\pi}} \left[ e^{-i\varphi} \left( \frac{e^{-i\omega_{\min} t}}{it} - \frac{e^{-i\omega_{\max} t}}{it} \right) + e^{i\varphi} \left( \frac{e^{i\omega_{\max} t}}{it} - \frac{e^{i\omega_{\min} t}}{it} \right) \right] \\ \mathcal{E}(t) &= \frac{\mathcal{E}_\omega}{\sqrt{2\pi}} \frac{1}{it} \left[ e^{-i\varphi} \left( e^{-i\omega_{\min} t} - e^{-i\omega_{\max} t} \right) + e^{i\varphi} \left( e^{i\omega_{\max} t} - e^{i\omega_{\min} t} \right) \right] \end{aligned} \tag{2.1.25}$$

Now we combine the $\omega_{\max}$ or $\omega_{\min}$ terms together to get phase-shifted unnormalized sinc functions:

$$\begin{aligned}
\mathcal{E}(t) &= \frac{\mathcal{E}_\omega}{\sqrt{2\pi}}\frac{2}{t}\left[\frac{e^{i(\omega_{\max}t+\varphi)}-e^{-i(\omega_{\max}t+\varphi)}}{2i} - \frac{e^{i(\omega_{\min}t+\varphi)}-e^{-i(\omega_{\min}t+\varphi)}}{2i}\right] \\
&= \frac{\mathcal{E}_\omega}{\sqrt{2\pi}}\frac{2}{t}[\sin(\omega_{\max}t+\varphi)-\sin(\omega_{\min}t+\varphi)] \\
\mathcal{E}(t) &= \frac{2\,\mathcal{E}_\omega}{\sqrt{2\pi}}\left[\frac{\sin(\omega_{\max}t+\varphi)-\sin(\omega_{\min}t+\varphi)}{t}\right]
\end{aligned} \tag{2.1.26}$$

This form has a clear intuitive picture: it is the inverse Fourier transform of a rectangle from $-\omega_{\max}$ to $\omega_{\max}$ with the inverse Fourier transform of a rectangle from $-\omega_{\min}$ to $\omega_{\min}$ removed. This is exactly what we should have expected to get since the Fourier transform is linear. We can continue simplifying to get it into the envelope-carrier form by using a sum-to-product identity

$$\sin(a)-\sin(b) = 2\sin\left(\frac{a-b}{2}\right)\cos\left(\frac{a+b}{2}\right). \tag{2.1.27}$$

Armed with this identity, we can combine the two terms:

$$\begin{aligned}
\mathcal{E}(t) &= \frac{4\,\mathcal{E}_\omega}{\sqrt{2\pi}}\frac{\sin\left(\frac{\omega_{\max}-\omega_{\min}}{2}\,t\right)}{t}\cos\left(\frac{\omega_{\max}+\omega_{\min}}{2}\,t+\varphi\right) \\
&= \frac{4\,\mathcal{E}_\omega}{\sqrt{2\pi}}\frac{\sin\left(\frac{\Delta_\omega}{2}\,t\right)}{t}\cos(\omega_c\,t+\varphi) \\
&= \frac{4\,\mathcal{E}_\omega}{\sqrt{2\pi}}\frac{\Delta_\omega}{2}\,\operatorname{sinc}\left(\frac{\Delta_\omega}{2}t\right)\cos(\omega_c\,t+\varphi) \\
&= \sqrt{\frac{2}{\pi}}\,\mathcal{E}_\omega\,\Delta_\omega\,\operatorname{sinc}\left(\frac{\Delta_\omega}{2}t\right)\cos(\omega_c\,t+\varphi) \\
\mathcal{E}(t) &= \mathcal{E}_t\,\operatorname{sinc}\left(\frac{\Delta_\omega}{2}t\right)\cos(\omega_c\,t+\varphi)
\end{aligned} \tag{2.1.28}$$

where $\omega_c = (\omega_{\max}+\omega_{\min})/2$ and $\mathcal{E}_t = \sqrt{2/\pi}\,\mathcal{E}_\omega\,\Delta_\omega$. Figure 2.1 shows examples of sinc pulses with various carrier-envelope phases. These pulse typically have a central region with two or three high-intensity electric field peaks, preceded and followed by a long train of decaying peaks.

For implementation purposes it is convenient to have $\mathcal{E}_t$ in terms of the pulse fluence. Referring

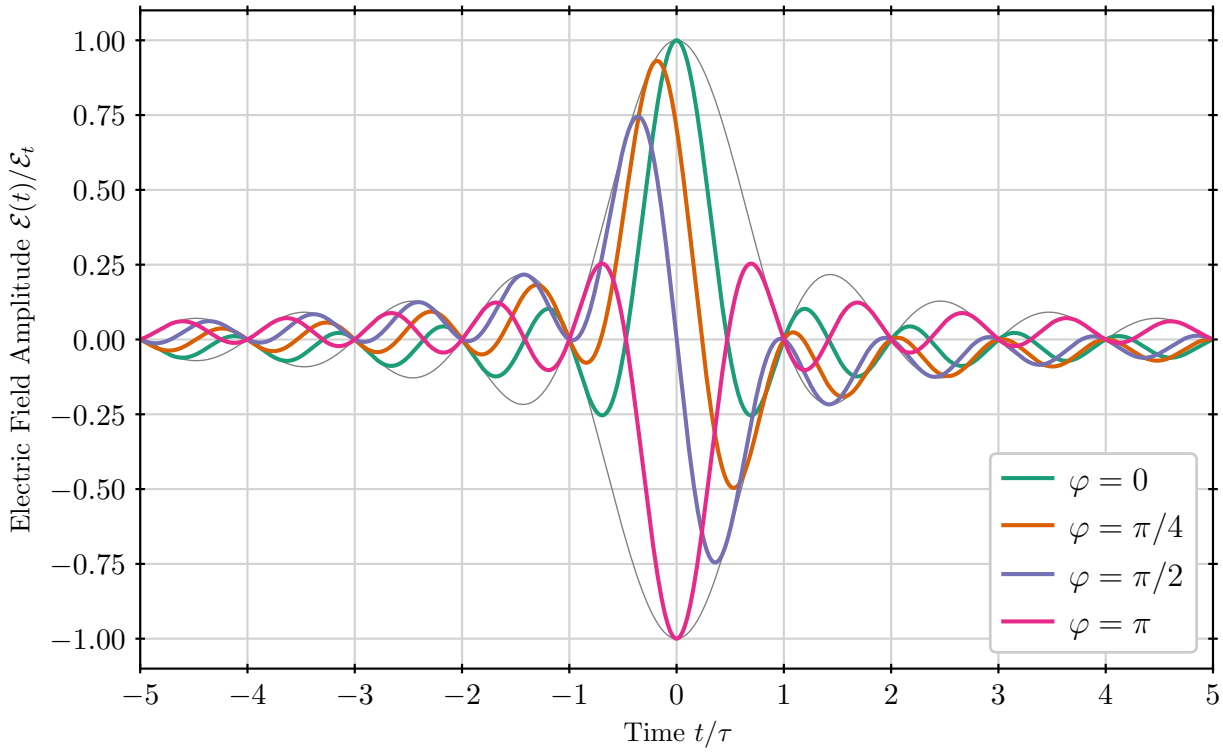


Figure 2.1: Electric fields of sub-cycle sinc pulses with various phases.

to (2.1.24), we have

$$\mathcal{E}_t = \sqrt{\frac{2}{\pi}}\,\mathcal{E}_\omega\,\Delta_\omega \tag{2.1.29}$$

$$= \sqrt{\frac{2}{\pi}}\sqrt{\frac{H}{2\,\epsilon_0\,c\,\Delta_\omega}}\,\Delta_\omega$$

$$\mathcal{E}_t = \sqrt{\frac{H\,\Delta_\omega}{\pi\,\epsilon_0\,c}} \tag{2.1.30}$$

In carrier-envelope form it is clear that the transform-limited sinc pulse is a cosine oscillating under a sinc envelope. Unlike the other envelope functions we consider, sinc can be both positive and negative, so it may reverse the sign of the cosine. Additionally, since sinc has its own zeros,

the overall pulse will have envelope-enforced zeros (regardless of the choice of $\varphi$) whenever

$$\operatorname{sinc}\left(\frac{\Delta_\omega}{2}t\right) = 0 \tag{2.1.31}$$

$$\implies \sin\left(\frac{\Delta_\omega}{2}t\right) = 0 \qquad t \neq 0 \tag{2.1.32}$$

$$\implies \frac{\Delta_\omega}{2}t = n\pi \qquad n \neq 0 \tag{2.1.33}$$

$$\implies t = \frac{2\pi}{\Delta_\omega}n \qquad n \neq 0 \tag{2.1.34}$$

as well as additional zeros from the carrier.

We define $\tau = 2\pi/\Delta_\omega = 1/\Delta_f$ to be the pulse width in the time domain. Although $t = \tau$ is not generally the position of the first electric field zero, it does define the region over which the pulse intensity will be dramatically larger than at earlier or later times. To highlight the role of the pulse width, we can write the pulse in the convenient form

$$\mathcal{E}(t) = \mathcal{E}_t \operatorname{sinc}\left(\pi\frac{t}{\tau}\right)\cos(\omega_c\, t + \varphi) \tag{2.1.35}$$

where the sinc function has been effectively replaced by the normalized sinc function.

At fixed fluence, the electric field amplitude decreases as the square root of the pulse width:

$$\mathcal{E}_t = \sqrt{\frac{H\,\Delta_\omega}{\pi\,\epsilon_0\,c}} = \sqrt{\frac{2\,H}{\epsilon_0\,c\,\tau}} \tag{2.1.36}$$

For a $\varphi = 0$ sinc pulse, the relationship between $H$ and $I_p$ is

$$I_p = 2\frac{H}{\tau} \tag{2.1.37}$$

#### 2.1.4.2 Gaussian Pulses

For the Gaussian pulse we will go in reverse (desired electric field to amplitude spectrum) because we want to make sure we get the right bandwidth from our pulse width. A transform-limited

Gaussian electric field pulse with a carrier frequency $\omega_c$, carrier phase $\varphi$, and pulse width $\tau$ is

$$\mathcal{E}(t) = \mathcal{E}_t \, \exp\left(-\frac{1}{2}\left(\frac{t}{\tau}\right)^2\right) \, \cos(\omega_c \, t + \varphi) \tag{2.1.38}$$

The Fourier transform is simple to compute using the results for the Fourier transform of a function multiplied by a cosine, and the Gaussian integral

$$\int_{-\infty}^{\infty} e^{-ax^2+bx} \, \mathrm{d}x = \sqrt{\frac{\pi}{a}} \, e^{b^2/4a} \tag{2.1.39}$$

Using these, we have

$$\widehat{\mathcal{E}}(\omega) = \mathcal{E}_t \frac{1}{2}\Big[e^{i\varphi}\widehat{f}(\omega+\omega_0) + e^{-i\varphi}\widehat{f}(\omega-\omega_0)\Big] \tag{2.1.40}$$

where

$$\widehat{f}(\omega) = \frac{1}{\sqrt{2\pi}} \int_{-\infty}^{\infty} \exp\left(-\frac{1}{2}\left(\frac{t}{\tau}\right)^2\right) e^{-i\omega t} \, \mathrm{d}t \tag{2.1.41}$$

$$= \frac{1}{\sqrt{2\pi}} \sqrt{\frac{\pi}{1/2\tau^2}} \exp\left(-\frac{1}{2}(\omega\tau)^2\right) \tag{2.1.42}$$

$$\widehat{f}(\omega) = \tau \exp\left(-\frac{1}{2}(\omega\tau)^2\right) \tag{2.1.43}$$

We can plug in to get the electric field amplitude spectrum:

$$\widehat{\mathcal{E}}(\omega) = \mathcal{E}_\omega \left[e^{i\varphi} \exp\left(-\frac{1}{2}[(\omega+\omega_c)\tau]^2\right) + e^{-i\varphi} \exp\left(-\frac{1}{2}[(\omega-\omega_c)\tau]^2\right)\right] \tag{2.1.44}$$

where $\mathcal{E}_\omega = \mathcal{E}_t\tau/2$. The amplitude spectrum is Hermitian: a Gaussian centered at $\omega_c$, with width determined by the pulse width $\tau$.

We can determine the pulse fluence from $\widehat{\mathcal{E}}(\omega)$:

$$H = \epsilon_0\, c \int_{-\infty}^{\infty} \left|\widehat{\mathcal{E}}(\omega)\right|^2 \mathrm{d}\omega \tag{2.1.45}$$

$$= 2\epsilon_0\, c \int_0^{\infty} \left|\mathcal{E}_\omega e^{-i\varphi} \exp\!\left(-\frac{1}{2}[(\omega-\omega_c)\tau]^2\right)\right|^2 \mathrm{d}\omega \tag{2.1.46}$$

$$= 2\epsilon_0\, c\, \mathcal{E}_\omega^2 \int_0^{\infty} \exp\!\left(-[(\omega-\omega_c)\tau]^2\right) \mathrm{d}\omega \tag{2.1.47}$$

$$= 2\epsilon_0\, c\, \mathcal{E}_\omega^2 \frac{\sqrt{\pi}}{\tau} \tag{2.1.48}$$

$$H = 2\sqrt{\pi}\,\epsilon_0\, c\, \frac{\mathcal{E}_\omega^2}{\tau} \tag{2.1.49}$$

$$\mathcal{E}_t = \sqrt{\frac{2H}{\sqrt{\pi}\,\epsilon_0\, c\, \tau}} \tag{2.1.50}$$

Note that we implicitly assumed that $\omega_c \gg 1/\tau$ in the second line. If this is not the case, there may be overlap between the two halves of the spectrum near $\omega = 0$ which introduces interference-like terms in the integral which we have not accounted for. Although for femtosecond pulses this is rarely a concern, attosecond pulses may require $\omega_c > 2000\,\mathrm{THz}$. This assumption is realistic because we do not expect any zero-frequency components in the pulse, which $\omega_c < \tau$ implies (i.e., if the bandwidth is larger than the center frequency, there must be amplitude at $\omega = 0$.). See Section 2.1.5 for more discussion on DC correction.

For a $\varphi = 0$ Gaussian pulse, the relationship between $H$ and $I_p$ is

$$I_p = \frac{2}{\sqrt{\pi}} \frac{H}{\tau}. \tag{2.1.51}$$

We recently became interested in nearly-single-cycle Gaussian pulses. The immediate question is: for a given pulse width, what is the smallest the carrier frequency can be? I think a sensible way to do this is to set some cutoff in the power spectrum based on the variance of the power spectrum. If we look at just the positive half of the amplitude spectrum and square it, we find

$$\left|\widehat{\mathcal{E}}(\omega > 0)\right|^2 = \mathcal{E}_\omega^2 \exp\!\left(-\left[\frac{\omega-\omega_c}{1/\tau}\right]^2\right) \tag{2.1.52}$$

$$\left|\widehat{\mathcal{E}}(\omega > 0)\right|^2 = \mathcal{E}_\omega^2 \exp\!\left(-\frac{1}{2}\left[\frac{\omega-\omega_c}{1/\sqrt{2}\tau}\right]^2\right). \tag{2.1.53}$$

So the standard deviation of the power spectrum in angular frequency is $1/\sqrt{2}\tau$. Let's say we want $N_\sigma$ standard deviations of exclusion between the carrier frequency and zero frequency. Then the minimum carrier frequency is

$$\omega_{c,\,\min} = \frac{\pi N_\sigma}{\sqrt{2}\tau} \tag{2.1.54}$$

$$f_{c,\,\min} = \frac{N_\sigma}{2\sqrt{2}\pi\tau}. \tag{2.1.55}$$

Example: for a $\tau = 200\,\text{as}$ Gaussian pulse, $f_{c,\,\min} \approx N_\sigma \times 563\,\text{THz}$.

Yet another parameterization would be to fix the number of cycles of the carrier under the envelope. We choose the number of pulse widths (i.e., standard deviations of the envelope) to consider, $N_\tau$, typically 3. The amount of time "under the envelope" is then $N_\tau\tau$. The number of cycles under the envelope is

$$N_c = \frac{N_\tau\tau}{T_c}, \tag{2.1.56}$$

where $T_c = 1/f_c = 2\pi/\omega_c$ is the period of the carrier wave. Therefore we choose

$$\omega_c = \frac{2\pi N_c}{N_\tau\tau} \tag{2.1.57}$$

to be the carrier frequency of the pulse.

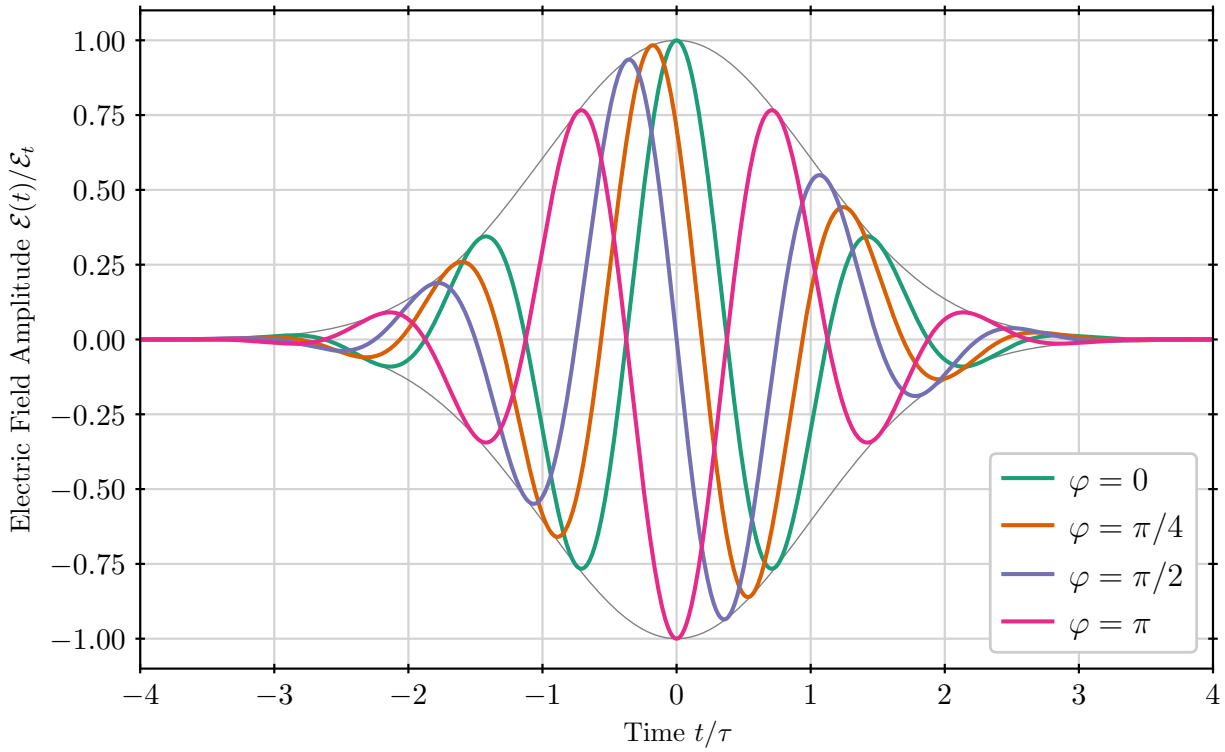


Figure 2.2: Electric fields of few-cycle Gaussian pulses with various phases. The pulses are created using the "number of cycles" method, with four cycles under the envelope.

#### 2.1.4.3 Sech Pulses

We will again go from the desired electric field,

$$\mathcal{E}(t) = \mathcal{E}_t \operatorname{sech}\left(\frac{t}{\tau}\right) \cos(\omega_c t + \varphi) \tag{2.1.58}$$

to the amplitude spectrum. The Fourier transform of $\mathcal{E}(t)$ is simple to compute using the tabulated result for the Fourier transform of a function multiplied by a cosine, once we know what the Fourier transform of sech is. It is reasonably straightforward to show that

$$F\{\operatorname{sech}(at)\}(\omega) = \frac{1}{\sqrt{2\pi}} \int_{-\infty}^{\infty} \operatorname{sech}(at)\, e^{-i\omega t}\, \mathrm{d}t = \frac{1}{a}\sqrt{\frac{\pi}{2}}\, \operatorname{sech}\left(\frac{\pi}{2a}\omega\right) \tag{2.1.59}$$

Using this, we find that the electric field amplitude spectrum of a sech pulse is

$$\widehat{\mathcal{E}}(\omega) = \mathcal{E}_\omega \left[ e^{i\varphi} \operatorname{sech}\left(\frac{\pi}{2}\tau\,(\omega + \omega_c)\right) + e^{-i\varphi} \operatorname{sech}\left(\frac{\pi}{2}\tau\,(\omega - \omega_c)\right)\right] \tag{2.1.60}$$

where $\mathcal{E}_\omega = \mathcal{E}_t \tau \sqrt{\pi/2}$. We can now determine the fluence in terms of $\mathcal{E}_t$ or $\mathcal{E}_\omega$:

$$
\begin{aligned}
H &= \epsilon_0\, c \int_{-\infty}^{\infty} \left|\widehat{\mathcal{E}}(\omega)\right|^2 \mathrm{d}\omega \\
H &= 2\epsilon_0\, c \int_{0}^{\infty} \left|\mathcal{E}_\omega e^{-i\varphi}\, \mathrm{sech}\Big(\frac{\pi}{2}\,\tau\,(\omega+\omega_c)\Big)\right|^2 \mathrm{d}\omega \\
H &= 2\epsilon_0\, c\, \mathcal{E}_\omega^2 \int_{0}^{\infty} \mathrm{sech}^2\Big(\frac{\pi}{2}\,\tau\,(\omega+\omega_c)\Big)\, \mathrm{d}\omega \\
H &= 2\epsilon_0\, c\, \mathcal{E}_\omega^2\, \frac{2}{\pi\tau}\, \tanh(x)\Big|_{-\infty}^{\infty} \\
H &= 2\epsilon_0\, c\, \mathcal{E}_\omega^2\, \frac{2}{\pi\tau} 2 \\
H &= \frac{8\epsilon_0\, c\, \mathcal{E}_\omega^2}{\pi\tau} \\
\mathcal{E}_t &= \sqrt{\frac{H}{\epsilon_0 c \tau}}
\end{aligned}
\tag{2.1.61}
$$

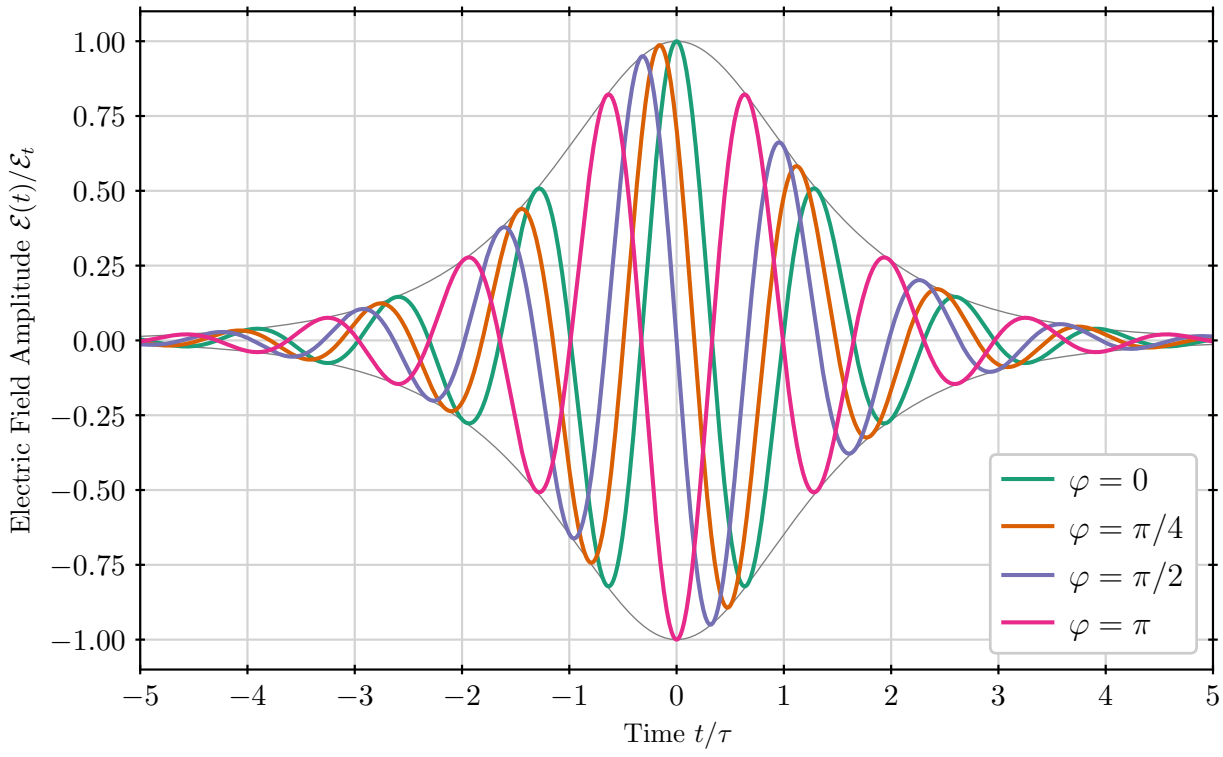


Figure 2.3: Electric fields of few-cycle sech pulses with various phases.

#### 2.1.4.4 Cosine-Squared Pulses

Cosine-squared pulses are interesting because, despite having a very smooth envelope, their Fourier transforms are very simple, looking similar to a frequency comb. They also have an extremely predictable envelope zero, which people use as the cutoff time. Such a pulse is typically parameterized directly by the number of cycles in the pulse, $N_c$:

$$\mathcal{E}(t) = \mathcal{E}_t \, \cos^2\!\left(\frac{\omega_c}{2N_c}\, t\right) \cos(\omega_c\, t + \varphi) \tag{2.1.62}$$

The term $\omega_c/2N_c$ needs the division by two because the $\cos^2$ has half the period of the carrier. To see this, locate the first envelope zeros. They occur when

$$\begin{aligned} \frac{\omega_c}{2N_c} t &= \pm\frac{\pi}{2} \\ t &= \pm\frac{2N_c}{\omega_c}\frac{\pi}{2} \\ t &= \pm\frac{2N_c}{2\pi f_c}\frac{\pi}{2} \\ t &= \pm\frac{N_c}{2\, f_c} \\ t &= \pm\frac{N_c\, T_c}{2} \end{aligned} \tag{2.1.63}$$

where $T_c$ is the period of the carrier wave. The total time between the inner pair of envelope zeros is then $N_c T_c$, which is exactly enough time for $N_c$ cycles of the carrier wave.

As mentioned above, the Fourier transform of a cosine-squared pulse is rather interesting. We evaluate it by multiplying in one cosine at a time inside the Fourier transform on the left, starting with just the carrier wave:

$$\begin{aligned} F\{\cos(\omega_c\, t + \varphi)\} &= \sqrt{\frac{\pi}{2}}\left[e^{i\varphi}\, \delta(\omega - \omega_c) + e^{-i\varphi}\, \delta(\omega + \omega_c)\right] \\ F\left\{\cos\!\left(\frac{\omega_c}{2N_c}\, t\right) \cos(\omega_c\, t + \varphi)\right\} &= \sqrt{\frac{\pi}{8}}\left[e^{i\varphi}\left\{\delta\!\left(\omega - \omega_c - \frac{\omega_c}{2N_c}\right) + \delta\!\left(\omega - \omega_c + \frac{\omega_c}{2N_c}\right)\right\}\right. \\ &\qquad \left. + e^{-i\varphi}\left\{\delta\!\left(\omega + \omega_c - \frac{\omega_c}{2N_c}\right) + \delta\!\left(\omega + \omega_c + \frac{\omega_c}{2N_c}\right)\right\}\right] \end{aligned} \tag{2.1.64}$$

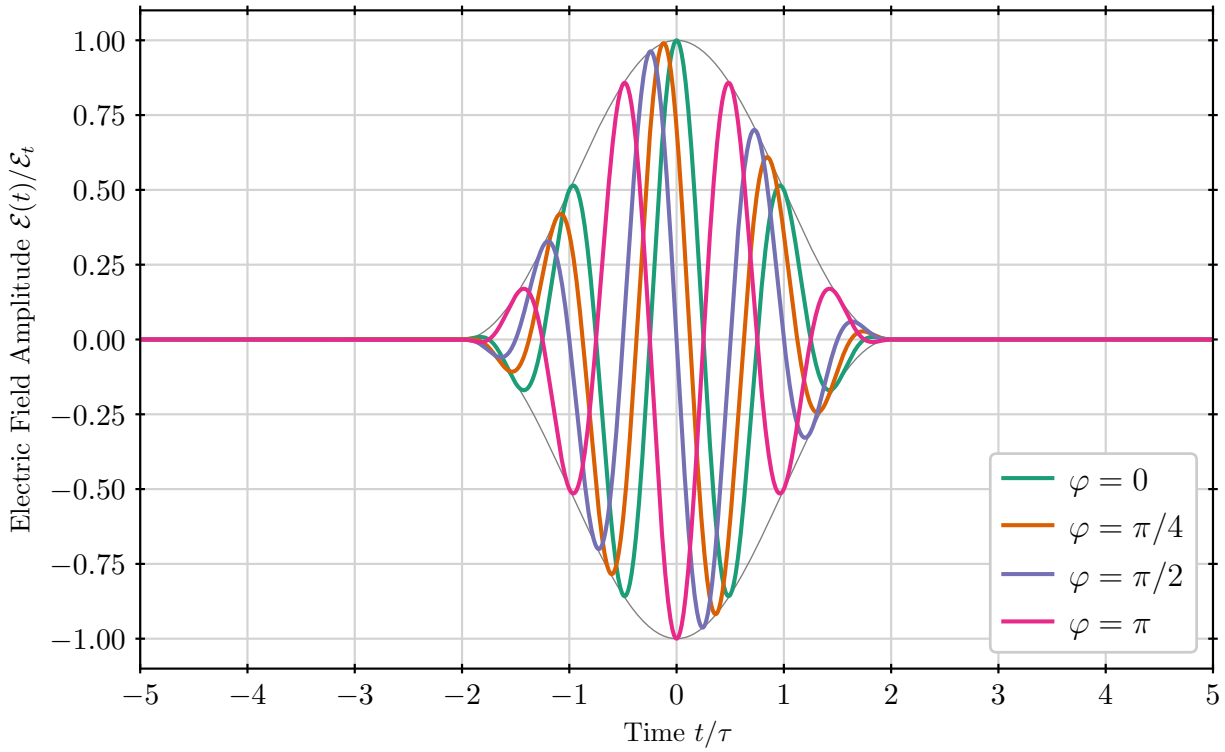


Figure 2.4: Electric fields of few-cycle cosine-squared pulses with various phases.

and finally,

$$
\begin{aligned}
F\left\{\cos^2\left(\frac{\omega_c}{2N_c}t\right)\cos(\omega_c t+\varphi)\right\} = \sqrt{\frac{\pi}{32}}\Bigg[e^{i\varphi}\Bigg\{&\delta\left(\omega-\omega_c-\frac{\omega_c}{2N_c}-\frac{\omega_c}{2N_c}\right)\\
&+\delta\left(\omega-\omega_c-\frac{\omega_c}{2N_c}+\frac{\omega_c}{2N_c}\right)\\
&+\delta\left(\omega-\omega_c+\frac{\omega_c}{2N_c}-\frac{\omega_c}{2N_c}\right)\\
&+\delta\left(\omega-\omega_c+\frac{\omega_c}{2N_c}+\frac{\omega_c}{2N_c}\right)\Bigg\}\\
+\ e^{-i\varphi}\Bigg\{&\delta\left(\omega+\omega_c-\frac{\omega_c}{2N_c}-\frac{\omega_c}{2N_c}\right)\\
&+\delta\left(\omega+\omega_c-\frac{\omega_c}{2N_c}+\frac{\omega_c}{2N_c}\right)\\
&+\delta\left(\omega+\omega_c+\frac{\omega_c}{2N_c}-\frac{\omega_c}{2N_c}\right)\\
&+\delta\left(\omega+\omega_c+\frac{\omega_c}{2N_c}+\frac{\omega_c}{2N_c}\right)\Bigg\}\Bigg]
\end{aligned}
\tag{2.1.65}
$$

Applying this to $\mathcal{E}(t)$, we have

$$\widehat{\mathcal{E}}(\omega) = \mathcal{E}_t\sqrt{\frac{\pi}{32}}\left[e^{i\varphi}\left\{\delta\left(\omega-\omega_c\left(1+\frac{1}{N_c}\right)\right)+2\,\delta(\omega-\omega_c)+\delta\left(\omega-\omega_c\left(1-\frac{1}{N_c}\right)\right)\right\}\right.$$
$$\left.+\,e^{-i\varphi}\left\{\delta\left(\omega+\omega_c\left(1-\frac{1}{N_c}\right)\right)+2\,\delta(\omega+\omega_c)+\delta\left(\omega+\omega_c\left(1+\frac{1}{N_c}\right)\right)\right\}\right] \quad (2.1.66)$$

### 2.1.5 DC and Fluence Correction

One concern throughout all of this is that we are doing Fourier transforms, which require continuous, infinite domains in time and frequency space. Any time-domain simulation will necessarily be performed using a finite, discrete set of times. This causes two kinds of distortion in the simulated pulses compared to the theoretical pulses.

1. The amplitude spectrum has an upper cutoff frequency determined by the simulation time step.

2. The amplitude spectrum is "binned" into bins whose size is determined by the upper cutoff frequency and the total number of time steps.

3. The simulated pulse will typically have some non-zero zero-frequency amplitude in its discrete Fourier transform, even if the Fourier transform of the theoretical pulse does not, because the total simulation time is not infinite.

4. The simulated pulse will typically not have the fluence that theory would predict (off by a fraction of a percent). This is roughly the same problem as any numerical integration technique will have at predicting the integral of a smooth function.

The first two problems are relatively easy to solve, at moderate computational cost: always use a time step smaller than the inverse Nyquist frequency of the largest frequency you want to model, and always run the simulation for several pulse widths before and after the main body of the pulse.

To deal with the third problem, we developed a **DC correction** technique ("DC" in analogy to electronics, where the "DC" component is the zero-frequency component). For every pulse but sinc, this problem can be largely neglected, because the pulse amplitude drops very rapidly beyond roughly a pulse width from the pulse center. For a sinc envelope, however, the pulse has very

long tails in both directions. The vector potential does not return to zero (equivalent to the DC component of the amplitude spectrum not being zero) cleanly without including an extraordinarily large number of pulse widths on either side of the pulse centers (hundreds) [1]. Worse, as a tradeoff to improve computation time, we generally simulate about 30 pulse widths on either side, and then cut the sinc pulse off with a symmetric logistic window. This only makes the problem worse.

As a solution, the DC correction algorithms adds a new, constants electric field under the same window as the pulse itself. The amplitude of this new field is numerically optimized to get the vector potential to zero at the end of the simulation. This field is typically extremely small compared to the pulse itself (by several orders of magnitude). Tests run with and without this correction are not significantly different, but it does assuage a real fear: the pulses we are modeling would not be physically possible without it. Including this correction is important to make sure we do not accumulate any subtle differences from reality.

We also implemented **fluence correction** to deal with the fourth problem. When asked to construct a pulse with the given fluence, it adjusts the $\mathcal{E}_t$ that is actually used to set the numerically-calculated fluence equal to the given value, instead of simply using the $\mathcal{E}_t$ predicted by theory. We have never found this difference to be significant, but that is at least partially a result of the low nonlinear order of the process at work in most of the discussion below. In a highly nonlinear process, small changes in the total fluence could indeed cause large changes in the dynamics.

## 2.2 Electron Dynamics in an Electromagnetic Wave

Just as we first analyzed the dynamics of the electromagnetic field by itself, we will now analyze the dynamics of an electron in that field without any other potentials.

[1] Pure sine-like pulses (no matter what envelope they have) never have DC components because any part of the spectrum at a low enough frequency destructively interferes with the complex-conjugated, frequency-shifted part of the spectrum (because the spectrum has to be Hermitian).

### 2.2.1 Classical Electron Dynamics in a Laser Field

The classical dynamics of an electron in an electromagnetic field is determined by Newton's laws and the Lorentz force [72]:

$$\dot{\mathbf{p}} = q[\boldsymbol{\mathcal{E}}(r,t) + \mathbf{v} \times \boldsymbol{\mathcal{B}}(r,t)]. \tag{2.2.1}$$

If $\boldsymbol{\mathcal{E}}$ and $\boldsymbol{\mathcal{B}}$ are the electric and magnetic fields of a traveling electromagnetic wave the force from the magnetic field will be smaller than the electric force by a factor of $v/c$, so we can ignore it (non-relativistic motion). This also lets us simplify $\mathbf{p} = \gamma m\mathbf{v} \approx m\mathbf{v}$. If we also assume that the electric field that the electron sees does not change appreciably over the volume that it moves in (i.e., the maximum excursion of the electron is much less than the wavelength of the electromagnetic field, $\mathbf{r}(t) - \mathbf{r}_0 \ll \lambda$), we can simplify (2.2.1) to

$$\dot{\mathbf{v}} = \frac{q}{m}\,\boldsymbol{\mathcal{E}}(\mathbf{r}_0, t). \tag{2.2.2}$$

If we integrate this equation once in time we have

$$\mathbf{v}(t) = \mathbf{v}_0 + \frac{q}{m}\int_{t_0}^{t} \boldsymbol{\mathcal{E}}(\mathbf{r}_0, \tau)\,\mathrm{d}\tau \tag{2.2.3}$$

$$\mathbf{v}(t) = \mathbf{v}_0 - \frac{q}{m}[\boldsymbol{\mathcal{A}}(\mathbf{r}_0, t) - \boldsymbol{\mathcal{A}}(\mathbf{r}_0, t_0)]. \tag{2.2.4}$$

Note that since $\boldsymbol{\mathcal{A}}(\mathbf{r}_0, \infty) = \boldsymbol{\mathcal{A}}(\mathbf{r}_0, -\infty) = \mathbf{0}$ for an isolated spatially homogeneous electric field pulse, *the electron can acquire no net velocity from the field.* A simple way to see this explicitly is to define the **canonical momentum** $\mathbf{p}_{\mathrm{can}}(t) = m\mathbf{v}(t) + q\,\boldsymbol{\mathcal{A}}(\mathbf{r}_0, t) = m\mathbf{v}_0$. Then (2.2.3) has the form of a conservation law:

$$\mathbf{v}(t) + \frac{q}{m}\,\boldsymbol{\mathcal{A}}(\mathbf{r}_0, t) = \mathbf{v}_0 + \frac{q}{m}\,\boldsymbol{\mathcal{A}}(\mathbf{r}_0, t_0) \tag{2.2.5}$$

$$\mathbf{p}_{\mathrm{can}}(t) = \mathbf{p}_{\mathrm{can}}(t_0). \tag{2.2.6}$$

This is the proof of the statement given in the introduction to this chapter: a free electron cannot absorb energy from a laser pulse under the dipole approximation.

Alternatively, if we define a drift velocity $\mathbf{v}_d = \mathbf{p}_{\text{can}}(t_0)/m$, it is clear that the electron's velocity has two components:

$$\mathbf{v}(t) = \mathbf{v}_d - \frac{q}{m}\boldsymbol{\mathcal{A}}(\mathbf{r}_0, t) \tag{2.2.7}$$

The drift velocity is constant. If we integrate this equation we find that

$$\mathbf{r}(t) = \boldsymbol{\alpha}(t, t_0) + (t - t_0)\mathbf{v}_d + \mathbf{r}_0, \tag{2.2.8}$$

where

$$\boldsymbol{\alpha}(t, t_0) = -\frac{q}{m}\int_{t_0}^{t} \boldsymbol{\mathcal{A}}(\mathbf{r}_0, \tau)\,\mathrm{d}\tau \tag{2.2.9}$$

is the displacement vector caused by the quiver motion.

Note the rather strict assumptions leading to this conclusion. In the dipole approximation, the electric field is treated as spatially homogeneous, and thus we can ignore the magnetic field. If the magnetic field cannot be ignored, or the electric field varies in space, the electron can gain energy from its interaction with the fields. This leads to "particle-like" scattering effects (like Compton scattering) when the photon energy is large (and thus the wavelength is short enough that we cannot use the dipole approximation). In these kinds of scattering events, free electrons (or charged particles in general) can indeed absorb energy and momentum from photons.

### 2.2.2 Quantum Electron Dynamics in a Laser Field

Armed with some knowledge about the classical problem (see Section 2.2.1), we can now tackle the quantum problem. The interaction of an electron with the laser field given by $\Phi(\mathbf{r}, t)$ and $\boldsymbol{\mathcal{A}}(\mathbf{r}, t)$ is controlled by the Hamiltonian [79]

$$\begin{aligned}
\widehat{\mathcal{H}}(\mathbf{r}, t) &= \frac{1}{2m}(\widehat{\mathbf{p}} - q\boldsymbol{\mathcal{A}})^2 + q\,\Phi \\
\widehat{\mathcal{H}}(\mathbf{r}, t) &= \frac{\widehat{\mathbf{p}}^2}{2m} - \frac{q}{2m}(\boldsymbol{\mathcal{A}} \cdot \widehat{\mathbf{p}} + \widehat{\mathbf{p}} \cdot \boldsymbol{\mathcal{A}}) + \frac{q^2}{2m}\boldsymbol{\mathcal{A}}^2 + q\,\Phi
\end{aligned} \tag{2.2.10}$$

In the position representation $\widehat{\mathbf{p}} = -i\hbar\boldsymbol{\nabla}$. If we plug this in we get

$$\widehat{\mathcal{H}}(\mathbf{r},t) = -\frac{\hbar^2}{2m}\nabla^2 + i\frac{q\hbar}{2m}(\boldsymbol{\mathcal{A}}\cdot\boldsymbol{\nabla} + \boldsymbol{\nabla}\cdot\boldsymbol{\mathcal{A}}) + \frac{q^2}{2m}\boldsymbol{\mathcal{A}}^2 + q\,\Phi \tag{2.2.11}$$

This is the master equation for laser-electron interactions. We will perform various manipulations and approximations of it to get it into forms that we can work with.

A simple way to reduce the complexity of (2.2.11) is to choose our gauge to eliminate some term. For example, in the Coulomb gauge,

$$\boldsymbol{\nabla}\cdot\boldsymbol{\mathcal{A}} = 0 \tag{2.2.12}$$

Using this we can simplify the symmetric term in the middle by using:

$$\begin{aligned}\boldsymbol{\nabla}\cdot(\boldsymbol{\mathcal{A}}\,\psi) &= \boldsymbol{\mathcal{A}}\cdot\boldsymbol{\nabla}\Psi + \Psi\cdot(\boldsymbol{\nabla}\cdot\boldsymbol{\mathcal{A}})\\ \boldsymbol{\nabla}\cdot(\boldsymbol{\mathcal{A}}\,\psi) &= \boldsymbol{\mathcal{A}}\cdot\boldsymbol{\nabla}\Psi\end{aligned} \tag{2.2.13}$$

which is just another copy of the first term in the symmetric pair. Therefore, in the Coulomb gauge, (2.2.11) reduces to

$$\widehat{\mathcal{H}}^C(\mathbf{r},t) = -\frac{\hbar^2}{2m}\nabla^2 + i\frac{q\hbar}{m}\boldsymbol{\mathcal{A}}(\mathbf{r},t)\cdot\boldsymbol{\nabla} + \frac{q^2}{2m}\boldsymbol{\mathcal{A}}^2(\mathbf{r},t) + q\,\Phi \tag{2.2.14}$$

Note that we have left $\Phi$ in the equation, despite being in the Coulomb gauge where $\Phi = 0$. This is to make it clear where it's supposed to go for later use when performing more gauge transformations.

Alternatively, if we neglect the spatial variation of the laser field we can dramatically simplify (2.2.11). This is a reasonable assumption as long as the size of the dynamic system is small compared to the wavelength of the laser. An implication of this is that there will be no magnetic effects under this approximation: if the size of the system is small compared to the wavelength of the laser, the velocities must be small as well, so that particles stay inside the system.

In fact, the lack of magnetic effects can be seen explicitly. If the electric field is spatially

homogeneous $\boldsymbol{\mathcal{A}}$ must be as well, since they are related only by time operations:

$$\boldsymbol{\mathcal{A}}(t) = -\int_{-\infty}^{t} \boldsymbol{\mathcal{E}}(\tau)\,\mathrm{d}\tau \tag{2.2.15}$$

$$\boldsymbol{\mathcal{E}}(t) = -\frac{\mathrm{d}\boldsymbol{\mathcal{A}}(t)}{\mathrm{d}t} \tag{2.2.16}$$

Since $\boldsymbol{\mathcal{A}}$ is not a function of $\mathbf{r}$, $\boldsymbol{\nabla} \times \boldsymbol{\mathcal{A}} = \boldsymbol{\mathcal{B}} = \mathbf{0}$. We also have $\boldsymbol{\nabla} \cdot \boldsymbol{\mathcal{A}} = 0$, which is similar to the result of going to the Coulomb gauge. Applying all of the above to (2.2.11), we get

$$\begin{aligned}
\widehat{\mathcal{H}}^D(\mathbf{r},t) &= -\frac{\hbar^2}{2m}\nabla^2 + i\frac{q\hbar}{2m}\boldsymbol{\mathcal{A}}(t)\cdot\boldsymbol{\nabla} + \frac{q^2}{2m}\boldsymbol{\mathcal{A}}^2(t) + q\,\Phi \\
\widehat{\mathcal{H}}^D(\mathbf{r},t) &= -\frac{\hbar^2}{2m}\nabla^2 - \frac{q}{m}\boldsymbol{\mathcal{A}}(t)\cdot\widehat{\mathbf{p}} + \frac{q^2}{2m}\boldsymbol{\mathcal{A}}^2(t) + q\,\Phi
\end{aligned} \tag{2.2.17}$$

Despite the apparent similarity in form of the resulting Hamiltonians for the Coulomb gauge and dipole approximation, they are quite different! In the Coulomb gauge we retain the full spatial dependence of $\boldsymbol{\mathcal{A}}$. The dipole approximation throws this information away, resulting in much simpler calculations, but also making it inappropriate in situations where magnetic effects may play a role (the distinction is quite important and often not paid attention to [76–78]).

We will now simplify (2.2.17) in two different ways. The first way will add a gradient to $\boldsymbol{\mathcal{A}}$ that eliminates the two middle terms of $\widehat{\mathcal{H}}^D$ and transforms the last term into a more intuitive operator. This method will produce the **length gauge Hamiltonian**. The second way will add a different gradient to $\boldsymbol{\mathcal{A}}$ to eliminate the last two terms in the Hamiltonian entirely. This method will produce the **velocity gauge Hamiltonian**.

Before we dive in it is important to review what happens when we perform a gauge transformation on the Schrödinger equation. A general gauge transformation of the electromagnetic potentials and the wavefunction is

$$\boldsymbol{\mathcal{A}} \to \boldsymbol{\mathcal{A}}' = \boldsymbol{\mathcal{A}} + \boldsymbol{\nabla}\Lambda \tag{2.2.18a}$$

$$\Phi \to \Phi' = \Phi - \frac{\partial\Lambda}{\partial t} \tag{2.2.18b}$$

$$\Psi \to \Psi' = e^{iq\Lambda/\hbar}\,\Psi \tag{2.2.18c}$$

The function $\Lambda$ can be an arbitrary real smooth function of $\mathbf{r}$ and $t$. The transformed wavefunction

$\Psi'$ satisfies the Schrödinger equation for the transformed potentials $\boldsymbol{\mathcal{A}}'$ and $\Phi'$. Any physical expectation value of $\Psi$ can be calculated from it by performing the above transformation in reverse, or by using transformed operators. Both the original wavefunction and the transformed wavefunction have the same physical expectation values.

If $\Psi'$ and $\Psi$ seem to have the same information, why bother transforming? They key is that, because the phase $\Lambda$ is a function of both position and time, it dramatically changes the spatial representation of the wavefunction, and can therefore influence the computational complexity of the dynamics, both analytically and numerically.

To go to the length gauge we want a gauge transformation that eliminates the presence of $\boldsymbol{\mathcal{A}}$ in (2.2.17). To do this we want

$$\begin{aligned} \boldsymbol{\mathcal{A}}'(t) &= \boldsymbol{\mathcal{A}}(t) + \boldsymbol{\nabla}\Lambda = 0 \\ \implies \boldsymbol{\nabla}\Lambda &= -\boldsymbol{\mathcal{A}}(t) \\ \implies \Lambda &= -\boldsymbol{\mathcal{A}}(t)\cdot\mathbf{r} \end{aligned} \tag{2.2.19}$$

which works out nicely because $\boldsymbol{\mathcal{A}}(t)$ is not a function of $\mathbf{r}$ in the dipole approximation. With this choice we have

$$\begin{aligned} \boldsymbol{\mathcal{A}} \to \boldsymbol{\mathcal{A}}' &= \boldsymbol{\mathcal{A}} - \boldsymbol{\nabla}\boldsymbol{\mathcal{A}}(t)\cdot\mathbf{r} \\ \Phi \to \Phi' &= \Phi + \frac{\partial}{\partial t}\boldsymbol{\mathcal{A}}(t)\cdot\mathbf{r} = 0 + \frac{\partial \boldsymbol{\mathcal{A}}}{\partial t}\cdot\mathbf{r} = -\boldsymbol{\mathcal{E}}(t)\cdot\mathbf{r} \\ \Psi \to \Psi^L &= \exp\Big(-i\frac{q}{\hbar}\boldsymbol{\mathcal{A}}(t)\cdot\mathbf{r}\Big)\,\Psi \end{aligned} \tag{2.2.20}$$

Now we plug this transformation into (2.2.17). We get a Schrödinger-like equation for $\psi^L$:

$$i\hbar\,\frac{\partial}{\partial t}\Psi^L(\mathbf{r},t) = \left(-\frac{\hbar^2}{2m}\nabla^2 - q\,\boldsymbol{\mathcal{E}}(t)\cdot\mathbf{r}\right)\Psi^L(\mathbf{r},t) \tag{2.2.21}$$

The name "length gauge" comes from the coupling of $\boldsymbol{\mathcal{E}}$ to the distance $\mathbf{r}$.

To go to the velocity gauge we want a gauge transformation that uses $\Phi'$ to eliminate the $\boldsymbol{\mathcal{A}}^2$

term in (2.2.17). In particular we want

$$\begin{aligned} q\Phi' = q\Phi - q\frac{\partial\Lambda}{\partial t} &= -q\frac{\partial\Lambda}{\partial t} = -\frac{q^2}{2m}\boldsymbol{\mathcal{A}}^2(t) \\ &\implies \frac{\partial\Lambda}{\partial t} = \frac{q}{2m}\boldsymbol{\mathcal{A}}^2(t) \\ &\implies \Lambda = \frac{q}{2m}\int_{-\infty}^{t}\boldsymbol{\mathcal{A}}^2(\tau)\,\mathrm{d}\tau \end{aligned} \tag{2.2.22}$$

Since $\Lambda$ is not a function of $\mathbf{r}$, we have

$$\begin{aligned} \boldsymbol{\mathcal{A}} \to \boldsymbol{\mathcal{A}}' &= \boldsymbol{\mathcal{A}} + \frac{q}{2m}\boldsymbol{\nabla}\boldsymbol{\mathcal{A}}^2(t) = \boldsymbol{\mathcal{A}} \\ \Phi \to \Phi' &= \Phi - \frac{\partial\Lambda}{\partial t} = 0 - \frac{q}{2m}\boldsymbol{\mathcal{A}}^2(t) = -\frac{q}{2m}\boldsymbol{\mathcal{A}}^2(t) \\ \Psi \to \Psi^V &= \exp\left(i\frac{q^2}{2m\hbar}\int_{-\infty}^{t}\boldsymbol{\mathcal{A}}^2(\tau)\,\mathrm{d}\tau\right)\Psi \end{aligned} \tag{2.2.23}$$

The Schrödinger-like equation for $\Psi^V$ is

$$i\hbar\frac{\partial}{\partial t}\Psi^V(\mathbf{r},t) = \left(-\frac{\hbar^2}{2m}\nabla^2 - \frac{q}{m}\boldsymbol{\mathcal{A}}(t)\cdot\widehat{\mathbf{p}}\right)\Psi^V(\mathbf{r},t) \tag{2.2.24}$$

The name "velocity gauge" comes from the coupling of $\boldsymbol{\mathcal{A}}$ to the "velocity" operator, $\widehat{\mathbf{p}}/m$. In this sense both the kinetic energy and the interaction term are of the form "momentum squared over mass", since $e\boldsymbol{\mathcal{A}}$ and $\widehat{\mathbf{p}}$ both have units of momentum.

The most important fact about these two gauge transformations (or any other gauge transformation) and associated wavefunctions $\Psi^L$ and $\Psi^V$ is that they have the same value for any physical observable quantity. Each wavefunction can be found from the other by concatenating the relevant phase transformations the connect it to the original dipole-approximated wavefunction $\Psi^D$:

$$\Psi^L = \exp\left(-i\frac{q}{\hbar}\boldsymbol{\mathcal{A}}(t)\cdot\mathbf{r}\right)\,\exp\left(-i\frac{q^2}{2m\hbar}\int_{-\infty}^{t}\boldsymbol{\mathcal{A}}^2(\tau)\,\mathrm{d}\tau\right)\Psi^V \tag{2.2.25a}$$

$$\Psi^V = \exp\left(i\frac{q}{\hbar}\boldsymbol{\mathcal{A}}(t)\cdot\mathbf{r}\right)\,\exp\left(i\frac{q^2}{2m\hbar}\int_{-\infty}^{t}\boldsymbol{\mathcal{A}}^2(\tau)\,\mathrm{d}\tau\right)\Psi^L \tag{2.2.25b}$$

See Appendix F for a discussion of what the differences are between these two wavefunctions numerically.

In general, in this work, when not specified, $\Psi$ means $\Psi^L$. Additionally, even though we used

gauge transformations to eliminate $\Phi$ (implicitly or explicitly) for both the length and velocity gauges in free space, we will usually add back in simple static potentials like the electric potential of the atomic nucleus and not transform them away. This choice makes it convenient to separate the **interaction Hamiltonian** ($\boldsymbol{\mathcal{E}} \cdot \mathbf{r}$, $\boldsymbol{\mathcal{A}} \cdot \widehat{\mathbf{p}}$, or similar) from the **internal Hamiltonian** of the system, which includes the kinetic energy operator and and any other parts of the Hamiltonian that we want to attribute to the steady-state behavior of the system, such as static potentials.

### 2.2.3 Gordon-Volkov States

Gordon-Volkov states are the states of an electron in a classical laser field under the dipole approximation. They correspond to the "simple harmonic motion plus drift velocity" result that we would expect from an electron exposed to a laser field. In the context of our simulations, they are mostly useful as a diagnostic tool for understanding the state of the wavefunction during the simulation.

We will look for a solution $|\chi\rangle$ using the Schrödinger equation under the dipole approximation in the velocity gauge (2.2.24):

$$\begin{aligned} i\hbar \frac{\partial}{\partial t}\chi^V(\mathbf{r},t) &= \widehat{\mathcal{H}}^V \chi^V(\mathbf{r},t) \\ i\hbar \frac{\partial}{\partial t}\chi^V(\mathbf{r},t) &= \left(\frac{\widehat{\mathbf{p}}^2}{2m} - \frac{q}{m}\boldsymbol{\mathcal{A}}(t)\cdot\widehat{\mathbf{p}}\right)\chi^V(\mathbf{r},t) \end{aligned} \tag{2.2.26}$$

Although $\chi^V$ will not be a momentum or energy eigenstate (the Hamiltonian is time-dependent, so it has no eigenstates), the momentum operator $\widehat{\mathbf{p}}$ does commute with the Hamiltonian, so we should look for a solution of the form

$$\chi^V_{\mathbf{k}}(\mathbf{r},t) = f_{\mathbf{k}}(t)\left[(2\pi)^{-3/2} e^{i\mathbf{k}\cdot\mathbf{r}}\right] \tag{2.2.27}$$

Note that $f_k(t)$ does not depend on $\mathbf{r}$, so the momentum operators don't interact with it. That means that if we plug this in to the original differential equation we can use the fact that $e^{i\mathbf{k}\cdot\mathbf{r}}$ is an eigenstate of $\widehat{\mathbf{p}}$ with eigenvalue $\hbar\mathbf{k}$ to reduce the Schrödinger equation to a first-order differential

equation for $f_{\mathbf{k}}(t)$:

$$\begin{aligned}
i\hbar\frac{\partial}{\partial t}\chi^V(\mathbf{r},t) &= \left(\frac{\widehat{\mathbf{p}}^2}{2m} - \frac{q}{m}\boldsymbol{\mathcal{A}}(t)\cdot\widehat{\mathbf{p}}\right)\chi^V(\mathbf{r},t) \\
i\hbar\frac{\partial}{\partial t}f_{\mathbf{k}}(t)\left[(2\pi)^{-3/2}e^{i\mathbf{k}\cdot\mathbf{r}}\right] &= \left(\frac{\widehat{\mathbf{p}}^2}{2m} - \frac{q}{m}\boldsymbol{\mathcal{A}}(t)\cdot\widehat{\mathbf{p}}\right)f_{\mathbf{k}}(t)\left[(2\pi)^{-3/2}e^{i\mathbf{k}\cdot\mathbf{r}}\right] \\
i\hbar\,\dot{f}_{\mathbf{k}}(t)\,e^{i\mathbf{k}\cdot\mathbf{r}} &= \left(\frac{\hbar^2k^2}{2m} - \frac{q}{m}\boldsymbol{\mathcal{A}}(t)\cdot\mathbf{k}\right)f_{\mathbf{k}}(t)\,e^{i\mathbf{k}\cdot\mathbf{r}} \\
i\hbar\,\dot{f}_{\mathbf{k}}(t) &= \left(\frac{\hbar^2k^2}{2m} - \frac{q}{m}\boldsymbol{\mathcal{A}}(t)\cdot\mathbf{k}\right)f_{\mathbf{k}}(t)
\end{aligned} \tag{2.2.28}$$

This equation can be integrated to find $f_{\mathbf{k}}(t)$:

$$\begin{aligned}
\dot{f}_{\mathbf{k}}(t) &= -i\left(\frac{E_k}{\hbar} - \frac{q}{m}\boldsymbol{\mathcal{A}}(t)\cdot\mathbf{k}\right)f_{\mathbf{k}}(t) \\
f_{\mathbf{k}}(t) &= \exp\left[-i\left(\frac{E_k}{\hbar}t - \frac{q}{m}\int_{-\infty}^{t}\mathrm{d}\tau\,\boldsymbol{\mathcal{A}}(\tau)\cdot\mathbf{k}\right)\right] \\
f_{\mathbf{k}}(t) &= \exp\left[-i\left(\frac{E_k}{\hbar}t + \boldsymbol{\alpha}(t)\cdot\mathbf{k}\right)\right]
\end{aligned} \tag{2.2.29}$$

where $E_k = \hbar^2k^2/2m$ is the energy of an electron with wavevector $\mathbf{k}$ in free space and $\boldsymbol{\alpha}(t)$ is the quiver motion displacement vector (2.2.9). The integration prefactor is chosen to be 1 so that the resulting wavefunction is $\delta$-normalized in $\mathbf{k}$. The full Gordon-Volkov wavefunction in the velocity gauge is then

$$\begin{aligned}
\chi^V_{\mathbf{k}}(\mathbf{r},t) &= (2\pi)^{-3/2}\exp[i\mathbf{k}\cdot\mathbf{r}]\exp\left[-i\left(\frac{E_k}{\hbar}t + \boldsymbol{\alpha}(t)\cdot\mathbf{k}\right)\right] \\
&= (2\pi)^{-3/2}\exp\left[-i\left(\frac{E_k}{\hbar}t + \boldsymbol{\alpha}(t)\cdot\mathbf{k} - \mathbf{k}\cdot\mathbf{r}\right)\right] \\
\chi^V_{\mathbf{k}}(\mathbf{r},t) &= (2\pi)^{-3/2}\exp\left[i\mathbf{k}\cdot(\mathbf{r}-\boldsymbol{\alpha}(t)) - i\frac{E_k}{\hbar}t\right]
\end{aligned} \tag{2.2.30}$$

This precisely matches the behavior of the classical electron in the same laser field: the electron's wavefunction is a plane wave with drift momentum $\hbar\mathbf{k}$ and energy $E_k$ which is "dressed" by the induced quiver motion.

Note that the momentum operator "sees through" the extra phase factors and extracts the drift

momentum:

$$\widehat{\mathbf{p}} \left|\chi_k^V(t)\right\rangle = \hbar\mathbf{k} \left|\chi_k^V(t)\right\rangle \tag{2.2.31}$$

This extends to the field-free Hamiltonian:

$$\frac{\widehat{\mathbf{p}}^2}{2m} \left|\chi_k^V(t)\right\rangle = \frac{\hbar^2 k^2}{2m} \left|\chi_k^V(t)\right\rangle \tag{2.2.32}$$

This indicates that the extra phase "information" is being stored "in" the vector potential itself, via the vector potential operator. Think of this as combining the Schrödinger and Heisenberg pictures: some information about the state is being stored in the ket, and some in the operator. It also hints as to the computational efficiency of the velocity gauge: because the extra phase information is stored in the vector potential, we don't need to include it in the main calculations.

The discussion in [72] provides $\chi^L(\mathbf{r}, t)$ as well as evolution operators written in the basis of Gordon-Volkov states.

## 2.3 Solving the Time-Dependent Schrödinger Equation Numerically

In this section we will develop techniques to solve the time-dependent Schrödinger equation numerically in "three" dimensions. Because we only work with linearly-polarized pulses, we have azimuthal symmetry. This lets us reduce the problem to two dimensions in all cases. We will begin by defining a simple mesh of cylindrical slices in Section 2.3.1, and then iteratively improve on it in the following sections.

### 2.3.1 Cylindrical-Slice Mesh

#### 2.3.1.1 The Mesh

In this simulation we discretize space into a cylindrically symmetric mesh of points. We enforce azimuthal symmetry and consider only a single $\phi$-slice of the mesh, which forces $m = 0$. The mesh

therefore has two coordinates, $\rho$ and $z$:

$$\rho \to \rho_j = \left(j + \frac{1}{2}\right)\Delta\rho \qquad j = 0, 1, 2, \cdots, N_\rho \tag{2.3.1a}$$

$$z \to z_k = \left(k - \frac{N_z}{2}\right)\Delta z \qquad k = 0, 1, 2, \cdots, N_z \tag{2.3.1b}$$

In these notes we will refer to "the mesh", "a mesh", and "the $g$ mesh". "The mesh" refers to the physical locations of the points, so that a function may be "defined on the mesh", for example. "A mesh" is some field that has a value at every point on the mesh. "The $g$ mesh" refers to the particular mesh that represents the wavefunction on the mesh (the notation will become clear in the next section). For example, the result of applying the Hamiltonian to the $g$ mesh produces a mesh that we could call $\widehat{\mathcal{H}}g$.

#### 2.3.1.2 The Wavefunction and Inner Products

The next step is to discretize the wavefunction. However, to simplify our calculations we will first make the transformation $\Psi \equiv g/\sqrt{2\pi\rho}$. To see why this is helpful, consider the inner product of two wavefunctions $\Psi_1(\rho, z)$ and $\Psi_2(\rho, z)$ on the mesh:

$$\begin{aligned}
\langle\Psi_1|\Psi_2\rangle &= \int_V \Psi_1^*(\mathbf{r})\,\Psi_2(\mathbf{r})\;\mathrm{d}V \\
&= \int_0^{2\pi}\int_{-\infty}^{\infty}\int_0^{\infty} \Psi_1^*(\rho, z)\,\Psi_2(\rho, z)\,\rho\;\mathrm{d}\rho\;\mathrm{d}z\;\mathrm{d}\phi \\
&= 2\pi\int_{-\infty}^{\infty}\int_0^{\infty} \Psi_1^*(\rho, z)\,\Psi_2(\rho, z)\,\rho\;\mathrm{d}\rho\;\mathrm{d}z \\
&= 2\pi\int_{-\infty}^{\infty}\int_0^{\infty} \frac{g_1^*(\rho, z)}{\sqrt{2\pi\rho}}\,\frac{g_2(\rho, z)}{\sqrt{2\pi\rho}}\,\rho\;\mathrm{d}\rho\;\mathrm{d}z \\
&= \int_{-\infty}^{\infty}\int_0^{\infty} g_1^*(\rho, z)\,g_2(\rho, z)\;\mathrm{d}\rho\;\mathrm{d}z \\
\langle\Psi_1|\Psi_2\rangle &\to \sum_{jk} g_{1,\,jk}^*\,g_{2,\,jk}\,\Delta\rho\,\Delta z \equiv \langle g_1|g_2\rangle
\end{aligned} \tag{2.3.2}$$

We see that with this transformation the discretized inner product on the mesh is simply a sum over the element-wise product of the wavefunction's associated $g$ meshes (with one of them complex-conjugated). This transformation will also facilitate calculation of the derivatives in the Schrödinger equation, as described in the next section. In fact, this method will work for any operator that

can be defined as an operation on the $g$ mesh that returns a mesh, and thus works for expectation values of operators as well.

This works so well because the transformation factor is the square root of the Jacobian integrated over the symmetric variables (in this case $\phi$, which gives the $2\pi$). This factor then cancels when we try to take the inner product. We are taking our initial 3-dimensional cylinder and collapsing it down into a 2-dimensional rectangle which we will perform calculations on.

#### 2.3.1.3 The Hamiltonian

All time evolution in this simulation is performed by numerically integrating the Schrödinger equation. To perform these calculations we must represent the Hamiltonian as a matrix operator acting on a "flattened" $g$ mesh, a $g$ vector. The time-dependent Schrödinger equation for a hydrogen atom's electron interacting with an electric field is

$$\begin{aligned} i\hbar\frac{\partial\Psi}{\partial t} &= \widehat{\mathcal{H}}\Psi \\ i\hbar\frac{\partial\Psi}{\partial t} &= \left[-\frac{\hbar^2}{2m}\nabla^2 - \frac{k_e q^2}{r} - qz\,\mathcal{E}(t)\right]\Psi \end{aligned} \tag{2.3.3}$$

Of the three terms on the right, only the Laplacian is nontrivial to implement numerically on a mesh (the other two can be evaluated at each point individually). Focus on that term, and write it in cylindrical coordinates:

$$\begin{aligned} i\hbar\frac{\partial\Psi}{\partial t} &= -\frac{\hbar^2}{2m}\nabla^2\Psi + \cdots \\ i\hbar\frac{\partial\Psi}{\partial t} &= -\frac{\hbar^2}{2m}\left[\frac{1}{\rho}\frac{\partial\Psi}{\partial\rho} + \frac{\partial^2\Psi}{\partial\rho^2} + \frac{\partial^2\Psi}{\partial z^2}\right] + \cdots \end{aligned} \tag{2.3.4}$$

Note the lack of an angular derivative, because we have already assumed angular symmetry (the derivative is zero). Now make the transformation $\Psi = g/\sqrt{2\pi\rho}$ (note that this does nothing to the two terms in the Hamiltonian that we are not considering):

$$\frac{1}{\sqrt{2\pi\rho}}\,i\hbar\frac{\partial g}{\partial t} = -\frac{\hbar^2}{2m}\frac{1}{\sqrt{2\pi}}\left[\frac{1}{\rho}\frac{\partial}{\partial\rho}\left(\frac{g}{\sqrt{\rho}}\right) + \frac{\partial^2}{\partial\rho^2}\left(\frac{g}{\sqrt{\rho}}\right) + \frac{1}{\sqrt{\rho}}\frac{\partial^2 g}{\partial z^2}\right] + \cdots \tag{2.3.5}$$

Now we will put this equation on the standard mesh. We use centered differences for the derivatives:

$$\begin{aligned}
\frac{\partial^2 g}{\partial z^2} &\to \frac{g_{j,k+1} + g_{j,k-1} - 2g_{j,k}}{\Delta z^2} \\
\frac{\partial}{\partial \rho}\left(\frac{g}{\sqrt{\rho}}\right) &\to \frac{1}{2\,\Delta\rho}\left(\frac{g_{j+1,k}}{\sqrt{(j+\frac{3}{2})\Delta\rho}} - \frac{g_{j-1,k}}{\sqrt{(j-\frac{1}{2})\Delta\rho}}\right) \\
\frac{\partial^2}{\partial \rho^2}\left(\frac{g}{\sqrt{\rho}}\right) &\to \frac{1}{\Delta\rho^2}\left(\frac{g_{j+1,k}}{\sqrt{(j+\frac{3}{2})\Delta\rho}} + \frac{g_{j-1,k}}{\sqrt{(j-\frac{1}{2})\Delta\rho}} - \frac{2g_{j,k}}{\sqrt{(j+\frac{1}{2})\Delta\rho}}\right)
\end{aligned} \tag{2.3.6}$$

The $z$ kinetic energy component separates out cleanly:

$$K^{(z)} g_{jk} = -\frac{\hbar^2}{2m}\frac{1}{\Delta z^2}[g_{j,k+1} + g_{j,k-1} - 2g_{j,k}] \tag{2.3.7}$$

where we now think of $K^{(z)}$ as an operator acting on $g$. The $\rho$ component can be simplified:

$$
\begin{aligned}
K^{(\rho)}g &= -\frac{\hbar^2}{2m}\left[\frac{1}{\sqrt{\rho}}\frac{\partial}{\partial\rho}\left(\frac{g}{\sqrt{\rho}}\right)+\sqrt{\rho}\frac{\partial^2}{\partial\rho^2}\left(\frac{g}{\sqrt{\rho}}\right)\right] \\
K^{(\rho)}g_{jk} &= -\frac{\hbar^2}{2m}\left[\frac{1}{2\,\Delta\rho\sqrt{(j+\frac{1}{2})\Delta\rho}}\left(\frac{g_{j+1,k}}{\sqrt{(j+\frac{3}{2})\Delta\rho}}-\frac{g_{j-1,k}}{\sqrt{(j-\frac{1}{2})\Delta\rho}}\right)\right. \\
&\qquad \left.+\sqrt{\left(j+\frac{1}{2}\right)\Delta\rho}\,\frac{1}{\Delta\rho^2}\left(\frac{g_{j+1,k}}{\sqrt{(j+\frac{3}{2})\Delta\rho}}+\frac{g_{j-1,k}}{\sqrt{(j-\frac{1}{2})\Delta\rho}}-\frac{2g_{j,k}}{\sqrt{(j+\frac{1}{2})\Delta\rho}}\right)\right] \\
&= -\frac{\hbar^2}{2m}\frac{1}{\Delta\rho^2}\left[\frac{1}{2\sqrt{j+\frac{1}{2}}}\left(\frac{g_{j+1,k}}{\sqrt{j+\frac{3}{2}}}-\frac{g_{j-1,k}}{\sqrt{j-\frac{1}{2}}}\right)\right. \\
&\qquad \left.+\sqrt{j+\frac{1}{2}}\left(\frac{g_{j+1,k}}{\sqrt{j+\frac{3}{2}}}+\frac{g_{j-1,k}}{\sqrt{j-\frac{1}{2}}}-\frac{2g_{j,k}}{\sqrt{j+\frac{1}{2}}}\right)\right] \\
&= -\frac{\hbar^2}{2m}\frac{1}{\Delta\rho^2}\left[\left(\frac{\frac{1}{2}}{\sqrt{(j+\frac{1}{2})(j+\frac{3}{2})}}+\frac{\sqrt{j+\frac{1}{2}}}{\sqrt{(j+\frac{3}{2})}}\right)g_{j+1,k}\right. \\
&\qquad \left.+\left(\frac{-\frac{1}{2}}{\sqrt{(j+\frac{1}{2})(j-\frac{1}{2})}}+\frac{\sqrt{j+\frac{1}{2}}}{\sqrt{(j-\frac{1}{2})}}\right)g_{j-1,k}-2\,g_{j,k}\right] \\
&= -\frac{\hbar^2}{2m}\frac{1}{\Delta\rho^2}\left[\left(\frac{\frac{1}{2}}{\sqrt{(j+\frac{1}{2})(j+\frac{3}{2})}}+\frac{j+\frac{1}{2}}{\sqrt{(j+\frac{3}{2})(j+\frac{1}{2})}}\right)g_{j+1,k}\right. \\
&\qquad \left.+\left(\frac{-\frac{1}{2}}{\sqrt{(j+\frac{1}{2})(j-\frac{1}{2})}}+\frac{j+\frac{1}{2}}{\sqrt{(j-\frac{1}{2})(j+\frac{1}{2})}}\right)g_{j-1,k}-2\,g_{j,k}\right] \\
&= -\frac{\hbar^2}{2m}\frac{1}{\Delta\rho^2}\left[\frac{j+1}{\sqrt{(j+\frac{1}{2})(j+\frac{3}{2})}}\,g_{j+1,k}+\frac{j}{\sqrt{(j-\frac{1}{2})(j+\frac{1}{2})}}\,g_{j-1,k}-2\,g_{j,k}\right] \\
K^{(\rho)}g_{jk} &= -\frac{\hbar^2}{2m}\frac{1}{\Delta\rho^2}[c_{j+1}\,g_{j+1,k}+c_j\,g_{j-1,k}-2\,g_{j,k}] \qquad (2.3.8)
\end{aligned}
$$

where

$$
c_j=\frac{j}{\sqrt{j^2-\frac{1}{4}}} \qquad\qquad c_0=0 \qquad (2.3.9)
$$

In matrix form with $g_{jk}$ flattened into a vector along the $j$ index, $K^{(\rho)}$ is

$$K^{(\rho)}g^{(\rho)} = -\frac{\hbar^2}{2m}\frac{1}{\Delta\rho^2}\begin{bmatrix} -2 & c_1 & 0 & 0 & \ddots \\ c_1 & -2 & c_2 & 0 & \ddots \\ 0 & c_2 & -2 & c_3 & \ddots \\ 0 & 0 & c_3 & -2 & \ddots \\ \ddots & \ddots & \ddots & \ddots & \ddots \end{bmatrix}\begin{bmatrix} g_{00} \\ g_{10} \\ g_{20} \\ g_{30} \\ \vdots \end{bmatrix} \tag{2.3.10}$$

Note that this matrix operator is tridiagonal. If we flatten $g_{jk}$ along the $k$ index instead, we see that $K^{(z)}$ is also tridiagonal:

$$K^{(z)}g^{(z)} = -\frac{\hbar^2}{2m}\frac{1}{\Delta z^2}\begin{bmatrix} -2 & 1 & 0 & 0 & \ddots \\ 1 & -2 & 1 & 0 & \ddots \\ 0 & 1 & -2 & 1 & \ddots \\ 0 & 0 & 1 & -2 & \ddots \\ \ddots & \ddots & \ddots & \ddots & \ddots \end{bmatrix}\begin{bmatrix} g_{00} \\ g_{01} \\ g_{02} \\ g_{03} \\ \vdots \end{bmatrix} \tag{2.3.11}$$

There are four important points about these matrix representations.

1. They are only tridiagonal when the mesh is flattened in the corresponding direction. Thus, to apply them efficiently, we must repeatedly flatten and unwrap the mesh.

2. The $c_j$ repeat in a cycle as we switch "rows" of the mesh.

3. Certain off-diagonal elements are zero, namely at the boundaries of the mesh (if these are not zero, we would have periodic boundary conditions).

4. Similarly, there is no modification of the terms to account for the boundaries having an "empty" point on their other side (note the first row of the matrix in particular). This is because we have effectively embedded our mesh in a slightly larger mesh that has Dirichlet ($g = 0$) boundary conditions on it (this is the main point of making the $g$ transformation).

To get the full Hamiltonian we must reincorporate the potential energy terms. We do this by putting half of each potential energy term into each component of the Hamiltonian. If we call the potential (Coulomb and external combined) at each point on the grid $W_{jk}$, we see that this part of the operator is simply a diagonal matrix when we operate on a flattened $g$ mesh:

$$\widehat{\mathcal{H}}g = \widehat{\mathcal{H}}^{(\rho)}g^{(\rho)} + \widehat{\mathcal{H}}^{(z)}g^{(z)} = \left[K^{(\rho)} + \frac{1}{2}W^{(\rho)}\right]g^{(\rho)} + \left[K^{(z)} + \frac{1}{2}W^{(z)}\right]g^{(z)} \tag{2.3.12a}$$

$$\begin{aligned}\widehat{\mathcal{H}}g = &\left(-\frac{\hbar^2}{2m}\frac{1}{\Delta\rho^2}\begin{bmatrix} -2 & c_1 & 0 & 0 & \ddots \\ c_1 & -2 & c_2 & 0 & \ddots \\ 0 & c_2 & -2 & c_3 & \ddots \\ 0 & 0 & c_3 & -2 & \ddots \\ \ddots & \ddots & \ddots & \ddots & \ddots \end{bmatrix} + \frac{1}{2}\begin{bmatrix} W_{00} & 0 & 0 & 0 & \ddots \\ 0 & W_{10} & 0 & 0 & \ddots \\ 0 & 0 & W_{20} & 0 & \ddots \\ 0 & 0 & 0 & W_{30} & \ddots \\ \ddots & \ddots & \ddots & \ddots & \ddots \end{bmatrix}\right)\begin{bmatrix} g_{00} \\ g_{10} \\ g_{20} \\ g_{30} \\ \vdots \end{bmatrix} \\ &+ \left(-\frac{\hbar^2}{2m}\frac{1}{\Delta z^2}\begin{bmatrix} -2 & 1 & 0 & 0 & \ddots \\ 1 & -2 & 1 & 0 & \ddots \\ 0 & 1 & -2 & 1 & \ddots \\ 0 & 0 & 1 & -2 & \ddots \\ \ddots & \ddots & \ddots & \ddots & \ddots \end{bmatrix} + \frac{1}{2}\begin{bmatrix} W_{00} & 0 & 0 & 0 & \ddots \\ 0 & W_{01} & 0 & 0 & \ddots \\ 0 & 0 & W_{02} & 0 & \ddots \\ 0 & 0 & 0 & W_{03} & \ddots \\ \ddots & \ddots & \ddots & \ddots & \ddots \end{bmatrix}\right)\begin{bmatrix} g_{00} \\ g_{01} \\ g_{02} \\ g_{03} \\ \vdots \end{bmatrix}\end{aligned} \tag{2.3.12b}$$

Note that the result is a $g$ mesh, so we must "wrap up" the resulting vectors from each direction before we add them together. Using the three different representations of $g$ (unwrapped in $\rho$, unwrapped in $z$, and the two-dimensional mesh itself) to ensure that the matrix operators are always tridiagonal is the key to the speed of the simulation.

#### 2.3.1.4 Time Evolution Operator

Now that we have the Hamiltonian we can think about the time evolution operator. We think of the time evolution as occurring in discrete time steps $\Delta t$. Then, using the unit operator $\hat{I}$ and

defining $\tau \equiv \Delta t/2\hbar$, time evolution can be performed using

$$g(t+\Delta t) = \left[\hat{I} + i\tau\widehat{\mathcal{H}}^{(\rho)}\right]^{-1}\left[\hat{I} - i\tau\widehat{\mathcal{H}}^{(z)}\right]\left[\hat{I} + i\tau\widehat{\mathcal{H}}^{(z)}\right]^{-1}\left[\hat{I} - i\tau\widehat{\mathcal{H}}^{(\rho)}\right]g(t) \tag{2.3.13}$$

where $g(t)$ must be flattened in the appropriate direction before each matrix multiplication. This is effectively a power series approximation in small $\Delta t$ of each operator.

To prove that (2.3.13) works, we will expand it in a power series for small $\tau$:

$$\begin{aligned}
g(t+\Delta t) &= \left[\hat{I} - i\tau\widehat{\mathcal{H}}^{(\rho)} - \tau^2\left(\widehat{\mathcal{H}}^{(\rho)}\right)^2 + \cdots\right]\left[\hat{I} - i\tau\widehat{\mathcal{H}}^{(z)}\right] \\
&\quad \times \left[\hat{I} - i\tau\widehat{\mathcal{H}}^{(z)} - \tau^2\left(\widehat{\mathcal{H}}^{(z)}\right)^2 + \cdots\right]\left[\hat{I} - i\tau\widehat{\mathcal{H}}^{(\rho)}\right]g(t) \\
&= \left[\hat{I} - i\tau\left(\widehat{\mathcal{H}}^{(\rho)} + 2\widehat{\mathcal{H}}^{(z)}\right) - \tau^2\left(\left(\widehat{\mathcal{H}}^{(\rho)}\right)^2 + \widehat{\mathcal{H}}^{(\rho)}\widehat{\mathcal{H}}^{(z)}\right) + \cdots\right] \\
&\quad \times \left[\hat{I} - i\tau\widehat{\mathcal{H}}^{(z)} - \tau^2\left(\widehat{\mathcal{H}}^{(z)}\right)^2 + \cdots\right]\left[\hat{I} - i\tau\widehat{\mathcal{H}}^{(\rho)}\right]g(t) \\
&= \left[\hat{I} - i\tau\left(\widehat{\mathcal{H}}^{(\rho)} + 2\widehat{\mathcal{H}}^{(z)}\right) - \tau^2\left(\left(\widehat{\mathcal{H}}^{(\rho)}\right)^2 + 2\widehat{\mathcal{H}}^{(\rho)}\widehat{\mathcal{H}}^{(z)} + 2\left(\widehat{\mathcal{H}}^{(z)}\right)^2\right) + \cdots\right] \\
&\quad \times \left[\hat{I} - i\tau\widehat{\mathcal{H}}^{(\rho)}\right]g(t) \\
&= \Big[\hat{I} - i\tau\left(2\widehat{\mathcal{H}}^{(\rho)} + 2\widehat{\mathcal{H}}^{(z)}\right) \\
&\quad -\tau^2\left(2\left(\widehat{\mathcal{H}}^{(\rho)}\right)^2 + 2\widehat{\mathcal{H}}^{(\rho)}\widehat{\mathcal{H}}^{(z)} + 2\widehat{\mathcal{H}}^{(z)}\widehat{\mathcal{H}}^{(\rho)} + 2\left(\widehat{\mathcal{H}}^{(z)}\right)^2\right) + \cdots\Big]g(t) \\
&= \left[\hat{I} - 2i\tau\left(\widehat{\mathcal{H}}^{(\rho)} + \widehat{\mathcal{H}}^{(z)}\right) - 2\tau^2\left(\widehat{\mathcal{H}}^{(\rho)} + \widehat{\mathcal{H}}^{(z)}\right)^2 + \cdots\right]g(t)
\end{aligned} \tag{2.3.14}$$

This agrees with the Taylor expansion of the standard time evolution operator through second order in $\Delta t$:

$$\begin{aligned}
g(t+\Delta t) &= \exp\left[-i\frac{\Delta t}{\hbar}\left(\widehat{\mathcal{H}}^{(\rho)} + \widehat{\mathcal{H}}^{(z)}\right)\right]g(t) \\
g(t+\Delta t) &= \left[\hat{I} - i\frac{\Delta t}{\hbar}\left(\widehat{\mathcal{H}}^{(\rho)} + \widehat{\mathcal{H}}^{(z)}\right) - \frac{1}{2}\left(\frac{\Delta t}{\hbar}\right)^2\left(\widehat{\mathcal{H}}^{(\rho)} + \widehat{\mathcal{H}}^{(z)}\right)^2 + \cdots\right]g(t)
\end{aligned} \tag{2.3.15}$$

Although (2.3.15) does seem to imply a more direct method of calculating time evolution where we simply perform point-wise multiplication on the mesh by the time evolution operator or its series expansion, these methods are not suitable for numerical calculations because they involve computing the squares (or even higher powers) of large matrices, which both scales poorly and

tends to cause overflow errors. Equation (2.3.13) deals with matrices in first order only, but is slower than direct multiplication due to the required multiplication by matrix inverses.

Note that which of $z$ and $\rho$ comes first can be swapped freely as long as the structure of the four-part matrix operation is preserved. The four steps can be thought of as, in order:

1. Evolve *forwards* by $+\Delta t/2$ using direction 1,
2. Evolve *backwards* by $-\Delta t/2$ using direction 2,
3. Evolve *forwards* by $+\Delta t/2$ using direction 2,
4. Evolve *backwards* by $-\Delta t/2$ using direction 1.

Evolving backwards in time by a negative time step is, of course, the same as evolving forwards in time. Such a time step is *implicit* as opposed to *explicit* and tends to have much better stability properties, at the cost of having to solve a linear system instead of a simple matrix multiplication.

The "multiplication by matrix inverse" steps look numerically daunting, but luckily, the matrices that we need to invert in this case are tridiagonal. The tridiagonal matrix algorithm (see D) can be used to efficiently determine the result of multiplying by the inverse without actually calculating the inverse, which makes this time evolution method practical.

#### 2.3.1.5 Probability Current

The probability current is defined as

$$\mathbf{J} = \frac{\hbar}{2mi}(\Psi^*\nabla\Psi - \Psi\nabla\Psi^*) \tag{2.3.16}$$

Break this into directional components, as we did for the evolution operators:

$$J^{(z)} = \frac{\hbar}{2mi}\left(\Psi^*\frac{\partial\Psi}{\partial z} - \Psi\frac{\partial\Psi^*}{\partial z}\right) \tag{2.3.17a}$$

$$J^{(\rho)} = \frac{\hbar}{2mi}\left(\Psi^*\frac{\partial\Psi}{\partial \rho} - \Psi\frac{\partial\Psi^*}{\partial \rho}\right) \tag{2.3.17b}$$

Using the same finite difference scheme as before, $J^{(z)}$ is simple:

$$
\begin{aligned}
J^{(z)} &= \frac{\hbar}{2mi}\frac{1}{2\pi\rho}\left[g^*\frac{\partial g}{\partial z} - g\frac{\partial g^*}{\partial z}\right] \\
J^{(z)}_{jk} &= \frac{\hbar}{2mi}\frac{1}{2\pi\left(j+\frac{1}{2}\right)\Delta\rho}\left[g^*_{jk}\left(\frac{g_{j,k+1}-g_{j,k-1}}{2\Delta z}\right) - g_{jk}\left(\frac{g^*_{j,k+1}-g^*_{j,k-1}}{2\Delta z}\right)\right] \\
J^{(z)}_{jk} &= \frac{\hbar}{2mi}\frac{1}{2\pi}\frac{1}{2\Delta\rho\,\Delta z}\left[g^*_{jk}\left(j+\frac{1}{2}\right)\left(g_{j,k+1}-g_{j,k-1}\right) - g_{jk}\left(j+\frac{1}{2}\right)\left(g^*_{j,k+1}-g^*_{j,k-1}\right)\right] \\
J^{(z)}_{jk} &= \frac{\hbar}{2m}\frac{1}{2\pi}\frac{1}{\Delta\rho\,\Delta z}\ \mathrm{Im}\left[g^*_{jk}\,\frac{1}{j+\frac{1}{2}}\left(g_{j,k+1}-g_{j,k-1}\right)\right]
\end{aligned}
\tag{2.3.18}
$$

where we have noted that the difference of a number and its complex conjugate is twice the imaginary part. Also note that (unlike in the kinetic energy matrix operator) the coefficient for the operator in the $k$-direction depends on the index $j$.

$J^{(\rho)}$ is slightly more complicated:

$$
\begin{aligned}
J^{(\rho)} &= \frac{\hbar}{2mi}\frac{1}{2\pi\sqrt{\rho}}\left[g^*\frac{\partial}{\partial\rho}\left(\frac{g}{\sqrt{\rho}}\right) - g\frac{\partial}{\partial\rho}\left(\frac{g^*}{\sqrt{\rho}}\right)\right] \\
J^{(\rho)}_{jk} &= \frac{\hbar}{2mi}\,\frac{1}{2\pi\sqrt{\left(j+\frac{1}{2}\right)\Delta\rho}}\left[g^*_{jk}\,\frac{1}{2\,\Delta\rho}\left(\frac{g_{j+1,k}}{\sqrt{(j+\frac{3}{2})\Delta\rho}} - \frac{g_{j-1,k}}{\sqrt{(j-\frac{1}{2})\Delta\rho}}\right)\right. \\
&\qquad\left. -g_{jk}\,\frac{1}{2\,\Delta\rho}\left(\frac{g_{j+1,k}}{\sqrt{(j+\frac{3}{2})\Delta\rho}} - \frac{g_{j-1,k}}{\sqrt{(j-\frac{1}{2})\Delta\rho}}\right)\right] \\
J^{(\rho)}_{jk} &= \frac{\hbar}{2mi}\,\frac{1}{2\pi}\frac{1}{2\Delta\rho^2}\frac{1}{\sqrt{j+\frac{1}{2}}}\left[g^*_{jk}\left(\frac{g_{j+1,k}}{\sqrt{j+\frac{3}{2}}} - \frac{g_{j-1,k}}{\sqrt{j-\frac{1}{2}}}\right) - g_{jk}\left(\frac{g_{j+1,k}}{\sqrt{j+\frac{3}{2}}} - \frac{g_{j-1,k}}{\sqrt{-\frac{1}{2}}}\right)\right] \\
J^{(\rho)}_{jk} &= \frac{\hbar}{2m}\,\frac{1}{2\pi}\frac{1}{\Delta\rho^2}\ \mathrm{Im}\left[g^*_{jk}\left(d_{j+1}\,g_{j+1,k} - d_j\,g_{j-1,k}\right)\right]
\end{aligned}
\tag{2.3.19, 2.3.20}
$$

where

$$
d_j = \frac{1}{\sqrt{j^2-\frac{1}{4}}} \tag{2.3.21}
$$

### 2.3.2 Spherical-Slice Mesh

Although the cylindrical-slice mesh was easy to work with, it does not have the same natural symmetry of the problem (namely, spherical). In particular, a lot of mesh is "wasted" in the

corners far from the nucleus, where the distance to the nucleus is larger than the straight-line bounds of the mesh and is thus untrustworthy. To solve this problem, we will instead use a mesh that is a single $\phi$ slice of a sphere. This section should be considered supplementary to the method described in Section 2.3.1: simply replace the necessary results with results from this section to switch which kind of mesh you're working on.

#### 2.3.2.1 The Mesh and Wavefunction

We discretize space with

$$r \to r_j = \left(j + \frac{1}{2}\right) \Delta r \qquad j = 0, 1, 2, \cdots, N_r \tag{2.3.22a}$$

$$\theta \to \theta_k = \left(k + \frac{1}{2}\right) \Delta\theta \qquad k = 0, 1, 2, \cdots, N_\theta \qquad \Delta\theta = \frac{\pi}{N_\theta - 1} \tag{2.3.22b}$$

The $g$ transformation is

$$g \equiv \sqrt{2\pi r^2 \sin\theta}\, \Psi \tag{2.3.23a}$$

$$\Psi = \frac{g}{\sqrt{2\pi r^2 \sin\theta}} \tag{2.3.23b}$$

which provides the desired form for the inner product:

$$\begin{aligned}
\langle \Psi_1 | \Psi_2 \rangle &= \int_V \Psi_1^*(\mathbf{r})\, \Psi_2(\mathbf{r})\, \mathrm{d}V \\
&= \int_0^{2\pi} \int_0^{\pi} \int_0^{\infty} \Psi_1^*(r,\theta)\, \Psi_2(r,\theta)\, r^2 \sin\theta\, \mathrm{d}r\, \mathrm{d}\theta\, \mathrm{d}\phi \\
&= 2\pi \int_0^{\pi} \int_0^{\infty} \Psi_1^*(r,\theta)\, \Psi_2(r,\theta)\, r^2 \sin\theta\, \mathrm{d}r\, \mathrm{d}\theta \\
&= 2\pi \int_0^{\pi} \int_0^{\infty} \frac{g_1^*(r,\theta)}{\sqrt{2\pi r^2 \sin\theta}} \frac{g_2(r,\theta)}{\sqrt{2\pi r^2 \sin\theta}}\, r^2 \sin\theta\, \mathrm{d}r\, \mathrm{d}\theta \\
&= \int_0^{\pi} \int_0^{\infty} g_1^*(r,\theta)\, g_2(r,\theta)\, \mathrm{d}r\, \mathrm{d}\theta \\
\langle \Psi_1 | \Psi_2 \rangle &\to \sum_{jk} g^*_{1,\,jk}\, g_{2,\,jk}\, \Delta r\, \Delta\theta \equiv \langle g_1 | g_2 \rangle
\end{aligned} \tag{2.3.24}$$

#### 2.3.2.2 Kinetic Energy Operator

The only difference between this mesh and the cylindrical-slice mesh lies in the evaluation of the kinetic energy term in the Hamiltonian. That means we need to understand how to evaluate the discretized Lagrangian on this mesh. The $\phi$-symmetric Laplacian in spherical coordinates is typically presented as

$$\nabla^2\Psi = \frac{1}{r^2}\frac{\partial}{\partial r}\left(r^2\frac{\partial\Psi}{\partial r}\right) + \frac{1}{r^2\sin\theta}\frac{\partial}{\partial\theta}\left(\sin\theta\,\frac{\partial\Psi}{\partial\theta}\right) \tag{2.3.25}$$

This form is not particularly useful since it contains compound derivatives (i.e., the derivative of a term that itself contains a derivative in addition to other variables), which will turn into a huge mess when we discretize the operators. There are two alternate ways to write the $r$ term:

$$\frac{1}{r^2}\frac{\partial}{\partial r}\left(r^2\frac{\partial\Psi}{\partial r}\right) = \frac{1}{r^2}\left(2r\frac{\partial\Psi}{\partial r} + r^2\frac{\partial^2\Psi}{\partial r^2}\right) = \frac{2}{r^2}\frac{\partial\Psi}{\partial r} + \frac{\partial^2\Psi}{\partial r^2} \tag{2.3.26}$$

or

$$\frac{1}{r}\frac{\partial^2}{\partial r^2}(r\,\Psi) = \frac{1}{r}\frac{\partial}{\partial r}\left(\Psi + r\frac{\partial\Psi}{\partial r}\right) = \frac{1}{r}\left(2\frac{\partial\Psi}{\partial r} + r\frac{\partial^2\Psi}{\partial r^2}\right) = \frac{2}{r}\frac{\partial\Psi}{\partial r} + \frac{\partial^2\Psi}{\partial r^2} \tag{2.3.27}$$

We will use (2.3.27), since it contains only a single second derivative. Second derivatives lead to much more complicated numerical equations than first derivatives do.

We can also remove the compound derivative from the $\theta$ term:

$$\frac{1}{r^2\sin\theta}\frac{\partial}{\partial\theta}\left(\sin\theta\,\frac{\partial\Psi}{\partial\theta}\right) = \frac{1}{r^2\sin\theta}\left(\cos\theta\,\frac{\partial\Psi}{\partial\theta} + \sin\theta\,\frac{\partial^2\Psi}{\partial\theta^2}\right) = \frac{1}{r^2}\left(\cot\theta\,\frac{\partial\Psi}{\partial\theta} + \frac{\partial^2\Psi}{\partial\theta^2}\right) \tag{2.3.28}$$

Substituting (2.3.27) and (2.3.28) into (2.3.25), we have

$$\nabla^2\Psi = \frac{1}{r}\frac{\partial^2}{\partial r^2}(r\,\Psi) + \frac{1}{r^2}\left(\cot\theta\,\frac{\partial\Psi}{\partial\theta} + \frac{\partial^2\Psi}{\partial\theta^2}\right) \tag{2.3.29}$$

The next step is to apply the transformation (2.3.23) to (2.3.29):

$$\begin{aligned}
\nabla^2\Psi &= \frac{1}{r}\frac{\partial^2}{\partial r^2}\left(\frac{r\,g}{\sqrt{2\pi r^2\sin\theta}}\right) + \frac{1}{r^2}\left[\cot\theta\,\frac{\partial}{\partial\theta}\left(\frac{g}{\sqrt{2\pi r^2\sin\theta}}\right) + \frac{\partial^2}{\partial\theta^2}\left(\frac{g}{\sqrt{2\pi r^2\sin\theta}}\right)\right] \\
i\hbar\frac{1}{\sqrt{2\pi r^2\sin\theta}}\frac{\partial g}{\partial t} &= \frac{1}{r}\frac{\partial^2}{\partial r^2}\left(\frac{r\,g}{\sqrt{2\pi r^2\sin\theta}}\right) + \frac{\cot\theta}{r^2}\,\frac{\partial}{\partial\theta}\left(\frac{g}{\sqrt{2\pi r^2\sin\theta}}\right) + \frac{1}{r^2}\frac{\partial^2}{\partial\theta^2}\left(\frac{g}{\sqrt{2\pi r^2\sin\theta}}\right) + \cdots \\
i\hbar\frac{\partial g}{\partial t} &= -\frac{\hbar^2}{2m}\sqrt{\sin\theta}\left[\frac{\partial^2}{\partial r^2}\left(\frac{g}{\sqrt{\sin\theta}}\right) + \frac{\cot\theta}{r^2}\,\frac{\partial}{\partial\theta}\left(\frac{g}{\sqrt{\sin\theta}}\right) + \frac{1}{r^2}\frac{\partial^2}{\partial\theta^2}\left(\frac{g}{\sqrt{\sin\theta}}\right)\right] + \cdots \\
i\hbar\frac{\partial g}{\partial t} &= -\frac{\hbar^2}{2m}\left[\frac{\partial^2 g}{\partial r^2} + \frac{\cot\theta\sqrt{\sin\theta}}{r^2}\,\frac{\partial}{\partial\theta}\left(\frac{g}{\sqrt{\sin\theta}}\right) + \frac{\sqrt{\sin\theta}}{r^2}\frac{\partial^2}{\partial\theta^2}\left(\frac{g}{\sqrt{\sin\theta}}\right)\right] + \cdots
\end{aligned} \tag{2.3.30}$$

We will now replace all of the derivatives in (2.3.30) with finite differences. Just like in the cylindrical case, we use centered finite differences:

$$\frac{\partial^2 g}{\partial r^2} \to \frac{g_{j+1,k} + g_{j-1,k} - 2g_{j,k}}{(\Delta r)^2} \tag{2.3.31a}$$

$$\begin{aligned}
\frac{\cot\theta\sqrt{\sin\theta}}{r^2}\,\frac{\partial}{\partial\theta}\left(\frac{g}{\sqrt{\sin\theta}}\right) \to\ & \frac{\cot\big((k+\frac{1}{2})\Delta\theta\big)\sqrt{\sin\big((k+\frac{1}{2})\Delta\theta\big)}}{2\,\Delta\theta\left[\big(j+\frac{1}{2}\big)\Delta r\right]^2} \\
& \times\left[\frac{g_{j,k+1}}{\sqrt{\sin\big((k+\frac{3}{2})\Delta\theta\big)}} - \frac{g_{j,k-1}}{\sqrt{\sin\big((k-\frac{1}{2})\Delta\theta\big)}}\right]
\end{aligned} \tag{2.3.31b}$$

$$\begin{aligned}
\frac{\sqrt{\sin\theta}}{r^2}\,\frac{\partial^2}{\partial\theta^2}\left(\frac{g}{\sqrt{\sin\theta}}\right) \to\ & \frac{\sqrt{\sin\big((k+\frac{1}{2})\Delta\theta\big)}}{\left[\big(j+\frac{1}{2}\big)\Delta r\,\Delta\theta\right]^2} \\
& \times\left[\frac{g_{j,k+1}}{\sqrt{\sin\big((k+\frac{3}{2})\Delta\theta\big)}} + \frac{g_{j,k-1}}{\sqrt{\sin\big((k-\frac{1}{2})\Delta\theta\big)}} - \frac{2g_{j,k}}{\sqrt{\sin\big((k+\frac{1}{2})\Delta\theta\big)}}\right]
\end{aligned} \tag{2.3.31c}$$

Apply the replacements to (2.3.30):

$$
\begin{aligned}
i\hbar\frac{\partial g}{\partial t} = &-\frac{\hbar^2}{2m}\left\{\frac{g_{j+1,k}+g_{j-1,k}-2g_{j,k}}{(\Delta r)^2}\right.\\
&+\frac{\cot\big((k+\frac{1}{2})\Delta\theta\big)\sqrt{\sin\big((k+\frac{1}{2})\Delta\theta\big)}}{2\,\Delta\theta\left[(j+\frac{1}{2})\Delta r\right]^2}\left[\frac{g_{j,k+1}}{\sqrt{\sin\big((k+\frac{3}{2})\Delta\theta\big)}}-\frac{g_{j,k-1}}{\sqrt{\sin\big((k-\frac{1}{2})\Delta\theta\big)}}\right]\\
&\left.+\frac{\sqrt{\sin\big((k+\frac{1}{2})\Delta\theta\big)}}{\left[(j+\frac{1}{2})\Delta r\,\Delta\theta\right]^2}\left[\frac{g_{j,k+1}}{\sqrt{\sin\big((k+\frac{3}{2})\Delta\theta\big)}}+\frac{g_{j,k-1}}{\sqrt{\sin\big((k-\frac{1}{2})\Delta\theta\big)}}-\frac{2g_{j,k}}{\sqrt{\sin\big((k+\frac{1}{2})\Delta\theta\big)}}\right]\right\}+\cdots\\
i\hbar\frac{\partial g}{\partial t} = &-\frac{\hbar^2}{2m}\left\{\frac{g_{j+1,k}+g_{j-1,k}-2g_{j,k}}{(\Delta r)^2}\right.\\
&+\frac{\cot\big((k+\frac{1}{2})\Delta\theta\big)\,\Delta\theta}{2}\frac{\sqrt{\sin\big((k+\frac{1}{2})\Delta\theta\big)}}{\left[(j+\frac{1}{2})\Delta r\,\Delta\theta\right]^2}\left[\frac{g_{j,k+1}}{\sqrt{\sin\big((k+\frac{3}{2})\Delta\theta\big)}}-\frac{g_{j,k-1}}{\sqrt{\sin\big((k-\frac{1}{2})\Delta\theta\big)}}\right]\\
&\left.+\frac{\sqrt{\sin\big((k+\frac{1}{2})\Delta\theta\big)}}{\left[(j+\frac{1}{2})\Delta r\,\Delta\theta\right]^2}\left[\frac{g_{j,k+1}}{\sqrt{\sin\big((k+\frac{3}{2})\Delta\theta\big)}}+\frac{g_{j,k-1}}{\sqrt{\sin\big((k-\frac{1}{2})\Delta\theta\big)}}-\frac{2g_{j,k}}{\sqrt{\sin\big((k+\frac{1}{2})\Delta\theta\big)}}\right]\right\}+\cdots\\
i\hbar\frac{\partial g}{\partial t} = &-\frac{\hbar^2}{2m}\left\{\frac{g_{j+1,k}+g_{j-1,k}-2g_{j,k}}{(\Delta r)^2}\right.\\
&+\left(1+\frac{\Delta\theta}{2}\cot([k+1/2]\Delta\theta)\right)\sqrt{\frac{\sin\big((k+\frac{1}{2})\Delta\theta\big)}{\sin\big((k+\frac{3}{2})\Delta\theta\big)}}\frac{1}{\left[(j+\frac{1}{2})\Delta r\,\Delta\theta\right]^2}\,g_{j,k+1}\\
&+\left(1-\frac{\Delta\theta}{2}\cot([k+1/2]\Delta\theta)\right)\sqrt{\frac{\sin\big((k+\frac{1}{2})\Delta\theta\big)}{\sin\big((k-\frac{1}{2})\Delta\theta\big)}}\frac{1}{\left[(j+\frac{1}{2})\Delta r\,\Delta\theta\right]^2}\,g_{j,k-1}\\
&\left.-\frac{2}{\left[(j+\frac{1}{2})\Delta r\,\Delta\theta\right]^2}\,g_{j,k}\right\}+\cdots
\end{aligned}
\tag{2.3.32}
$$

This result can be used to construct matrix operators in the $r$ and $\theta$ directions for the kinetic energy and the full Hamiltonian using identical methodology to the cylindrical-slice mesh.

#### 2.3.2.3 Radial Probability Current

The probability current is defined as

$$\mathbf{J} = \frac{\hbar}{2mi}(\Psi^*\nabla\Psi - \Psi\nabla\Psi^*) \tag{2.3.33}$$

The radial vector component of this is

$$J^{(r)} = \frac{\hbar}{2mi}\left(\Psi^* \frac{\partial \Psi}{\partial r} - \Psi \frac{\partial \Psi^*}{\partial r}\right) \tag{2.3.34}$$

Apply the finite difference scheme to $J^{(r)}$:

$$\begin{aligned}
J^{(r)} &= \frac{\hbar}{2mi}\left(\Psi^* \frac{\partial \Psi}{\partial r} - \Psi \frac{\partial \Psi^*}{\partial r}\right) \\
J^{(r)} &= \frac{\hbar}{2mi} \frac{1}{\sqrt{2\pi r^2 \sin\theta}}\left(g^* \frac{\partial}{\partial r}\left(\frac{g}{\sqrt{2\pi r^2 \sin\theta}}\right) - g \frac{\partial}{\partial r}\left(\frac{g^*}{\sqrt{2\pi r^2 \sin\theta}}\right)\right) \\
J^{(r)} &= \frac{\hbar}{2mi} \frac{1}{2\pi r \sin\theta}\left(g^* \frac{\partial}{\partial r}\left(\frac{g}{r}\right) - g \frac{\partial}{\partial r}\left(\frac{g^*}{r}\right)\right) \\
J^{(r)}_{jk} &= \frac{\hbar}{2mi} \frac{1}{2\pi\left(j+\frac{1}{2}\right)\Delta r \sin\left(\left(k+\frac{1}{2}\right)\Delta\theta\right)}\left(g^* \frac{\partial}{\partial r}\left(\frac{g}{r}\right) - g \frac{\partial}{\partial r}\left(\frac{g^*}{r}\right)\right)
\end{aligned} \tag{2.3.35}$$

### 2.3.3 Spherical Harmonic Mesh

The advantages offered by switching to the spherical slice coordinate system indicate that it should be possible to choose an even better coordinate system, that uses more symmetries of the problem at hand. In fact, such a coordinate system does exist, but not in physical space. Instead, one of the coordinates on the mesh will be the angular momentum of the wavefunction. Since we know that the angular momentum is already quantized, this description of the wavefunction will have major accuracy improvements over other methods, since we won't be trying to model the spherical harmonics in a discretized physical space when they already have a perfectly good discretized description.

This motivates us to perform a partial-wave expansion of the wavefunction:

$$|\Psi(\mathbf{r},t)\rangle = \sum_{\ell=0}^{\infty} \Psi_\ell(r,t)\,|\ell\rangle \approx \sum_{\ell=0}^{\ell_{\max}} \Psi_\ell(r,t)\,|\ell\rangle \tag{2.3.36}$$

where $|\ell\rangle \equiv |\ell, m=0\rangle$, a state of definite orbital ($\ell$) and azimuthal ($m$) angular momentum. We will also discretize the wavefunction over radial points given by

$$r_j = \left(j+\frac{1}{2}\right)\Delta r \qquad j = 0, 1, \cdots, N_r - 1 \tag{2.3.37}$$

where $N_r$ is the number of radial points. Then a full discretization of the wavefunction is

$$|\Psi(\mathbf{r},t)\rangle \approx \sum_{\ell=0}^{\ell_{\max}} \sum_{j=0}^{N-1} \Psi_\ell^j(t)\,|\ell\rangle$$
$$|\Psi(\mathbf{r},t)\rangle \approx \sum_{\ell=0}^{\ell_{\max}} \sum_{j=0}^{N-1} \frac{g_\ell^j(t)}{r_j}\,|\ell\rangle \tag{2.3.38}$$

As usual, we store the "expansion coefficients" as a mesh of $g$ values, $g_\ell^j$.

So, why is this strange mesh going to lead to an improvement? Both previous methods used the same basic model of evolution equation: a Crank-Nicholson split-operator method based on a time-evolution operator generated by discretizing the Hamiltonian $\mathcal{H}$. One problem with this method as presented so far is that it does not properly account for the boundary conditions of the problem (in fact, they don't account for them at all except for avoiding edge-wrapping and ensuring the exterior boundary is zero). This causes the derivatives near the boundaries to not be particularly accurate. Interestingly, this problem is actually *worse* for the spherical-expansion meshes than the cylindrical-expansion mesh because there are more mesh points near the $r = 0$ boundary, the only boundary region where the wavefunction is consistently large. We are also not yet taking advantage of the structure of the interaction term in the spherical harmonic expansion basis. We will fix these problems in the next two sections.

#### 2.3.3.1 Lagrangian Evolution Equations

Currently, the mesh uses the Dirichlet boundary condition $g = 0$ on all mesh boundaries and nothing else. However, we also have the Neumann boundary condition $\partial_r \Psi = 0$ at $r = 0$, which has not been accounted for anywhere in the previous mesh derivations. This is the source of the problems with accurately evaluating the derivative near the $r = 0$ boundary. To include it, we need to take a step back and find a different differential equation to solve for the time evolution of $\Psi$ (or, rather, $g$). To do so, consider the Lagrangian density operator $\widehat{\mathcal{L}}$ for the electron wavefunction

$\Psi(\mathbf{r},t)$ [80, 81][2]. The expectation value of $\widehat{\mathcal{L}}$ is the Lagrangian $\mathcal{L}$:

$$\begin{aligned}\mathcal{L} &= \langle\Psi|\widehat{\mathcal{L}}|\Psi\rangle\,,\\ \mathcal{L} &= \langle\Psi|i\hbar\,\frac{\partial}{\partial t} - \widehat{T_r} - \widehat{V} - \widehat{\mathcal{H}}_I^L|\Psi\rangle\end{aligned} \tag{2.3.39}$$

where $\widehat{T_r}$ is the radial kinetic energy operator $-(\hbar^2/2\mu)\,\partial_{rr}$, $\widehat{V}$ is the operator for the static atomic electric potential plus the centrifugal effective potential $\ell(\ell+1)\,\hbar^2/\mu r^2$, and $\widehat{\mathcal{H}}_I^L$ is the interaction Hamiltonian for the external electric field. In the following calculation we will take the electric field to be spatially uniform and polarized along the $\hat{\mathbf{z}}$ direction. There are many other valid Lagrangian densities for this problem, but this form is convenient to perform the necessary calculations with.

The action $\mathcal{S}$ is the integral of the Lagrangian over a path through time:

$$\begin{aligned}\mathcal{S} &= \int_{t_1}^{t_2} \mathrm{d}t\,\mathcal{L}\\ &= \int_{t_1}^{t_2} \mathrm{d}t\ \ \langle\Psi|i\hbar\,\frac{\partial}{\partial t} - \widehat{T_r} - \widehat{V} - \widehat{\mathcal{H}}_I^L|\Psi\rangle\\ &= \int_{t_1}^{t_2} \mathrm{d}t \int_x \mathrm{d}^3x\ \Psi^*\left(i\hbar\,\frac{\partial}{\partial t} - \widehat{T_r} - \widehat{V} - \widehat{\mathcal{H}}_I^L\right)\Psi\\ \mathcal{S} &= \int_{t_1}^{t_2} \mathrm{d}t \int_x \mathrm{d}^3x\ \Psi^*\left[\left(i\hbar\,\frac{\partial}{\partial t} - \widehat{T_r} - \widehat{V} - \widehat{\mathcal{H}}_I^L\right)\Psi\right]\end{aligned} \tag{2.3.40}$$

The principle of stationary action tells us that if $\Psi$ and $\Psi^*$ are the actual trajectory of the wavefunction through time, the action must be extremized. Therefore, we must have $\frac{\partial\mathcal{S}}{\partial\Psi^*} = 0$ or $\frac{\partial\mathcal{S}}{\partial\Psi} = 0$. The first is much easier to work with because $\Psi^*$ is not being hit by $\mathcal{L}$. That condition can only be satisfied if the term inside the square brackets is equal to zero for any variation in $\Psi^*$. For a continuous wavefunction, this leads immediately to the time-dependent Schrödinger equation:

$$\begin{aligned}\left(i\hbar\,\frac{\partial}{\partial t} - \widehat{T_r} - \widehat{V} - \widehat{\mathcal{H}}_I^L\right)\Psi &= 0\\ i\hbar\,\frac{\partial\Psi}{\partial t} &= \left(\widehat{T_r} + \widehat{V} + \widehat{\mathcal{H}}_I^L\right)\Psi\\ i\hbar\,\frac{\partial\Psi}{\partial t} &= \widehat{\mathcal{H}}\Psi\end{aligned} \tag{2.3.41}$$

[2]The first of those references contains numerous typos. It is best to cross-reference the two and check the calculation yourself to reconcile any differences, which is what we have done for this section.

We will instead discretize $\mathcal{L}$ before varying $\Psi^*$, using the spherical harmonic decomposition from (2.3.38). This will provide a discretized differential equation for $\Psi$. Note that in order to make the inner products look nice we will actually transform to $g = r\Psi, g^* = r\Psi^*$ during the calculation. Varying $g^*$ is equivalent to varying $\Psi^*$.

$$\begin{aligned}
\mathcal{L} &= \langle\Psi| i\hbar \frac{\partial}{\partial t} - \widehat{T_r} - \widehat{V} - \widehat{\mathcal{H}}_I^L |\Psi\rangle \\
\mathcal{L} &= \langle\Psi| i\hbar \frac{\partial}{\partial t} |\Psi\rangle + \langle\Psi| -\widehat{T_r} |\Psi\rangle + \langle\Psi| -\widehat{V} |\Psi\rangle + \langle\Psi| -\widehat{\mathcal{H}}_I^L |\Psi\rangle
\end{aligned} \tag{2.3.42}$$

We will tackle each term individually. The first term is the one involving the time derivative:

$$\begin{aligned}
\langle\Psi| i\hbar \frac{\partial}{\partial t} |\Psi\rangle &= i\hbar \int_0^\infty r^2 \,\mathrm{d}r \int_\Omega \mathrm{d}\Omega \; \Psi^* \frac{\partial \Psi}{\partial t} \\
&= i\hbar \int_0^\infty r^2 \,\mathrm{d}r \int_\Omega \mathrm{d}\Omega \sum_\ell \sum_{\ell'} \Psi_\ell^* \langle\ell| \frac{\partial \Psi_{\ell'}}{\partial t} |\ell'\rangle \\
&= i\hbar \int_0^\infty r^2 \,\mathrm{d}r \sum_\ell \sum_{\ell'} \Psi_\ell^* \langle\ell| \frac{\partial \Psi_{\ell'}}{\partial t} |\ell'\rangle \\
&= i\hbar \sum_\ell \int_0^\infty r^2 \,\mathrm{d}r \; \Psi_\ell^* \frac{\partial \Psi_\ell}{\partial t} \\
&= i\hbar \sum_\ell \int_0^\infty \mathrm{d}r \, g_\ell^* \frac{\partial g_\ell}{\partial t} \\
\langle\Psi| i\hbar \frac{\partial}{\partial t} |\Psi\rangle &\approx i\hbar \,\Delta r \sum_{\ell,\,j} \left(g_\ell^j\right)^* \frac{\partial g_\ell^j}{\partial t}
\end{aligned} \tag{2.3.43}$$

The potential energy term is also very straightforward (remember that $V(r)$ include the effective potential):

$$\begin{aligned}
\langle\Psi| -\widehat{V} |\Psi\rangle &= -\int_0^\infty r^2 \,\mathrm{d}r \int_\Omega \mathrm{d}\Omega \; \Psi^* \, \widehat{V} \, \Psi \\
&= -\int_0^\infty r^2 \,\mathrm{d}r \int_\Omega \sum_\ell \sum_{\ell'} \mathrm{d}\Omega \; \Psi_\ell^* \, \langle\ell| \, \widehat{V} \, |\ell'\rangle \, \Psi_{\ell'} \\
&= -\sum_\ell \int_0^\infty r^2 \,\mathrm{d}r \; \Psi_\ell^* \, \widehat{V}_\ell \, \Psi_\ell \\
&\approx -\Delta r \sum_{\ell,\,j} r_j^2 \left(\Psi_\ell^j\right)^* V_\ell^j \, \Psi_\ell^j \\
\langle\Psi| -\widehat{V} |\Psi\rangle &\approx -\Delta r \sum_{\ell,\,j} \left(g_\ell^j\right)^* V_\ell^j \, g_\ell^j
\end{aligned} \tag{2.3.44}$$

The kinetic energy term requires some rearranging:

$$\begin{aligned}
\langle\Psi|-\widehat{T_r}|\Psi\rangle &= -\int_0^\infty r^2\,\mathrm{d}r \int_\Omega \mathrm{d}\Omega\ \Psi^*\,\widehat{T_r}\,\Psi \\
&= -\int_0^\infty r^2\,\mathrm{d}r \sum_\ell \sum_{\ell'} \int_\Omega \mathrm{d}\Omega\ \Psi_\ell^*\ \langle\ell| - \frac{\hbar^2}{2m}\nabla_r^2\,\Psi_{\ell'}\,\big|\ell'\big\rangle \\
&= \frac{\hbar^2}{2m}\int_0^\infty r^2\,\mathrm{d}r \sum_\ell \Psi_\ell^*\,\frac{1}{r^2}\frac{\partial}{\partial r}\left(r^2\,\frac{\partial\Psi_\ell}{\partial r}\right) \\
&= \frac{\hbar^2}{2m}\int_0^\infty \mathrm{d}r \sum_\ell \Psi_\ell^*\,\frac{\partial}{\partial r}\left(r^2\,\frac{\partial\Psi_\ell}{\partial r}\right) \\
\langle\Psi|-\widehat{T_r}|\Psi\rangle &= \frac{\hbar^2}{2m}\sum_\ell \left\{\left[r^2\,\Psi_\ell^*\,\frac{\partial\Psi_\ell}{\partial r}\right|_0^\infty - \int_0^\infty \mathrm{d}r\,r^2\,\frac{\partial\Psi_\ell^*}{\partial r}\,\frac{\partial\Psi_\ell}{\partial r}\right\}
\end{aligned} \tag{2.3.45}$$

The first term under the sum (the boundary term from the integration by parts) is zero because $\lim_{r\to 0} r\,\Psi_l = 0$ by assumption. We have now applied the Neumann boundary condition. We are left with the second term, which can be discretized as

$$\begin{aligned}
\langle\Psi|-\widehat{T_r}|\Psi\rangle &= -\frac{\hbar^2}{2m}\sum_\ell \int_0^\infty \mathrm{d}r\ r^2\,\frac{\partial\Psi_\ell^*}{\partial r}\,\frac{\partial\Psi_\ell}{\partial r} \\
&= -\frac{\hbar^2}{2m}\sum_\ell \int_0^\infty \mathrm{d}r\ r^2\left|\frac{\partial\Psi_\ell}{\partial r}\right|^2 \\
\langle\Psi|-\widehat{T_r}|\Psi\rangle &\approx -\frac{\hbar^2}{2m}\,\Delta r \sum_{\ell,\,j} r_{j+\frac{1}{2}}^2\left|\frac{\Psi_\ell^{j+1}-\Psi_\ell^j}{\Delta r}\right|^2
\end{aligned} \tag{2.3.46}$$

Note that we did not transform from $\Psi_\ell$ to $g_\ell$ yet. This is because the discretization scheme in the last line is taken at the midpoint of each grid interval, so in going from the third to fourth line $r$ does not actually match the position of either $\Psi_\ell^{j+1}$ or $\Psi_\ell^j$. We aren't quite done with this term: it looks nice in the form above, but we will have to rearrange it even more to fit into the final combined $\ell, j$ sum. In particular, let's remove the absolute value and make $\left(g_\ell^j\right)^*$ the prefactor

common to each term in the sum:

$$\langle\Psi|-\widehat{T_r}|\Psi\rangle = -\frac{\hbar^2}{2m(\Delta r)^2}\,\Delta r \sum_{\ell,\,j} r_{j+\frac{1}{2}}^2 \left[\left(\Psi_\ell^{j+1}\right)^* - \left(\Psi_\ell^{j}\right)^*\right]\left[\Psi_\ell^{j+1} - \Psi_\ell^{j}\right]$$
$$\langle\Psi|-\widehat{T_r}|\Psi\rangle = -\frac{\hbar^2}{2m(\Delta r)^2}\,\Delta r \sum_{\ell,\,j} r_{j+\frac{1}{2}}^2 \left[\left(\Psi_\ell^{j+1}\right)^*\Psi_\ell^{j+1} - \left(\Psi_\ell^{j+1}\right)^*\Psi_\ell^{j} - \left(\Psi_\ell^{j}\right)^*\Psi_\ell^{j+1} + \left(\Psi_\ell^{j}\right)^*\Psi_\ell^{j}\right] \tag{2.3.47}$$

The last two terms in the square brackets will be kept in this term in the sum. However, we push the two $\left(\Psi_\ell^{j+1}\right)^*$ terms into the next term in the overall sum, and bring the $j+1$ terms from the previous term in the overall sum to this term:

$$\begin{aligned}
\langle\Psi|-\widehat{T_r}|\Psi\rangle &= -\frac{\hbar^2}{2m\,\Delta r}\sum_{\ell,\,j}\left\{r_{j+\frac{1}{2}}^2\left[-\left(\Psi_\ell^{j}\right)^*\Psi_\ell^{j+1} + \left(\Psi_\ell^{j}\right)^*\Psi_\ell^{j}\right] + r_{j-\frac{1}{2}}^2\left[\left(\Psi_\ell^{j}\right)^*\Psi_\ell^{j} - \left(\Psi_\ell^{j}\right)^*\Psi_\ell^{j-1}\right]\right\} \\
&= \frac{\hbar^2}{2m\,\Delta r}\sum_{\ell,\,j}\left(\Psi_\ell^{j}\right)^*\left\{r_{j+\frac{1}{2}}^2\left[\Psi_\ell^{j+1} - \Psi_\ell^{j}\right] - r_{j-\frac{1}{2}}^2\left[\Psi_\ell^{j} - \Psi_\ell^{j-1}\right]\right\} \\
&= \frac{\hbar^2}{2m\,\Delta r}\sum_{\ell,\,j}\left(\Psi_\ell^{j}\right)^* r_j^2\left\{\frac{r_{j+\frac{1}{2}}^2}{r_j^2}\left[\Psi_\ell^{j+1} - \Psi_\ell^{j}\right] - \frac{r_{j-\frac{1}{2}}^2}{r_j^2}\left[\Psi_\ell^{j} - \Psi_\ell^{j-1}\right]\right\} \\
\langle\Psi|-\widehat{T_r}|\Psi\rangle &= \frac{\hbar^2}{2m\,\Delta r}\sum_{\ell,\,j}\left(\Psi_\ell^{j}\right)^* r_j^2\left[\frac{r_{j+\frac{1}{2}}^2}{r_j^2}\,\Psi_\ell^{j+1} - \frac{r_{j+\frac{1}{2}}^2 + r_{j-\frac{1}{2}}^2}{r_j^2}\,\Psi_\ell^{j} + \frac{r_{j-\frac{1}{2}}^2}{r_j^2}\,\Psi_\ell^{j-1}\right]
\end{aligned} \tag{2.3.48}$$

We are finally in a position to transform $\Psi_\ell$ to $g_\ell$:

$$\begin{aligned}
\langle\Psi|-\widehat{T_r}|\Psi\rangle &= \frac{\hbar^2}{2m(\Delta r)^2}\,\Delta r \sum_{\ell,\,j}\left(g_\ell^{j}\right)^*\left[r_j\frac{r_{j+\frac{1}{2}}^2}{r_j^2}\,\frac{g_\ell^{j+1}}{r_{j+1}} - \frac{r_{j+\frac{1}{2}}^2 + r_{j-\frac{1}{2}}^2}{r_j^2}\,g_\ell^{j} + r_j\frac{r_{j-\frac{1}{2}}^2}{r_j^2}\,\frac{g_\ell^{j-1}}{r_{j-1}}\right] \\
&= \frac{\hbar^2}{2m(\Delta r)^2}\,\Delta r \sum_{\ell,\,j}\left(g_\ell^{j}\right)^*\left[\frac{r_{j+\frac{1}{2}}^2}{r_j\,r_{j+1}}\,g_\ell^{j+1} - \frac{r_{j+\frac{1}{2}}^2 + r_{j-\frac{1}{2}}^2}{r_j^2}\,g_\ell^{j} + \frac{r_{j-\frac{1}{2}}^2}{r_j\,r_{j-1}}\,g_\ell^{j-1}\right] \\
\langle\Psi|-\widehat{T_r}|\Psi\rangle &= \frac{\hbar^2}{2m(\Delta r)^2}\,\Delta r \sum_{\ell,\,j}\left(g_\ell^{j}\right)^*\left[\alpha_j\,g_\ell^{j+1} - 2\beta_j\,g_\ell^{j} + \alpha_{j-1}\,g_\ell^{j-1}\right]
\end{aligned} \tag{2.3.49}$$

where

$$\alpha_j = \frac{(j+1)^2}{\left(j+\frac{1}{2}\right)\left(j+\frac{3}{2}\right)} = \frac{j^2+2j+1}{j^2+2j+\frac{3}{4}}\,; \qquad \beta_j = \frac{1}{2}\,\frac{(j+1)^2 - j^2}{\left(j+\frac{1}{2}\right)^2} = \frac{2j^2+2j+1}{2j^2+2j+\frac{1}{2}} \tag{2.3.50}$$

We also make a small correction to $\beta_0$ for the $\ell = 0$ manifold, as suggested in [81]:

$$\beta_0 \to \beta_0 + Z\frac{\Delta r}{8\,a_0}\left(1 + Z\frac{\Delta r}{a_0}\right). \tag{2.3.51}$$

This helps get the energies of the low-$n$, $\ell = 0$ states more accurately.

The last term deals with the interaction with the electric field, $\langle\Psi|-\widehat{\mathcal{H}}_I^L|\Psi\rangle$:

$$\langle\Psi|-\widehat{\mathcal{H}}_I^L|\Psi\rangle = -\int_0^\infty r^2\,\mathrm{d}r \int_\Omega \mathrm{d}\Omega\ \Psi^*\,\widehat{\mathcal{H}}_I^L\,\Psi \tag{2.3.52}$$

In the length gauge, the interaction is given by $\widehat{\mathcal{H}}_I^L = q\,\mathcal{E}(t)\,z = q\,\mathcal{E}(t)\,r\cos\theta$:

$$\begin{aligned}
\langle\Psi|-\widehat{\mathcal{H}}_I^L|\Psi\rangle &= -\int_0^\infty r^2\,\mathrm{d}r \int_\Omega \mathrm{d}\Omega\ \Psi^*\,\widehat{\mathcal{H}}_I^L\,\Psi \\
&= -\int_0^\infty r^2\,\mathrm{d}r \int_\Omega \mathrm{d}\Omega\ \Psi^*\,q\,\mathcal{E}(t)\,r\cos\theta\,\Psi \\
&= -q\,\mathcal{E}(t)\int_0^\infty r^2\,\mathrm{d}r \sum_\ell \sum_{\ell'} \int_\Omega \mathrm{d}\Omega\ \Psi_\ell^*\,\langle\ell|\ r\cos\theta\,\Psi_{\ell'}\,\big|\ell'\big\rangle \\
&= -q\,\mathcal{E}(t)\int_0^\infty r^3\,\mathrm{d}r \sum_\ell \sum_{\ell'} \int_\Omega \mathrm{d}\Omega\ \Psi_\ell^*\big[c_{\ell'}\,\big\langle\ell\big|\ell'+1\big\rangle\,\Psi_{\ell'} + c_{\ell'-1}\,\big\langle\ell\big|\ell'-1\big\rangle\,\Psi_{\ell'}\big] \\
&= -q\,\mathcal{E}(t)\int_0^\infty r^3\,\mathrm{d}r \sum_\ell \Psi_\ell^*[c_{\ell-1}\Psi_{\ell-1} + c_\ell\Psi_{\ell+1}] \\
\langle\Psi|-\widehat{\mathcal{H}}_I^L|\Psi\rangle &\approx -q\,\mathcal{E}(t)\,\Delta r \sum_{\ell,\,j} r_j\,g_\ell^*\Big[c_{\ell-1}\,g_{\ell-1}^j + c_\ell\,g_{\ell+1}^j\Big]
\end{aligned} \tag{2.3.53}$$

where

$$c_\ell = \frac{\ell+1}{\sqrt{(2\ell+1)(2\ell+3)}} \qquad\qquad c_{-1} = 0 \tag{2.3.54}$$

is a $3j$ coefficient. This operator is bi-diagonal (zero along the diagonal, nonzero along the first super and sub-diagonals) when acting on a mesh flattened over the $\ell$ index, since the interaction term couples spherical harmonics with angular momentums that differ by one (because the photon carries $\ell = 1$ itself, this is guaranteed by conservation laws).

Combining all of the terms, we have

$$\begin{aligned}\mathcal{L} = &\langle\Psi|i\hbar\frac{\partial}{\partial t}|\Psi\rangle + \langle\Psi|-\widehat{T_r}|\Psi\rangle + \langle\Psi|-\widehat{V}|\Psi\rangle + \langle\Psi|-\widehat{\mathcal{H}}_I^L|\Psi\rangle \\ \mathcal{L} \approx &\Delta r \sum_{\ell,\,j}\left(g_\ell^j\right)^*\left\{i\hbar\frac{\partial g_\ell^j}{\partial t} + \frac{\hbar^2}{2m(\Delta r)^2}\Big[\alpha_j\, g_\ell^{j+1} - 2\beta_j\, g_\ell^j + \alpha_{j-1}\, g_\ell^{j-1}\Big] - V_\ell^j\, g_\ell^j\right. \\ &\left. -q\,\mathcal{E}(t) r_j\Big[c_{\ell-1}\, g_{\ell-1}^j + c_\ell\, g_{\ell+1}^j\Big]\right\} \end{aligned} \tag{2.3.55}$$

If we allow $\left(g_\ell^j\right)^*$ to vary, we get an Euler-Lagrange equation for each $g_\ell^j$:

$$i\hbar\frac{\partial g_\ell^j}{\partial t} = -\frac{\hbar^2}{2m(\Delta r)^2}\Big[\alpha_j\, g_\ell^{j+1} - 2\beta_j\, g_\ell^j + \alpha_{j-1}\, g_\ell^{j-1}\Big] + V_\ell^j\, g_\ell^j + q\,\mathcal{E}(t)\, r_j\,\Big[c_{l-1}\, g_{\ell-1}^j + c_\ell\, g_{\ell+1}^j\Big] \tag{2.3.56}$$

This Lagrangian-based evolution equation is strongly reminiscent of previous versions, but is significantly more accurate. The key difference is that $\alpha_j$ and $\beta_j$ now smoothly encode the boundary behavior at $r = 0$.

#### 2.3.3.2 Split Operator Method

Now that we have a better evolution equation we need to figure out how to use it numerically. We can use a split-operator algorithm (see Appendix E), with

$$\begin{aligned}\Psi(t+\Delta t) &= e^{-i\widehat{\mathcal{H}}(t)\,\Delta t/\hbar}\,\Psi(t) \\ &= e^{-i\left(\widehat{H_r}+\widehat{H_I^L}(t)\right)\Delta t/\hbar}\,\Psi(t) \\ \Psi(t+\Delta t) &\approx e^{-i\widehat{H_I^L}(t)\,\Delta t/2\hbar}\, e^{-i\widehat{H_r}\,\Delta t/\hbar}\, e^{-i\widehat{H_I^L}(t)\,\Delta t/2\hbar}\,\Psi(t)\end{aligned} \tag{2.3.57}$$

where

$$\widehat{H_r} = -\frac{\hbar^2}{2m(\Delta r)^2}\Big[\alpha_j\, g_\ell^{j+1} - 2\beta_j\, g_\ell^j + \alpha_{j-1}\, g_\ell^{j-1}\Big] + V_\ell^j\, g_\ell^j \tag{2.3.58a}$$

$$\widehat{H_I^L} = q\,\mathcal{E}(t)\, r_j\,\Big[c_\ell\, g_{\ell+1}^j + c_{l-1}\, g_{\ell-1}^j\Big] \tag{2.3.58b}$$

The propagation caused by the position-indexed Hamiltonian $\widehat{H_r}$ will be done using the same Crank-Nicholson form used previously, namely

$$e^{-i\widehat{H_r}\,\Delta t/\hbar} \approx \left[1 + i\widehat{H_r}\,\frac{\Delta t}{2}\right]^{-1}\left[1 - i\widehat{H_r}\,\frac{\Delta t}{2}\right] \tag{2.3.59}$$

This operator is tridiagonal (since it contains the kinetic energy derivatives) when acting on a mesh unwrapped over the $r$-index, so the tridiagonal matrix algorithm (see Appendix D) can be used to calculate multiplication by the first term quickly. The second term is simply sparse matrix multiplication and requires no special treatment.

The angular-momentum-indexed Hamiltonian $\widehat{H_I^L}$ could also be dealt with using the Crank-Nicholson form, but there's a more accurate way. In particular, note that the matrix form of $\widehat{H_I^L}$

can be constructed from the sum of two block-diagonal matrices:

$$\widehat{H_I^L} = \begin{bmatrix} 0 & a_0 & & & & & \\ a_0 & 0 & a_1 & & & & \\ & a_1 & 0 & a_2 & & & \\ & & a_2 & 0 & a_3 & & \\ & & & a_3 & 0 & a_4 & \\ & & & & a_4 & 0 & \ddots \\ & & & & & \ddots & \ddots \end{bmatrix}$$

$$-i\,\widehat{H_I^L} = -i \left\{ \begin{bmatrix} \boxed{\begin{matrix} 0 & a_0 \\ a_0 & 0 \end{matrix}} & & & & & \\ & 0 & \boxed{\begin{matrix} 0 & a_2 \\ a_2 & 0 \end{matrix}} & & & \\ & & 0 & \boxed{\begin{matrix} 0 & a_4 \\ a_4 & 0 \end{matrix}} & & \\ & & & 0 & \ddots & \\ & & & & \ddots & \ddots \end{bmatrix} + \begin{bmatrix} 0 & 0 & & & & \\ 0 & \boxed{\begin{matrix} 0 & a_1 \\ a_1 & 0 \end{matrix}} & 0 & & & \\ & 0 & \boxed{\begin{matrix} 0 & a_3 \\ a_3 & 0 \end{matrix}} & 0 & & \\ & & 0 & 0 & \ddots & \\ & & & \ddots & \ddots & \end{bmatrix} \right\} \tag{2.3.60}$$

where $a_\ell = q\,\mathcal{E}(t)\,c_\ell\,r_j\,\Delta t/2\hbar$ (note the implicit $j$-index dependence, which must be accounted for when actually constructing the matrix). Call the first matrix $\widehat{H_e}$ (even) and the second $\widehat{H_o}$ (odd). Each of these block-diagonal matrices can be exponentiated efficiently using

$$\exp\left\{ -i \begin{bmatrix} 0 & a \\ a & 0 \end{bmatrix} \right\} = \begin{bmatrix} \cos a & -i\,\sin a \\ -i\,\sin a & \cos a \end{bmatrix} \tag{2.3.61}$$

Neglecting the extra terms in the Baker-Campbell-Hausdorff formula for expanding an exponentiated operator (which will contribute to the error), we have a final evolution propagator given

by

$$\Psi(t+\Delta t) \approx e^{-i\widehat{H_e}}\, e^{-i\widehat{H_o}} \left[1 + i\widehat{H_r}\,\frac{\Delta t}{2}\right]^{-1} \left[1 - i\widehat{H_r}\,\frac{\Delta t}{2}\right] e^{-i\widehat{H_o}}\, e^{-i\widehat{H_e}}\, \Psi(t) \tag{2.3.62}$$

This evolution algorithm does require more steps to evaluate than the evolution methods for the previous methods do, but it more than makes up for it in stability and accuracy. It is the one that we chose to use in practice for all of our TDSE simulations. The other contender was the velocity-gauge version of this method. We discuss that method in detail, as well as why we chose not to use it, in Appendix F.

#### 2.3.3.3 Radial Probability Current

The radial probability current $J_r$ is defined as

$$\begin{aligned} J_r &= \frac{\hbar}{2mi}\left(\Psi^* \frac{\partial \Psi}{\partial r} - \Psi \frac{\partial \Psi *}{\partial r}\right) \\ J_r &= \frac{\hbar}{m}\ \mathrm{Im}\left\{\Psi^* \frac{\partial \Psi}{\partial r}\right\} \end{aligned} \tag{2.3.63}$$

Our goal is to find a discrete matrix operator so that we can calculate this value efficiently on the mesh. We transform to $g_r^\theta$ and use a centered difference on the derivative, yielding

$$\begin{aligned} (J_r)_j^\theta &= \frac{\hbar}{m}\ \mathrm{Im}\left\{\frac{\left(g_j^\theta\right)^*}{r_j}\left[\frac{g_{j+1}^\theta}{r_{j+1}} - \frac{g_{j-1}^\theta}{r_{j-1}}\right]/(2\,\Delta r)\right\} \\ (J_r)_j^\theta &= \frac{\hbar}{2m\,\Delta r^3}\ \mathrm{Im}\left\{\frac{\left(g_j^\theta\right)^*}{j+\frac{1}{2}}\left[\frac{g_{j+1}^\theta}{j+\frac{3}{2}} - \frac{g_{j-1}^\theta}{j-\frac{1}{2}}\right]\right\} \end{aligned} \tag{2.3.64}$$

We can write this operation as a matrix operator:

$$(J_r)_j^\theta = \frac{\hbar}{2m\,\Delta r^3}\ \mathrm{Im}\left\{ \left(g_j^\theta\right)^* \begin{bmatrix} 0 & \gamma_1 & 0 & 0 & \ddots \\ -\gamma_1 & 0 & \gamma_2 & 0 & \ddots \\ 0 & -\gamma_2 & 0 & \gamma_3 & \ddots \\ 0 & 0 & -\gamma_3 & 0 & \ddots \\ \ddots & \ddots & \ddots & \ddots & \ddots \end{bmatrix} g_j^\theta \right\} \tag{2.3.65}$$

where the $g_j^\theta$ is flattened along $j$ and $\gamma_j = 1/\left(j^2 - 1/4\right)$. A typical use case is to sum over $\theta$ to find the total probability flux at each radius.

#### 2.3.3.4 Plane Wave Overlaps

It's fairly easy to represent plane waves on and therefore perform overlaps with spherical plane waves on previous mesh types because both mesh coordinates were physical, making it simple to evaluate the dot product $\mathbf{k}\cdot\mathbf{r}$. To do the same with the spherical harmonic mesh we need to represent the plane waves in the spherical harmonic basis. This can be accomplished via the spherical harmonic addition formula, which tells us that

$$\begin{aligned} \phi_{\mathbf{k}}(\mathbf{r}) &= \frac{\exp(i\,\mathbf{k}\cdot\mathbf{r})}{(2\pi)^{3/2}} \\ \phi_{\mathbf{k}}(\mathbf{r}) &= \sqrt{\frac{2}{\pi}} \sum_{\ell=0}^{\infty} \sum_{m=-\ell}^{\ell} i^\ell\, j_\ell(kr) \left(Y_\ell^m(\hat{\mathbf{k}})\right)^* Y_\ell^m(\hat{\mathbf{r}}) \end{aligned} \tag{2.3.66}$$

where $j_\ell$ is a spherical Bessel function and $Y_\ell^m(\hat{\mathbf{a}})$ means "evaluate $Y_\ell^m$ at $(\theta,\phi)$ in the direction of $\hat{\mathbf{a}}$".

We can use this to determine the overlap between a plane wave and a generic state $\Psi(r,\theta,\phi)$. Due to the number of terms to keep track of it is convenient to build up the inner product in stages. First, let's just look at the product of the two wavefunctions, which is what we'll need to integrate

over all space to get the inner product:

$$\Psi(\mathbf{r},t) = \sum_{\ell=0}^{\infty}\sum_{m=-\ell}^{\ell} \psi_{\ell,m}(r,t)\, Y_\ell^m(\hat{\mathbf{r}})$$

$$\phi_{\mathbf{k}}^*(\mathbf{r})\,\Psi(\mathbf{r},t) = \left(\sqrt{\frac{2}{\pi}}\sum_{\ell'=0}^{\infty}\sum_{m'=-\ell'}^{\ell'} i^{\ell'}\, j_{\ell'}(kr)\left(Y_\ell^m(\hat{\mathbf{k}})\right)^* Y_{\ell'}^{m'}(\hat{\mathbf{r}})\right)^* \left(\sum_{\ell=0}^{\infty}\sum_{m=-\ell}^{\ell} \psi_{\ell,m}(r,t)\, Y_\ell^m(\hat{\mathbf{r}})\right)$$

$$\phi_{\mathbf{k}}^*(\mathbf{r})\,\Psi(\mathbf{r},t) = \sqrt{\frac{2}{\pi}}\sum_{\ell'=0}^{\infty}\sum_{\ell=0}^{\infty}\sum_{m'=-\ell'}^{\ell'}\sum_{m=-\ell}^{\ell} (-i)^{\ell'}\, j_{\ell'}(kr)\,\psi_{\ell,m}(r,t)\, Y_{\ell'}^{m'}(\hat{\mathbf{k}})\left(Y_{\ell'}^{m'}(\hat{\mathbf{r}})\right)^* Y_\ell^m(\hat{\mathbf{r}}) \quad (2.3.67)$$

Integrating over angles will collapse the pairs of $\ell$ and $m$ sums into single sums because of the orthogonality between the last two terms on the right, which are the only terms that the integral will actually hit:

$$\begin{aligned}\int_\Omega \phi_{\mathbf{k}}^*(\mathbf{r})\,\Psi(\mathbf{r},t)\;\mathrm{d}\Omega &= \sqrt{\frac{2}{\pi}}\sum_{\ell'=0}^{\infty}\sum_{\ell=0}^{\infty}\sum_{m'=-\ell'}^{\ell'}\sum_{m=-\ell}^{\ell} (-i)^{\ell'}\, j_{\ell'}(kr)\,\psi_{\ell,m}(r,t)\, Y_{\ell'}^{m'}(\hat{\mathbf{k}}) \\ &\qquad \times \int_\Omega \left(Y_{\ell'}^{m'}(\hat{\mathbf{r}})\right)^* Y_\ell^m(\hat{\mathbf{r}})\;\mathrm{d}\Omega \\ \int_\Omega \phi_{\mathbf{k}}^*(\mathbf{r})\,\Psi(\mathbf{r},t)\;\mathrm{d}\Omega &= \sqrt{\frac{2}{\pi}}\sum_{\ell=0}^{\infty}\sum_{m=-\ell}^{\ell} (-i)^{\ell}\, j_{\ell}(kr)\,\psi_{\ell,m}(r,t)\, Y_{\ell}^{m}(\hat{\mathbf{k}}) \end{aligned} \quad (2.3.68)$$

Now we perform the radial integration:

$$\begin{aligned}\int_0^\infty\int_\Omega \phi_{\mathbf{k}}^*(\mathbf{r})\,\Psi(\mathbf{r},t)\,r^2\,\mathrm{d}r\,\mathrm{d}\Omega &= \sqrt{\frac{2}{\pi}}\sum_{\ell=0}^{\infty}\sum_{m=-\ell}^{\ell} (-i)^{\ell}\, Y_\ell^m(\hat{\mathbf{k}})\int_0^\infty j_\ell(kr)\,\psi_{\ell,m}(r,t)\,r^2\,\mathrm{d}r \\ \langle\phi_k|\Psi(t)\rangle &= \sqrt{\frac{2}{\pi}}\sum_{\ell=0}^{\infty}\sum_{m=-\ell}^{\ell} (-i)^{\ell}\, Y_\ell^m(\hat{\mathbf{k}})\int_0^\infty [r\,j_\ell(kr)]\,g_{\ell,m}(r,t)\,\mathrm{d}r \end{aligned} \quad (2.3.69)$$

where $g_{\ell,m} = r\,\psi_{\ell,m}$. The combination $r\,j_\ell$ can be identified as the same kind of transformation, although there's no particular symbol for it. If we assume that $\Psi(t)$ has no $m$ components, the inner product can be simplified further:

$$\langle\phi_{\mathbf{k}}|\Psi(t)\rangle = \sqrt{\frac{2}{\pi}}\sum_{\ell=0}^{\infty}(-i)^{\ell}\, Y_\ell^0(\hat{\mathbf{k}})\int_0^\infty [r\,j_\ell(kr)]\,g_\ell(r,t)\,\mathrm{d}r\,. \quad (2.3.70)$$

Finally, discretize the integral:

$$\langle \phi_{\mathbf{k}} | \Psi(t) \rangle \approx \sqrt{\frac{2}{\pi}}\, \Delta r \sum_{\ell=0}^{\ell_{\max}} \sum_{j=0}^{N_r - 1} (-i)^{\ell}\, Y_{\ell}^{0}(\hat{\mathbf{k}})\, [r_j\, j_{\ell}(k r_j)]\, g_{\ell}^{j}(t) \tag{2.3.71}$$

If performing a large number of these overlaps it is highly recommended to memoize the results of $j_\ell(kr_j)$ and $Y_\ell^0(\hat{\mathbf{k}})$. Note that since the plane waves are a complete basis by themselves, the inner product calculated above includes the contributions of any part of the wavefunction that is in a bound state. To get only the free-state overlap, the bound states must be removed from $g$ by the simple substitution

$$g(t) \to g(t) - \sum_{n,\ell} g_{n,\ell}\, \langle g_{n,\ell} | g(t) \rangle \tag{2.3.72}$$

Unfortunately, the overlaps above have a serious drawback: although they correctly characterize the *current* state of the system, they do not necessarily characterize the state of the system *at the detector*. Since the Coulomb interaction has infinite range the plane waves are not momentum eigenstates and their wavenumber at any given time is not the wavenumber they will arrive at the detector with. To get around this we must first overlap the wavefunction with Coulomb states, which are the positive-energy (i.e., unbound) eigenstates of the Coulomb potential. As $r \to \infty$ (i.e., at the detector) the Coulomb states go over to plane waves with a Coulomb phase shift $\delta_\ell(k)$, so the correct transition amplitude to a plane wave with wavenumber $k$ and angle relative to the electric field polarization vector $\theta$ is [82]

$$\langle \phi_{\mathbf{k}} | \Psi(t) \rangle = \frac{1}{\sqrt{4\pi k}} \sum_{\ell} e^{i\delta_\ell(k)} \sqrt{2\ell + 1}\, P_\ell(\cos\theta)\ \langle g_{k,\ell} | g(t) \rangle \tag{2.3.73}$$

### 2.3.4 Numerical Eigenbasis

An important consideration when treating the problem using linear algebra is that the matrix operators have certain eigenvectors and eigenvalues on the flattened mesh. These eigenvectors ("numerical eigenstates"), not the analytic eigenstate wavefunctions evaluated on the mesh, are the true basis for the system. There are several methods for finding these numerical eigenstates, which will be discussed later in this section.

Before diving in to the methods, we should consider the implications of these numerical eigenstates. For example, one concerning thought is that the analytic hydrogen Hamiltonian's spectrum has a discrete but infinite set of bound states as well as an infinite continuum of unbound states. The discrete hydrogen Hamiltonian's spectrum is discrete and finite: it has exactly as many eigenstates as the total number of mesh points. Since that number is generally very large (several million), it is not practical to find all of the numerical eigenstates for a given mesh and static potential.

For bound states, a rough cutoff criteria is that the grid only has a numerical eigenstate of energy $E_n$ if the corresponding wavefunction's nodes are all inside the mesh. As $n$ grows $\psi_{n,\ell,m}$ has nodes further and further from $r = 0$, and if these nodes (or their nearby anti-nodes) appear too close or beyond the mesh boundary the mesh wouldn't be able to give them a sensible eigenenergy. Occasionally a high-$n$ bound state will happen to have a node near the mesh boundary. In this case a numerical eigenstate with similar shape and energy can appear on the mesh.

Some of these numerical eigenenergies may be degenerate, although in practice it is exceedingly rare. For example, on a $100\,a_0$ mesh with $0.25\,a_0$ spacing, the numerical eigenstates for $|\psi_{2,0,0}\rangle$ and $|\psi_{2,1,0}\rangle$ have eigenenergies of $-3.4000\,\text{eV}$ and $-3.3995\,\text{eV}$ respectively, while the analytic eigenenergy for both is roughly $-3.4014\,\text{eV}$.

#### 2.3.4.1 Imaginary Time Evolution

Imaginary time evolution is a simple way to find the ground state eigenvector. We begin the system in some arbitrary initial guess state (ideally close to the ground state, perhaps by using the analytic ground state evaluated on the mesh). By evolving the system in imaginary time $t = -i\tau$, we convert the normal evolution operator $e^{-i\widehat{\mathcal{H}}t/\hbar}$ to

$$\begin{aligned} e^{-i\widehat{\mathcal{H}}t/\hbar} &= e^{-i\widehat{\mathcal{H}}(-i\tau)/\hbar} \\ &= e^{-\widehat{\mathcal{H}}\tau/\hbar} \end{aligned} \tag{2.3.74}$$

This forces an exponential decay or growth (depending on the sign of the eigenvalues of $\widehat{\mathcal{H}}$) on the system for each numerical eigenstate separately. The numerical eigenstate with the most negative eigenvalue (i.e., the numerical ground state) will grow the fastest, so after a few time steps you simply normalize the wavefunction and call that the numerical ground state. After

finding the ground state you can then generate the other numerical eigenstates via Gram-Schmidt orthogonalization or diagonalization of the state overlap matrix [83].

#### 2.3.4.2 Inverse Power Method

A more flexible method of finding numerical eigenstates is to begin with an arbitrary initial guess state and repeatedly apply the matrix $(H - EI)^{-1}$ to it. The result will converge to the numerical eigenstate with the closest eigenvalue to $E$ [83]. This is the "inverse" of the normal **power method**, which finds the eigenvector with largest eigenvalue of a matrix $A$ by repeatedly multiplying a test vector $v$ by $A$. That is,

$$\begin{aligned} v_{\lambda_{\max}} &= \lim_{n\to\infty} A^n u \\ v_{\lambda_{\max}} &\approx A^n u \qquad n \gg 1. \end{aligned} \tag{2.3.75}$$

To see how the inverse power method works, note that the eigenvectors of $A$ and $(A - \mu I)^{-1}$ are the same (for arbitrary constant $\mu$), since

$$\begin{aligned} Av_{\lambda_i} &= \lambda_i v_{\lambda_i} \\ (A - \mu I)v_{\lambda_i} &= (\lambda_i - \mu)v_{\lambda_i} \\ (\lambda_i - \mu)^{-1}v_{\lambda_i} &= (A - \mu I)^{-1}v_{\lambda_i} \end{aligned} \tag{2.3.76}$$

Therefore, if we call $(A - \mu I)^{-1} = B$, $B^n u$ will converge to the $v_{\lambda_i}$ with the largest $\left|(\lambda_i - \mu)^{-1}\right|$. The largest of those is the one where $\lambda_i - \mu$ is closest to zero, which is the $\lambda_i$ closest to $\mu$.

Unfortunately it's not immediately obvious how to do this efficiently in higher than 1D for our discretized Hamiltonians. In 1D the discrete Hamiltonian is typically tri-diagonal and the result of multiplying by its inverse can be computed efficiently. In 2D the discrete Hamiltonian has non-zero elements along extra diagonals far from the main diagonal, and the problem would be even worse in higher dimensions. Even with sparse matrix techniques these inverses would be hard to calculate, because the inverse of a sparse matrix is not necessarily sparse. Worse, even if we did all of this, it would be very difficult to distinguish between numeric eigenvectors with degenerate eigenvalues.

However, for the spherical harmonic mesh (see 2.3.3), we get lucky. The field-free radial Hamil-

tonian is block-diagonal in the $\ell$ coordinate, so we can break the full-mesh Hamiltonian into tridiagonal blocks for each spherical harmonic. The field-free angular Hamiltonian is zero, so we don't have to include it in the calculations. The inverse power method can be used on each subspace individually to generate numerical eigenvectors for that spherical harmonic. This is significantly more efficient than using the full-mesh Hamiltonian because the matrix is smaller by a factor of $\ell_{\max}$ in both dimensions. As an added benefit, we don't see any mixing between eigenstates with eigenenergies degenerate over their $\ell$ quantum number, because they belong to different subspaces.

You might be thinking: if we know how to find a single eigenstate and eigenvalue with this method, why don't we just scan through possible eigenvalues and solve the entire eigensystem? You're absolutely right, and someone did it already: the Lanczos algorithm is an iterative procedure for finding a given number of numeric eigenvectors and eigenvalues of a matrix [84]. We use the Lanczos algorithm in our simulations to find a suitable basis and initial state. We have also implemented the first step of imaginary time evolution, so we can find the numeric ground state via that method, but not perform the subsequence orthogonalization procedure that would yield more eigenvectors.

## 2.4 Ionization of Hydrogen by Intense Sub-Cycle Pulses

Now that we've laid the foundations, we can discuss the details and results of our recent investigations. To review: the physical system we are interested in is a hydrogen atom interacting with a sub-femtosecond, sub-cycle, linearly-polarized laser pulse. We have the tools to numerically simulate the effects of this laser pulse.

Using these tools, we looked at a wide variety of possibly-interesting questions, but ended up finding interesting (and counterintuitive) behavior in the ionization probability when the pulse width is close to the classical orbit time. Surprisingly, we find that pulses with sine-like shapes can have greater ionization probabilities than cosine-like pulses that have the same power spectrum. This result is the opposite of what is expected from an intuitive tunneling-like model, which would predict that the pulses with the largest electric field amplitudes would ionize more than pulses with smaller amplitudes. It also known that the carrier-envelope phase has a negligible effect on the final ionization probability for many-cycle pulses [85], so this effect must only occur when the pulse

contains very few cycles.

To develop this idea, we represent the electric field in carrier-envelope form (see 2.1.4) with an additional window function,

$$\mathcal{E}(t) = W_\tau(t)[\mathcal{E}_0\, F_\tau(t)\, \cos(\omega_c\, t + \varphi) + \mathcal{E}_c] \tag{2.4.1}$$

where $\mathcal{E}_0$ is an amplitude prefactor, $\tau$ is the pulse width, $F_\tau$ is an envelope function, $W_\tau$ is a window function, $\omega_c$ is the carrier frequency, $\varphi$ is the carrier-envelope phase (CEP), $\mathcal{E}_c$ is the DC correction field amplitude.

The CEP $\varphi$ is what determines the shape of the pulse. We describe $\varphi = 0$ pulses as "cosine-like" and $\varphi = \pi/2$ pulses as "sine-like" based on their behaviors near $t = 0$, which are similar to envelope-less cosine or sine waves, respectively. For the same power spectrum (and therefore the same fluence) a cosine-like pulse has a peak electric field approximately $\sqrt{2}$ times larger than the sine-like pulse.

We choose to use a sinc-shaped envelope, $\mathrm{sinc}(x) \equiv \sin(x)/x$, because its Fourier transform has constant power over its bandwidth, like an ideal supercontinuum source. Specifically, we use $F_\tau(t) = \mathrm{sinc}(\pi\, t/\tau)$. This envelope has zeros at $t = n\,\tau$, $n = \pm 1, \pm 2, \cdots$, and $\tau$ is the inverse of the cyclic frequency bandwidth of the pulse. We set a small fixed minimum frequency for the spectrum so that the pulse shape is nearly constant as we change $\tau$. For the pulses discussed here, $\omega_{\min} = 2\pi \times 30\,\mathrm{THz}$ (a wavelength of $\lambda \approx 10\,\mu\mathrm{m}$), so that $\omega_c = \omega_{\min} + \pi/\tau$. For more details on sinc pulses, see Section 2.1.4.1.

The window function cuts the electric field off with a logistic rise/decay:

$$W_\tau(t) = \frac{1}{1 + \exp(-(t + t_w)/t_d)} - \frac{1}{1 + \exp(-(t - t_w)/t_d)} \tag{2.4.2}$$

Typical parameters are $t_w = 30\,\tau$ and $t_d = \tau/5$. The window decreases the numeric fluence of the pulses compared to the analytic value by at most a few tenths of a percent. It also introduces Gibbs ringing at the edges of the spectrum.

To correct for the introduction of a zero-frequency electric field component that is caused by windowing when $\varphi \neq \pi/2$, we add a small constant electric field $\mathcal{E}_c$ that shares the same window

function as the pulse, with an amplitude numerically chosen so that $\int_{t_i}^{t_f} dt\, \mathcal{E}(t) = 0$. This correction also causes small changes in the low-frequency components of the electric field. Combined, these effects cause perturbations in the ionization probability (compared to a simulation with infinite time bounds and no window) on the level of $\sim 0.5\%$ (verified by simulations with longer time bounds and without DC correction, or with fluence correction), which, as we will see, is insignificant compared to the large variations caused by changing the CEP. See Section 2.1.5 for more details on how we do these corrections.

### 2.4.1 Numerical TDSE Results

Pulse width scans showing the initial state overlap after interacting with a laser pulse for various fluences and CEPs are shown in Fig. 2.5.

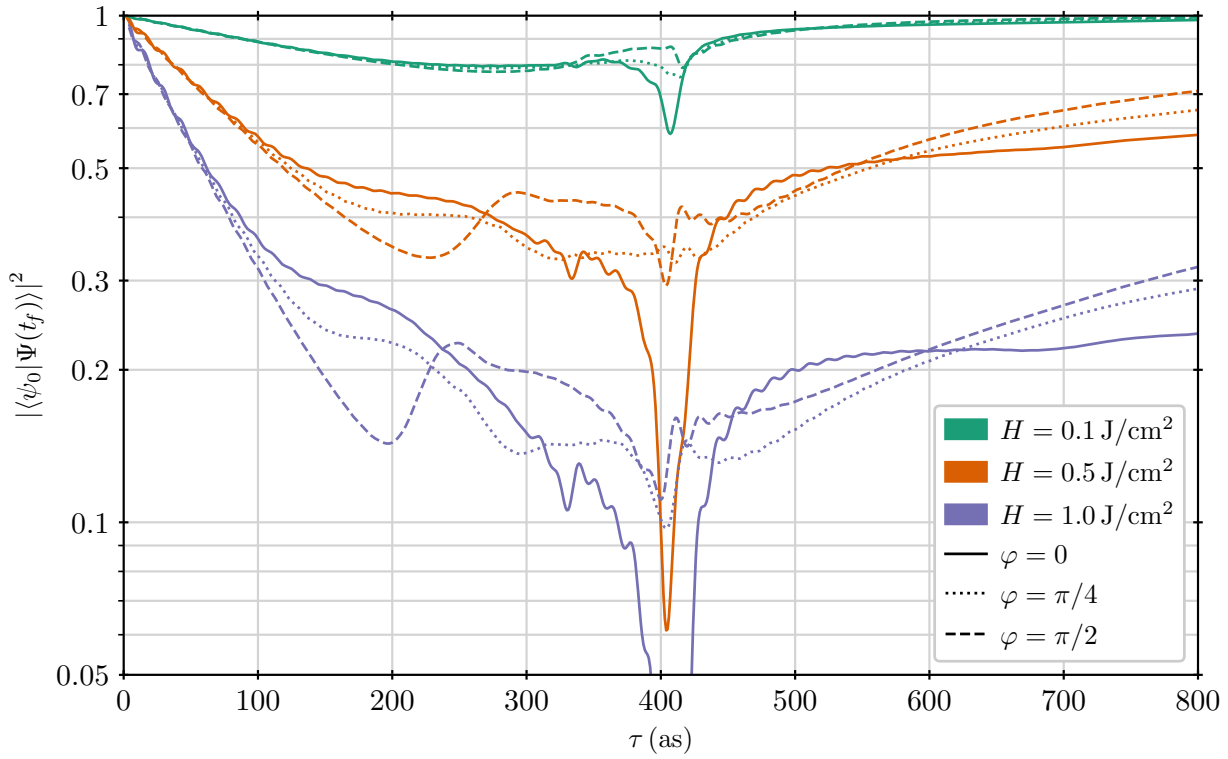


Figure 2.5: The population remaining in the initial $1s$ state of hydrogen after interacting with a laser pulse as the pulse width $\tau$ is varied for three different carrier-envelope phases $\varphi$. As the pulse width becomes comparable to the classical orbital period of the initial hydrogen ground state ($T_{cl} \approx 150$ as) the sine-like pulse ($\varphi = \pi/2$) ionizes much more than the cosine-like pulse ($\varphi = 0$), even though its peak electric field amplitude is lower by a factor of approximately $\sqrt{2}$.

Note that because we keep the pulse's fluences fixed their bandwidths become very broad

(hundreds of eV) and their electric fields become very large (tens of atomic electric fields) at short pulse widths. We expect our simulations to be less accurate in this regime since we neglect relativistic effects and spatial variation of the electric field. As a conservative limit, we cut the curves and heatmap off when the peak electric field of the cosine-like pulse reaches three atomic electric fields. Also note the large perturbations to the otherwise-smooth curves near $\tau \approx 400\,\text{as}$. This seems to be caused by the first inclusion of 10.4 eV photons to the pulse's spectrum, which allow single-photon transitions from the $1s$ ground state to the excited bound state $2p$. Unlike the rest of the scan, the simulations near this pulse width are quite sensitive to the perturbations of the pulse spectrum caused by windowing. We do not attempt to describe the behavior near $\tau \approx 400\,\text{as}$ in the following discussion.

We are primarily concerned with the strong CEP-dependence of the ionization probability at short pulse widths, comparable to the classical orbit time of the hydrogen ground state ($T_{\text{cl}} \approx 150\,\text{as}$). That such a dependence exists is not inherently surprising. For example, at longer pulse widths ($\tau \approx 1\,\text{fs}$), cosine-like pulses ionize more than sine-like pulses. This is what we should expect from electric field amplitudes below the barrier-suppression regime: the dominant ionization mechanism is tunneling, and therefore the dominant dependence of the ionization is on the maximum electric field amplitude [72]. Since the maximum electric field amplitude is larger for a cosine-like pulse than a sine-like pulse, the cosine-like pulse ionizes more. However, at pulse widths comparable to the classical orbit time, we see exactly the opposite behavior over a continuous range of pulse widths and fluences: sine-like pulses consistently ionize more than cosine-like pulses. Our intuition about how instantaneous field amplitude relates to final ionization probability is not correct when the pulse is extremely short and has very high amplitude (large enough to be in the barrier-suppression regime instead of the tunneling regime).

### 2.4.2 A Simple Model

To investigate why the CEP-dependence at short pulse widths develops, and in particular why the sine-like pulses ionize more than the cosine-like pulses do, despite having lower amplitudes, we developed a simple description of the nonlinear strong-field interaction at these timescales. In this section we will briefly describe the derivation and show how the resulting model produces qualitatively similar result to the full TDSE simulations. The next sections, 2.5 and 2.6, will cover

the full details of the derivation and possible paths to take in the future, respectively.

Consider a system with a single bound state produced by a field-free Hamiltonian $\widehat{\mathcal{H}}_0$ that interacts with a linearly-polarized external electric field $\mathcal{E}(t)$, calculated in the length gauge, $\widehat{\mathcal{H}}_I = -q\,\mathcal{E}(t)\,\widehat{z}$. We expand the wavefunction as

$$|\Psi(t)\rangle = c_b(t)\;|b\rangle + \int_0^\infty dk \sum_{\ell,|m|\leq\ell} c_{k\ell m}(t)\;|k\ell m\rangle \tag{2.4.3}$$

where $|b\rangle$ is the ket of the bound state, $|k\ell m\rangle$ is the ket of a delta-normalized (in wavenumber) continuum state labeled by free-space wavenumber $k$ and angular momentum quantum numbers $\ell$ and $m$, and $c_b(t)$ and $c_{k\ell m}(t)$ are the probability amplitudes for the bound and continuum states respectively.

If we plug (2.4.3) into the TDSE, take the inner product with $\langle b|$ or $\langle k\ell m|$, and make the SFA, we get a set of coupled ordinary differential equations (written without explicit time dependences here for compactness):

$$\dot{c}_b = -\,i\omega_b\,c_b + i\frac{q}{\hbar}\,\mathcal{E}\sum_{\ell,|m|\leq\ell}\int_0^\infty dk\,c_{k\ell m}\,\langle b|\,\widehat{z}\,|k\ell m\rangle \tag{2.4.4a}$$

$$\begin{aligned}\dot{c}_{k\ell m} = &-\,i\omega_{k\ell m}\,c_{k\ell m} + i\frac{q}{\hbar}\,\mathcal{E}\,c_b\;\langle k\ell m|\,\widehat{z}\,|b\rangle \\ &+ i\frac{q}{\hbar}\,\mathcal{E}\sum_{\ell,|m|\leq\ell}\int_0^\infty dk'\,c_{k'\ell'm'}\,\langle k\ell m|\,\widehat{z}\,\big|k'\ell'm'\big\rangle\end{aligned} \tag{2.4.4b}$$

where $\omega_b = E_b/\hbar$ and $\omega_{k\ell m} = E_{k\ell m}/\hbar$ are the angular frequencies of the bound and continuum states respectively. The last term in (2.4.4b) is the direct continuum-continuum coupling. There has been much discussion of ways to treat this interaction due to its importance in HHG [86–90]. In this discussion we will neglect it entirely and formally integrate the rest of (2.4.4b), yielding

$$c_{k\ell m}(t) = -i\frac{q}{\hbar}\,\langle k\ell m|\,\widehat{z}\,|b\rangle\int_{t_i}^t dt'\,c_b(t')\,\mathcal{E}(t')\,e^{-i\omega_{k\ell m}(t-t')} \tag{2.4.5}$$

where $t_i$ is the initial time, $c_b(t_i) = 1$, and we take the limit $t_i \to -\infty$. Neglecting the continuum-continuum interaction seems to be a reasonable approximation for the ultra-short timescales we are considering (at least for investigating the source of the CEP-dependence reversal, as we will see).

Plugging (2.4.5) back in to (2.4.4a) results in a single integro-differential equation:

$$\dot{b}(t) = -\frac{q^2}{\hbar^2}\,\mathcal{E}(t)\int_{-\infty}^{t} dt'\, b(t')\,\mathcal{E}(t')\,K_b(t-t') \tag{2.4.6}$$

where $b(t) = c_b(t)\exp(i\omega_b t)$, and

$$K_b(t-t') = \sum_{\ell,|m|\leq\ell}\int_0^\infty dk\,|\langle k\ell m|\,\widehat{z}\,|b\rangle|^2\,e^{-i\,(\omega_{k\ell m}-\omega_b)\,(t-t')} \tag{2.4.7}$$

is the kernel function. We use this integro-differential equation (IDE) to analyze the behavior of the hydrogen atom, keeping in mind that it only describes coherent transitions between a single bound state and the continuum states that it can directly transition to, and that it ignores tunneling-like effects.

### 2.4.3 Comparison of TDSE and IDE

To compare the IDE to the TDSE we numerically integrate the IDE with an approximate kernel. The bound state is the analytic hydrogen ground state, but the continuum states are approximated by wavenumber-delta-normalized spherical partial waves, $\phi_{k\ell m}(r,\theta,\phi) \approx \sqrt{2/\pi}\,k\,j_\ell(kr)\,Y_\ell^m(\theta,\phi)$, where $k$ is the free-space wavenumber and $j_\ell$ is the spherical Bessel function with index $\ell$. The resulting kernel, normalized by $K_b(0) = a_0^2$ (the Bohr radius squared) is shown in Fig. 2.6.

We numerically integrate the IDE using a fixed-time-step fourth-order Runge-Kutta algorithm (RK4) with $\Delta t \approx 1\,\text{as}$. To check the accuracy of this method we compared it a general iterative algorithm for solving IDEs [1, 91]. Both algorithms converged to the same results. We also tried using an RK4 algorithm with adaptive step size, but found no particular advantages in computational accuracy or time [92].

Pulse width scans calculated using the IDE are shown in Fig. 2.7, where they are compared to TDSE simulation scans. The IDE ionization probabilities do not have as much structure as those calculated using the TDSE, and don't predict any significant ionization when the pulse amplitudes become small as the pulse width increases at constant fluence. Nevertheless, the IDE scans display qualitatively similar features to the short-pulse-width regime of the TDSE scans: they predict that the ionization probability has a reversed CEP-dependence when the pulse width becomes

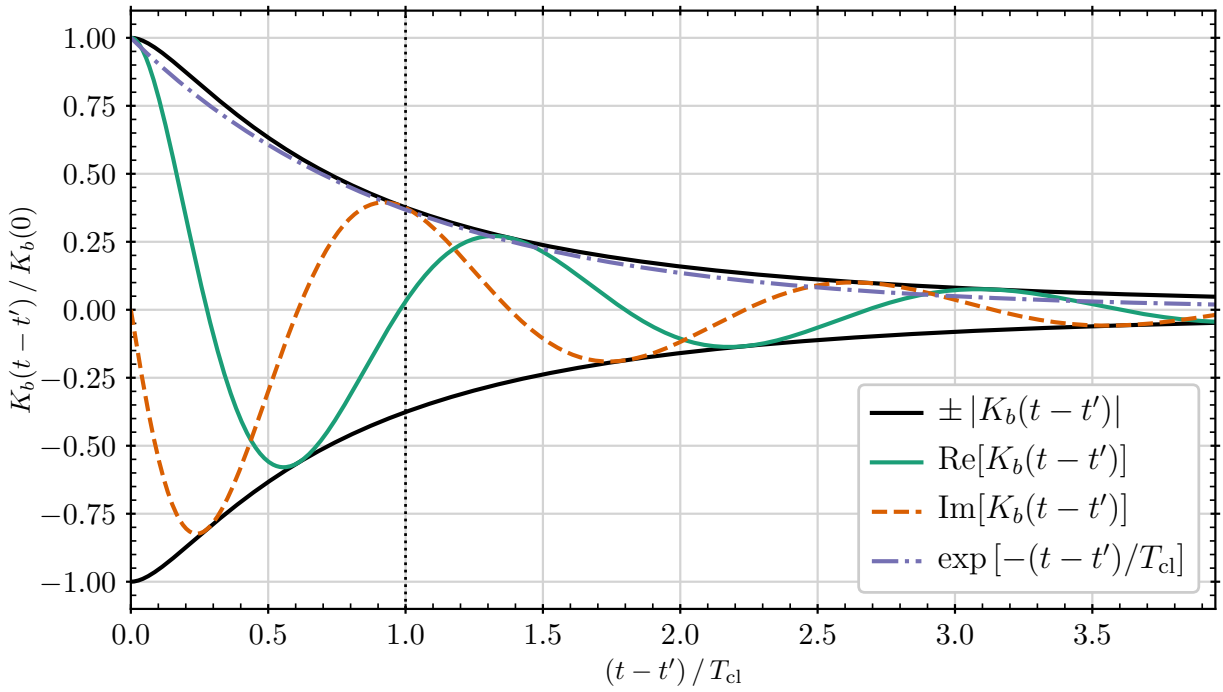


Figure 2.6: The approximate kernel function $K_b(t-t')$ of the hydrogen ground state, calculated using delta-normalized spherical partial waves $\phi_{k\ell m}(r,\theta,\phi) \approx \sqrt{2/\pi}\,k\,j_\ell(k\,r)\,Y_\ell^m(\theta,\phi)$, where $k$ is the free-space wavenumber and $j_\ell$ is the spherical Bessel function with index $\ell$, as the continuum states. The kernel has been normalized by $K_b(0) = a_0^2$, the Bohr radius squared. The timescale of the kernel is close to the classical orbit period of the ground state, $T_{\mathrm{cl}} \approx 150\,\mathrm{as}$ (vertical black dotted line), and the magnitude of the kernel decays roughly as an exponential with time constant equal to the classical orbit time.

comparable to the classical orbit time. There is also somewhat-reasonable quantitative agreement between the two models. Since the IDE is modeling the second-order interaction between the bound state and the continuum states that it can transition to, we conclude that the primary driver of the CEP-dependence in this regime is interference between the low-$\ell$ continuum electron wavefunction and the remaining bound state population, as described by $K_b(t-t')$.

An intuitive picture of what this model is saying can be seen by approximating the IDE. We will restrict the integral in (2.4.6) to going back only by a time $\Delta \approx T_{cl}$ (on the basis that the kernel amplitude decreases exponentially as the time difference grows). We can then approximate

$b(t') \approx b(t)$, pull it out of the integral, and write

$$\dot{b}(t) \approx -\frac{1}{\hbar^2}\left[q\,\mathcal{E}(t)\right]b(t)\int_{t-\Delta}^{t} dt'\left[q\,\mathcal{E}(t')\right]K_b(t-t')$$
$$\dot{b}(t) \approx -F(t)\,\tilde{v}(t,t-\Delta)\,b(t)\,/\,E_h \tag{2.4.8}$$

where $F(t)$ is the electric force on the electron, $E_h$ is the Hartree energy, and $\tilde{v}(t,t-\Delta)$ is interpreted as the velocity of an electron in the laser field at time $t$ after ionization at time $t-\Delta$. This interpretation comes from the Lewenstein model of HHG, where the electron's action is integrated forwards from the time of ionization to determine its dynamics [93]. The driving term can then be thought of as a quasi-classical quantity: the power (force multiplied by velocity) that the laser field is delivering to the electron compared to the binding energy. That power depends on the current amplitude of the electric field and the current velocity of the electron, which itself depends on the history of the electron's interaction with the laser and binding potential.

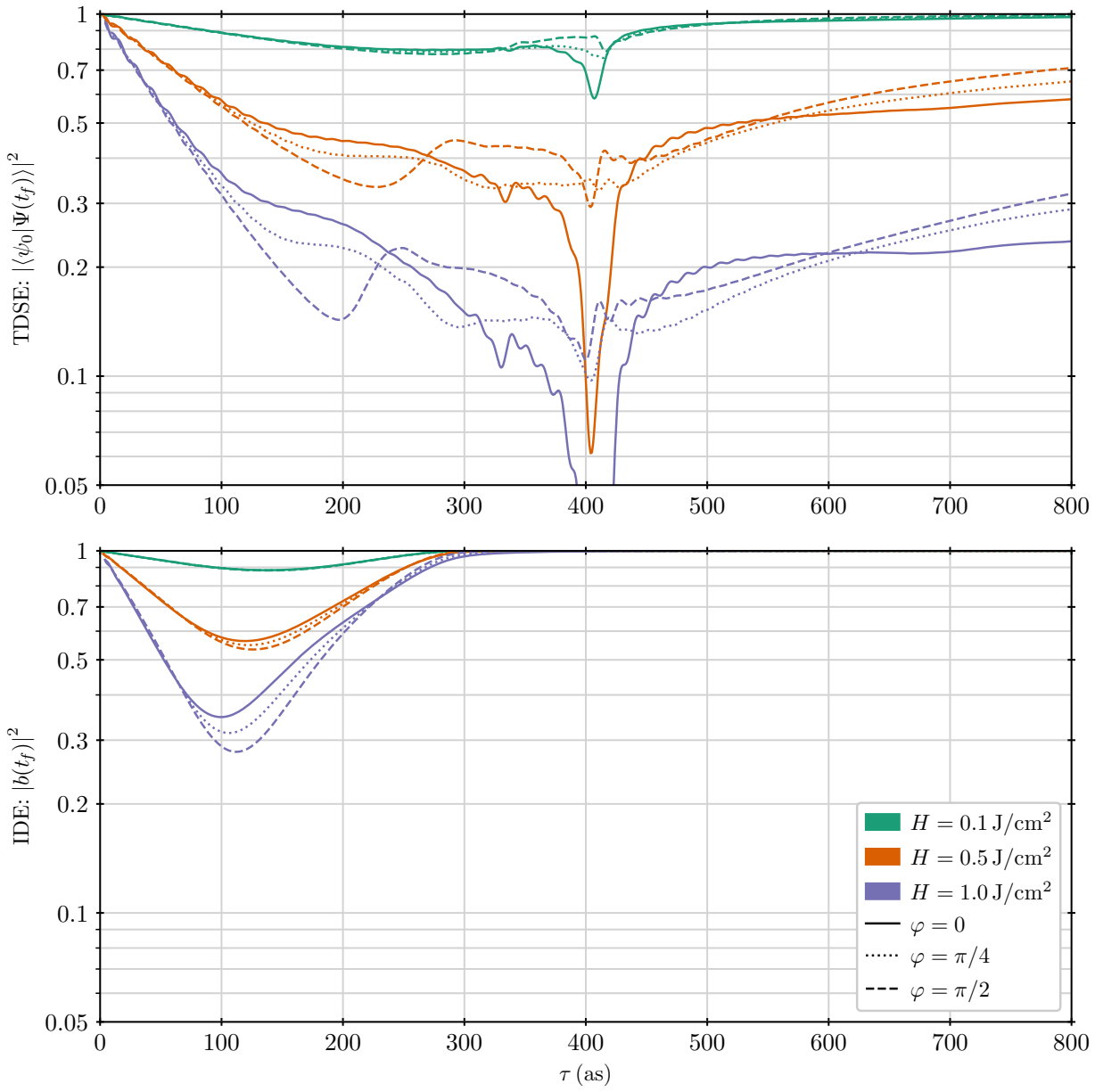


Figure 2.7: A comparison of TDSE and IDE pulse width scans for various pulse fluences and carrier-envelope phases. The IDE does not predict much ionization at large pulse widths, but at short pulse widths, it captures the qualitative behavior of the TDSE. In the region of 100–200 as (near the classical orbit time), the ionization probability is roughly correct, and the phases are in the correct order.

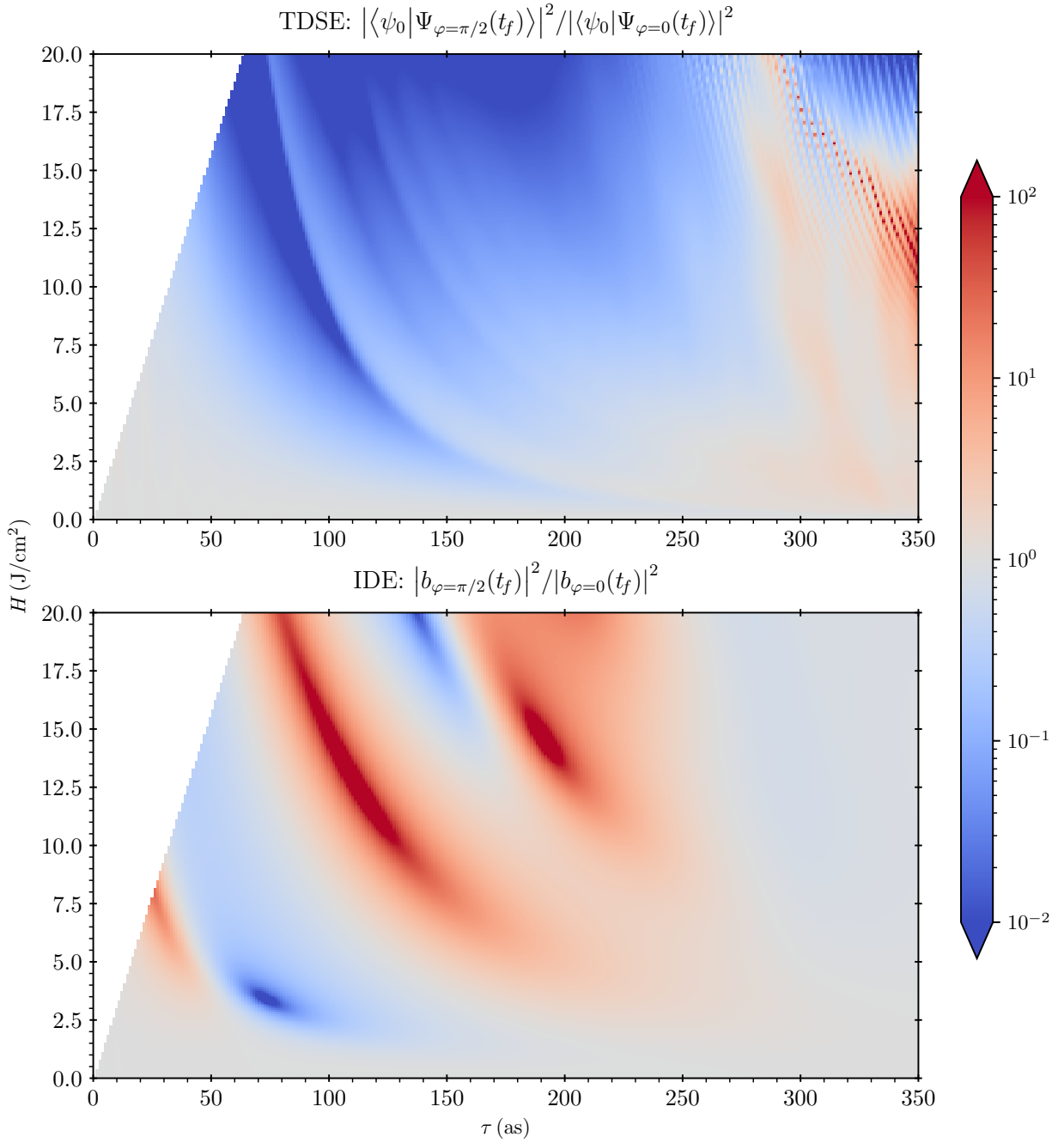


Figure 2.8: The ratio of the population remaining in the initial $1s$ state of hydrogen post-interaction for sine-like ($\varphi = \pi/2$) and cosine-like ($\varphi = 0$) pulses, calculated using the TDSE and IDE over a range of fluences $H$ and pulse widths $\tau$. Blue (red) coloration means that the sine-like pulse ionized more (less) than the cosine-like pulse. The blank region is a result of cutting off the heatmap when the pulse's peak electric field amplitude reaches three atomic electric fields. The fractional difference in remaining population can be very large (several orders of magnitude), despite the two pulses having the same fluence and pulse width.

## 2.5 Details of the IDE Model

In the previous section, we introduced the idea of a minimal IDE-based model for describing the ionization of a hydrogen atom. In this section, we will derive that model in detail and discuss how to numerically solve it. In the next section, we will discuss extensions of the IDE model that go beyond our investigation into CEP-dependent ionization.

### 2.5.1 Minimal IDE Model

The derivation begins with an expansion often used to analyze high-harmonic generation (HHG) using the strong field approximation (SFA) [94]. Our approach is similar to the techniques that lead to continuum state probability amplitudes that include rescattered electrons [93], but we instead focus on calculating the bound state population directly. In a typical ATI/HHG calculation our goal would be to calculate the continuum state amplitudes $c_{k\ell m}(t)$ and determine the photoelectron spectrum [94]. Instead, we will calculate the bound state amplitude $c_b(t)$ to directly determine the ionization rate. This version of the model will be "minimal" because it only includes a single bound state, and the continuum states will not be allowed to interact with each other directly.

Consider a central potential with a single bound state, which we label $|b\rangle$, as well a continuum of free states which we label $|\phi_{k\ell m}\rangle$. Then the wavefunction can be expanded as

$$|\Psi(t)\rangle = c_b(t)\ |b\rangle + \int_{-\infty}^{\infty} \mathrm{d}k \sum_{\ell=0}^{\infty} \sum_{m=-\ell}^{\ell} c_{k\ell m}(t)\ |\phi_{k\ell m}\rangle \tag{2.5.1}$$

where $|b\rangle$ is the single bound state, $|\phi_{k\ell m}\rangle$ is a delta-normalized continuum state, and $c_b$ and $c_{k\ell m}$ are their associated probability amplitudes. We will begin at time $t_0$ (which might be $infty$) with initial conditions $c_b(t_0) = 1$ and $c_{k\ell m}(t_0) = 0$. We are interesting in calculating $c_b(t)$ for times $t > t_0$.

If we think of the Hamiltonian as the sum of the steady-state central potential $\widehat{\mathcal{H}}_0$ and an

interaction Hamiltonian $\widehat{\mathcal{H}}_I$, we can write the Schrödinger equation as

$$i\hbar \frac{\partial}{\partial t} |\Psi(t)\rangle = \left(\widehat{\mathcal{H}}_0 + \widehat{\mathcal{H}}_I\right) |\Psi(t)\rangle$$

$$i\hbar \left( \dot{c}_b \, |b\rangle + \sum_{\ell,\, m} \int_0^\infty \mathrm{d}k \, \dot{c}_{k\ell m} \, |\phi_{k\ell m}\rangle \right) = \left(\widehat{\mathcal{H}}_0 + \widehat{\mathcal{H}}_I\right) \left( c_b \, |b\rangle + \sum_{\ell,\, m} \int_0^\infty \mathrm{d}k \, c_{k\ell m} \, |\phi_{k\ell m}\rangle \right) \tag{2.5.2}$$

Multiply from the left by $\langle b|$ to get a differential equation for $c_b$:

$$i\hbar \, \dot{c}_b = E_b \, c_b + \sum_{\ell,\, m} \int_0^\infty \mathrm{d}k \, c_{k\ell m} \, \langle b|\widehat{\mathcal{H}}_I|\phi_{k\ell m}\rangle \tag{2.5.3}$$

and by $\langle \phi_{k\ell m}|$ to get an equation for $c_{k\ell m}$:

$$i\hbar \, \dot{c}_{k\ell m} = E_{k\ell m} \, c_{k\ell m} + c_b \, \langle \phi_{k\ell m}|\widehat{\mathcal{H}}_I|b\rangle + \sum_{\ell,\, m} \int_0^\infty \mathrm{d}k \, c_{k'\ell'm'} \, \langle \phi_{k\ell m}|\widehat{\mathcal{H}}_I|\phi_{k'\ell'm'}\rangle \tag{2.5.4}$$

For the moment will neglect the last term in (2.5.4), which represents the continuum-continuum interactions, and rearrange to get

$$\dot{c}_{k\ell m} + i \, \omega_{k\ell m} \, c_{k\ell m} = -\frac{i}{\hbar} \, c_b \, \langle \phi_{k\ell m}|\widehat{\mathcal{H}}_I|b\rangle \tag{2.5.5}$$

We will solve this differential equation by finding an integrating factor:

$$I = \exp\left( \int_{t_0}^t \mathrm{d}t' \, i \, \omega_{k\ell m} t' \right) = e^{i\omega_{k\ell m} t} e^{-i\omega_{k\ell m} t_0} \tag{2.5.6}$$

Multiply both sides of the equation by this integrating factor and cancel the irrelevant phase factor to get

$$\begin{aligned}
\frac{\partial}{\partial t} \left[ e^{i\omega_{k\ell m} t} \, c_{k\ell m} \right] &= -\frac{i}{\hbar} \, c_b \, \langle \phi_{k\ell m}|\widehat{\mathcal{H}}_I|b\rangle \; e^{i\omega_{k\ell m} t} \\
e^{i\omega_{k\ell m} t} \, c_{k\ell m}(t) - \, c_{k\ell m}(0) &= -\frac{i}{\hbar} \int_{t_0}^t \mathrm{d}t' \, c_b(t') \, \langle \phi_{k\ell m}|\widehat{\mathcal{H}}_I(t')|b\rangle \; e^{i\omega_{k\ell m} t'} \\
c_{k\ell m}(t) &= -\frac{i}{\hbar} \int_{t_0}^t \mathrm{d}t' \, c_b(t') \, \langle \phi_{k\ell m}|\widehat{\mathcal{H}}_I(t')|b\rangle \; e^{-i\omega_{k\ell m}(t-t')}
\end{aligned} \tag{2.5.7}$$

Plug this back into (2.5.3) to get

$$\dot{c}_b(t) = -i\,\omega_b\,c_b(t) - \frac{i}{\hbar}\sum_{\ell,\,m}\int_0^\infty \mathrm{d}k\left(-\frac{i}{\hbar}\int_{t_0}^t \mathrm{d}t'\,c_b(t')\,\langle\phi_{k\ell m}|\widehat{\mathcal{H}}_I(t')|b\rangle\;e^{-i\omega_{k\ell m}(t-t')}\right)\langle b|\widehat{\mathcal{H}}_I(t)|\phi_{k\ell m}\rangle$$

$$\dot{c}_b(t) = -i\,\omega_b\,c_b(t) - \frac{1}{\hbar^2}\sum_{\ell,\,m}\int_0^\infty \mathrm{d}k\int_{t_0}^t \mathrm{d}t'\,c_b(t')\,\langle\phi_{k\ell m}|\widehat{\mathcal{H}}_I(t')|b\rangle\;\langle b|\widehat{\mathcal{H}}_I(t)|\phi_{k\ell m}\rangle\;e^{-i\omega_{k\ell m}(t-t')} \quad (2.5.8)$$

We will now insert our interaction Hamiltonian, $\widehat{\mathcal{H}}_I(t) = -q\,\mathcal{E}(t)\,\widehat{z}$, an electric field linearly polarized along the $z$-axis. This allows us to combine the two matrix elements:

$$\dot{c}_b(t) = -i\,\omega_b\,c_b(t) - \frac{q^2}{\hbar^2}\sum_{\ell,\,m}\int_0^\infty \mathrm{d}k\int_{t_0}^t \mathrm{d}t'\,c_b(t')\mathcal{E}(t)\mathcal{E}(t')\,\langle\phi_{k\ell m}|\widehat{z}|b\rangle\;\langle b|\widehat{z}|\phi_{k\ell m}\rangle\;e^{-i\omega_{k\ell m}(t-t')}$$

$$\dot{c}_b(t) = -i\,\omega_b\,c_b(t) - \frac{q^2}{\hbar^2}\sum_{\ell,\,m}\int_0^\infty \mathrm{d}k\int_{t_0}^t \mathrm{d}t'\,c_b(t')\,\mathcal{E}(t)\,\mathcal{E}(t')\,|\,\langle\phi_{k\ell m}|\widehat{z}|b\rangle|^2\,e^{-i\omega_{k\ell m}(t-t')} \quad (2.5.9)$$

We can now push the wavenumber integral through the time integral, resulting in

$$\dot{c}_b(t) = -i\,\omega_b\,c_b(t) - \frac{q^2}{\hbar^2}\,\mathcal{E}(t)\int_{t_i}^t \mathrm{d}t'\,c_b(t')\,\mathcal{E}(t')\sum_{\ell,\,m}\int_0^\infty \mathrm{d}k\,|\,\langle\phi_{k\ell m}|\widehat{z}|b\rangle|^2\,e^{-i\omega_{k\ell m}(t-t')} \quad (2.5.10)$$

We can also remove the annoying first term by defining $c_b(t) = b(t)\,e^{-i\,\omega_b t}$, so that $\dot{c}_b(t) = \dot{b}(t)\,e^{-i\,\omega_b t} - i\,\omega_b\,b(t)\,e^{-i\,\omega_b t}$ (this is equivalent to going into the interaction picture). Then we have

$$\begin{aligned}
\dot{b}(t)\,e^{-i\,\omega_b t} - i\,\omega_b\,b(t)\,e^{-i\,\omega_b t} &= -\,i\,\omega_b\,b(t)\,e^{-i\,\omega_b t} \\
&\quad - \frac{q^2}{\hbar^2}\,\mathcal{E}(t)\int_{t_i}^t \mathrm{d}t'\,b(t')\,e^{-i\,\omega_b t'}\mathcal{E}(t')\sum_{\ell,\,m}\int_0^\infty \mathrm{d}k\,|\,\langle\phi_{k\ell m}|\widehat{z}|b\rangle|^2 e^{-i\omega_{k\ell m}(t-t')} \\
\dot{b}(t) &= -\,\frac{q^2}{\hbar^2}\,\mathcal{E}(t)\int_{t_i}^t \mathrm{d}t'\,b(t')\,\mathcal{E}(t')\sum_{\ell,\,m}\int_0^\infty \mathrm{d}k\,|\,\langle\phi_{k\ell m}|\widehat{z}|b\rangle|^2\,e^{-i(\omega_{k\ell m}-\omega_b)(t-t')}
\end{aligned} \quad (2.5.11)$$

Determining $b(t)$ is equivalent to determining $c_b(t)$ up to a phase factor, and therefore doesn't matter at all when considering the probability to be in state $|b\rangle$, $\mathcal{P}(b) = |c_b(t)|^2 = |b(t)|^2$.

We write the final form of the "minimal IDE model" as

$$\dot{b}(t) = -\frac{q^2}{\hbar^2}\,\mathcal{E}(t)\int_{t_i}^{t} \mathrm{d}t'\, b(t')\,\mathcal{E}(t')\,K_b(t-t') \tag{2.5.12}$$

where

$$K_b(t-t') = \sum_{\ell,\,m}\int_0^\infty \mathrm{d}k\,|\,\langle\phi_{k\ell m}|\widehat{z}|b\rangle|^2\,e^{-i(\omega_{k\ell m}-\omega_b)(t-t')} \tag{2.5.13}$$

is the kernel of the IDE. We can also represent the IDE as a double-integral equation,

$$b(t) = b(t_i) - \frac{q^2}{\hbar^2}\int_{t_i}^{t} \mathrm{d}t'\,\mathcal{E}(t')\int_{t_i}^{t'} \mathrm{d}t''\, b(t'')\,\mathcal{E}(t'')\,K_b(t'-t'') \tag{2.5.14}$$

We cannot go any farther without specifying $|b\rangle$ and $|k\ell m\rangle$.

### 2.5.2 Approximate Kernel for the Hydrogen Ground State

The simplest version of the kernel calculation (2.5.13) is to use the analytic hydrogen ground state as the bound state and to approximate the continuum states with wavenumber-normalized spherical Bessel waves,

$$\phi_{k\ell m}(r,\,\theta,\,\phi) \approx \sqrt{\frac{2}{\pi}}\,k\,j_\ell(kr)\,Y_\ell^m(\theta,\phi) \tag{2.5.15}$$

The matrix element is

$$\begin{aligned}
\langle\phi_{k\ell m}|\widehat{z}|b\rangle &= \sum_{\ell,\,m}\sqrt{\frac{2}{\pi}}\,k\int_0^\infty \mathrm{d}r\,r^2\,j_\ell(kr)\,R_{10}(r)\,r\int_\Omega \mathrm{d}\Omega\,Y_\ell^m\,\cos\theta\,Y_0^0\\
\langle\phi_{k\ell m}|\widehat{z}|b\rangle &= \sum_{\ell,\,m}\sqrt{\frac{2}{\pi}}\,k\int_0^\infty \mathrm{d}r\,r^3\,j_\ell(kr)\,R_{10}(r)\int_\Omega \mathrm{d}\Omega\,Y_\ell^m\left(2\sqrt{\frac{\pi}{3}}\,Y_1^0\right)Y_0^0\\
\langle\phi_{k\ell m}|\widehat{z}|b\rangle &= \sum_{\ell,\,m}\sqrt{\frac{2}{\pi}}2\sqrt{\frac{\pi}{3}}\frac{1}{\sqrt{4\pi}}\,k\int_0^\infty \mathrm{d}r\,r^3\,j_\ell(kr)\,R_{10}(r)\int_\Omega \mathrm{d}\Omega\,Y_\ell^m\,Y_1^0\\
\langle\phi_{k\ell m}|\widehat{z}|b\rangle &= \sqrt{\frac{2}{3\pi}}\sum_{\ell,\,m}\delta_{\ell,1}\,\delta_{m,0}\,k\int_0^\infty \mathrm{d}r\,r^3\,j_\ell(kr)\,R_{10}(r)
\end{aligned} \tag{2.5.16}$$

The sum collapses the Kronecker deltas, and we're left with

$$\begin{aligned}
\langle \phi_{k\ell m} | \widehat{z} | b \rangle &= \sqrt{\frac{2}{3\pi}}\, k \int_0^\infty \mathrm{d}r\, r^3\, j_1(kr)\, R_{10}(r) \\
\langle \phi_{k\ell m} | \widehat{z} | b \rangle &= \sqrt{\frac{2}{3\pi}} \frac{2}{\sqrt{a^3}}\, k \int_0^\infty \mathrm{d}r\, r^3 \left[ \frac{\sin kr}{k^2 r^2} - \frac{\cos kr}{kr} \right] e^{-r/a_0} \\
\langle \phi_{k\ell m} | \widehat{z} | b \rangle &= \sqrt{\frac{512}{3\pi}}\, a_0^{7/2}\, \frac{k^2}{\left(1 + a_0^2 k^2\right)^3}
\end{aligned} \tag{2.5.17}$$

The term that enters the kernel is the square of the matrix element,

$$\left| \langle \phi_{k\ell m} | \widehat{z} | b \rangle \right|^2 = \frac{512}{3\pi}\, a_0^7\, \frac{k^4}{\left(1 + a_0^2 k^2\right)^6} \tag{2.5.18}$$

The kernel is the integral of the product of this matrix element with the frequency difference term:

$$\begin{aligned}
K_b(t - t') &= \sum_{\ell,\, m} \int_0^\infty \mathrm{d}k \left| \langle \phi_{k\ell m} | \widehat{z} | b \rangle \right|^2 e^{-i(\omega_{k\ell m} - \omega_b)(t - t')} \\
&= \frac{512}{3\pi}\, a_0^7\, e^{i\,\omega_b (t - t')} \int_0^\infty \mathrm{d}k\, \frac{k^4}{\left(1 + a_0^2 k^2\right)^6}\, e^{-i\,\omega_k (t - t')} \\
&= \frac{512}{3\pi}\, a_0^7\, e^{i\,\omega_b (t - t')} \int_0^\infty \mathrm{d}k\, \frac{k^4}{\left(1 + a_0^2 k^2\right)^6}\, e^{-i\,\frac{\hbar}{2m} k^2 (t - t')} \\
K_b(t - t') &= \frac{512}{3\pi}\, a_0^3\, e^{i\,\omega_b (t - t')} \int_0^\infty \mathrm{d}x\, \frac{x^4}{\left(1 + x^2\right)^6}\, e^{-i\,\tau x^2}
\end{aligned} \tag{2.5.19}$$

where $\tau = \hbar(t - t')/2ma_0^2$ is a dimensionless time ratio.

The asymptotic behavior of $K_b(t - t')$ is

$$\lim_{(t - t') \to 0} K_b(t - t') = a_0^2 \tag{2.5.20a}$$

$$\lim_{(t - t') \to \infty} K_b(t - t') = 0 \tag{2.5.20b}$$

$K_b(t - t')$ is not defined for negative $t - t'$, and these times are never referenced in the IDE (this is good: causality in action). The $(t - t') \to 0$ limit is particularly important because it may need to be hard-coded in software.

This kernel is plotted in Figure 2.6.

### 2.5.3 Numerical Solution

The IDE model derived above is an integro-differential equation of the form

$$\frac{\mathrm{d}b}{\mathrm{d}t} = A\, f(t) \int_{t_0}^{t} \mathrm{d}t'\, b(t')\, f(t')\, K(t - t') \tag{2.5.21}$$

for a prefactor $A$, function $f$, kernel function $K$, and unknown function $b(t)$. Such equations are tricky to solve numerically because to accurately approximate the derivative we need to accurately approximate the integral. More advanced techniques involving Laplace transforms and series solutions seem to be the "proper" way to solve such equations [95], but we find that more straightforward methods are easier to use and test.

We typically use a fourth-order Runge-Kutta method to find $a(t_{n+1})$ from $a(t_n)$, so we would like to use an integration method that is at least fourth-order in time as well to keep the error small. A simple option is to use the composite Simpson's rule. Simpson's rule is actually fourth-order in the time step, so we expect the overall accuracy of the scheme to be fourth-order.

An added complication is that the kernel causes the value of the entire integrand to change at every time step. This means that we cannot compute the integral "iteratively", i.e., using the value of the integral at the previous time step to jump-start the calculation of the integral for the current time step. This causes a quadratic slowdown in computation time for the $n$-th time step.

To help combat this slowdown we sometimes use an RK4 algorithm with an adaptive time step as described in [92]. The algorithm monitors the local truncation error by computing each time step in two different ways. When the local truncation errors grows too large the algorithm recomputes the step with a smaller $\Delta t$ until the error goes back below whatever cutoff criteria is imposed. We ultimately found that this was not terribly effective, and simply used a small fixed time step for our simulations.

We also confirmed than an alternate solution method based on an iterative algorithm produced the same results, but again found that it was not significantly more effective than RK4 with a fixed time step. See G for details.

## 2.6 Next Steps for the IDE Model

The results described in the previous two sections mostly focused on the essential elements needed to derive the IDE model in the first place, and to understand its relationship to the counterintuitive CEP-dependent ionization probabilities we discussed in Section 2.4. Those ideas were all discussed in our paper on the subject ([73]).

In this section, we go beyond that specific application. We discuss various properties of the IDE model itself, as well as some possible extensions and applications.

### 2.6.1 Carrier-Envelope Phase Symmetries of the Minimal IDE Model

We can rewrite the minimal IDE slightly more generically as an integro-differential equation of the form

$$\frac{\mathrm{d}b}{\mathrm{d}t} = A\,\mathcal{E}(t)\int_{t_0}^{t}\mathrm{d}t'\,b(t')\,\mathcal{E}(t')\,K(t-t') \tag{2.6.1}$$

When solving the IDE we observe three phase symmetries: $|b(t\to\infty)|^2$ is the same if we transform the carrier-envelope phase of the electric field $\varphi$ as any of

1. $\varphi \to \pi + \varphi$

2. $\varphi \to \pi - \varphi$

3. $\varphi \to -\varphi \simeq 2\pi - \varphi$

The pulses that are produced by applying these transformations to a sub-cycle sinc pulse with $\varphi = \pi/4$ are shown in Figure 2.9. The results of IDE simulations run with these pulses are shown in Figure 2.10.

In this section, we will analytically prove that the IDE obeys these symmetries. Let's write the electric field in carrier-envelope form (2.1.17),

$$\mathcal{E}(t) = \mathcal{E}_t\,F(t)\,\cos(\omega_c\,t+\varphi). \tag{2.6.2}$$

Without loss of generality we assume the pulse is centered at $t = 0$ so that the envelope function

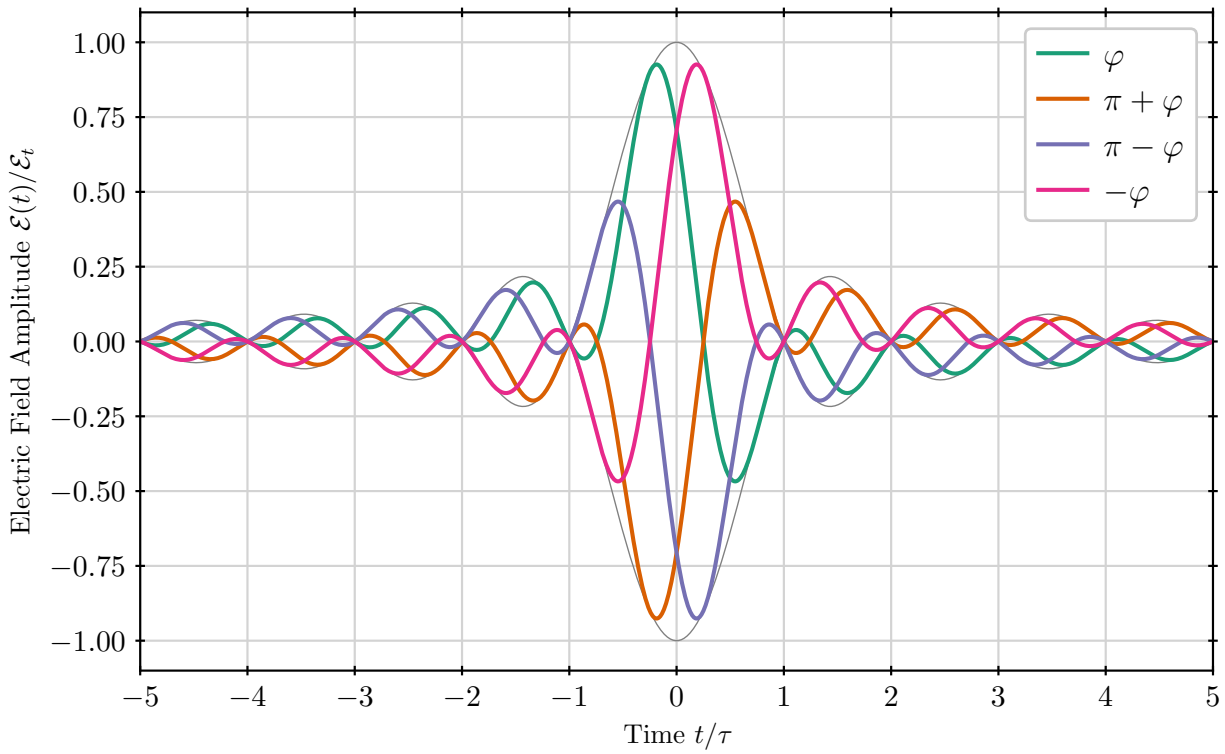


Figure 2.9: These four pulses, produced from the base carrier-envelope phase $\varphi = \pi/4$, all produce the same $|b(t \to \infty)|^2$ under the minimal IDE model. The same would be true of any base carrier-envelop phase; $\varphi = \pi/4$ has been chosen to make this figure intelligible.

$F(t)$ is even ($F(t) = F(-t)$). If we plug this into the generic form of the IDE (2.6.1) we get

$$\begin{aligned}
\frac{\mathrm{d}b}{\mathrm{d}t} &= A\,\mathcal{E}_t\,F(t)\,\cos(\omega_c\,t+\varphi)\int_{t_0}^{t}\mathrm{d}t'\,b(t')\,\mathcal{E}_t\,F(t')\,\cos\big(\omega_c\,t'+\varphi\big)\,K(t-t') \\
\frac{\mathrm{d}b}{\mathrm{d}t} &= A\,\mathcal{E}_t^2\,F(t)\,\cos(\omega_c\,t+\varphi)\int_{t_0}^{t}\mathrm{d}t'\,b(t')\,F(t')\,\cos\big(\omega_c\,t'+\varphi\big)\,K(t-t') \\
\frac{\mathrm{d}b}{\mathrm{d}t} &= A\,\mathcal{E}_t^2\int_{t_0}^{t}\mathrm{d}t'\,(t')\,F(t)F(t')\,\cos(\omega_c t+\varphi)\cos\big(\omega_c\,t'+\varphi\big)\,K(t-t')
\end{aligned} \tag{2.6.3}$$

The first symmetry property is simply a result of

$$\begin{aligned}
\cos(\omega_c t+\varphi+\pi)\cos\big(\omega_c\,t'+\varphi+\pi\big) &= (-1)^2\cos(\omega_c t+\varphi)\cos\big(\omega_c\,t'+\varphi\big) \\
\cos(\omega_c t+\varphi+\pi)\cos\big(\omega_c\,t'+\varphi+\pi\big) &= \cos(\omega_c t+\varphi)\cos\big(\omega_c\,t'+\varphi\big)
\end{aligned} \tag{2.6.4}$$

So in this case the symmetry is stronger, and in fact $b(t)$ is identical for the two pulses for all $t$. In real space this corresponds to simply negating the electric field, which would effect the emission

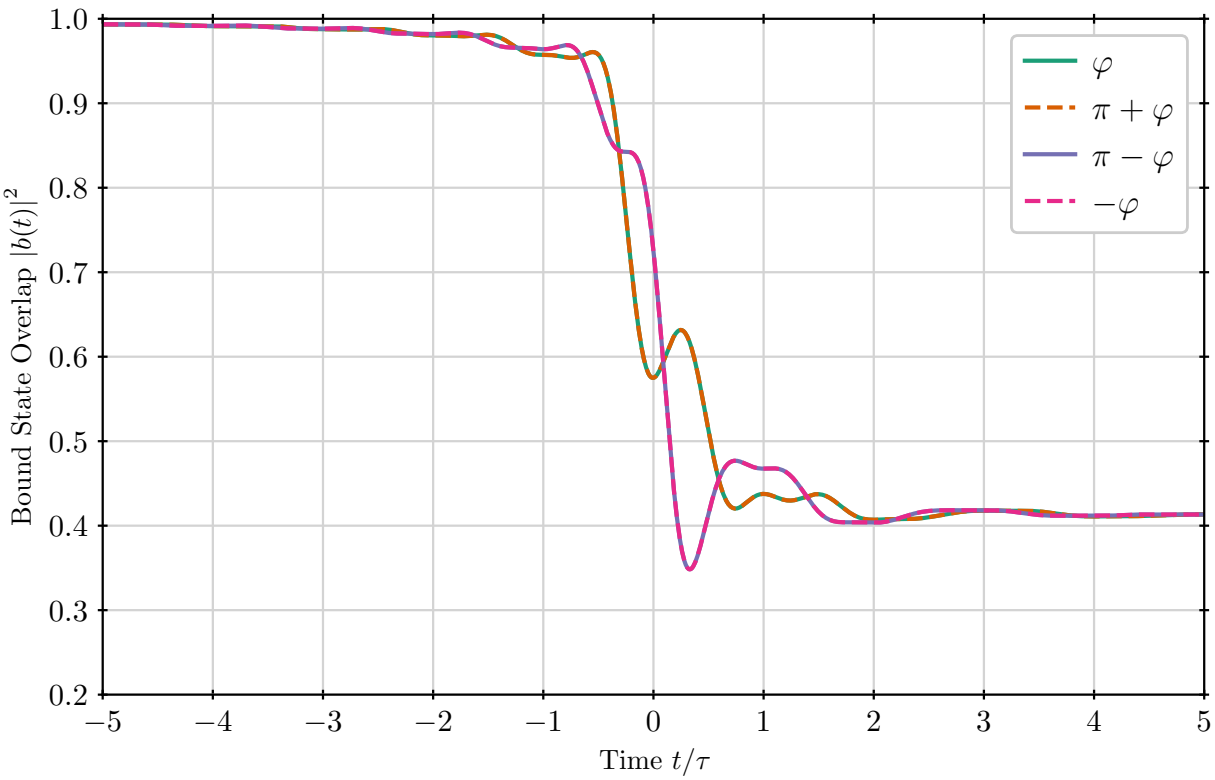


Figure 2.10: The $|b(t)|^2$ produced by each pulse in Figure 2.9 through the minimal IDE model. The base carrier-envelope phase is $\varphi = \pi/4$. Each symmetry pair has the same $|b(t)|^2$, and all four pulses have the same $|b(t \to \infty)|^2$.

direction of photoelectrons in the lab frame but not the ionization process itself. The other two symmetries are related in the same way as $\varphi$ and $\pi + \varphi$:

$$\pi - \varphi + \pi = 2\pi - \varphi \simeq -\varphi \tag{2.6.5}$$

so we expect them to give the same $b(t)$ as each other. The consequence of this behavior is visible in Figure 2.10, where each pair's $|b(t)|^2$ is completely overlapped.

However, we have not yet determined that $|b(t \to \infty)|$ is the same between the two classes of symmetries. For $\varphi \neq 0$ or $\pi/2$, the difference between CEP $\varphi$ and $-\varphi$ is whether the higher-amplitude central peak comes before or after the lower-amplitude one (see Figure 2.9). This is

effectively a time reversal of the electric field. If write the phase-reversed field as $\overline{\mathcal{E}}(t)$, we have

$$\begin{aligned}\overline{\mathcal{E}}(t) &= F(t)\cos(\omega_c t - \varphi)\\ \overline{\mathcal{E}}(t) &= F(t)\cos(-\omega_c t + \varphi)\\ \overline{\mathcal{E}}(t) &= \mathcal{E}(-t)\end{aligned} \tag{2.6.6}$$

because $F(t) = F(-t)$.

To prove that $b(t \to \infty)$ is the same when $\mathcal{E}(t)$ is time-reversed [3], consider integrating the IDE to get a single double-integral equation:

$$b(t) = 1 + A\int_{-\infty}^{t} \mathrm{d}t' \int_{-\infty}^{t'} \mathrm{d}t''\, \mathcal{E}(t')\,\mathcal{E}(t'')\,K(t'-t'')\,b(t'') \tag{2.6.7}$$

where we used the initial condition $b(0) = 1$ (although any initial condition would work). Plug the solution back into the equation:

$$\begin{aligned} b(t) &= 1 + A\int_{-\infty}^{t} \mathrm{d}t_1' \int_{-\infty}^{t_1'} \mathrm{d}t_1''\, \mathcal{E}(t_1')\,\mathcal{E}(t_1'')\,K(t_1'-t_1'')\\ &\qquad \times \left[1 + A\int_{-\infty}^{t_1''} \mathrm{d}t_2' \int_{-\infty}^{t_2'} \mathrm{d}t_2''\, \mathcal{E}(t_2')\,\mathcal{E}(t_2'')\,K(t_2'-t_2'')\,b(t_2'')\right]\\ b(t) &= 1 + A\int_{-\infty}^{t} \mathrm{d}t_1' \int_{-\infty}^{t_1'} \mathrm{d}t_1''\, \mathcal{E}(t_1')\,\mathcal{E}(t_1'')\,K(t_1'-t_1'')\\ &\quad + A^2\int_{-\infty}^{t} \mathrm{d}t_1' \int_{-\infty}^{t_1'} \mathrm{d}t_1'' \int_{-\infty}^{t_1''} \mathrm{d}t_2' \int_{-\infty}^{t_2'} \mathrm{d}t_2''\, \mathcal{E}(t_1')\,\mathcal{E}(t_1'')\,K(t_1'-t_1'')\,\mathcal{E}(t_2')\,\mathcal{E}(t_2'')\,K(t_2'-t_2'')\,b(t_2'') \end{aligned} \tag{2.6.8}$$

Call $\chi(t_n', t_n'') = \mathcal{E}(t_n')\,\mathcal{E}(t_n'')\,K(t_n'-t_n'')$ and continue plugging the original IDE solution back in so

[3] This proof courtesy of Benjamin Lemberger.

that we get a power series solution in $A$:

$$\begin{aligned}
b(t) &= 1 + A\int_{-\infty}^{t} \mathrm{d}t_1' \int_{-\infty}^{t_1'} \mathrm{d}t_1''\ \chi(t_1', t_1'') \\
&\quad + A^2 \int_{-\infty}^{t} \mathrm{d}t_1' \int_{-\infty}^{t_1'} \mathrm{d}t_1'' \int_{-\infty}^{t_1''} \mathrm{d}t_2' \int_{-\infty}^{t_2'} \mathrm{d}t_2''\ \chi_1(t_1', t_1'')\, \chi_1(t_2', t_2'')\, b(t_2') \\
b(t) &= 1 + A\int_{-\infty}^{t} \mathrm{d}t_1' \int_{-\infty}^{t_1'} \mathrm{d}t_1''\ \chi(t_1', t_1'') \\
&\quad + A^2 \int_{-\infty}^{t} \mathrm{d}t_1' \int_{-\infty}^{t_1'} \mathrm{d}t_1'' \int_{-\infty}^{t_1''} \mathrm{d}t_2' \int_{-\infty}^{t_2'} \mathrm{d}t_2''\ \chi_1(t_1', t_1'')\, \chi_1(t_2', t_2'') \\
&\quad + A^3 \int_{-\infty}^{t} \mathrm{d}t_1' \int_{-\infty}^{t_1'} \mathrm{d}t_1'' \int_{-\infty}^{t_1''} \mathrm{d}t_2' \int_{-\infty}^{t_2'} \mathrm{d}t_2'' \int_{-\infty}^{t_2''} \mathrm{d}t_3' \int_{-\infty}^{t_3'} \mathrm{d}t_3''\ \chi(t_1', t_1'')\, \chi(t_2', t_2'')\, \chi(t_3', t_3'') \\
&\quad + \cdots \\
b(t) &= \sum_{p=0}^{\infty} A^p I_p(t)
\end{aligned} \tag{2.6.9}$$

where

$$I_p(t) = \int_{-\infty}^{t} \mathrm{d}t_1' \int_{-\infty}^{t_1'} \mathrm{d}t_1'' \int_{-\infty}^{t_1''} \mathrm{d}t_2' \int_{\infty}^{t_2'} \mathrm{d}t_2'' \int_{-\infty}^{t_2''} \mathrm{d}t_3' \cdots \int_{-\infty}^{t_{p-1}''} \mathrm{d}t_p' \int_{-\infty}^{t_p'} \mathrm{d}t_p''\ \chi(t_1', t_1'')\chi(t_2', t_2'') \cdots \chi(t_p', t_p'') \tag{2.6.10}$$

We will now show that $I_p(t \to \infty) = \overline{I}_p(t \to \infty)$, where $\overline{I}_p(t)$ uses $\overline{\mathcal{E}}(t)$ in $\chi$ instead of $\mathcal{E}(t)$. In terms of this original $\mathcal{E}(t)$, we have

$$\begin{aligned}
\overline{I}_p(t \to \infty) = \int_{-\infty}^{\infty} \mathrm{d}t_1' \int_{-\infty}^{t_1'} \mathrm{d}t_1'' \int_{-\infty}^{t_1''} \mathrm{d}t_2' \cdots \int_{-\infty}^{t_{p-1}''} \mathrm{d}t_p' \int_{-\infty}^{t_p'} \mathrm{d}t_p''\ \mathcal{E}(-t_1')\, \mathcal{E}(-t_1'')\mathcal{E}(-t_2') \cdots \\
\times K(t_1' - t_1'')\, K(t_2' - t_2'') \cdots
\end{aligned} \tag{2.6.11}$$

Flip the signs and bounds of all of the integrals by appropriate substitution and renaming. Note that this flips the signs of everything in the integrand:

$$\begin{aligned}
\overline{I}_p(t \to \infty) = \int_{-\infty}^{\infty} \mathrm{d}t_1' \int_{t_1'}^{\infty} \mathrm{d}t_1'' \int_{t_1''}^{\infty} \mathrm{d}t_2' \cdots \int_{t_{p-1}''}^{\infty} \mathrm{d}t_p' \int_{t_p'}^{\infty} \mathrm{d}t_p''\ \mathcal{E}(t_1')\, \mathcal{E}(t_1'')\mathcal{E}(t_2') \cdots \\
\times K(t_1'' - t_1')\, K(t_2'' - t_2') \cdots
\end{aligned} \tag{2.6.12}$$

Now we can use Heaviside theta functions to extend all of the integration bounds to infinity:

$$\begin{aligned}\overline{I}_p(t\to\infty) = \int_{-\infty}^{\infty}\mathrm{d}t_1'\int_{-\infty}^{\infty}\mathrm{d}t_1''\int_{-\infty}^{\infty}\mathrm{d}t_2'\cdots\int_{-\infty}^{\infty}\mathrm{d}t_p'\int_{-\infty}^{\infty}\mathrm{d}t_p''\;\mathcal{E}(t_1')\,\mathcal{E}(t_1'')\mathcal{E}(t_2')\;\cdots\\ \times K(t_1''-t_1')\,K(t_2''-t_2')\cdots\\ \times\Theta(t_1''-t_1')\,\Theta(t_2'-t_1'')\,\Theta(t_2''-t_2')\;\cdots\;\Theta(t_p'-t_{p-1}'')\,\Theta(t_p''-t_p')\end{aligned}\tag{2.6.13}$$

Since the bounds of the integrals no longer depend on each other we can reverse the order of the integrals so that we do $t_p''$ first:

$$\begin{aligned}\overline{I}_p(t\to\infty) = \int_{-\infty}^{\infty}\mathrm{d}t_p''\int_{-\infty}^{\infty}\mathrm{d}t_p'\int_{-\infty}^{\infty}\mathrm{d}t_{p-1}''\cdots\int_{-\infty}^{\infty}\mathrm{d}t_1''\int_{-\infty}^{\infty}\mathrm{d}t_1'\;\mathcal{E}(t_1')\,\mathcal{E}(t_1'')\mathcal{E}(t_2')\;\cdots\\ \times K(t_1''-t_1')\,K(t_2''-t_2')\cdots\\ \times\Theta(t_1''-t_1')\,\Theta(t_2'-t_1'')\,\Theta(t_2'-t_2'')\;\cdots\;\Theta(t_p'-t_{p-1}'')\,\Theta(t_p'-t_p'')\end{aligned}\tag{2.6.14}$$

Now we collapse the Heaviside theta functions. Because we're going in reverse order, the bounds will go from $-\infty$ upwards (instead of thinking of $t_1''$ as larger than $t_1'$, we now need $t_1'$ to be smaller than $t_1''$):

$$\begin{aligned}\overline{I}_p(t\to\infty) = \int_{-\infty}^{\infty}\mathrm{d}t_p''\int_{-\infty}^{t_p''}\mathrm{d}t_p'\int_{-\infty}^{t_p'}\mathrm{d}t_{p-1}''\cdots\int_{-\infty}^{t_2'}\mathrm{d}t_1''\int_{-\infty}^{t_1''}\mathrm{d}t_1'\;\mathcal{E}(t_1')\,\mathcal{E}(t_1'')\mathcal{E}(t_2')\;\cdots\\ \times K(t_1''-t_1')\,K(t_2''-t_2')\cdots\end{aligned}\tag{2.6.15}$$

Finally, rename variables:

$$t_n''\to t_{p-n+1}'\tag{2.6.16a}$$

$$t_n'\to t_{p-n+1}''\tag{2.6.16b}$$

The result is

$$\begin{aligned}\overline{I}_p(t\to\infty) = \int_{-\infty}^{\infty}\mathrm{d}t_1'\int_{-\infty}^{t_1'}\mathrm{d}t_1''\int_{-\infty}^{t_1''}\mathrm{d}t_2'\cdots\int_{-\infty}^{t_{p-1}''}\mathrm{d}t_p'\int_{-\infty}^{t_p'}\mathrm{d}t_p''\;\mathcal{E}(t_1')\,\mathcal{E}(t_1'')\mathcal{E}(t_2')\;\cdots\\ \times K(t_p'-t_p'')\,K(t_{p-1}'-t_{p-1}'')\cdots\end{aligned}\tag{2.6.17}$$

which is identical to $I_p(t \to \infty)$. Therefore

$$b(t \to \infty) = \sum_{p=0}^{\infty} A^p I_p(t \to \infty) = \sum_{p=0}^{\infty} A^p \overline{I}_p(t \to \infty) = \overline{b}(t \to \infty) \tag{2.6.18}$$

which is actually stronger than the symmetry we were looking for! All four pulses created by the transformations produce an identical final state.

We should note that although these symmetries are exactly obeyed by the minimal IDE, the TDSE does not display the time-reversal symmetry, as shown in Figure 2.11. Although the field-direction-reversed pairs still produce the same ground state overlap, the time-reversed pairs do not. This is likely due to the presence of continuum-continuum interactions, which we will discuss in more detail in Section 2.6.3. IDE simulations run with that kernel also do not obey the time-reversal symmetries.

### 2.6.2 Delta-Kicks

This is an attempt to bring classical intuition to bear on what the IDE model is telling us. We will replace the continuous electric field by a series of delta-function "kicks":

$$\mathcal{E}(t) \to \sum_{n=-\infty}^{\infty} \eta_n \, \delta(t - t_n) \tag{2.6.19}$$

We will figure out what the IDE tells us about these non-physical kicks, and then compare to what the motion of a quasi-classical Bohr model electron initially orbiting the nucleus would be when kicked in the same way.

We begin with the double-integral form of the IDE

$$b(t) = -\frac{q^2}{\hbar^2} \int_{t_i}^{t} \mathrm{d}t' \, \mathcal{E}(t') \int_{t_0}^{t'} \mathrm{d}t'' \, b(t'') \, \mathcal{E}(t'') \, K_b(t' - t''). \tag{2.6.20}$$

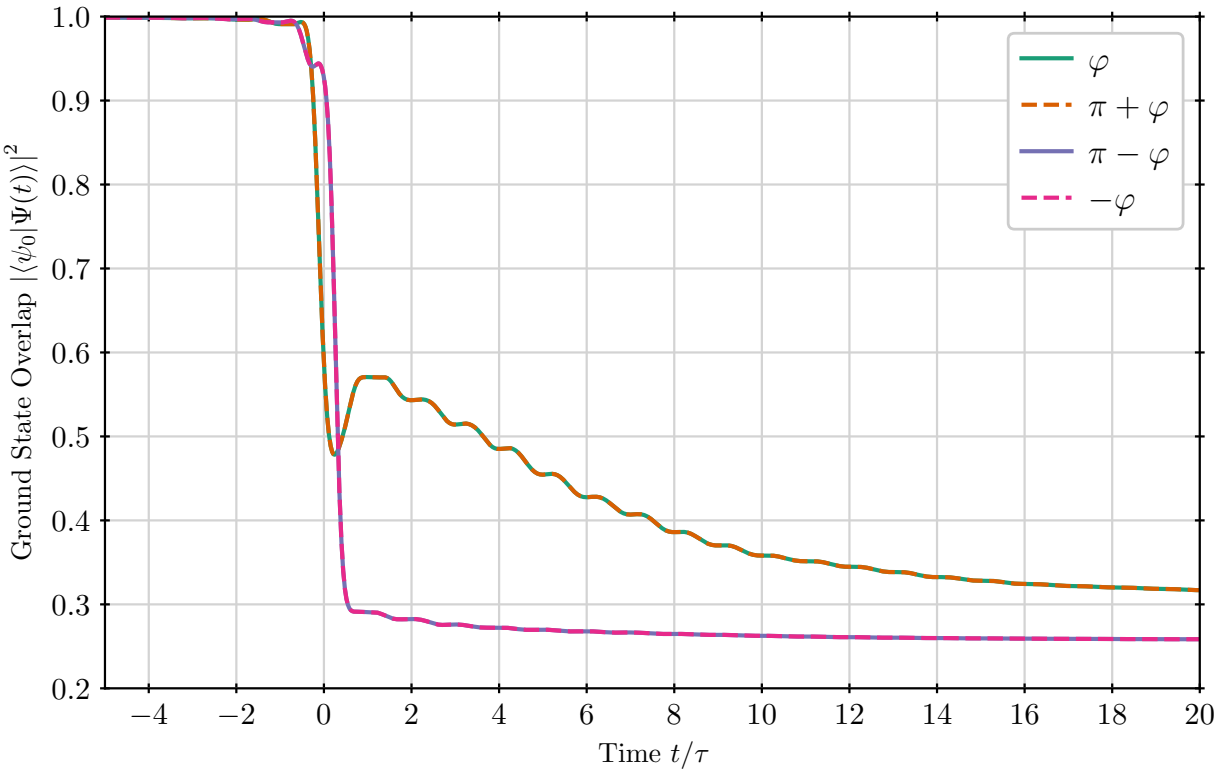


Figure 2.11: The same pulses as in Figure 2.9, applied to a hydrogen atom under the full TDSE. Although the field-direction-reversed pairs still produce the same ground state population, the time-reversal symmetry does not hold, so the four pulses do not all produce the same ground state overlap as $t \to \infty$. Note that the timescale has been expanded to much later times compared Figure 2.10, because there is much more action far from the center of the pulse in the full TDSE than there is in the minimal IDE model.

Plug the electric field from above in and simplify, using the delta functions to collapse the integrals:

$$
\begin{aligned}
b(t) &= b(t_i) - \frac{q^2}{\hbar^2} \int_{t_i}^{t} \mathrm{d}t' \sum_n \eta_n \, \delta(t' - t_n) \int_{t_0}^{t'} \mathrm{d}t'' \, b(t'') \sum_m \eta_m \, \delta(t'' - t_m) \, K_b(t' - t'') \\
b(t) &= b(t_i) - \frac{q^2}{\hbar^2} \int_{t_i}^{t} \mathrm{d}t' \int_{t_0}^{t'} \mathrm{d}t'' \sum_n \sum_m \eta_n \, \eta_m \, \delta(t' - t_n) \, \delta(t'' - t_m) \, b(t'') \, K_b(t' - t'') \\
b(t) &= b(t_i) - \frac{q^2}{\hbar^2} \int_{t_i}^{t} \mathrm{d}t' \sum_n \sum_{\substack{t_i \le m \\ t_m \le t'}} \eta_n \, \eta_m \, \delta(t' - t_n) \, b(t_m) \, K_b(t' - t_m) \\
b(t) &= b(t_i) - \frac{q^2}{\hbar^2} \sum_{\substack{n,m \\ t_i \le t_m \le t_n \le t}} \eta_n \, \eta_m \, b(t_m) \, K_b(t_n - t_m)
\end{aligned}
\tag{2.6.21}
$$

The resulting equation (2.6.21) is basically equivalent to a backward Euler algorithm[4] for solving

[4]We can also rephrase the iterative procedure described by (2.6.21) as a single lower-triangular matrix equation

the continuous-field version of the IDE. Backward Euler is not nearly as efficient as RK4, but it has good stability properties, so we don't have too worry too much about our poor discretization making the problem unstable.

To get some intuition about what's going on, we can evaluate (2.6.21) in closed form for a small number of time steps. As an example, let's do that for a "sine-like pulse" made of two delta-kicks of opposite sign but equal amplitude, $\eta_0 = -\eta_1$, delayed by a time $\Delta$. Plugging in, we can find the bound state amplitude at the first two time steps:

$$\begin{aligned} b(t_0) &= b(t_i) - \frac{q^2}{\hbar^2}\,\eta_0^2\, b(t_0)\, K_b(0) \\ b(t_1) &= b(t_i) - \frac{q^2}{\hbar^2}\,\eta_0^2\, b(t_0)\, K_b(0) - \frac{q^2}{\hbar^2}\,\eta_1^2\, b(t_1)\, K_b(0) - \frac{q^2}{\hbar^2}\,\eta_0(\eta_1)\, b(t_0)\, K_b(\delta) \\ b(t_1) &= b(t_0) - \frac{q^2}{\hbar^2}\,\eta_0^2\, b(t_1)\, K_b(0) + \frac{q^2}{\hbar^2}\eta_0^2\, b(t_0)\, K_b(\Delta) \end{aligned} \tag{2.6.22a}$$

First we solve for $b(t_0)$ (and insert the initial condition $b(t_i) = 1$):

$$\begin{aligned} b(t_0)\left(1 + \frac{q^2}{\hbar^2}\,\eta_0^2\, K_b(0)\right) &= 1 \\ b(t_0) &= \frac{1}{1 + \frac{q^2}{\hbar^2}\,\eta_0^2\, K_b(0)} \end{aligned} \tag{2.6.23}$$

Sanity check: this is always less than one, because $K_b(0)$ is a positive real number.

Now we can solve for $b(t_1)$:

$$\begin{aligned} b(t_1)\left[1 + \frac{q^2}{\hbar^2}\,\eta_0^2\, K_b(0)\right] &= b(t_0)\left[1 + \frac{q^2}{\hbar^2}\,\eta_0^2\, K_b(\Delta)\right] \\ b(t_1) &= \frac{1 + \frac{q^2}{\hbar^2}\,\eta_0^2\, K_b(\Delta)}{\left[1 + \frac{q^2}{\hbar^2}\,\eta_0^2\, K_b(0)\right]^2} \end{aligned} \tag{2.6.24}$$

We can immediately see that the only dependence on the "pulse delay" $\delta$ comes from the $K_b(\Delta)$ in the numerator. Because $K_b(\Delta)$ is a complex number, $b(t_1)$ depends greatly on the amplitude and phase of the kernel evaluated at the time difference between the kicks, and even in this simple form it can display the reversed CEP-dependence we found in Section 2.4.

---

and solve it using linear algebra techniques, but this quickly becomes much more memory-intensive than the iterative procedure.

Although this delta-kick model is indeed very simple, it is difficult to draw any conclusions from it because the situation it presents is not very realistic. It also also seems difficult to extend it in any meaningful way. It may be helpful for building intuition about what the IDE is saying, but otherwise appears to be a dead end.

### 2.6.3 Hydrogen IDE Kernel with Partial Continuum-Continuum Interaction

One of the main things lacking from the minimal IDE derivation in Section 2.5.1 was a treatment of direct continuum-continuum interactions. These interactions become especially important when the ionization probability is large and the interaction time is long, because that is precisely when there is a lot of amplitude in the continuum and it has time to interact under the laser pulse. The interaction time being short was the primary reason we could ignore these interactions in [73].

To include the continuum-continuum interactions in some form, we need to take a different and more technical approach to the derivation. The approach below is based on the treatment of the continuum-continuum interaction presented in [90] [5].

We decompose the wavefunction into a single bound state and a continuum of momentum eigenstates (plane waves):

$$|\Psi(t)\rangle = c_b(t)\,|b\rangle + \int \mathrm{d}^3p\; c_{\mathbf{p}}(t)\,|\mathbf{p}\rangle \tag{2.6.25}$$

We write the Hamiltonian as a sum of three terms:

$$\widehat{\mathcal{H}} = \widehat{\mathcal{H}}_0 + \widehat{\mathcal{H}}_C + \widehat{\mathcal{H}}_I \tag{2.6.26a}$$

$$\widehat{\mathcal{H}}_0 = \frac{\widehat{p}^2}{2m} \tag{2.6.26b}$$

$$\widehat{\mathcal{H}}_C = -\frac{1}{4\pi\epsilon_0}\frac{1}{r} \tag{2.6.26c}$$

$$\widehat{\mathcal{H}}_I = -q\,\boldsymbol{\mathcal{E}}(t)\cdot\widehat{\mathbf{r}} \tag{2.6.26d}$$

[5] With thanks to Jeff Schmidt for helping me understand the technique described there.

Now use the Schrödinger equation to write down coupled differential equations:

$$
\begin{aligned}
i\hbar\,\dot{c}_b(t) &= c_b(t)\,\langle b|\widehat{\mathcal{H}}|b\rangle + \int \mathrm{d}^3p\, c_{\mathbf{p}}(t)\,\langle b|\widehat{\mathcal{H}}|\mathbf{p}\rangle \\
\dot{c}_b(t) &= -i\frac{1}{\hbar}c_b(t)\Big[\,\langle b|\widehat{\mathcal{H}}_0 + \widehat{\mathcal{H}}_C|b\rangle + \,\langle b|\widehat{\mathcal{H}}_I|b\rangle\Big] - i\frac{1}{\hbar}\int \mathrm{d}^3p\, c_{\mathbf{p}}(t)\Big[\,\langle b|\widehat{\mathcal{H}}_0|\mathbf{p}\rangle + \,\langle b|\widehat{\mathcal{H}}_C|\mathbf{p}\rangle + \,\langle b|\widehat{\mathcal{H}}_I|\mathbf{p}\rangle\Big]
\end{aligned}
\tag{2.6.27}
$$

We can simplify $\langle b|\widehat{\mathcal{H}}_0 + \widehat{\mathcal{H}}_C|b\rangle$: it's just $E_b$, the energy of the bound state (it is necessarily an energy eigenstate). Additionally, $\langle b|\widehat{\mathcal{H}}_I|b\rangle$ is zero by symmetry (using, for example, the hydrogen ground state). We will assume that $\langle b|\widehat{\mathcal{H}}_0|\mathbf{p}\rangle$ and $\langle b|\widehat{\mathcal{H}}_C|\mathbf{p}\rangle$ are zero. The first is not so good: we are pretending that the plane waves are the true continuum states, which would immediately make their overlaps with the bound state zero, and which is obviously not true. The second is the strong field approximation, i.e., that the free electrons do not interact with the Coulomb potential, which is quite reasonable for an intense pulse with a long interaction time. We are left with

$$
\dot{c}_b(t) = -i\omega_b\, c_b(t) - i\frac{1}{\hbar}\int \mathrm{d}^3p\, c_{\mathbf{p}}(t)\,\langle b|\widehat{\mathcal{H}}_I|\mathbf{p}\rangle \tag{2.6.28}
$$

For $\dot{c}_{\mathbf{p}}$, we have

$$
\begin{aligned}
i\hbar\dot{c}_{\mathbf{p}}(t) &= c_b(t)\,\langle \mathbf{p}|\widehat{\mathcal{H}}|b\rangle + \int \mathrm{d}^3p'\, c_{\mathbf{p}'}(t)\,\big\langle \mathbf{p}\big|\widehat{\mathcal{H}}\big|\mathbf{p}'\big\rangle \\
i\hbar\dot{c}_{\mathbf{p}}(t) &= c_b(t)\Big[\,\langle \mathbf{p}|\widehat{\mathcal{H}}_0 + \widehat{\mathcal{H}}_C|b\rangle + \,\langle \mathbf{p}|\widehat{\mathcal{H}}_I|b\rangle\Big] + \int \mathrm{d}^3p'\, c_{\mathbf{p}'}(t)\Big[\,\big\langle \mathbf{p}\big|\widehat{\mathcal{H}}_0\big|\mathbf{p}'\big\rangle + \,\big\langle \mathbf{p}\big|\widehat{\mathcal{H}}_C\big|\mathbf{p}'\big\rangle + \,\big\langle \mathbf{p}\big|\widehat{\mathcal{H}}_I\big|\mathbf{p}'\big\rangle\Big] \\
i\hbar\dot{c}_{\mathbf{p}}(t) &= c_b(t)\,\langle \mathbf{p}|\widehat{\mathcal{H}}_I|b\rangle + E_p c_{\mathbf{p}}(t) + \int \mathrm{d}^3p'\, c_{\mathbf{p}'}(t)\,\big\langle \mathbf{p}\big|\widehat{\mathcal{H}}_I\big|\mathbf{p}'\big\rangle
\end{aligned}
\tag{2.6.29}
$$

where similar assumptions to those made for $\dot{c}_b$ have been made.

In the past, we have simply neglected the last term of (2.6.29), $\langle \mathbf{p}|\widehat{\mathcal{H}}_I|\mathbf{p}'\rangle$, which represents the continuum-continuum interaction induced by the electric field. It turns out that a reasonable way to treat this term is to decompose it into two parts: a part that is singular at $p = p'$, which corresponds to absorbing a photon and changing direction and angular momentum but not magnitude of momentum, and a non-singular part which handles everything else [90]. This looks

something like

$$\begin{aligned}\langle \mathbf{p}|\widehat{\mathcal{H}}_I|\mathbf{p}'\rangle &= \langle \mathbf{p}|-\boldsymbol{\mathcal{E}}(t)\cdot\widehat{\mathbf{r}}|\mathbf{p}'\rangle \\ &= -\boldsymbol{\mathcal{E}}(t)\cdot\langle \mathbf{p}|\widehat{\mathbf{r}}|\mathbf{p}'\rangle \\ \langle \mathbf{p}|\widehat{\mathcal{H}}_I|\mathbf{p}'\rangle &= -q\boldsymbol{\mathcal{E}}(t)\cdot\left[i\hbar\,\boldsymbol{\nabla}_{\mathbf{p}}\delta\big(p-p'\big)+\mathbf{g}(p,p')\right]\end{aligned} \tag{2.6.30}$$

The form of the singular part is suggested by the representation of the position operator in momentum space. Taking only the singular part, the continuum-continuum interaction integral becomes (being careful about how we order the terms, now that we have some weird operators in play)

$$\begin{aligned}\int \mathrm{d}^3p'\, c_{\mathbf{p}'}(t)\,\langle \mathbf{p}|\widehat{\mathcal{H}}_I|\mathbf{p}'\rangle &= -iq\hbar\int \mathrm{d}^3p'\,\boldsymbol{\mathcal{E}}(t)\cdot\boldsymbol{\nabla}_{\mathbf{p}}\delta\big(p-p'\big)c_{\mathbf{p}'}(t) \\ \int \mathrm{d}^3p'\, c_{\mathbf{p}'}(t)\,\langle \mathbf{p}|\widehat{\mathcal{H}}_I|\mathbf{p}'\rangle &= -iq\hbar\,\boldsymbol{\mathcal{E}}(t)\cdot\boldsymbol{\nabla}_{\mathbf{p}}c_{\mathbf{p}}(t)\end{aligned} \tag{2.6.31}$$

If we expand $\langle \mathbf{p}|\widehat{\mathcal{H}}_I|b\rangle = -q\boldsymbol{\mathcal{E}}(t)\cdot\langle \mathbf{p}|\widehat{\mathbf{r}}|b\rangle \equiv -q\boldsymbol{\mathcal{E}}(t)\cdot\mathbf{d}(\mathbf{p})$ (the spatial dipole moment), we have

$$\begin{aligned}i\hbar\,\dot{c}_{\mathbf{p}}(t) &= -q\boldsymbol{\mathcal{E}}(t)\cdot\mathbf{d}(\mathbf{p})c_b(t)+E_pc_{\mathbf{p}}(t)-iq\hbar\,\boldsymbol{\mathcal{E}}(t)\cdot\boldsymbol{\nabla}_{\mathbf{p}}c_{\mathbf{p}}(t) \\ \dot{c}_{\mathbf{p}}(t) &= i\frac{q}{\hbar}\boldsymbol{\mathcal{E}}(t)\cdot\mathbf{d}(\mathbf{p})c_b(t)-i\omega_p\,c_{\mathbf{p}}(t)-q\,\boldsymbol{\mathcal{E}}(t)\cdot\boldsymbol{\nabla}_{\mathbf{p}}c_{\mathbf{p}}(t)\end{aligned} \tag{2.6.32}$$

Although this differential equation doesn't look pleasant, it's actually solvable by finding an integrating factor, although we need to be much more formal about it than typically required. Let's do it one dimension (this is sufficient because the equation is linear, so we can just add up the solutions across the dot products).

First, move all the differential operators to one side:

$$\left[\partial_t+q\,\mathcal{E}(t)\partial_p\right]c_p(t) = -i\omega_p\,c_p(t)+i\frac{q}{\hbar}\,\mathcal{E}(t)\,d(p)\,c_b(t) \tag{2.6.33}$$

Recall that the electric field is the negative derivative of the vector potential: $\mathcal{E}(t) = -\dot{\mathcal{A}}$. Insert that, and drop the explicit time dependences for simplicity:

$$\Big[\partial_t-q\,\dot{\mathcal{A}}(t)\,\partial_p\Big]\,c_p = -i\omega_p\,c_p-i\frac{q}{\hbar}\dot{\mathcal{A}}(t)\,d(p)\,c_b \tag{2.6.34}$$

Let's solve the homogeneous problem first. Drop the last term:

$$\Big[\partial_t - q\,\dot{\mathcal{A}}\,\partial_p\Big]\,c_p = -i\omega_p\,c_{\mathbf{p}} \tag{2.6.35}$$

Suppose the solution has the form $c_{\mathbf{p}}(t) = \exp[N(p,t)]$ for some $N(p,t)$, as yet undetermined. Then we have

$$\begin{aligned}\Big[\partial_t - q\,\dot{\mathcal{A}}\,\partial_p\Big]\,e^{N(p,t)} &= -i\omega_p\,e^{N(p,t)}\\ \Big[\partial_t - q\,\dot{\mathcal{A}}\,\partial_p\Big]\,N(p,t) &= -i\omega_p\\ \Big[\partial_t - q\,\dot{\mathcal{A}}\,\partial_p\Big]\,N(p,t) &= f(p)\end{aligned} \tag{2.6.36}$$

We need to guess a solution to this differential equation. If $f = 0$, this would be a wave equation, and the solution could be any function $N(p + q\mathcal{A})$. If $\dot{\mathcal{A}} = 0$ and $f = h(p,t)$, the solution is just

$$N = \int_{t_i}^{t} \mathrm{d}t'\,h(p,t') \tag{2.6.37}$$

Let's try a "combination" of those solutions:

$$N = \int_{t_i}^{t} \mathrm{d}t'\,f(p + Q(t,t')) \tag{2.6.38}$$

where $Q$ is an undetermined function. Plug this back into the differential equation (this requires the Leibniz integration rule because the bounds of the integral depend on the variable we're taking the derivative in):

$$\begin{aligned}\partial_t N(p,t) - q\,\dot{\mathcal{A}}\,\partial_p N(p,t) &= f(p)\\ f(p + Q(t,t)) + \int_{t_i}^{t} \mathrm{d}t'\,\dot{f}(p + Q(t,t'))\dot{Q}(t,t') - q\,\dot{\mathcal{A}}\int_{t_i}^{t} \mathrm{d}t'\,\dot{f}(p + Q(t,t')) &= f(p)\end{aligned} \tag{2.6.39}$$

Suppose we choose $Q(t,t) = 0$. Then the first term on the left will cancel the driving term on the right:

$$\int_{t_i}^{t} \mathrm{d}t'\,\dot{f}(p + Q(t,t'))\dot{Q}(t,t') = q\,\dot{\mathcal{A}}\int_{t_i}^{t} \mathrm{d}t'\,\dot{f}(p + Q(t,t')) \tag{2.6.40}$$

Let's guess that $Q(t,t') = q\,\mathcal{A}(t) - q\,\mathcal{A}(t')$, because any such function will automatically have $Q(t,t) = 0$, and we know $\mathcal{A}$ should matter somehow. Then

$$\dot{Q}(t,t') = q\dot{\mathcal{A}}(t), \tag{2.6.41}$$

which satisfies the above condition. So we have a solution to

$$\Big[\partial_t - q\,\dot{\mathcal{A}}\,\partial_p\Big]\,N(p,t) = \widehat{L}\,c_p = f(p)\,c_p \tag{2.6.42}$$

which is

$$c_p = \exp\Big[\int_{t_i}^{t} \mathrm{d}t'\,f(p + q\,\mathcal{A}(t) - q\,\mathcal{A}(t'))\Big] \tag{2.6.43}$$

Note that this is equivalent to

$$\widehat{L}^{-1}[f(p)\,c_p] = \exp\Big[\int_{t_i}^{t} \mathrm{d}t'\,f(p + q\,\mathcal{A}(t) - q\,\mathcal{A}(t'))\Big] \tag{2.6.44}$$

which will be useful shortly.

Armed with this, we can solve the inhomogeneous equation:

$$\widehat{L}\,c_p = f(p)\,c_p + R(p,t) \tag{2.6.45}$$

where $R(p,t) = -iq\dot{\mathcal{A}}(t)\,d(p)\,c_b/\hbar$. We're going to attempt to find an integrating factor $M(p,t)$, such that

$$M\,\widehat{L}\,c_p = M\,f(p)\,c_p + M\,R \tag{2.6.46}$$

For this to work as an integrating factor, we need to be able to move the $M$ on the left inside the operator $\widehat{L}$. To check whether we can do that, let's just try it:

$$\begin{aligned}\widehat{L}[Mc_p] &= M\,\widehat{L}c_p + c_p\,\widehat{L}M \\ \widehat{L}[Mc_p] &= M\,f(p)\,c_p + MR + c_p\,\widehat{L}M\end{aligned} \tag{2.6.47}$$

Let's choose $\widehat{L}M = -Mf(p)$. Then the first and last terms on the right cancel, and $\widehat{L}[Mc_p] = MR$. This statement is very powerful! Observe:

$$\begin{aligned}\widehat{L}[Mc_p] &= MR \\ Mc_p &= \widehat{L}^{-1}[MR] \\ c_p &= M^{-1}\widehat{L}^{-1}[MR]\end{aligned} \tag{2.6.48}$$

Let's tackle that last part, since we already know how $\widehat{L}^{-1}$ acts on things:

$$\widehat{L}^{-1}[MR] = \int_{t_i}^{t} \mathrm{d}t'\, M(p + q\,\mathcal{A}(t) - q\,\mathcal{A}(t'), t')\, R(p + q\,\mathcal{A}(t) - q\,\mathcal{A}(t'), t') \tag{2.6.49}$$

Now we just need $M$ and $M^{-1}$. Well, earlier, we chose

$$\widehat{L}M = -f(p)M \tag{2.6.50}$$

This look a lot like $\partial_x f = -fx$, which is solved by $\exp(-fx)$, so let's say that

$$M(p,t) = \exp\left[-\int_{t_i}^{t} \mathrm{d}t'\, f(p + q\,\mathcal{A}(t) - q\,\mathcal{A}(t'), t')\right] \tag{2.6.51}$$

Now we can write the full solution:

$$\begin{aligned}c_p(t) &= \exp\left[\int_{t_i}^{t} \mathrm{d}t''\, f(p + q\,\mathcal{A}(t) - q\,\mathcal{A}(t''), t'')\right] \int_{t_i}^{t} \mathrm{d}t' \exp\left[-\int_{t_i}^{t'} \mathrm{d}t''\, f(p + q\,\mathcal{A}(t') - q\,\mathcal{A}(t''), t'')\right] \\ &\qquad \times R(p + q\,\mathcal{A}(t) - q\,\mathcal{A}(t'), t') \\ c_p(t) &= \int_{t_i}^{t} \mathrm{d}t' \exp\left[\int_{t_i}^{t} \mathrm{d}t''\, f(p + q\,\mathcal{A}(t) - q\,\mathcal{A}(t''), t'') - \int_{t_i}^{t'} \mathrm{d}t''\, f(p + q\,\mathcal{A}(t') - q\,\mathcal{A}(t''), t'')\right] \\ &\qquad \times R(p + q\,\mathcal{A}(t) - q\,\mathcal{A}(t'), t') \\ c_p(t) &= \int_{t_i}^{t} \mathrm{d}t'\, R(p + q\,\mathcal{A}(t) - q\,\mathcal{A}(t'), t') \exp\left[\int_{t'}^{t} \mathrm{d}t''\, f(p + q\,\mathcal{A}(t) - q\,\mathcal{A}(t''), t'')\right]\end{aligned} \tag{2.6.52}$$

Plugging everything back in and going back to three dimensions, we have

$$c_{\mathbf{p}}(t) = i\frac{q}{\hbar}\int_{t_i}^{t} \mathrm{d}t'\, c_b(t')\boldsymbol{\mathcal{E}}(t')\cdot\mathbf{d}(\mathbf{p}+q\,\boldsymbol{\mathcal{A}}(t)-q\,\boldsymbol{\mathcal{A}}(t'))\,\exp\!\left[-i\frac{1}{2m\hbar}\int_{t'}^{t}\mathrm{d}t''\,\left[\mathbf{p}+q\,\boldsymbol{\mathcal{A}}(t)-q\,\boldsymbol{\mathcal{A}}(t'')\right]^2\right] \tag{2.6.53}$$

Let's plug back into the equation for $\dot{c}_b$, (2.6.28):

$$\begin{aligned}
\dot{c}_b(t) &= -i\omega_b\, c_b(t) - i\frac{1}{\hbar}\int \mathrm{d}^3p\, c_{\mathbf{p}}(t)\,\langle b|\widehat{\mathcal{H}}_I|\mathbf{p}\rangle \\
\dot{c}_b(t) &= -i\omega_b\, c_b(t) + i\frac{q}{\hbar}\int \mathrm{d}^3p\, c_{\mathbf{p}}(t)\,\boldsymbol{\mathcal{E}}(t)\cdot\mathbf{d}(\mathbf{p}) \\
\dot{c}_b(t) &= -i\omega_b\, c_b(t) - \frac{q^2}{\hbar^2}\int \mathrm{d}^3p\,\boldsymbol{\mathcal{E}}(t)\cdot\mathbf{d}(\mathbf{p})\int_{t_i}^{t}\mathrm{d}t'\, c_b(t')\boldsymbol{\mathcal{E}}(t')\cdot\mathbf{d}(\mathbf{p}+q\,\boldsymbol{\mathcal{A}}(t)-q\,\boldsymbol{\mathcal{A}}(t')) \\
&\qquad\times\exp\!\left[-i\frac{1}{2m\hbar}\int_{t'}^{t}\mathrm{d}t''\,\left[\mathbf{p}+q\,\boldsymbol{\mathcal{A}}(t)-q\,\boldsymbol{\mathcal{A}}(t'')\right]^2\right]
\end{aligned} \tag{2.6.54}$$

Remove the first term on the right by defining $b(t) = \exp(-i\omega_b t)\, c_b(t)$, and define $\boldsymbol{\mathcal{A}}(t,t') = \boldsymbol{\mathcal{A}}(t) - \boldsymbol{\mathcal{A}}(t')$ for notational compactness:

$$\begin{aligned}
\dot{b}(t) &= -\frac{q^2}{\hbar^2}\int \mathrm{d}^3p\,\boldsymbol{\mathcal{E}}(t)\cdot\mathbf{d}(\mathbf{p})\int_{t_i}^{t}\mathrm{d}t'\, b(t')\boldsymbol{\mathcal{E}}(t')\cdot\mathbf{d}(\mathbf{p}+q\,\boldsymbol{\mathcal{A}}(t,t')) \\
&\qquad\times\exp\!\left[i\omega_b(t-t') - i\frac{1}{2m\hbar}\int_{t'}^{t}\mathrm{d}t''\,\left[\mathbf{p}+q\,\boldsymbol{\mathcal{A}}(t,t'')\right]^2\right]
\end{aligned} \tag{2.6.55}$$

This equation is far too difficult to solve analytically, so let's start approximating things aggressively. First, we'll use an electric field that is linearly polarized along the $z$-axis.

$$\begin{aligned}
\dot{b}(t) &= -\frac{q^2}{\hbar^2}\mathcal{E}(t)\int_{t_i}^{t}\mathrm{d}t'\, b(t')\mathcal{E}(t')\exp\!\big[i\omega_b(t-t')\big]\int \mathrm{d}^3p\;\, d_z(\mathbf{p})\, d_z(\big|\mathbf{p}+q\,\mathcal{A}(t,t')\hat{\mathbf{z}}\big|) \\
&\qquad\times\exp\!\left[-i\frac{1}{2m\hbar}\int_{t'}^{t}\mathrm{d}t''\,\left[p^2+q\,p_z\,\mathcal{A}(t,t'')+q^2\mathcal{A}^2(t,t'')\right]\right]
\end{aligned} \tag{2.6.56}$$

Next we'll remove the two things that are hardest to deal with by replacing $d_z(|\mathbf{p}+q\,\mathcal{A}(t,t')\hat{\mathbf{z}}|)$ with $d_z(p)$ and neglecting $q\,p_z\,\mathcal{A}(t,t'')$ in the phase factor.

$$\dot{b}(t) = -\frac{q^2}{\hbar^2}\mathcal{E}(t)\int_{t_i}^{t}\mathrm{d}t'\, b(t')\mathcal{E}(t')\exp\!\left(-i\frac{q^2}{2m\hbar}\int_{t'}^{t}\mathrm{d}t''\,\mathcal{A}^2(t'')\right)\int \mathrm{d}^3p\;\,|d_z(\mathbf{p})|^2\exp\!\left(-i\frac{t-t'}{2m\hbar}p^2\right) \tag{2.6.57}$$

To do the momentum integral we need to know what $d_z(p)$ is. The calculation can be performed by expanding the plane wave in spherical partial waves:

$$\phi_{\mathbf{p}}(\mathbf{r}) = \frac{e^{i\mathbf{p}\cdot\mathbf{r}/\hbar}}{(2\pi\hbar)^{3/2}} = \frac{4\pi}{(2\pi\hbar)^{3/2}} \sum_{\ell,\,m} i^{\ell}\, j_{\ell}(pr/\hbar)\, Y_{\ell}^{m}(\hat{\mathbf{p}})\, [Y_{\ell}^{m}(\hat{\mathbf{r}})]^{*} \tag{2.6.58}$$

where $j_\ell$ is the spherical Bessel function with index $\ell$. The dipole moment integral becomes

$$\begin{aligned} d_z(\mathbf{p}) = \langle \mathbf{p}|\hat{\mathbf{z}}|b\rangle &= \int \mathrm{d}^3 r\, \phi_{\mathbf{p}}(\mathbf{r})\, z\, [\psi_{100}(\mathbf{r})]^{*} \\ &= \int_0^{\infty} \mathrm{d}r \int_0^{\pi} \mathrm{d}\theta \int_0^{2\pi} \mathrm{d}\phi\, r^2 \sin\theta\, r\cos\theta\, \frac{1}{\sqrt{4\pi}} \frac{2}{a_0^{3/2}} e^{-r/a_0}\, \frac{4\pi}{(2\pi\hbar)^{3/2}} \\ &\qquad \times \sum_{\ell,\,m} i^{\ell}\, j_{\ell}(pr/\hbar)\, Y_{\ell}^{m}(\hat{\mathbf{p}})\, [Y_{\ell}^{m}(\hat{\mathbf{r}})]^{*} \\ d_z(\mathbf{p}) &= \frac{8\pi}{2\sqrt{\pi}(2\pi\hbar a_0)^{3/2}} \int_0^{\infty} \mathrm{d}r\, r^3 e^{-r/a_0} \\ &\qquad \times \int_0^{\pi} \mathrm{d}\theta \int_0^{2\pi} \mathrm{d}\phi \sin\theta\cos\theta \sum_{\ell,\,m} i^{\ell}\, j_{\ell}(pr/\hbar)\, [Y_{\ell}^{m}(\hat{\mathbf{r}})]^{*}\, Y_{\ell}^{m}(\hat{\mathbf{p}}) \end{aligned} \tag{2.6.59}$$

The angular integral collapses to $2\sqrt{\pi/3}$ for $(\ell = 1, m = 0)$, and is zero otherwise.

$$d_z(\mathbf{p}) = i\frac{8\pi}{\sqrt{3}(2\pi\hbar a_0)^{3/2}} Y_1^0(\hat{\mathbf{p}}) \int_0^{\infty} \mathrm{d}r\, r^3 e^{-r/a_0} j_1(pr/\hbar) \tag{2.6.60}$$

Mathematica can do the radial integral:

$$d_z(\mathbf{p}) = i\frac{8\pi}{\sqrt{3}(2\pi\hbar a_0)^{3/2}} Y_1^0(\hat{\mathbf{p}})\, 8\frac{a_0^5}{\hbar} \frac{p}{\left(1+\frac{a_0^2}{\hbar^2}p^2\right)^3} \tag{2.6.61}$$

The quantity that enters the kernel integral is the squared magnitude of the matrix element:

$$|d_z(\mathbf{p})|^2 = \frac{512}{3\pi}\frac{3}{4\pi}\frac{a_0^7}{\hbar^5} \frac{p^2}{\left(1+\frac{a_0^2}{\hbar^2}p^2\right)^6} \cos^2\theta_p \tag{2.6.62}$$

Now we can evaluate the momentum integral

$$\begin{aligned}
\int \mathrm{d}^3p\ |d_z(\mathbf{p})|^2 \exp\!\left(-i\frac{t-t'}{2m\hbar}p^2\right) &= \int \mathrm{d}^3p\ \frac{512}{3\pi}\frac{3}{4\pi}\frac{a_0^7}{\hbar^5}\frac{p^2}{\left(1+\frac{a_0^2}{\hbar^2}p^2\right)^6}\cos^2\theta_p \exp\!\left(-i\frac{t-t'}{2m\hbar}p^2\right) \\
&= \frac{512}{3\pi}\frac{3}{4\pi}\frac{a_0^7}{\hbar^5}\int_0^\infty \mathrm{d}p \int_0^\pi \mathrm{d}\theta_p \int_0^{2\pi} \mathrm{d}\phi_p\, p^2 \sin\theta \\
&\qquad \times \frac{p^2}{\left(1+\frac{a_0^2}{\hbar^2}p^2\right)^6}\cos^2\theta_p \exp\!\left(-i\frac{t-t'}{2m\hbar}p^2\right) \\
&= \frac{512}{3\pi}\frac{3}{4\pi}\frac{a_0^7}{\hbar^5}\int_0^\infty \mathrm{d}p\, p^2 \frac{p^2}{\left(1+\frac{a_0^2}{\hbar^2}p^2\right)^6} \exp\!\left(-i\frac{t-t'}{2m\hbar}p^2\right) \\
&\qquad \times \int_0^\pi \mathrm{d}\theta_p \int_0^{2\pi} \mathrm{d}\phi_p \sin\theta\cos^2\theta_p
\end{aligned} \tag{2.6.63}$$

The angular integral is $4\pi/3$, which cancels the $3/4\pi$ in the prefactor. Now we have

$$\begin{aligned}
\int \mathrm{d}^3p\ |d_z(\mathbf{p})|^2 \exp\!\left(-i\frac{t-t'}{2m\hbar}p^2\right) &= \frac{512}{3\pi}\frac{a_0^7}{\hbar^5}\int_0^\infty \mathrm{d}p\, \frac{p^4}{\left(1+\frac{a_0^2}{\hbar^2}p^2\right)^6} \exp\!\left(-i\frac{t-t'}{2m\hbar}p^2\right) \\
\int \mathrm{d}^3p\ |d_z(\mathbf{p})|^2 \exp\!\left(-i\frac{t-t'}{2m\hbar}p^2\right) &= \frac{512}{3\pi}\frac{a_0^7}{\hbar^5}\frac{\hbar^5}{a_0^5}\int_0^\infty \mathrm{d}x\, \frac{x^4}{(1+x^2)^6} \exp\!\left(-i\,\frac{1}{2}\frac{\hbar}{ma_0^2}(t-t')x^2\right) \\
\int \mathrm{d}^3p\ |d_z(\mathbf{p})|^2 \exp\!\left(-i\frac{t-t'}{2m\hbar}p^2\right) &= \frac{512}{3\pi}\,a_0^2\int_0^\infty \mathrm{d}x\, \frac{x^4}{(1+x^2)^6} \exp\!\left(-i\,\frac{1}{2}\frac{\hbar}{ma_0^2}(t-t')x^2\right)
\end{aligned} \tag{2.6.64}$$

where we've changed variables to $x = a_0 p/\hbar = a_0 k$. Note that $\hbar/m\,a_0^2$ is the inverse of the atomic time, so the phase factor is measuring time differences in atomic times.

I'm not sure how to compute this integral by hand, but Mathematica or Sympy can provide a closed form expression. It ends up being exactly the original kernel $K_b(t-t')$, once we add in the bound state frequency shift term. We will lump this in with the extra phase terms that we got and define

$$K_b^{\mathrm{cc}}(t,t') = \exp\!\left[-i\frac{q^2}{2m\hbar}\int_{t'}^{t}\mathrm{d}t''\,\mathcal{A}^2(t,t'')\right]K_b(t-t') \tag{2.6.65}$$

where $K_b(t-t')$ is the original hydrogen-Bessel kernel, given by

$$K_b(t-t') = \frac{512}{3\pi}\,a_0^2\,e^{i\omega_b(t-t')}\int_0^\infty \mathrm{d}x\, \frac{x^4}{(1+x^2)^6} \exp\!\left(-i\,\frac{1}{2}\frac{\hbar}{ma_0^2}(t-t')x^2\right) \tag{2.6.66}$$

The $\mathcal{A}^2$ phase factor must be calculated numerically for a given pulse, while $K_b(t-t')$ is independent of the pulse parameters. The limits $t-t'=0$ and $t-t'=\infty$ are the same as the original kernel:

$$K_b^{\mathrm{cc}}(t,t) = a_0^2 \tag{2.6.67a}$$

$$K_b^{\mathrm{cc}}(t,-\infty) = 0 \tag{2.6.67b}$$

This is unsurprising, because the extra phase factors are only important when the vector potential is important, which is over "medium" timescales, during the pulse. At short times there is no phase difference, and at long times the exponential in the original kernel still dominates.

### 2.6.4 Instantaneous Ionization Rates in the Barrier-Suppression Regime

One of the primary mechanisms for ionization at small electric field amplitudes (relative to the electric field of the nucleus) is **tunneling**. When the electric field of the laser pulse comes through, it creates regions of space where the electron would have positive classical kinetic energy, as shown in Figure 2.12. Parts of the electron wavefunction can tunnel through the remaining potential barrier formed by the nucleus to these **classically-allowed regions**, and from there escape to infinity.

A great deal of work has been done to estimate the tunneling rate in a variety of regimes, but estimates generally disagree with each other [96]. Even worse, all of the above calculations stop being reasonable when the electric field becomes large enough to lower the total potential below the energy of the initial bound state (i.e., if there is no potential barrier at all), as illustrated in Figure 2.13. We believe that the IDE model may provide some insight into this regime without most of the extensive mathematical machinery employed by other approaches.

The minimum electric field amplitude for there to be no potential barrier is called the "critical" field amplitude $\mathcal{E}_{\mathrm{crit}}$. When the electric field amplitude is larger than this critical field, we are in the **barrier-suppression regime** [6]. We can approximate $\mathcal{E}_c$ for a hydrogenic atom by looking for the electric field amplitude that makes the potential maximum along the polarization axis $z$ equal to the ionization potential of the state we're interested in.

The total electric potential is the sum of the Coulomb potential $V_{\mathrm{Coulomb}}$ and the potential

[6] Barrier-suppression ionization (BSI) is also known as over-the-barrier ionization (OBI).

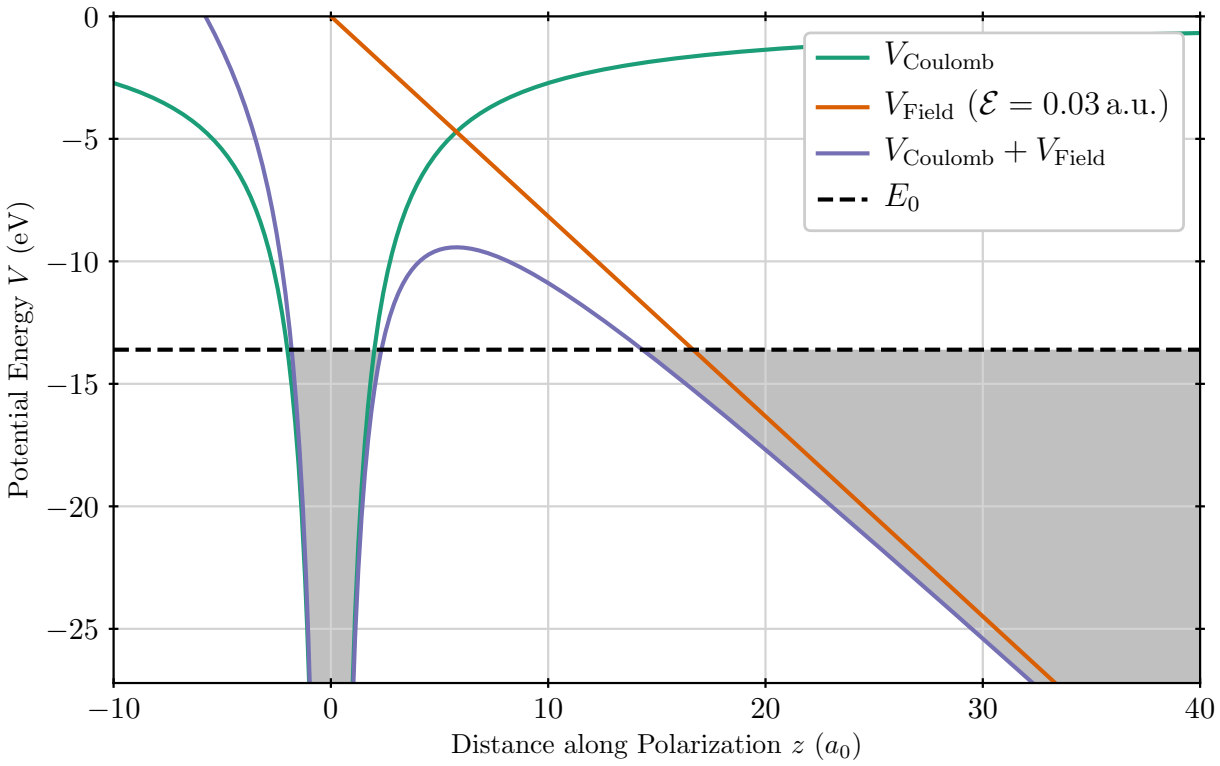


Figure 2.12: The electric potential as a function of distance along the polarization direction near a hydrogen atom as a linearly polarized electric field is applied. The field amplitude is three hundredths of the atomic electric field. The shaded region is the classically-allowed region for an electron with the ground state's energy (shown as a horizontal black dashed line). The combined Coulomb and external field potential create another classically-allowed region for the electron beyond a potential barrier. In this regime, the dominant ionization mechanism is tunneling.

caused by a static external electric field $\mathcal{E}$, $V_{\text{Field}}$:

$$\begin{aligned} V(z) &= V_{\text{Coulomb}}(z) + V_{\text{Field}}(z) \\ V(z) &= -\frac{e^2}{4\pi\epsilon_0}\frac{1}{z} - e\,\mathcal{E}\,z \end{aligned} \tag{2.6.68}$$

where $n$ is the number of unscreened protons in the nucleus of the hydrogenic atom. The potential maximum occurs when the derivative of $V(z)$ is zero. We call the position where this occurs $z_0$ and

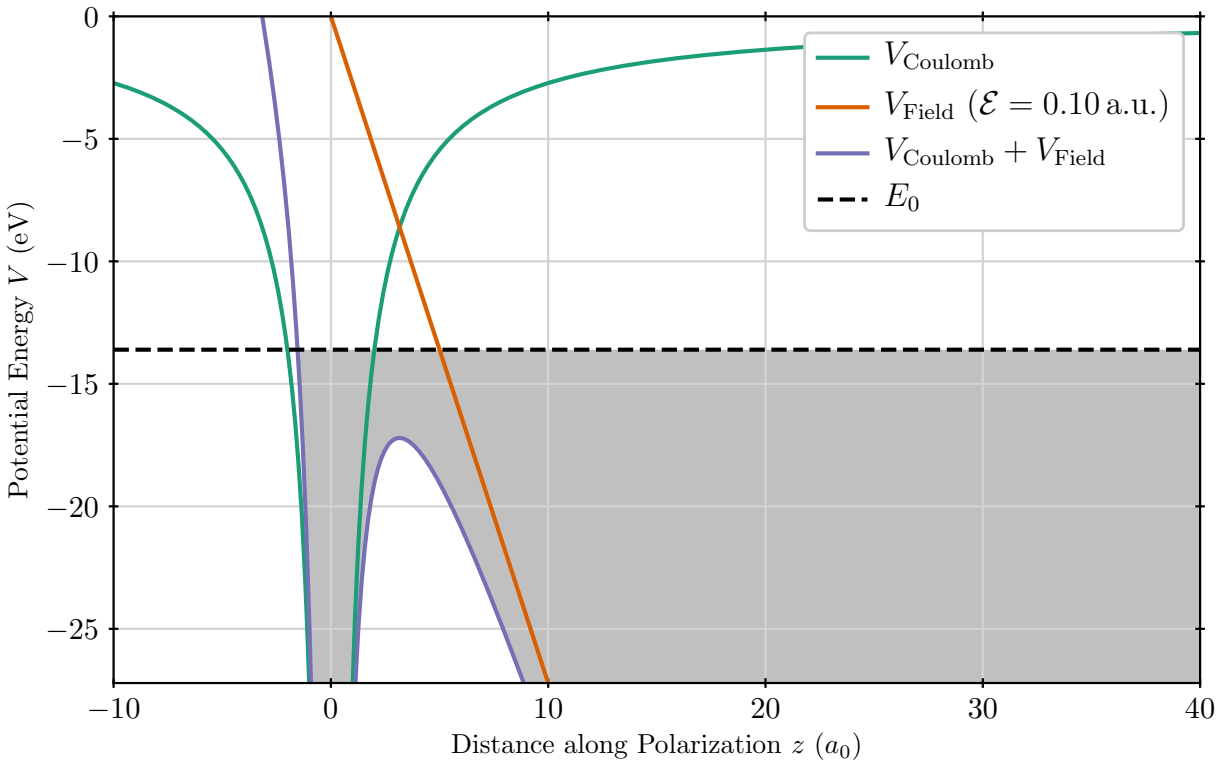


Figure 2.13: The electric potential as a function of distance along the polarization direction near a hydrogen atom as a linearly polarized electric field is applied. The field amplitude is one tenth of the atomic electric field. The shaded region is the classically-allowed region for an electron with the ground state's energy (shown as a horizontal black dashed line). The electric field amplitude is large enough that there is no potential barrier between the ground state and large $z$. This is the barrier-suppression regime.

solve for it:

$$\begin{aligned} \frac{\partial V(z)}{\partial z} &= \frac{ne^2}{4\pi\epsilon_0}\frac{1}{z^2} - e\,\mathcal{E} \\ \implies z_0 &= \sqrt{\frac{ne}{4\pi\epsilon_0\,\mathcal{E}_c}} \end{aligned} \tag{2.6.69}$$

Now plug this back into $V(z)$ to determine the potential at that distance:

$$\begin{aligned} V(z_0) &= -\frac{e^2}{4\pi\epsilon_0}\frac{1}{z_0} - e\,\mathcal{E}\,z_0 \\ &= -\frac{e^2}{4\pi\epsilon_0}\frac{1}{\sqrt{\frac{ne}{4\pi\epsilon_0\,\mathcal{E}_c}}} - e\,\mathcal{E}\,\sqrt{\frac{ne}{4\pi\epsilon_0\,\mathcal{E}_c}} \\ V(z_0) &= -\sqrt{\frac{ne^3\mathcal{E}_c}{\pi\epsilon_0}} \end{aligned} \tag{2.6.70}$$

Now we set $V(z_0) = \Phi$, the ionization potential of the bound state, and solve for $\mathcal{E}_c$:

$$\begin{aligned} V(z_0) = -\sqrt{\frac{ne^3\mathcal{E}_c}{\pi\epsilon_0}} &= \Phi \\ \mathcal{E}_c &= \frac{\pi\epsilon_0}{ne^3}\Phi^2 \end{aligned} \tag{2.6.71}$$

The instantaneous critical intensity $P_c$ is

$$P_c = \frac{\pi^2 c\epsilon_0^3}{n^2 e^6}\Phi^4 \tag{2.6.72}$$

For hydrogen, $\mathcal{E}_c$ is one-sixteenth of the atomic electric field, $\mathcal{E}_c \approx 3.2 \times 10^{10}\,\mathrm{V\,m^{-1}}$. This calculation is very crude, and other estimates place the critical field somewhat higher, at $\mathcal{E} \approx 0.15\,\mathrm{a.u.}$ [97]. The problems with this model are that it only considers the dimension along the polarization axis, while in reality the electron wavefunction deforms in all three dimensions in response to the electric field, and that the barrier opens more like a hole in a sphere than a wall dropping. Since the barrier does not completely vanish, some of the electron wavefunction can "leak", while other parts are still tunneling, so the transition between the two regions should also be somewhat smooth. However, all of these estimates are relatively close, and give us a rough idea of the electric field amplitude where the transition occurs: about a fifth of an atomic electric field.

A series of papers by various Bauers ([96–98]) is basically a chronicle of attempts to convince people that BSI is fundamentally different than tunneling ionization and that different and better techniques are needed to understand the electron's behavior in that regime correctly. Of particular interest to us is an empirical observation from [96]: in the BSI regime, the bound state population

$\Gamma$ (this is Bauer's notation) appears to obey

$$\Gamma(t) = \exp\left( - \int_{t_0}^{t} \mathrm{d}t' \, W\big[\mathcal{E}(t')\big] \right) \tag{2.6.73}$$

where the bound state population implicitly begins at 1, and

$$W[\mathcal{E}(t)] = \begin{cases} W'[\mathcal{E}(t)] & \mathcal{E} < \mathcal{E}_{\text{crit}} \\ 2.4\,\mathcal{E}(t)^2 & \mathcal{E} \geq \mathcal{E}_{\text{crit}} \end{cases} \tag{2.6.74}$$

where $W'(t)$ is some tunneling ionization rate used when below the critical field. The electric field amplitude $\mathcal{E}$ is expressed in atomic units, so that $W$ is the fractional decay rate of the bound state probability per atomic time. Bauer chooses $\mathcal{E}_{\text{crit}}$ such that $W[\mathcal{E}(t)]$ is continuous (this means that $\mathcal{E}_{\text{crit}}$ depends on the tunneling model you choose for $W'$, *not* on any other way of estimating the critical field, such as the one demonstrated above). The numerical prefactor 2.4 was chosen by averaging over the simulated instantaneous ionization rates caused by a variety of different pulses.

A comparison between TDSE simulations and Bauer's "Tunneling + BSI" rate for femtosecond-scale multi-cycle Gaussian pulses (parameterized by the amplitude prefactor $\mathcal{E}_0$, the center frequency $\omega$, and the number of cycles $N$) is shown in Figure 2.14. They are quite similar, both qualitatively and quantitatively, although not perfect, as might be expected of a model that depends so sensitively on a single constant obtained by averaging over disparate simulations.

Our interest in this is that the IDE model looks like $\mathcal{E}(t) \int \mathrm{d}t' \, \mathcal{E}(t')$, which looks like $\mathcal{E}^2(t)$ if you squint. Is there a way to go to some limit and get an instantaneous ionization rate similar to Bauer's empirical formula?

To see if there is, we will begin with the IDE (2.5.12):

$$\dot{b}(t) = -\frac{q^2}{\hbar^2} \, \mathcal{E}(t) \int_{-\infty}^{t} \mathrm{d}t' \, b(t') \, \mathcal{E}(t') \, K_b(t - t'). \tag{2.6.75}$$

We will assume that the timescales over which $b(t)$ and $\mathcal{E}(t)$ change are much slower than the kernel timescale $\tau_b$. Equivalent, we assume that they are constant over the range that the kernel amplitude is non-negligible. This is appropriate for the pulses used by Bauer, which are femtosecond-scale multi-cycle Gaussian pulses. Then we can say that $b(t') \, \mathcal{E}(t') \to b(t) \, \mathcal{E}(t)$ and pull them out of the

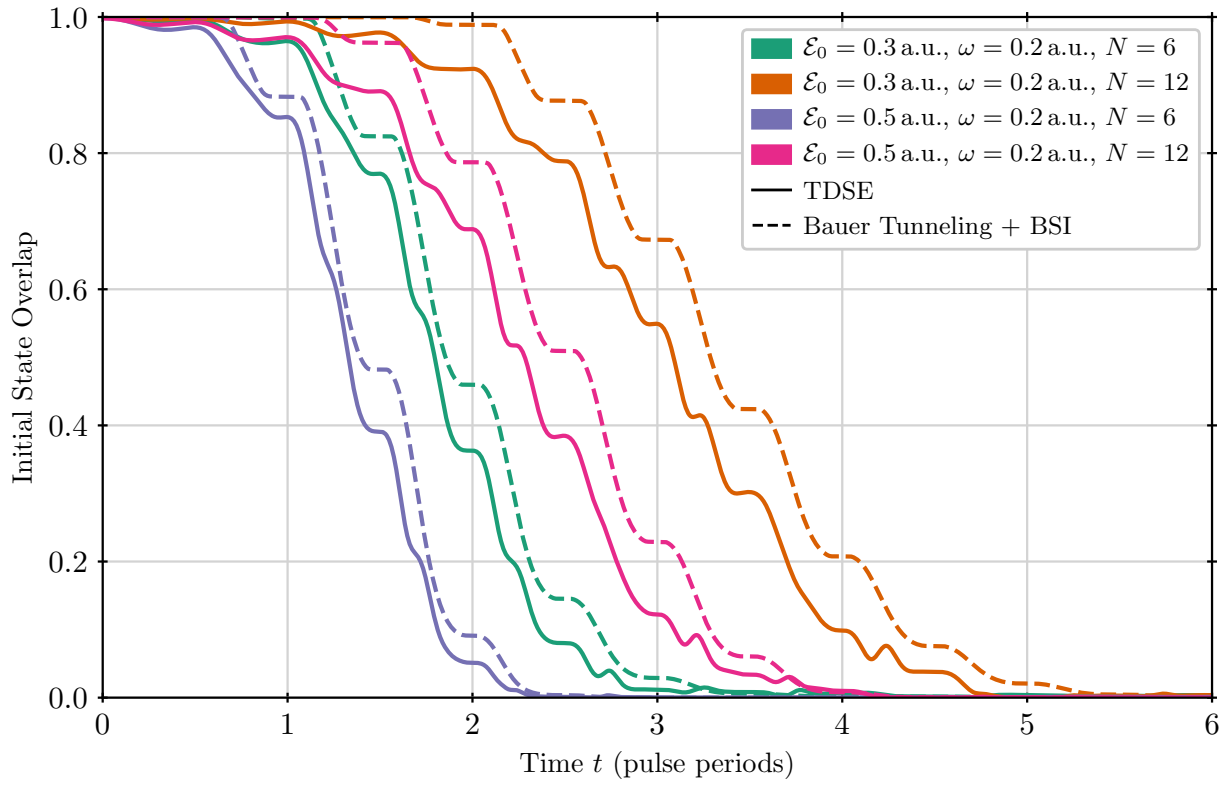


Figure 2.14: A comparison between between the full TDSE and the empirical Bauer Tunneling + BSI model (2.6.74). This empirical model is capturing the basic behavior of the ionization process. This is a reproduction of a figure from [96].

integral:

$$\dot{b}(t) = -b(t)\,\frac{q^2}{\hbar^2}\,\mathcal{E}(t)^2 \int_{-\infty}^{t} \mathrm{d}t'\; K_b(t-t'). \tag{2.6.76}$$

Numerically integrating the right hand side results in

$$\dot{b}(t) = -i\gamma \frac{\hbar}{m a_0^2}\,\mathcal{E}(t)^2\, b(t) \tag{2.6.77}$$

where $\gamma = 1.16$ for the approximate hydrogen kernel from Section 2.5.2 Note that $\hbar/ma_0^2$ is the inverse of the atomic time, so the number $\gamma$ is precisely the ionization rate (for the bound state amplitude) expressed in atomic units (per atomic electric field squared, per atomic time), The

formal solution to the differential equation (2.6.77) is

$$b(t) = \exp\left(-i \int_{-\infty}^{t} \mathrm{d}t' \, A \, \mathcal{E}(t)^2\right) \tag{2.6.78}$$

so the remaining bound state population is

$$|b(t)|^2 = \exp\left(-i \int_{-\infty}^{t} \mathrm{d}t' \, 2\gamma \, \mathcal{E}(t)^2\right) \tag{2.6.79}$$

This is exactly the same form as in Bauer's instantaneous ionization rate formula (2.6.73). We would say that the numeric prefactor in front of $\mathcal{E}(t)^2$ in that formula is $2\gamma = 2.33i$, compared to the empirical $-2.4$ that Bauer found. Although this is close in magnitude (which is promising), the phase is completely wrong. The $i$ should switch the result from decay to oscillation, and this is precisely what we see in simulations.

We performed simulations using the minimal IDE model, but also included the Landau tunneling rate when below the critical electric field amplitude predicted by Bauer's method. As shown in Figure 2.15, for the pulses used in [96], the IDE tends to oscillate instead of decay.

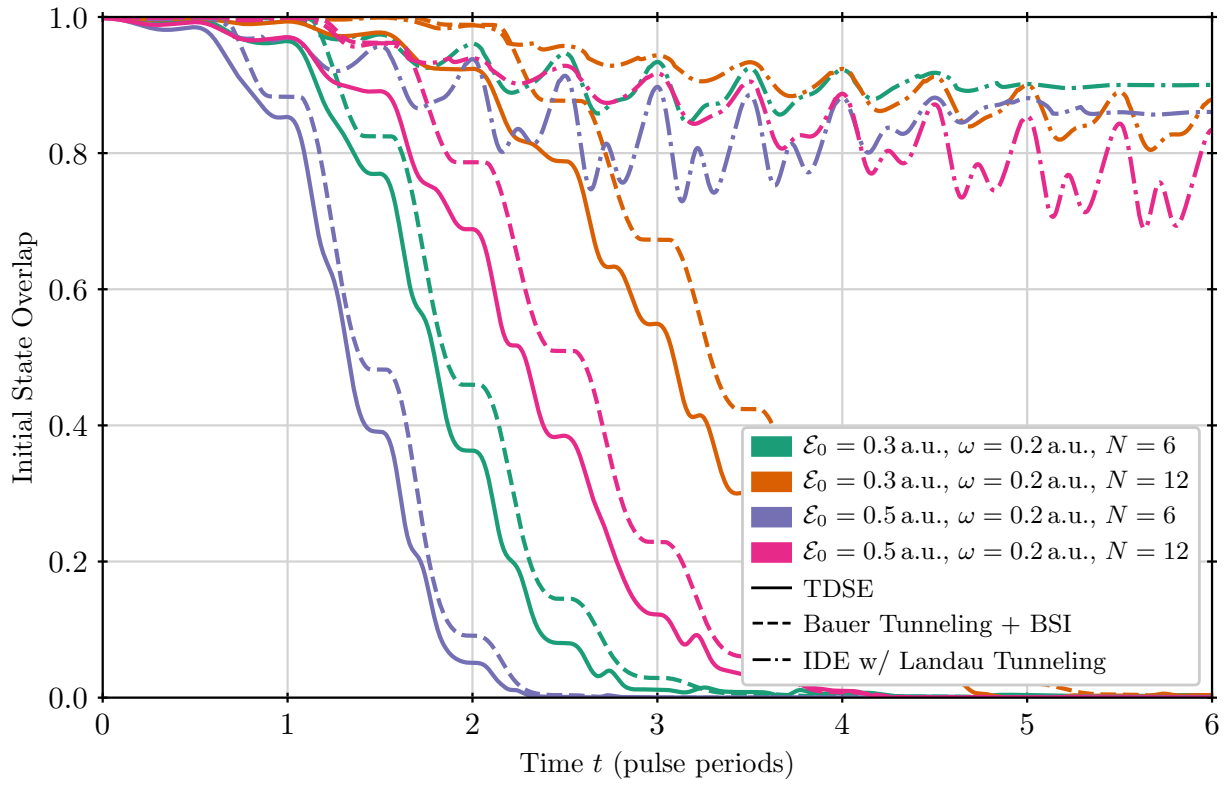


Figure 2.15: A comparison between between the full TDSE, the empirical Bauer Tunneling + BSI model (2.6.74), and the minimal IDE model (2.5.12). The minimal IDE model is not behaving like the TDSE: instead of the initial state overlap decaying, it predicts that it remains large and oscillates.

However, the fact that *something* is happening indicates we might still be on the right track. That we get oscillations instead of decay indicates that the overall phase of the term in the exponent may be wrong. If we shifted the phase so that the overall exponent became mostly-real instead of mostly-imaginary, it would cause decay (or growth) instead of oscillations. If we arbitrarily modify the kernel by phase-shifting it like $K(t,t') \to i\,K(t,t')$, such that the above calculation that resulted in $2\gamma = 2.33i$ would instead give $2\gamma = -2.33$, we get a startlingly good result, as shown in Figure 2.16.

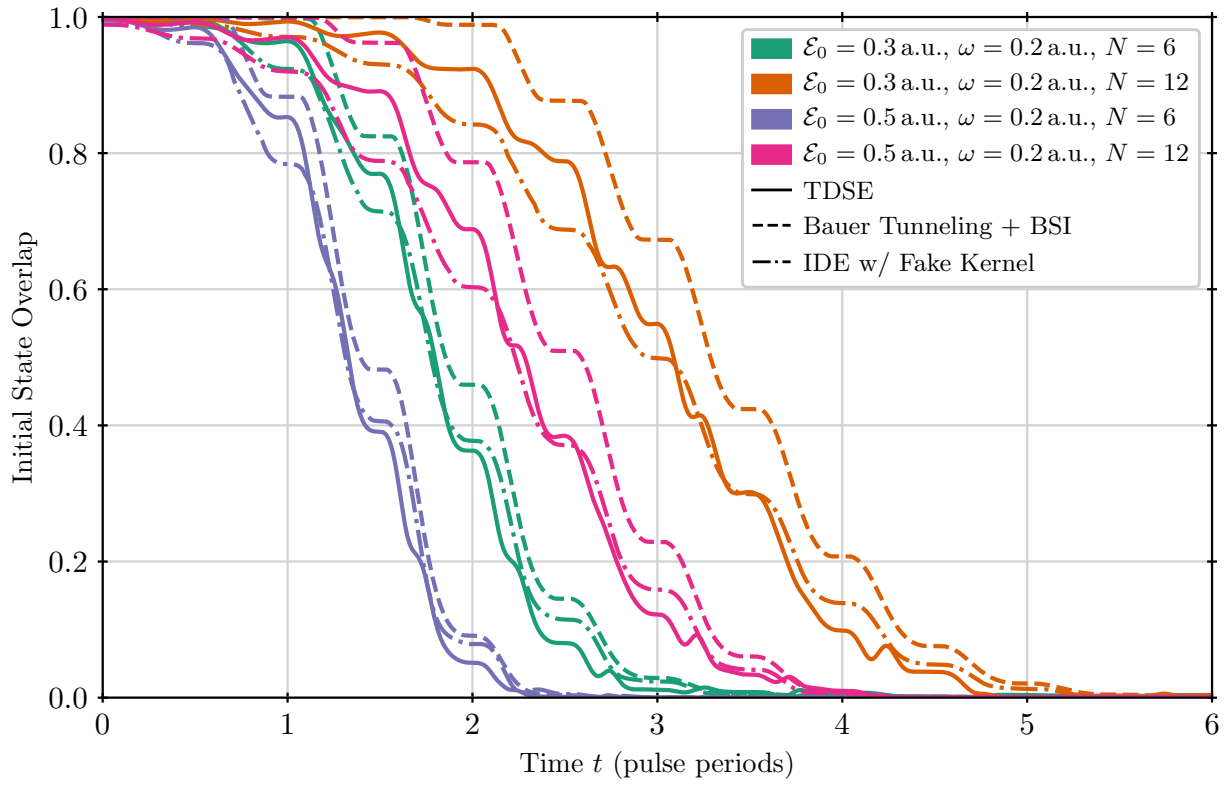


Figure 2.16: A comparison between between the full TDSE, the empirical Bauer Tunneling + BSI model (2.6.74), and an empirically-modified IDE model, where the kernel has been phase-shifted by multiplying it by $i$. The empirically-modified IDE model is behaving much better than the minimal IDE model: it is approximately as wrong as the empirical tunneling model is.

Of course, this is not terribly meaningful, because we don't yet understand where such a phase shift might arise from. One possibility is that it arises from the continuum-continuum interactions, which we learned how to treat in the previous section. If we use the improved kernel with partial continuum-continuum interactions (2.6.65), we lose the ability to simply perform the integral as we did above (because the kernel now depends on the pulse shape), but we can certainly plug in some numbers and see what happens. We ran IDE simulations with this kernel, shown in Figure 2.17. The results are improved from Figure 2.15, but still far from the empirically-modified kernel of Figure 2.16.

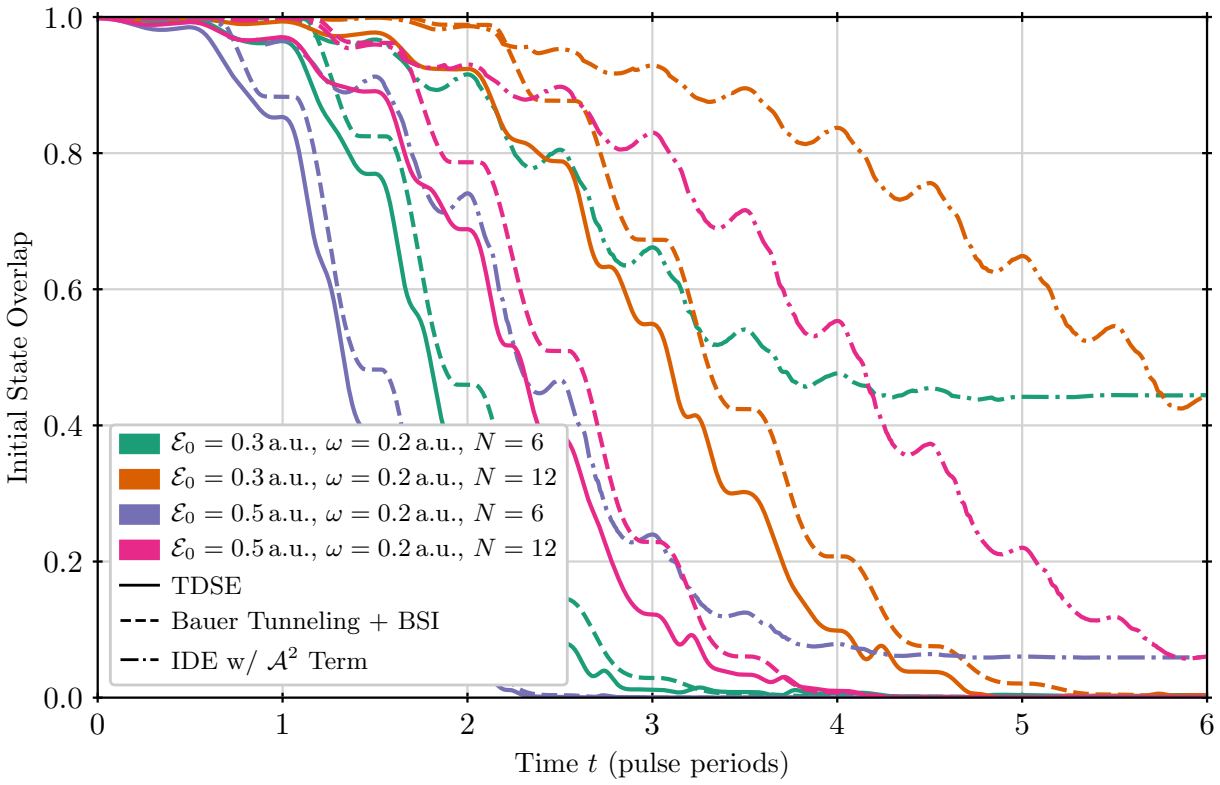


Figure 2.17: A comparison between between the full TDSE, the empirical Bauer Tunneling + BSI model (2.6.74), and an IDE model with partial continuum-continuum interactions (2.6.65). This is certainly closer to the TDSE and empirical tunneling model, but we have not progressed as far as the empirically-modified IDE model using in Figure 2.16.

Further improvements to the IDE model may be able to capture the simple ionization rate model proposed by Bauer more accurately.

## 2.7 Conclusions and Future Work

The work discussed in this chapter began with trying to answer a focused question about timescale-dependence in ionization probability for ultrashort intense pulses. To answer that question, the scope of the investigation necessarily grew larger, and we found a different question, regarding the CEP-dependence of the ionization instead. Despite being able to answer the CEP-dependence question, we were unable to satisfactorily address our original question about how the ionization probability depends on the pulse duration.

Thus, there are two obvious possible next steps for this project. The first is to pursue that

original question: to understand the necessary coupled quantum-electrodynamic model for such short and intense pulses, so we can validate whether the apparent decrease shown in Figure 2.5 is truly what it appears to be. One can image building a simple model of the ionization probability, perhaps based on the same IDE model we used in this research, that explains in a quantum sense how the classical intuition about bound particles translates (or doesn't translate) to this situation.

This path is intriguing because it hints at possible applications of ultrafast science. Krausz predicts that ultrafast control of electrons will become an important part of technology in the coming years [68]. For example, we have considered the idea of using the pulse duration and CEP to selectively ionize the inner-shell electrons of large atoms while leaving outer-shell electrons untouched. This creates population inversion, which could then be used to drive a laser system, likely at a very high photon frequency that is unreachable by other techniques. However, simulating any such process is beyond the technical capabilities that have been implemented for this project so far. Substantial work would need to be done to model that kind of device using our computational techniques.

The other possible next step is to continue pursuing connections to barrier-suppression ionization. As discussed in Section 2.6, we are tantalizingly close to understanding where certain empirical observations about the tunneling rate in the BSI regime come from. Perhaps there are additional physically-motivated modifications that we can make to the IDE model that will bring it more in line with what we observe in TDSE simulations.

# Appendices

These appendices are a mix of long-form derivations extracted from the main text due to their length, and shorter derivations of specific, focused techniques that support the numerical methods used in the simulations.

## A Finding Microsphere Modes Numerically

Finding the free-space wavelengths (or, equivalently, frequencies) of a microsphere's whispering gallery resonator modes requires solving a transcendental equation called the modal equation, which can be written in terms of the cylindrical Bessel and Neumann functions $J$ and $Y$ (i.e., Bessel functions of the first and second kind) as

$$M_\ell(k) = \frac{Y_{\ell-1/2}(k_0\,R)}{Y_{\ell+1/2}(k_0\,R)} - P\frac{J_{\ell-1/2}(k\,R)}{J_{\ell+1/2}(k\,R)} - \ell\left(\frac{1}{k_0\,R} - \frac{P}{k\,R}\right) \tag{A.1}$$

where $k_0 = 2\pi/\lambda$ is the free-space wavenumber, $k = nk_0$ is the wavenumber inside the resonator, $\ell$ is the angular momentum number of the whispering gallery mode, and $P$ is a correction factor that depends on the desired mode's polarization. For this discussion, the only important thing about this equation is that the resonator has modes at the zeros (or roots, used interchangeably) of this function in $k$ (or, equivalently, $\lambda$, if we know $n(\lambda)$, perhaps from the material's Sellmeier coefficients).

The standard technique to find a root of this equation is to use some kind of bracket-based root finding algorithm (think Newton's method, although we typically use the more-advanced Brent's method provided by SciPy [92]). One identifies a bracket where the function's value at the endpoints are of opposite sign, then uses the algorithm to walk steadily inward until one finds a root. This works perfectly well for this equation, except for two problems:

- As shown in Figure A.1, this equation has many roots (i.e., the resonator has many modes).

- We don't know where to put the brackets without looking at the plot, because we don't know where the roots are.

Finding any one zero wouldn't be too bad, but we need a little more power to extract *all* the zeros (i.e., to find all of the modes), which is really what we're after. For large $\lambda$, the modal equation has a very regular structure of alternating asymptotes and zeros. These asymptotes turn out to occur at the zeros of the denominator of the second term. Between each pair of asymptotes there is a zero of the modal equation.

As $\lambda$ becomes smaller, the regular pattern becomes distorted by the asymptotes caused by the denominator of the first term. In each interval between two of the second-term asymptotes ("good" asymptotes), there is only a zero if there is *not* also an asymptote from the first term (a "bad" asymptote). Eventually, as $\lambda$ continues to decreases, there are so many bad asymptotes that there are no longer any zeros.

Based on this analysis, our algorithm for finding all of the modes is this:

1. Identify all of the good and bad asymptotes.

2. Iterate through the good asymptotes in overlapping pairs $((G0, G1), (G1, G2), (G2, G3), \cdots)$, where each pair defines an interval to possibly search for a root in.

3. If there is no bad asymptote between the pair of good asymptotes, use a root finder to get the modal equation root in this interval.

The second and third steps are mostly trivial using SciPy, but for the first we need some mathematical backup. We can identify the locations of the asymptotes using some semi-analytic techniques. Unfortunately there is no analytic formula for the zeros of the Bessel functions, but luckily there is an approximation for them that is accurate to inverse-third-order in the Bessel order and is uniformly accurate in the Bessel argument [99]. This is exactly what we need for whispering gallery modes, which all have large $\ell$ (corresponding to large Bessel order).

Denote the $m^{\text{th}}$ zero of the Bessel function $J_\nu$ as $\mathcal{J}_{\nu,m}$. Then we have

$$\mathcal{J}_{\nu,m} \approx \nu\, z(\zeta) + \frac{z(\zeta)\,[h(\zeta)]^2\, B_0(\zeta)}{2\nu} \tag{A.2}$$

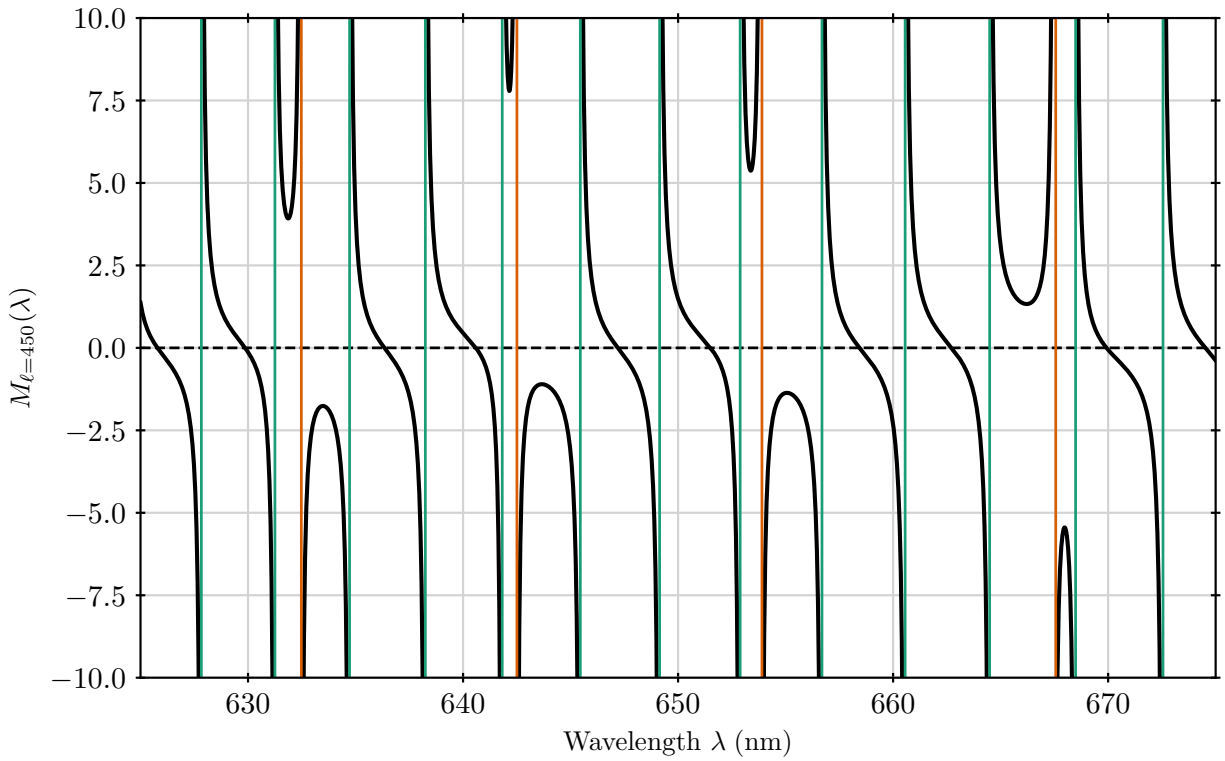


Figure A.1: The value of the microsphere whispering gallery mode modal equation in a 50 µm radius silica microsphere for $\ell = 450$ near $\lambda = 650\,\text{nm}$. "Good" asymptotes are marked in green, and "bad" asymptotes are marked in red. There is a modal equation zero between every pair of good asymptotes *unless* there is a bad asymptote between them, in which case there is never a zero. As $\lambda$ decreases, the density of bad asymptotes increases.

where

$$\zeta = \nu^{-2/3}\, a_m \tag{A.3}$$

$$h(\zeta) = \left(\frac{4\zeta}{1 - [z(\zeta)]^2}\right)^{1/4} \tag{A.4}$$

where $a_m$ is the $m^{\text{th}}$ zero of the Airy function Ai. The function $z(\zeta)$ is defined by

$$\frac{2}{3}(-\zeta)^{3/2} - \sqrt{z^2 - 1} + \arccos(1/z) = 0 \tag{A.5}$$

where $z$ must be determined numerically from a known $\zeta$. $B_0$ is given by

$$B_0 = i(-\zeta)^{-1/2} U \tag{A.6}$$

where

$$U = \frac{1}{24}\left(3u - 5u^3\right) \tag{A.7}$$

$$u = i(z^2 - 1)^{-1/2} \tag{A.8}$$

Note that $B_0$ always ends up being real, because there are an even number of $i$ in each term.

The above is for the good asymptotes, which come from the Bessel function $J$. The bad asymptotes come from the Nuemann function. Luckily the only difference for them is to replace the zeros of the Airy function with the zeros of the Airy function of the second kind Bi (everything else stays the same). Functions to calculate the zeros of the Airy function are also available via SciPy, so we can accomplish the first step of the algorithm without too much hassle.

# B Reducing to the Sideband Model

We start with the polarization propagation equation (1.2.45):

$$\dot{\mathcal{E}}_q = i\,\frac{N}{2}\,\frac{\omega_q}{\epsilon_0\,\epsilon^{(1)}(\omega_q)}\,\frac{C^2}{4\hbar^3}\sum_{r,s,t}\mathcal{E}_r\mathcal{E}_s^*\mathcal{E}_t\,\frac{V_{rstq}}{V_{qq}}\left(\frac{1}{\Delta_{st}^*} + \frac{1}{\Delta_{ts}}\right)e^{-i\Delta_{rstq}t} \tag{B.1}$$

We choose the cavity modes to be sidebands whose frequency are given by $\omega_q = \omega_P + q\,\omega_m$, where $\omega_P$ is the **pump frequency** and $\omega_m$ is the **modulation frequency** ($\omega_m = \omega_b - \omega_a$). This arrangement is often called a "ladder", because it has equally-spaced "rungs", where each rung is a sideband mode.

Using this set of cavity modes, we can simplify (B.1). Recall that

$$\Delta_{xy} = (\omega_x - \omega_y) - \omega_m + i\gamma_b \tag{B.2}$$

so

$$\begin{aligned}\Delta_{ts} &= (\omega_t - \omega_s) - \omega_m + i\gamma_b \\ &= (\omega_P + t\,\omega_m - \omega_P - s\,\omega_m) - \omega_m + i\gamma_b \\ &= (t - s - 1)\,\omega_m + i\gamma_b \end{aligned} \tag{B.3}$$

The real part of (B.3) is only zero if $s = t + 1$. Since this is also the point where $\Delta_{st}$ has the smallest magnitude, it is the term that matters the most in the sum in (B.1).

If we do make this assumption, we'll be left with two terms from each sum. When $t = s+1 \implies s = t - 1$, we get the $1/\Delta_{ts}$ term, and when $t = s - 1 \implies s = t + 1$ we get the $1/\Delta^*_{st}$ term.

$$\dot{\mathcal{E}}_q = i\,\frac{N}{2}\frac{\omega_q}{\epsilon_0\,\epsilon^{(1)}(\omega_q)}\frac{C^2}{4\hbar^3 V_{qq}}\left[\sum_{r,s}\mathcal{E}_r\mathcal{E}^*_s\mathcal{E}_{s+1}\frac{V_{r,s,s+1,q}}{\Delta_{s+1,s}}e^{-i\Delta_{r,s,s+1,q}t} + \mathcal{E}_r\mathcal{E}^*_s\mathcal{E}_{s-1}\frac{V_{r,s,s-1,q}}{\Delta^*_{s,s-1}}e^{-i\Delta_{r,s,s-1,q}t}\right] \tag{B.4}$$

Now notice that the four-mode detunings look like

$$\begin{aligned}\Delta_{r,s,s\pm1,q} &= \omega_r - \omega_s + \omega_{s\pm1} - \omega_q \\ &= \omega_P + r\,\omega_m - \omega_P - s\,\omega_m + \omega_P + (s \pm 1)\omega_m - \omega_P - q\,\omega_q \\ &= [r - s + (s \pm 1) - q]\,\omega_m \\ \Delta_{r,s,s\pm1,q} &= [r - q \pm 1]\,\omega_m \end{aligned} \tag{B.5}$$

Since $\omega_m$ is large, this exponential factor will be large enough to kill the term it is attached to if $r - q \pm 1 \neq 0$. Therefore we must have $r = q \mp 1$:

$$\begin{aligned}\dot{\mathcal{E}}_q = i\,\frac{N}{2}\frac{\omega_q}{\epsilon_0\,\epsilon^{(1)}(\omega_q)}\frac{C^2}{4\hbar^3 V_{qq}}\Bigg[&\sum_{s}\mathcal{E}_{q-1}\mathcal{E}^*_s\mathcal{E}_{s+1}\frac{V_{q-1,s,s+1,q}}{\Delta_{s+1,s}}e^{-i\Delta_{q-1,s,s+1,q}t} \\ &+\mathcal{E}_{q+1}\mathcal{E}^*_s\mathcal{E}_{s-1}\frac{V_{q+1,s,s-1,q}}{\Delta^*_{s,s-1}}e^{-i\Delta_{q+1,s,s-1,q}t}\Bigg]\end{aligned} \tag{B.6}$$

Finally, we will assume that only *adjacent* sidebands can affect each other. Note that this is a huge assumption, and is not supported by anything we're seeing in (B.6) itself! When running simulations with the full model, one needs to be careful of accidently putting the sideband modes

in a perfect ladder, allowing them all to talk to each in unexpected ways (because the four-mode detuning is more important than the two-mode detuning when the Raman linewidth is large). In reality, the modes are never organized in a perfect ladder, and the four-mode detunings that result from that will kill any "ladder-jumping" interactions.

To implement this assumption, set $s = q - 1$ in the first term and $s = q + 1$ in the second term (which removes the sum over $s$):

$$\begin{aligned}\dot{\mathcal{E}}_q = i\,\frac{N}{2}\frac{\omega_q}{\epsilon_0\,\epsilon^{(1)}(\omega_q)}\frac{C^2}{4\hbar^3 V_{qq}}\Bigg[&\mathcal{E}_{q-1}\mathcal{E}_{q-1}^{*}\mathcal{E}_q\frac{V_{q-1,q-1,q,q}}{\Delta_{q,q-1}}e^{-i\Delta_{q-1,q-1,q,q}t}\\ &+\mathcal{E}_{q+1}\mathcal{E}_{q+1}^{*}\mathcal{E}_q\frac{V_{q+1,q+1,q,q}}{\Delta_{q+1,q}^{*}}e^{-i\Delta_{q+1,q+1,q,q}t}\Bigg]\\ \dot{\mathcal{E}}_q = \frac{N}{2}\frac{\omega_q}{\epsilon_0\,\epsilon^{(1)}(\omega_q)}\frac{C^2}{4\hbar^3 V_{qq}\gamma_b}\,&\mathcal{E}_q\Big[\left|\mathcal{E}_{q-1}\right|^2 V_{q-1,q-1,q,q} - \left|\mathcal{E}_{q+1}\right|^2 V_{q+1,q+1,q,q}\Big]\end{aligned} \tag{B.7}$$

This is identical in form to the standard sideband model, with the usual generic prefactor $G$ expanded out to its component parts. Since no phases remain on the right hand side of the equation, the $\mathcal{E}_q$ can be modeled as being purely real. This makes the sideband model simple enough to work with by hand, although it clearly does not account for most of the possible interactions in the Raman system.

We have confirmed that our model (in both this reduced form and in the original) reproduces well-known results of the sideband model, such as the stair-step pattern of mode energies in cascaded stimulated Raman scattering [60]. A scan where we increase the launched pump power with a sideband ladder of Stokes modes above the pump mode is shown in Figure B.1. To get this scan to behave correctly, each sideband mode has been dithered from its ideal sideband frequency by a few GHz to prevent the accidental-resonance problems discussed above. Without this dithering, energy would be able to "skip" modes in a way that is perfectly allowed, but doesn't actually occur in physical systems because they are not perfect sideband ladders.

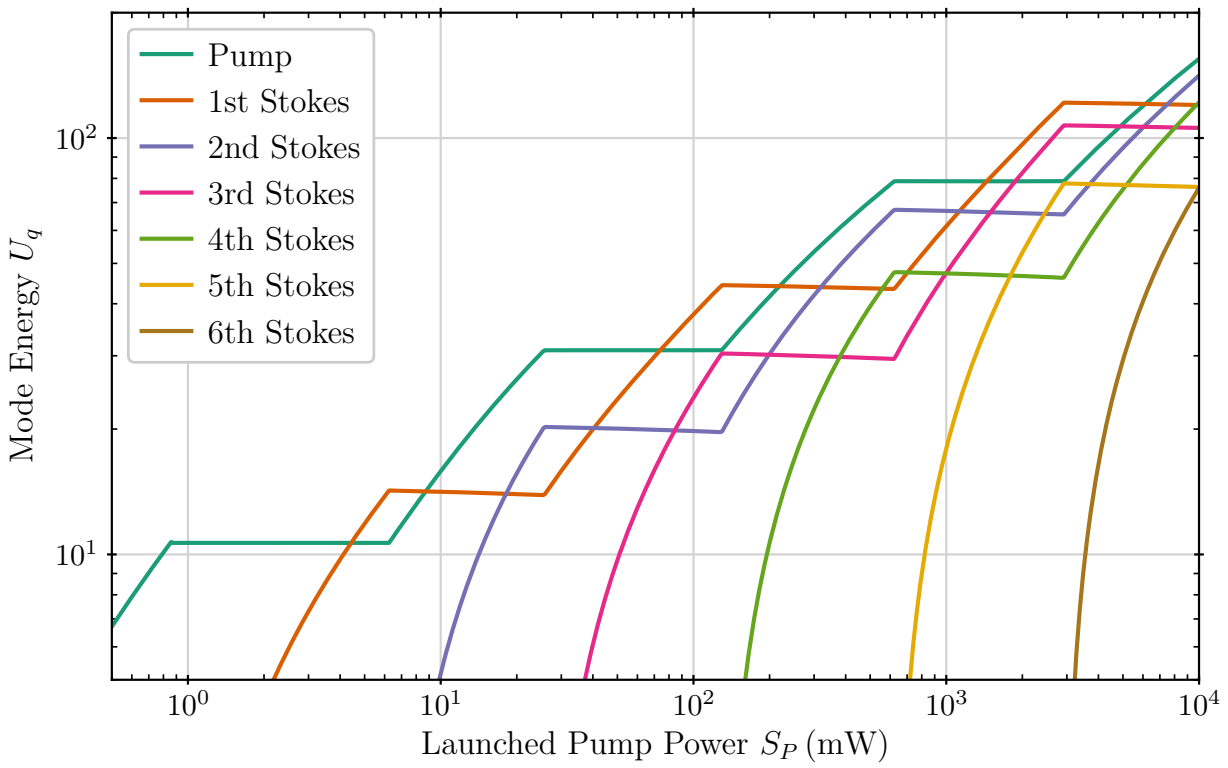


Figure B.1: The energy stored in each resonator mode during cascaded stimulated Raman scattering. Each Stokes mode in turn is pumped by the mode below it. While each mode pumps the one above it, its own energy is clamped at threshold, producing a "stair-step" pattern. At any given launched pump power, either all of the even-numbered modes are increasing and the odd modes are clamped, or vice-versa.

# C Spherical Harmonic Recurrence Relationships

When working with whispering gallery modes in spherical microresonators, one may need to perform numerical calculations involving vectors spherical harmonics. This is straightforward when the angular momentum numbers $\ell$ and $m$ are small, but becomes problematic when they are large because factors like $(\ell + m)!$ appear in the normalization factors. These huge factors cancel by the end of the calculation (spherical harmonic values are order 1 or smaller for any $\ell$ and $m$, no matter how large), but in the intermediate steps these numbers are far too large to work with in 64-bit floating-point arithmetic.

The solution to this problem is to calculate the spherical harmonics by way of *recurrence relationships*. This is an iterative solution, where the value under consideration will stay small at each step of the calculation. The trade-off, of course, is that there are many more steps to the

calculation. However, the additional computational cost is still much smaller than the cost of doing the very-large-number, high-precision arithmetic required by direct evaluation.

The recurrence-based technique we use is adapted from [100]. The actual recurrence relations will be defined on the **normalized associated Legendre polynomials** $\overline{P}_\ell^m$, which are defined by a normalization relationship to the standard associated Legendre polynomials $P_\ell^m$, which can be found by the Rodrigues formula:

$$\overline{P}_\ell^m = \sqrt{\frac{(2\ell+1)(\ell-m)!}{2\pi\,(l+m)!}} P_\ell^m \tag{C.1}$$

$$P_\ell^m = \frac{(-1)^m}{2^\ell \ell!}\left(1-x^2\right)^{m/2} \frac{\mathrm{d}^{\ell+m}}{\mathrm{d}x^{\ell+m}}\left(x^2-1\right)^\ell \tag{C.2}$$

This normalization handles most of the normalization factors of the spherical harmonics. To get to the spherical harmonic $Y_\ell^m$ from $\overline{P}_\ell^m$, we mainly neeed to handle the phase:

$$Y_\ell^m(\theta,\phi) = \overline{P}_\ell^m(\theta,\phi)\,\frac{e^{im\phi}}{\sqrt{2}} \tag{C.3}$$

and multiply by an additional $(-1)^m$ if $m<0$.

Because most of the spherical harmonics we want to evaluate have large $\ell$ and $|m| \approx \ell$, we identify these three recurrence relationships as being particularly efficient:

$$\text{(1)}\quad \overline{P}_m^m = -\sqrt{1+\frac{1}{2m}}\,\sin\theta\,\overline{P}_{m-1}^{m-1} \tag{C.4a}$$

$$\text{(2)}\quad \overline{P}_{m+1}^m = -\sqrt{2m+3}\,\cos\theta\,\overline{P}_m^m \tag{C.4b}$$

$$\text{(3)}\quad \overline{P}_\ell^m = -a_\ell^m\left(\cos\theta\,\overline{P}_{\ell-1}^m + b_\ell^m\,\overline{P}_{\ell-2}^m\right) \tag{C.4c}$$

Figure C.1 shows how these recurrence relationships can be used to compute higher-order $\overline{P}_\ell^m$ from lower-order ones. The idea is to move up the "side" of the $\overline{P}_\ell^m$ inverted-pyramid until reaching the correct $m$, then move straight up to the correct $\ell$. The base case is $\overline{P}_0^0 = 1/\sqrt{2}$. It takes $\ell+m+1$ steps to get to $\overline{P}_\ell^m$ from the base case, and then an additional step to go to $Y_\ell^m$.

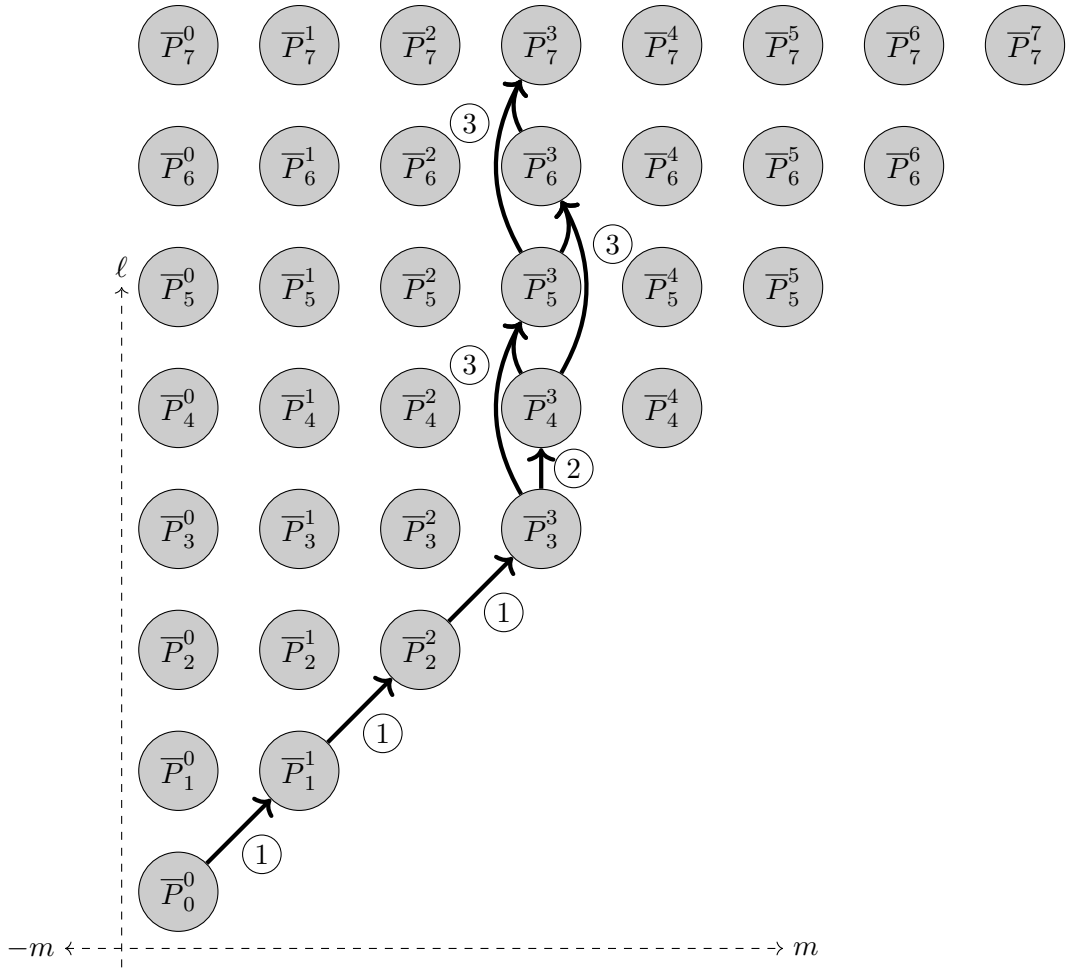


Figure C.1: Constructing $\overline{P}_7^3$ from $\overline{P}_0^0$ using the recurrence relationships of (C.4), which are represented as arrows. The first relationship lets us generate $\overline{P}_{m+1}^{m+1}$ from $\overline{P}_m^m$. The second lets us generate $\overline{P}_{m+1}^m$ from $\overline{P}_m^m$. The third lets us generate $\overline{P}_\ell^m$ from $\overline{P}_{\ell-1}^m$ and $\overline{P}_{\ell-2}^m$.

# D The Tridiagonal Matrix Algorithm

Most of the time evolution algorithms for the TDSE implemented in Section 2.3 depends on being able to perform four matrix operations. Two of the operations are simply multiplication of a vector by a very sparse matrix, and are easily and quickly accomplished by standard techniques for working with sparse matrices. The other two steps are complicated, since they involve multiplying by the inverse of a very sparse matrix: not an easy thing to find.

Luckily, there is a fast algorithm to determine the *result* of that multiplication (but not the matrix inverse itself) if the matrix is **tridiagonal**. A tridiagonal matrix is a sparse matrix where only the main diagonal and the first upper and lower off-diagonals are non-zero. Boringly, this

algorithm is usually called The Tridiagonal Matrix Algorithm (TDMA).

Consider the problem of finding $\mathbf{y}$ given

$$\mathbf{A}^{-1}\,\mathbf{x} = \mathbf{y} \tag{D.1}$$

$$\mathbf{x} = \mathbf{A}\,\mathbf{y}, \tag{D.2}$$

where $\mathbf{x}$ and $\mathbf{A}$ are known but $\mathbf{A}^{-1}$ is not. The second line indicates that such a multiplication is equivalent to solving a linear system of equations. If $A$ is tridiagonal, the expanded form of this equation is

$$\begin{bmatrix} x_0 \\ x_1 \\ \vdots \\ x_{n-1} \\ x_n \end{bmatrix} = \begin{bmatrix} a_0 & b_0 & & & 0 \\ c_0 & a_1 & b_1 & & \\ & c_1 & a_1 & \ddots & \\ & & \ddots & \ddots & b_{n-1} \\ 0 & & & c_{n-1} & a_n \end{bmatrix} \begin{bmatrix} y_0 \\ y_1 \\ \vdots \\ y_{n-1} \\ y_n \end{bmatrix} \tag{D.3}$$

The derivation of the TDMA is somewhat involved, but to summarize, one "merely" performs Gaussian elimination in a specific order. A pattern will emerge that leads to a recursive method of computing each $y_i$, as follows.

First, one calculates a "modified superdiagonal":

$$b'_i = \begin{cases} b_i/c_i & i = 0 \\ \frac{b_i}{c_i - a_i b'_{i-1}} & i = 1, 2, \cdots, n-1 \end{cases} \tag{D.4}$$

Note that the definition is recursive: $b'_i$ depends on $b'_{i-1}$. This unfortunate limitation makes it impossible to vectorize the calculation of $b'$. Next, $b'$ is used to calculate a modified $\mathbf{x}$ which we call $\mathbf{x}'$:

$$x'_i = \begin{cases} x_i/b_i & i = 0 \\ \frac{x_i - c_i x'_{i-1}}{c_i - c_i b'_{i-1}} & i = 1, 2, \cdots, n \end{cases} \tag{D.5}$$

One can then calculate the $y_i$ (in reverse order, starting from $y_n$):

$$y_i = \begin{cases} x_i/a_i & i = n \\ x'_i - b'_i y_{i+1} & i = n-1, n-2, \cdots, 0 \end{cases} \tag{D.6}$$

This algorithm requires three passes through the matrix diagonals or vectors, each of length $\mathcal{O}(n)$, so the overall algorithm is $\mathcal{O}(n)$. Plain Gaussian elimination is $\mathcal{O}(n^3)$, so, where applicable, the TDMA can represent a tremendous speedup over a naive implementation.

# E Split-Operator Methods

Suppose that we have a PDE of the form

$$\partial_t u = (\widehat{A} + \widehat{B})u \tag{E.1}$$

for some operators $\widehat{A}$ and $\widehat{B}$ and unknown function $u(\mathbf{x}, t)$. Assuming we know how to apply the operators $\widehat{A}$ and $\widehat{B}$ individually we can write the analytic solutions to each of them between time step $n$ and $n+1$, given $u^n$:

$$\begin{aligned} u^{n+1} &\approx e^{\widehat{A}\,\Delta t}\, u^n \\ u^{n+1} &\approx e^{\widehat{B}\,\Delta t}\, u^n \end{aligned} \tag{E.2}$$

This is not the solution to the original differential equation, because we applied each operator individually, as if the other did not exist. However, they *can* both be thought of as very poor estimates of the solution to the original problem.

To "merge" these two wrong estimates into a better estimate, consider a scheme that uses the result of the first calculation as the starting point for the second:

$$\begin{aligned} u^* &= e^{\widehat{A}\,\Delta t}\, u^n \\ u^{n+1} &\approx e^{\widehat{B}\,\Delta t}\, u^* = e^{\widehat{B}\,\Delta t}\, e^{\widehat{A}\,\Delta t}\, u^n \end{aligned} \tag{E.3}$$

This is called a **split-operator method**, because we have "split" the evolution operator into two parts and evaluated each individually. It can also be recognized as approximating the analytic solution $u^{n+1} = e^{(\widehat{A}+\widehat{B})\,\Delta t}\,u^n$ using the first term in the Baker-Campbell-Hausdorff (BCH) formula. The truncation error $\tau$ for a single step is the difference between our approximate solution and the true solution, which we can evaluate by using the BCH formula to expand the true solution:

$$\begin{aligned}
\tau &= e^{\widehat{B}\,\Delta t}\,e^{\widehat{A}\,\Delta t}\,u^n - e^{(\widehat{A}+\widehat{B})\,\Delta t}\,u^n \\
&= \left[e^{\widehat{B}\,\Delta t}\,e^{\widehat{A}\,\Delta t} - e^{(\widehat{A}+\widehat{B})\,\Delta t}\right]u^n \\
&= \left[\left(\widehat{I} + \Delta t\,\widehat{B} + \frac{(\Delta t)^2}{2}\widehat{B}^2 + \cdots\right)\left(\widehat{I} + \Delta t\,\widehat{A} + \frac{(\Delta t)^2}{2}\widehat{A}^2 + \cdots\right)\right. \\
&\qquad \left. - \left(\widehat{I} + \Delta t\left(\widehat{A}+\widehat{B}\right) + \frac{(\Delta t)^2}{2}\left(\widehat{A}+\widehat{B}\right)^2 + \cdots\right)\right]u^n \\
&= \left[\left(\widehat{I} + \Delta t\left(\widehat{A}+\widehat{B}\right) + \frac{(\Delta t)^2}{2}\left(\widehat{A}^2 + 2\widehat{A}\widehat{B} + \widehat{B}^2\right) + \cdots\right)\right. \\
&\qquad \left. - \left(\widehat{I} + \Delta t\left(\widehat{A}+\widehat{B}\right) + \frac{(\Delta t)^2}{2}\left(\widehat{A}+\widehat{B}\right)^2 + \cdots\right)\right]u^n \\
&= \left[\frac{(\Delta t)^2}{2}\left(\widehat{A}^2 + 2\widehat{A}\widehat{B} + \widehat{B}^2 - \widehat{A}^2 - \widehat{A}\widehat{B} - \widehat{B}\widehat{A} - \widehat{B}^2\right) + \cdots\right]u^n \\
&= \left[\frac{(\Delta t)^2}{2}\left(\widehat{A}\widehat{B} - \widehat{B}\widehat{A}\right) + \cdots\right]u^n \\
\tau &= \left[\frac{(\Delta t)^2}{2}\left[\widehat{A},\widehat{B}\right] + \cdots\right]u^n
\end{aligned} \tag{E.4}$$

So the truncation error is $\mathcal{O}\left(\Delta t^2\right)$ if $\widehat{A}$ and $\widehat{B}$ don't commute and $\mathcal{O}\left(\Delta t^3\right)$ if they do, with the total errors after many such steps being one order lower. The worst case scenario (and the most common for a situation where we need a numerical solution) is for non-commuting operators, so we should expect an overall error of $\mathcal{O}(\Delta t)$ just from the splitting, before we even consider any additional numerical error from evaluating the operators. Since many operator-evaluation schemes involving spatial derivatives will be second-order in space, we should try to bring the splitting error down to the same order in time.

Is there a way to get rid of that pesky commutator and bring the error down to third order?

Yes: using a scheme called **Strang splitting**.

$$u^{n+1} = e^{\widehat{A}\,\frac{\Delta t}{2}} e^{\widehat{B}\,\Delta t}\, e^{\widehat{A}\,\frac{\Delta t}{2}}\, u^n \tag{E.5}$$

This scheme is an order more accurate than the basic split-operator method, so we need to keep terms up to third order in $\Delta t$ when we calculate the truncation error $\tau$:

$$\begin{aligned}
\tau &= e^{\widehat{A}\,\frac{\Delta t}{2}} e^{\widehat{B}\,\Delta t}\, e^{\widehat{A}\,\frac{\Delta t}{2}}\, u^n - e^{(\widehat{A}+\widehat{B})\,\Delta t}\, u^n \\
&= \left[e^{\widehat{A}\,\frac{\Delta t}{2}} e^{\widehat{B}\,\Delta t}\, e^{\widehat{A}\,\frac{\Delta t}{2}} - e^{(\widehat{A}+\widehat{B})\,\Delta t}\right] u^n \\
&= \left[\left(\widehat{I} + \frac{\Delta t}{2}\,\widehat{A} + \frac{(\Delta t)^2}{8}\widehat{A}^2 + \frac{(\Delta t)^3}{48}\widehat{A}^3 + \cdots\right)\left(\widehat{I} + \Delta t\,\widehat{B} + \frac{(\Delta t)^2}{2}\widehat{B}^2 + \frac{(\Delta t)^3}{6}\widehat{B}^3 + \cdots\right)\right. \\
&\qquad \left.\times \left(\widehat{I} + \frac{\Delta t}{2}\,\widehat{A} + \frac{(\Delta t)^2}{8}\widehat{A}^2 + \frac{(\Delta t)^3}{48}\widehat{A}^3 + \cdots\right)\right. \\
&\quad \left. - \left(\widehat{I} + \Delta t\left(\widehat{A}+\widehat{B}\right) + \frac{(\Delta t)^2}{2}\left(\widehat{A}+\widehat{B}\right)^2 + \frac{(\Delta t)^3}{6}\left(\widehat{A}+\widehat{B}\right)^3 + \cdots\right)\right] u^n \\
&= \left[\left(\widehat{I} + \frac{\Delta t}{2}\widehat{A} + \frac{(\Delta t)^2}{8}\widehat{A}^2 + \frac{(\Delta t)^3}{48}\widehat{A}^3 + \Delta t\,\widehat{B} + \frac{(\Delta t)^2}{2}\widehat{B}^2 + \frac{(\Delta t)^3}{6}\widehat{B}^3 + \frac{(\Delta t)^2}{2}\widehat{A}\widehat{B} + \frac{(\Delta t)^3}{4}\widehat{A}\widehat{B}^2\right.\right. \\
&\qquad \left.\left. + \frac{(\Delta t)^3}{8}\widehat{A}^2\widehat{B} + \cdots\right) \times \left(\widehat{I} + \frac{\Delta t}{2}\,\widehat{A} + \frac{(\Delta t)^2}{8}\widehat{A}^2 + \frac{(\Delta t)^3}{48}\widehat{A}^3 + \cdots\right)\right. \\
&\qquad \left. - \left(\widehat{I} + \Delta t\left(\widehat{A}+\widehat{B}\right) + \frac{(\Delta t)^2}{2}\left(\widehat{A}+\widehat{B}\right)^2 + \frac{(\Delta t)^3}{6}\left(\widehat{A}+\widehat{B}\right)^3 + \cdots\right)\right] u^n \\
&= \left[\left(\widehat{I} + \Delta t\,\widehat{A} + \Delta t\,\widehat{B} + \frac{(\Delta t)^2}{2}\widehat{A}^2 + \frac{(\Delta t)^2}{2}\widehat{A}\widehat{B} + \frac{(\Delta t)^2}{2}\widehat{B}\widehat{A} + \frac{(\Delta t)^2}{2}\widehat{B}^2\right.\right. \\
&\qquad \left.\left. + \frac{(\Delta t)^3}{6}\widehat{A}^3 + \frac{(\Delta t)^3}{2}\widehat{A}\widehat{B}^2 + \frac{(\Delta t)^3}{2}\widehat{A}^2\widehat{B} + \frac{(\Delta t)^3}{6}\widehat{B}^3 + \cdots\right)\right. \\
&\qquad \left. - \left(\widehat{I} + \Delta t\left(\widehat{A}+\widehat{B}\right) + \frac{(\Delta t)^2}{2}\left(\widehat{A}+\widehat{B}\right)^2 + \frac{(\Delta t)^3}{6}\left(\widehat{A}+\widehat{B}\right)^3 + \cdots\right)\right] u^n \\
&= \left[\left(\frac{(\Delta t)^3}{6}\widehat{A}^3 + \frac{(\Delta t)^3}{2}\widehat{A}\widehat{B}^2 + \frac{(\Delta t)^3}{2}\widehat{A}^2\widehat{B} + \frac{(\Delta t)^3}{6}\widehat{B}^3 - \frac{(\Delta t)^3}{6}\left(\widehat{A}+\widehat{B}\right)^3 + \cdots\right)\right] u^n
\end{aligned} \tag{E.6}$$

This remaining terms do not fully cancel away, so the single-step error is $\mathcal{O}\left(\Delta t^3\right)$, and the error after many such steps is $\mathcal{O}\left(\Delta t^2\right)$. I find that with this method, the time step required for good frequency-space properties is more than small enough to saturate the accuracy compared to the spatial errors.

If you don't care about intermediate results, most of the operators can be contracted:

$$\begin{aligned} u^n &= e^{\widehat{A}\frac{\Delta t}{2}} e^{\widehat{B}\,\Delta t}\, e^{\widehat{A}\frac{\Delta t}{2}} e^{\widehat{A}\frac{\Delta t}{2}} e^{\widehat{B}\,\Delta t}\, e^{\widehat{A}\frac{\Delta t}{2}} \cdots e^{\widehat{A}\frac{\Delta t}{2}} e^{\widehat{B}\,\Delta t}\, e^{\widehat{A}\frac{\Delta t}{2}}\, u^0 \\ u^n &= e^{\widehat{A}\frac{\Delta t}{2}} e^{\widehat{B}\,\Delta t}\, e^{\widehat{A}\,\Delta t} e^{\widehat{B}\,\Delta t}\, e^{\widehat{A}\,\Delta t} \cdots e^{\widehat{B}\,\Delta t}\, e^{\widehat{A}\frac{\Delta t}{2}}\, u^0 \\ u^n &= e^{\widehat{A}\frac{\Delta t}{2}} \left(e^{\widehat{B}\,\Delta t}\, e^{\widehat{A}\,\Delta t}\right)^{n-1} e^{\widehat{B}\,\Delta t}\, e^{\widehat{A}\frac{\Delta t}{2}}\, u^0 \end{aligned} \tag{E.7}$$

Note that the inner term $\left(e^{\widehat{B}\,\Delta t}\, e^{\widehat{A}\,\Delta t}\right)^{n-1}$ is roughly what we would have done without Strang splitting! Only a small, fixed extra cost (the few extra operators on either side) is required to go to second-order in time in the *final* result, which is fairly remarkable. Our current implementation does not use this trick, but it may be a useful optimization technique in future work.

# F Velocity Gauge TDSE Evolution Operators

In Section 2.2.2 we found that the wavefunction could be represented in either the length gauge ($\Psi^L$) or the velocity gauge ($\Psi^V$):

$$\Psi^L = \exp\!\left(-i\frac{q}{\hbar}\boldsymbol{\mathcal{A}}(t)\cdot\mathbf{r}\right) \exp\!\left(-i\frac{q^2}{2m\hbar}\int_{-\infty}^{t}\boldsymbol{\mathcal{A}}^2(\tau)\,\mathrm{d}\tau\right)\Psi^V \tag{F.1a}$$

$$\Psi^V = \exp\!\left(i\frac{q}{\hbar}\boldsymbol{\mathcal{A}}(t)\cdot\mathbf{r}\right) \exp\!\left(i\frac{q^2}{2m\hbar}\int_{-\infty}^{t}\boldsymbol{\mathcal{A}}^2(\tau)\,\mathrm{d}\tau\right)\Psi^L \tag{F.1b}$$

Apparently $\Psi^L$ and $\Psi^V$ are quite different from each other. In fact, $\Psi^V$ typically requires far fewer spherical harmonics in its partial-wave expansion to get the same numerical accuracy [72, 81].

To see why this is the case, consider the partial-wave expansion of the exponential phase term $\exp\!\big(i\frac{e}{\hbar}\boldsymbol{\mathcal{A}}(t)\cdot\mathbf{r}\big)$:

$$\begin{aligned} \exp\!\left(i\frac{e}{\hbar}\boldsymbol{\mathcal{A}}(t)\cdot\mathbf{r}\right) &= \exp\!\left(i\frac{e}{\hbar}\mathcal{A}\hat{\mathbf{z}}\cdot\mathbf{r}\right) \\ &= \exp\!\left(i\frac{e}{\hbar}\mathcal{A}z\right) \\ &= \sum_{\ell=0}^{\infty} i^\ell\,(2\ell+1)\,j_\ell\!\left(\frac{e}{\hbar}\mathcal{A}\,r\right)P_\ell(\cos\theta) \end{aligned} \tag{F.2}$$

where $j_\ell$ is the spherical Bessel function with index $\ell$ and $P_\ell$ is the $\ell^{\text{th}}$ Legendre polynomial.

Now consider the size of the system. Suppose it is bounded by a sphere of radius $r_{\max}$. One way

to get an estimate of $r_{\max}$ is to consider what would happen if we had a monochromatic electric field of amplitude $\mathcal{E}_0$ and angular frequency $\omega$, and the electron motion was purely classical. Then the electron would have a quiver-motion amplitude of

$$\alpha_0 = \frac{e\mathcal{E}_0}{m\omega^2} \approx r_{\max}, \tag{F.3}$$

where $\omega$ is the angular frequency of the electric field. The largest value of the argument of the spherical Bessel function in F.2 is then approximately

$$\frac{e}{\hbar}\mathcal{A}_0\, r_{\max} \approx \frac{e}{\hbar}\frac{\mathcal{E}_0}{\omega}\frac{e\mathcal{E}_0}{m\omega^2} = \frac{e^2\mathcal{E}_0^2}{\hbar m\omega^2}. \tag{F.4}$$

To get detailed angular resolution over that same (unitless) length scale we also need that many partial waves, regardless of whether there is any physical (not purely phase) information contained in those high-$\ell$ spherical harmonics. It isn't immediately clear which wavefunction initially "includes" this extraneous phase information, such that "undoing" that phase by going to the other representation reduces the complexity of $\Psi$. However, the literature indicates that it is the velocity-gauge representation which has the more compact partial-wave expansion [81].

At first glance this may be very counter-intuitive. For example, consider measuring the angular momentum of the electron. This is an gauge-independent physical observable and therefore its expectation value must be the same in the two representations. This seems to raise a contradiction: the velocity gauge representation is "missing" many higher-$\ell$ partial waves, so how can it possibly give the same expectation value as we get the from the length gauge? The answer is that when we make the transformation to the velocity gauge, the operators whose expectation values are invariant are the *kinetic momentum and angular momentum*, not the the *canonical momentum and angular momentum*. The kinetic versions of the operators correspond to the actual velocity of the particle (or it's expectation value, thinking about Ehrenfest's theorem). They are defined by

$$\widehat{\mathbf{p}}_{\text{can}} = \widehat{\mathbf{p}} - e\boldsymbol{\mathcal{A}} \tag{F.5a}$$

$$\widehat{\mathbf{L}}_{\text{can}} = \mathbf{r} \times (\widehat{\mathbf{p}} - e\boldsymbol{\mathcal{A}}). \tag{F.5b}$$

When there is no electric field, the canonical and kinetic momenta are the same, and the distinction

between which expectation values vanishes. Note that in the length gauge $\boldsymbol{\mathcal{A}} = \mathbf{0}$, so the canonical and kinetic momenta are actually always the same. But in the velocity gauge, the expectation value of the kinetic momentum will have terms that look like $\langle \Psi^V | \boldsymbol{\mathcal{A}} | \Psi^V \rangle$, or $\langle \Psi^V | \mathbf{r} \times \boldsymbol{\mathcal{A}} | \Psi^V \rangle$ for the kinetic angular momentum. These terms contain the information about the high-$\ell$ components via the partial-wave expansion of $\boldsymbol{\mathcal{A}}$. In this sense, going to the velocity gauge is like going to the Heisenberg picture from the Schrödinger picture: information about the state is being shifted from the wavefunction to the operators that act on it. Unlike the Heisenberg picture, the dependence has not been fully shifted, and we are left with some time-dependence information in both the operators and the wavefunction.

So, performing the time evolution in the velocity gauge is more efficient in certain cases, and leads to the same results. How do we get the velocity gauge evolution operator? We need to go back to the derivation in Section 2.3.3.1 and switch out $\widehat{\mathcal{H}}_I^L$ for $\widehat{\mathcal{H}}_I^V = \boldsymbol{\mathcal{A}}(t) \cdot \widehat{\mathbf{p}} = i\hbar\, \mathcal{A}(t)\, \partial_z$ [80, 81]. The resulting evolution operator is significantly more complicated to work with than the length gauge evolution operator, and in fact we found that for our particular simulations it provided no performance benefits because we did not need to propagate the wavefunction out to distances very far from the nucleus. However, the derivation has been still been included here for completeness, and because it may be useful in the future.

The first thing we need to do is determine the action of $\partial_z$ on a spherical harmonic:

$$\frac{\partial}{\partial z} |\ell\rangle = \left( \cos\theta \frac{\partial}{\partial r} - \frac{\sin\theta}{r} \frac{\partial}{\partial \theta} \right) |\ell\rangle \tag{F.6}$$

The first term can be computed in the same way technique we used for the length gauge. The relevant identity is

$$\cos(\theta) |\ell\rangle = c_\ell |\ell + 1\rangle + c_{\ell-1} |\ell - 1\rangle \tag{F.7}$$

$$c_\ell = \frac{\ell + 1}{\sqrt{(\ell + 1)(\ell + 3)}} \tag{F.8}$$

Using that, the first term is just

$$\cos\theta \frac{\partial}{\partial r} |\ell\rangle = \frac{\partial}{\partial r} \cos\theta |\ell\rangle = c_\ell \frac{\partial}{\partial r} |\ell + 1\rangle + c_{\ell-1} \frac{\partial}{\partial r} |\ell - 1\rangle \tag{F.9}$$

To evaluate the second term we need to figure out what a $\theta$ derivative does to a spherical harmonic. We need to go one step down and figure out what happens to an associated Legendre polynomial first. Remember that the spherical harmonics are defined as

$$Y_\ell^m(\theta,\phi) = (-1)^m \sqrt{\frac{2\ell+1}{4\pi}\frac{(\ell-|m|)!}{(\ell+|m|)!}} e^{im\phi} P_\ell^m(\cos\theta) \tag{F.10}$$

where $P_\ell^m(\cos\theta)$ is an associated Legendre polynomial, and is the only term hit by the $\theta$ derivative. There are many ways to write the result, but the recurrence relation

$$(1-x^2)\frac{\partial}{\partial x}P_\ell^m(x) = \frac{1}{2\ell+1}\big[(\ell+1)(\ell+m)P_{\ell-1}^m(x) - \ell(\ell-m+1)P_{\ell+1}^m(x)\big] \tag{F.11}$$

is useful because it recurs at fixed $m$, which is what we want to eventually get back to in order to match (F.9). Now we just evaluate the recurrence relation at $m=0$ using the chain rule:

$$\begin{aligned}
\frac{\partial P_\ell^0(\cos\theta)}{\partial\theta} &= \frac{1}{1-\cos^2\theta}\frac{1}{2\ell+1}\big[(\ell+1)(\ell+0)P_{\ell-1}^0(\cos\theta) - \ell(\ell-0+1)P_{\ell+1}^0(\cos\theta)\big]\frac{\partial\sin\theta}{\partial\theta} \\
&= -\frac{\sin\theta}{\sin^2\theta}\frac{1}{2\ell+1}\big[(\ell+1)\ell P_{\ell-1}^0(\cos\theta) - \ell(\ell+1)P_{\ell+1}^0(\cos\theta)\big] \\
&= -\frac{\sin\theta}{\sin^2\theta}\frac{\ell(\ell+1)}{2\ell+1}\big[P_{\ell-1}^0(\cos\theta) - P_{\ell+1}^0(\cos\theta)\big] \\
\frac{\partial P_\ell^0(\cos\theta)}{\partial\theta} &= -\frac{1}{\sin\theta}\frac{\ell(\ell+1)}{2\ell+1}\big[P_{\ell-1}^0(\cos\theta) - P_{\ell+1}^0(\cos\theta)\big]
\end{aligned} \tag{F.12}$$

Now we multiply by the correct prefactors to turn these back into spherical harmonics:

$$\begin{aligned}
\sqrt{\frac{2\ell+1}{4\pi}}\frac{\partial P_\ell^0(\cos\theta)}{\partial\theta} &= -\frac{1}{\sin\theta}\frac{\ell(\ell+1)}{2\ell+1}\sqrt{\frac{2\ell+1}{4\pi}}\left[\sqrt{\frac{2\ell-1}{2\ell-1}}P_{\ell-1}^0(\cos\theta) - \sqrt{\frac{2\ell+3}{2\ell+3}}P_{\ell+1}^0(\cos\theta)\right] \\
\frac{\partial Y_\ell^0(\cos\theta)}{\partial\theta} &= -\frac{1}{\sin\theta}\frac{\ell(\ell+1)}{\sqrt{2\ell+1}}\left[\frac{1}{\sqrt{2\ell-1}}Y_{\ell-1}^0(\cos\theta) - \frac{1}{\sqrt{2\ell+3}}Y_{\ell+1}^0(\cos\theta)\right] \\
\frac{\partial Y_\ell^0(\cos\theta)}{\partial\theta} &= -\frac{1}{\sin\theta}\left[\frac{\ell(\ell+1)}{\sqrt{(2\ell-1)(2\ell+1)}}Y_{\ell-1}^0(\cos\theta) - \frac{\ell(\ell+1)}{\sqrt{(2\ell+1)(2\ell+3)}}Y_{\ell+1}^0(\cos\theta)\right] \\
\partial_\theta|\ell\rangle &= -\frac{1}{\sin\theta}[c_{\ell-1}(\ell+1)|\ell-1\rangle - c_\ell\,\ell\,|\ell+1\rangle]
\end{aligned} \tag{F.13}$$

Now we can evaluate the second term of (F.6):

$$
\begin{aligned}
-\frac{\sin\theta}{r}\frac{\partial}{\partial\theta}\left|\ell\right\rangle &= \frac{1}{r}\sin\theta\,\frac{1}{\sin\theta}[c_{\ell-1}(\ell+1)\left|\ell-1\right\rangle - c_\ell\,\ell\left|\ell+1\right\rangle] \\
-\frac{\sin\theta}{r}\frac{\partial}{\partial\theta}\left|\ell\right\rangle &= \frac{1}{r}[c_{\ell-1}(\ell+1)\left|\ell-1\right\rangle - c_\ell\,\ell\left|\ell+1\right\rangle]
\end{aligned}
\tag{F.14}
$$

Combine the two terms to get

$$
\partial_z\left|\ell\right\rangle = c_\ell\left(\frac{\partial}{\partial r} - \frac{\ell}{r}\right)\left|\ell+1\right\rangle + c_{\ell-1}\left(\frac{\partial}{\partial r} + \frac{\ell+1}{r}\right)\left|\ell-1\right\rangle \tag{F.15}
$$

Now we can finally start evaluating the expectation value of $\widehat{\mathcal{H}}_I^V$:

$$
\begin{aligned}
\langle\Psi|-\widehat{\mathcal{H}}_I^V|\Psi\rangle &= -\int_0^\infty r^2\,\mathrm{d}r\int_\Omega \mathrm{d}\Omega\;\Psi^*\widehat{\mathcal{H}}_I^V\Psi \\
&= -\int_0^\infty r^2\,\mathrm{d}r\sum_\ell\sum_{\ell'}\int_\Omega \mathrm{d}\Omega\;\Psi_\ell^*\left\langle\ell\right|-\frac{q}{m}\boldsymbol{\mathcal{A}}(t)\cdot\widehat{\mathbf{p}}\left|\ell'\right\rangle\Psi_{\ell'} \\
&= i\hbar\frac{q}{m}\,\mathcal{A}(t)\int_0^\infty r^2\,\mathrm{d}r\sum_\ell\sum_{\ell'}\int_\Omega \mathrm{d}\Omega\;\Psi_\ell^*\left\langle\ell\right|\partial_z\left|\ell'\right\rangle\Psi_{\ell'} \\
&= i\hbar\frac{q}{m}\,\mathcal{A}(t)\int_0^\infty r^2\,\mathrm{d}r\sum_\ell\sum_{\ell'}\int_\Omega \mathrm{d}\Omega\;\Psi_\ell^*\left\langle\ell\right|\left[c_{\ell'}\left(\frac{\partial}{\partial r} - \frac{\ell'}{r}\right)\left|\ell'+1\right\rangle\right. \\
&\qquad\qquad \left. + c_{\ell'-1}\left(\frac{\partial}{\partial r} + \frac{\ell'+1}{r}\right)\left|\ell'-1\right\rangle\right]\Psi_{\ell'} \\
\langle\Psi|-\widehat{\mathcal{H}}_I^V|\Psi\rangle &= i\hbar\frac{q}{m}\,\mathcal{A}(t)\int_0^\infty r^2\,\mathrm{d}r\sum_\ell\;\Psi_\ell^*\left[c_{\ell-1}\left(\frac{\partial}{\partial r} - \frac{\ell-1}{r}\right)\Psi_{\ell-1} + c_\ell\left(\frac{\partial}{\partial r} + \frac{\ell+2}{r}\right)\Psi_{\ell+1}\right]
\end{aligned}
\tag{F.16}
$$

Unfortunately, discretizing this expression does not give a Hermitian matrix [80]. We can get a better expression by performing integration by parts on the $\Psi_\ell^*\,\partial_r\Psi_{\ell+1}$ term:

$$
\begin{aligned}
\int_0^\infty \left(r^2\Psi_\ell^*\right)\frac{\partial\Psi_{\ell+1}}{\partial r}\,\mathrm{d}r &= \left[r^2\Psi_\ell^*\Psi_{\ell+1}\right|_0^\infty - \int_0^\infty\left(2r\Psi_\ell^* + r^2\frac{\partial\Psi_\ell^*}{\partial r}\right)\Psi_{\ell+1}\,\mathrm{d}r \\
\int_0^\infty \left(r^2\Psi_\ell^*\right)\frac{\partial\Psi_{\ell+1}}{\partial r}\,\mathrm{d}r &= \int_0^\infty r^2\left(-\frac{2}{r}\Psi_\ell^* - \frac{\partial\Psi_\ell^*}{\partial r}\right)\Psi_{\ell+1}\,\mathrm{d}r
\end{aligned}
\tag{F.17}
$$

Using this, the expectation value becomes

$$\begin{aligned}
\langle\Psi|-\widehat{\mathcal{H}}_I^V|\Psi\rangle &= i\hbar\frac{q}{m}\,\mathcal{A}(t)\int_0^\infty r^2\,\mathrm{d}r\sum_\ell\Bigg[c_{\ell-1}\Psi_\ell^*\frac{\partial\Psi_{\ell-1}}{\partial r}-c_{\ell-1}\Psi_\ell^*\frac{\ell-1}{r}\Psi_{\ell-1}\\
&\qquad\qquad +c_\ell\Psi_\ell^*\frac{\partial\Psi_{\ell+1}}{\partial r}+c_\ell\Psi_\ell^*\frac{\ell+2}{r}\Psi_{\ell+1}\Bigg]\\
&= i\hbar\frac{q}{m}\,\mathcal{A}(t)\int_0^\infty r^2\,\mathrm{d}r\sum_\ell\Bigg[c_{\ell-1}\Psi_\ell^*\frac{\partial\Psi_{\ell-1}}{\partial r}-c_{\ell-1}\Psi_\ell^*\frac{\ell-1}{r}\Psi_{\ell-1}\\
&\qquad\qquad -c_\ell\frac{2}{r}\Psi_\ell^*\Psi_{\ell+1}-c_\ell\frac{\partial\Psi_\ell^*}{\partial r}\Psi_{\ell+1}+c_\ell\Psi_\ell^*\frac{\ell+2}{r}\Psi_{\ell+1}\Bigg]\\
\langle\Psi|-\widehat{\mathcal{H}}_I^V|\Psi\rangle &= i\hbar\frac{q}{m}\,\mathcal{A}(t)\int_0^\infty r^2\,\mathrm{d}r\sum_\ell\Bigg[c_{\ell-1}\Psi_\ell^*\frac{\partial\Psi_{\ell-1}}{\partial r}-c_{\ell-1}\Psi_\ell^*\frac{\ell-1}{r}\Psi_{\ell-1}\\
&\qquad\qquad -c_\ell\frac{\partial\Psi_\ell^*}{\partial r}\Psi_{\ell+1}-c_\ell\Psi_\ell^*\frac{\ell}{r}\Psi_{\ell+1}\Bigg]\\
\langle\Psi|-\widehat{\mathcal{H}}_I^V|\Psi\rangle &= i\hbar\frac{q}{m}\,\mathcal{A}(t)\int_0^\infty r^2\,\mathrm{d}r\sum_\ell\left[c_{\ell-1}\Psi_\ell^*\left(\frac{\partial}{\partial r}-\frac{\ell-1}{r}\right)\Psi_{\ell-1}-c_\ell\left(\frac{\partial\Psi_\ell^*}{\partial r}-\Psi_\ell^*\frac{\ell}{r}\right)\Psi_{\ell+1}\right]
\end{aligned}\tag{F.18}$$

We will now discretize in the radial coordinate. The derivatives will be evaluated using the centered difference at $r_j$, but thinking of it explicitly as the average of the forward and backwards difference:

$$\left.\frac{\partial f}{\partial r}\right|_{r=r_j}=\frac{f^{j+1}-f^{j-1}}{2\,\Delta r}=\frac{f^{j+1}-f^j+f^j-f^{j-1}}{2\,\Delta r}=\frac{f^{j+1}-f^j}{2\,\Delta r}+\frac{f^j-f^{j-1}}{2\,\Delta r}.\tag{F.19}$$

The reason that we do this is that the forward difference is evaluated at $r_{j+\frac{1}{2}}$ and the backwards difference is evaluated at $r_{j-\frac{1}{2}}$. The non-derivative terms will be evaluated directly at $r_j$.

$$\begin{aligned}
\langle\Psi|-\widehat{\mathcal{H}}_I^V|\Psi\rangle = i\hbar\frac{q}{m}\,\mathcal{A}(t)\,\Delta r\sum_{\ell,\,j}\Bigg[&-r_j^2\,c_{\ell-1}\frac{\ell-1}{r_j}\left(\Psi_\ell^j\right)^*\Psi_{\ell-1}^j+r_j^2\,c_\ell\frac{\ell}{r_j}\left(\Psi_\ell^j\right)^*\Psi_{\ell+1}^j\\
&+\frac{1}{2\,\Delta r}c_{\ell-1}\left(\Psi_\ell^j\right)^*\left(r_{j+\frac{1}{2}}^2\left\{\Psi_{\ell-1}^{j+1}-\Psi_{\ell-1}^j\right\}+r_{j-\frac{1}{2}}^2\left\{\Psi_{\ell-1}^j-\Psi_{\ell-1}^{j-1}\right\}\right)\\
&-\frac{1}{2\,\Delta r}c_\ell\left(r_{j+\frac{1}{2}}^2\left\{\left(\Psi_\ell^{j+1}\right)^*-\left(\Psi_\ell^j\right)^*\right\}+r_{j-\frac{1}{2}}^2\left\{\left(\Psi_\ell^j\right)^*-\left(\Psi_\ell^{j-1}\right)^*\right\}\right)\Psi_{\ell+1}^j\Bigg]
\end{aligned}\tag{F.20}$$

We need to push terms containing $\left(\Psi_\ell^{j+1}\right)^*$ and $\left(\Psi_\ell^{j+1}\right)^*$ down and up in the sum, respectively.

Then we can pull out an overall factor of $\left(\Psi_\ell^j\right)^*$, leaving us with

$$\begin{aligned}
\langle\Psi|-\widehat{\mathcal{H}}_I^V|\Psi\rangle = i\hbar\frac{q}{m}\,\mathcal{A}(t)\,\Delta r\sum_{\ell,\,j}\left(\Psi_\ell^j\right)^*\Bigg[&-r_j^2\,c_{\ell-1}\frac{\ell-1}{r_j}\Psi_{\ell-1}^j + r_j^2\,c_\ell\frac{\ell}{r_j}\Psi_{\ell+1}^j \\
&+\frac{1}{2\,\Delta r}c_{\ell-1}\Big(r_{j+\frac{1}{2}}^2\Psi_{\ell-1}^{j+1} - r_{j+\frac{1}{2}}^2\Psi_{\ell-1}^j + r_{j-\frac{1}{2}}^2\Psi_{\ell-1}^j - r_{j-\frac{1}{2}}^2\Psi_{\ell-1}^{j-1}\Big) \\
&-\frac{1}{2\,\Delta r}c_\ell\Big(r_{j-\frac{1}{2}}^2\Psi_{\ell+1}^{j-1} - r_{j+\frac{1}{2}}^2\Psi_{\ell+1}^j + r_{j-\frac{1}{2}}^2\Psi_{\ell+1}^j - r_{j+\frac{1}{2}}^2\Psi_{\ell+1}^{j+1}\Big)\Bigg] \\
\langle\Psi|-\widehat{\mathcal{H}}_I^V|\Psi\rangle = i\hbar\frac{q}{m}\,\mathcal{A}(t)\,\Delta r\sum_{\ell,\,j}\left(g_\ell^j\right)^*\Bigg[&-c_{\ell-1}\frac{\ell-1}{r_j}g_{\ell-1}^j + c_\ell\frac{\ell}{r_j}g_{\ell+1}^j \\
&+\frac{1}{2\,\Delta r}c_{\ell-1}\left(\frac{r_{j+\frac{1}{2}}^2}{r_j r_{j+1}}\,g_{\ell-1}^{j+1} - \frac{r_{j+\frac{1}{2}}^2}{r_j^2}\,g_{\ell-1}^j + \frac{r_{j-\frac{1}{2}}^2}{r_j^2}\,g_{\ell-1}^j - \frac{r_{j-\frac{1}{2}}^2}{r_j r_{j-1}}\,g_{\ell-1}^{j-1}\right) \\
&-\frac{1}{2\,\Delta r}c_\ell\left(\frac{r_{j-\frac{1}{2}}^2}{r_j r_{j-1}}\,g_{\ell+1}^{j-1} - \frac{r_{j+\frac{1}{2}}^2}{r_j^2}\,g_{\ell+1}^j + \frac{r_{j-\frac{1}{2}}^2}{r_j^2}\,g_{\ell+1}^j - \frac{r_{j+\frac{1}{2}}^2}{r_j r_{j+1}}\,g_{\ell+1}^{j+1}\right)\Bigg]
\end{aligned} \tag{F.21}$$

Now redistribute and collect terms by which $g$ point they are associated with, recognizing the presence of the same $\alpha_j$ and $\alpha_{j-1}$ we got in the kinetic term (2.3.50) earlier:

$$\begin{aligned}
\langle\Psi|-\widehat{\mathcal{H}}_I^V|\Psi\rangle = i\hbar\frac{q}{m}\,\mathcal{A}(t)\,\Delta r\sum_{\ell,\,j}\left(g_\ell^j\right)^*\Bigg[&-c_{\ell-1}\left(\frac{\ell-1}{r_j} + \frac{1}{2\,\Delta r}\frac{r_{j+\frac{1}{2}}^2 - r_{j-\frac{1}{2}}^2}{r_j^2}\right)g_{\ell-1}^j \\
&+c_\ell\left(\frac{\ell}{r_j} + \frac{1}{2\,\Delta r}\frac{r_{j+\frac{1}{2}}^2 - r_{j-\frac{1}{2}}^2}{r_j^2}\right)g_{\ell+1}^j \\
&+\frac{1}{2\,\Delta r}\Big\{c_{\ell-1}\Big(\alpha_j\,g_{\ell-1}^{j+1} - \alpha_{j-1}\,g_{\ell-1}^{j-1}\Big) + c_\ell\Big(\alpha_j\,g_{\ell+1}^{j+1} - \alpha_{j-1}\,g_{\ell+1}^{j-1}\Big)\Big\}\Bigg]
\end{aligned} \tag{F.22}$$

We are left with some strange-looking terms fractions on the two $g^j$ terms, but it turns out they simplify dramatically:

$$\begin{aligned}
\frac{1}{2\,\Delta r}\frac{r_{j+\frac{1}{2}}^2 - r_{j-\frac{1}{2}}^2}{r_j^2} &= \frac{1}{2\,\Delta r}\frac{\left(r_j + \frac{\Delta r}{2}\right)^2 - \left(r_j - \frac{\Delta r}{2}\right)^2}{r_j^2} \\
&= \frac{1}{2\,\Delta r}\frac{r_j^2 + 2\frac{r_j\,\Delta r}{2} + \frac{\Delta r^2}{4} - r_j^2 + 2\frac{r_j\,\Delta r}{2} - \frac{\Delta r^2}{4}}{r_j^2} \\
&= \frac{1}{2\,\Delta r}\frac{2r_j\,\Delta r}{r_j^2} \\
\frac{1}{2\,\Delta r}\frac{r_{j+\frac{1}{2}}^2 - r_{j-\frac{1}{2}}^2}{r_j^2} &= \frac{1}{r_j}
\end{aligned} \tag{F.23}$$

With this simplification, the expectation value becomes

$$\langle\Psi|-\widehat{\mathcal{H}}_I^V|\Psi\rangle = i\hbar\frac{q}{m}\,\mathcal{A}(t)\,\Delta r\sum_{\ell,j}\left(g_\ell^j\right)^*\Bigg[-c_{\ell-1}\frac{\ell}{r_j}g_{\ell-1}^j + c_\ell\frac{\ell+1}{r_j}g_{\ell+1}^j \\ +\frac{1}{2\,\Delta r}\Big\{c_{\ell-1}\Big(\alpha_j\,g_{\ell-1}^{j+1}-\alpha_{j-1}\,g_{\ell-1}^{j-1}\Big)+c_\ell\Big(\alpha_j\,g_{\ell+1}^{j+1}-\alpha_{j-1}\,g_{\ell+1}^{j-1}\Big)\Big\}\Bigg] \tag{F.24}$$

From this sum we can extract the single-$g_\ell^j$ interaction propagator in two pieces, the first which is tridiagonal in $\ell$, and second which couples the radial and angular coordinates to each other and is not purely tridiagonal in either mesh unwrapping:

$$-\left[H_1^V\,g\right]_\ell^j = i\hbar\frac{q}{m}\,\mathcal{A}(t)\frac{1}{r_j}\Big[c_\ell(\ell+1)g_{\ell+1}^j - c_{\ell-1}\ell\,g_{\ell-1}^j\Big] \\ -\left[H_2^V\,g\right]_\ell^j = i\hbar\frac{q}{m}\,\mathcal{A}(t)\frac{1}{2\,\Delta r}\Big[c_{\ell-1}\Big(\alpha_j\,g_{\ell-1}^{j+1}-\alpha_{j-1}\,g_{\ell-1}^{j-1}\Big)+c_\ell\Big(\alpha_j\,g_{\ell+1}^{j+1}-\alpha_{j-1}\,g_{\ell+1}^{j-1}\Big)\Big] \tag{F.25}$$

Now that we have the interaction Hamiltonian matrix operators, we need to figure out how to apply them. Unlike the length-gauge interaction Hamiltonian matrix operators, $\left[H_2^V\,g\right]_\ell^j$ is not tridiagonal in either wrapping direction. We can handle $\left[H_1^V\,g\right]_\ell^j$ with the techniques described in Section 2.3.3.1, but we'll need a slightly more involved technique for $\left[H_2^V\,g\right]_\ell^j$. Roughly, one performs the same splitting as above twice; see [81] for details.

# G IDESolver

While investigating the possibilities of the IDE-based ionization model (see Section 2.5), we found it necessary to numerically solve the model quickly and efficiently. Initially, we simply used RK4, but found it to be computationally expensive and unwieldy. In particular, working with IDE models that included vector potentials involved writing tricky code.

It became obvious that, although using RK4 as a giant hammer on our round peg was providing good results, we should look for a more appropriate solution. This led us to an iterative scheme devised by Gelmi and Jorquera [91], where the solution to an integro-differential is successively approximated. Although derivatives and integrals need to be performed many times during this procedure, one does not have to solve a combined integro-differential equation at any point.

Their algorithm is quite general, but their reference implementation was in MATLAB. We

decided to write our own implementation in Python, which eventually became IDESolver, a separate package in its own right that implements Gelmi and Jorquera's algorithm as a flexible Python package, styled after SciPy's differential equation solvers [1].

The IDESolver algorithm solves integro-differential equations of the form

$$\begin{aligned} \frac{dy}{dx} &= c(y,x) + d(x)\int_{\alpha(x)}^{\beta(x)} k(x,s)\,F(y(s))\,ds, \\ x &\in [a,b], \quad y(a) = y_0 \end{aligned} \tag{G.1}$$

First, we generate an initial guess $y^{(0)}$ by solving

$$\frac{dy^{(0)}}{dx} = c(y^{(0)},x) \qquad\qquad x \in [a,b], \quad y^{(0)}(a) = y_0 \tag{G.2}$$

using a standard differential equation solver. Next, generate another guess by solving

$$\begin{aligned} \frac{dy^{(1/2)}}{dx} &= c(y^{(0)},x) + d(x)\int_{\alpha(x)}^{\beta(x)} k(x,s)\,F(y^{(0)}(s))\,ds, \\ x &\in [a,b], \quad y^{(1/2)}(a) = y_0 \end{aligned} \tag{G.3}$$

Note that, again, this is just a normal differential equation (not integro-differential), because $y^{(1/2)}$ does not appear on the right-hand side. Now we compute a global error estimate $G(y^{(0)}, y^{(1/2)})$, which by default is

$$G(a,b) = \sqrt{\sum_{x_i} |a(x_i) - b(x_i)|} \tag{G.4}$$

At this point, this most likely does not represent the "real" global error compared to the solution. Instead, it is simply a measure of how different the two trial solutions are. If $G$ is smaller than the cutoff, we accept $y^{(1/2)}$ as the solution. If $G$ is larger than the cutoff, we smoothly combine the two solutions into a new trial solution to take the place of $y^{(0)}$:

$$y^{(1)} = \alpha y^{(0)} + (1-\alpha) y^{(1/2)} \tag{G.5}$$

where $\alpha = 1/2$ by default. This smoothing helps prevent wild jumps between iterations. One iterates the above procedure, solving

$$\frac{dy^{(i+1/2)}}{dx} = c(y^{(i)}, x) + d(x) \int_{\alpha(x)}^{\beta(x)} k(x,s)\, F(y^{(i)}(s))\, ds, \tag{G.6}$$
$$x \in [a,b], \quad y^{(i+1/2)}(a) = y_0$$

and producing a new $y^{(i+1)}$ until $G$ falls below the given cutoff, at which point you stop the iteration and accept $y^{(i+1)}$ as the solution.

We confirmed that this algorithm does produce the same results as our single-pass RK4 solver. Unfortunately, we also confirmed that it is slightly slower, and that because it uses global instead of local error control, it was more difficult to determine the correct parameters to get a satisfactory solution. Ultimately, we continued to work with the simple, straightforward RK4 solver.

# Bibliography


[1] Joshua T. Karpel. "IDESolver: a general purpose integro-differential equation solver". In: *J. Open Source Softw.* 3.21 (2018), p. 542. DOI: 10.21105/joss.00542 (cit. on pp. 2, 122, 183).

[2] Travis E. Oliphant. "Python for Scientific Computing". In: *Comput. Sci. Eng.* 9.3 (2007), pp. 10–20. DOI: 10.1109/MCSE.2007.58 (cit. on p. 3).

[3] Marek Chaciński et al. "Monolithically Integrated 100 GHz DFB-TWEAM". In: *J. Light. Technol.* 27.16 (2009), pp. 3410–3415 (cit. on p. 4).

[4] G. T. Reed, G. Mashanovich, F. Y. Gardes, and D. J. Thomson. "Silicon optical modulators". In: *Nat. Photonics* 4.8 (2010), pp. 518–526. DOI: 10.1038/nphoton.2010.179 (cit. on p. 4).

[5] Christopher T. Phare, Yoon Ho Daniel Lee, Jaime Cardenas, and Michal Lipson. "Graphene electro-optic modulator with 30 GHz bandwidth". In: *Nat. Photonics* 9.8 (2015), pp. 511–514. DOI: 10.1038/nphoton.2015.122 (cit. on p. 4).

[6] Yasufum Enami et al. "Bandwidth Optimization for Mach-Zehnder Polymer/Sol-Gel Modulators". In: *J. Light. Technol.* 36.18 (2018), pp. 4181–4189 (cit. on p. 4).

[7] Mohammad Reza Javid, Mehdi Miri, and Abbas Zarifkar. "Design of a compact high-speed optical modulator based on a hybrid plasmonic nanobeam cavity". In: *Opt. Commun.* 410.November 2017 (2018), pp. 652–659. DOI: 10.1016/j.optcom.2017.11.016 (cit. on p. 4).

[8] Michael Hochberg et al. "Terahertz all-optical modulation in a silicon–polymer hybrid system". In: *Nat. Mater.* 5.9 (2006), pp. 703–709. DOI: 10.1038/nmat1719 (cit. on p. 4).

[9] Xu Fang et al. "Ultrafast all-optical switching via coherent modulation of metamaterial absorption". In: *Appl. Phys. Lett.* 104.14 (2014). DOI: 10.1063/1.4870635 (cit. on p. 4).

[10] Wei Li et al. "Ultrafast All-Optical Graphene Modulator". In: *Nano Lett.* 14.2 (2014), pp. 955–959. DOI: 10.1021/nl404356t (cit. on p. 4).

[11] J. K. Brasseur, K. S. Repasky, and John L. Carlsten. "Continuous-wave Raman laser in $H_2$". In: *Opt. Lett.* 23.5 (1998), p. 367. DOI: 10.1364/OL.23.000367 (cit. on p. 4).

[12] J. K. Brasseur, Peter A. Roos, K. S. Repasky, and John L. Carlsten. "Characterization of a continuous-wave Raman laser in $H_2$". In: *J. Opt. Soc. Am. B* 16.8 (1999), p. 1305. DOI: 10.1364/JOSAB.16.001305 (cit. on p. 4).

[13] Kazuki Ihara et al. "Molecular-optic modulator". In: *Appl. Phys. Lett.* 88.7 (2006), pp. 9–11. DOI: 10.1063/1.2174091 (cit. on p. 4).

[14] Shin-ichi Zaitsu, Chihiro Eshima, Kazuki Ihara, and Totaro Imasaka. "Generation of a continuous-wave pulse train at a repetition rate of 176THz". In: *J. Opt. Soc. Am. B* 24.5 (2007), p. 1037. DOI: 10.1364/josab.24.001037 (cit. on p. 4).

[15] J. T. Green, D. E. Sikes, and D. D. Yavuz. "Continuous-wave high-power rotational Raman generation in molecular deuterium". In: *Opt. Lett.* 34.17 (2009), p. 2563. DOI: 10.1364/OL.34.002563 (cit. on p. 4).

[16] J. T. Green, J. J. Weber, and D. D. Yavuz. "Continuous-wave light modulation at molecular frequencies". In: *Phys. Rev. A* 82.1 (2010), p. 011805. DOI: 10.1103/PhysRevA.82.011805 (cit. on p. 4).

[17] J. T. Green, J. J. Weber, and D. D. Yavuz. "Continuous-wave, multiple-order rotational Raman generation in molecular deuterium". In: *Opt. Lett.* 36.6 (2011), p. 897. DOI: 10.1364/OL.36.000897 (cit. on p. 4).

[18] J. J. Weber, J. T. Green, and D. D. Yavuz. "17 THz continuous-wave optical modulator". In: *Phys. Rev. A* 85.1 (2012), pp. 1–4. DOI: 10.1103/PhysRevA.85.013805 (cit. on p. 4).

[19] David C. Gold, Joshua J. Weber, and Deniz D. Yavuz. "Continuous-Wave Molecular Modulation Using a High-Finesse Cavity". In: *Appl. Sci.* 4.4 (2014), pp. 498–514. DOI: 10.3390/app4040498 (cit. on p. 4).

[20] D. C. Gold, J. T. Karpel, E. A. Mueller, and D. D. Yavuz. "Continuous-wave modulation of a femtosecond oscillator using coherent molecules". In: *Opt. Lett.* 43.5 (2018), p. 1003. DOI: 10.1364/OL.43.001003 (cit. on p. 4).

[21] A. E. Kaplan. "Subfemtosecond Pulses in Mode-Locked $2\pi$ Solitons of the Cascade Stimulated Raman Scattering". In: *Phys. Rev. Lett.* 73.9 (1994), pp. 1243–1246. DOI: 10.1103/PhysRevLett.73.1243 (cit. on p. 4).

[22] S E Harris and A V Sokolov. "Broadband spectral generation with refractive index control". In: *Phys. Rev. A* 55.6 (1997), R4019–R4022. DOI: 10.1103/PhysRevA.55.R4019 (cit. on p. 4).

[23] S E Harris and A V Sokolov. "Subfemtosecond Pulse Generation by Molecular Modulation". In: *Phys. Rev. Lett.* 81.14 (1998), pp. 2894–2897. DOI: 10.1103/PhysRevLett.81.2894 (cit. on p. 4).

[24] H. Kawano, Y. Hirakawa, and Totaro Imasaka. "Generation of more than 40 rotational Raman lines by picosecond and femtosecond Ti:sapphire laser for Fourier synthesis". In: *Appl. Phys. B Lasers Opt.* 65.1 (1997), pp. 1–4. DOI: 10.1007/s003400050240 (cit. on p. 4).

[25] Hiroyuki Kawano, Yasuyuki Hirakawa, and Totaro Imasaka. "Generation of high-order rotational lines in hydrogen by four-wave raman mixing in the femtosecond regime". In: *IEEE J. Quantum Electron.* 34.2 (1998), pp. 260–268. DOI: 10.1109/3.658704 (cit. on p. 4).

[26] A. V. Sokolov, D. R. Walker, D. D. Yavuz, G. Y. Yin, and S. E. Harris. "Raman generation by phased and antiphased molecular states". In: *Phys. Rev. Lett.* 85.3 (2000), pp. 562–565. DOI: 10.1103/PhysRevLett.85.562 (cit. on p. 4).

[27] J Q Liang, M Katsuragawa, Fam Le Kien, and K Hakuta. "Sideband Generation Using Strongly Driven Raman Coherence in Solid Hydrogen". In: *Phys. Rev. Lett.* 85.12 (2000), pp. 2474–2477. DOI: 10.1103/PhysRevLett.85.2474 (cit. on p. 4).

[28] M Katsuragawa, J Q Liang, Fam Le Kien, and K Hakuta. "Efficient frequency conversion of incoherent fluorescent light". In: *Phys. Rev. A* 65.2 (2002), p. 25801. DOI: 10.1103/PhysRevA.65.025801 (cit. on p. 4).

[29] M Y Shverdin, D R Walker, D D Yavuz, G Y Yin, and S E Harris. "Generation of a Single-Cycle Optical Pulse". In: *Phys. Rev. Lett.* 94.3 (2005), p. 33904. DOI: 10.1103/PhysRevLett.94.033904 (cit. on p. 4).

[30] Wei Jan Chen et al. "Sub-single-cycle optical pulse train with constant carrier envelope phase". In: *Phys. Rev. Lett.* 100.16 (2008), pp. 5–8. DOI: 10.1103/PhysRevLett.100.163906 (cit. on p. 4).

[31] Kai Wang, Alexandra Zhdanova, Miaochan Zhi, Xia Hua, and Alexei Sokolov. "Multicolored Femtosecond Pulse Synthesis Using Coherent Raman Sidebands in a Reflection Scheme". In: *Appl. Sci.* 5.2 (2015), pp. 145–156. DOI: 10.3390/app5020145 (cit. on p. 4).

[32] C. Ohae et al. "Tailored Raman-resonant four-wave-mixing processes". In: *Opt. Express* 26.2 (2018), p. 1452. DOI: 10.1364/OE.26.001452 (cit. on p. 4).

[33] D. D. Yavuz. "High-frequency modulation of continuous-wave laser beams by maximally coherent molecules". In: *Phys. Rev. A* 76.1 (2007), p. 011805. DOI: 10.1103/PhysRevA.76.011805 (cit. on pp. 4, 54).

[34] Andrey B. Matsko and Vladimir S. Ilchenko. "Optical resonators with whispering-gallery modes - Part I: Basics". In: *IEEE J. Sel. Top. Quantum Electron.* 12.1 (2006), pp. 3–14. DOI: 10.1109/JSTQE.2005.862952 (cit. on pp. 4, 30).

[35] Vladimir S. Ilchenko and Andrey B. Matsko. "Optical resonators with whispering-gallery modes - Part II: Applications". In: *IEEE J. Sel. Top. Quantum Electron.* 12.1 (2006), pp. 15–32. DOI: 10.1109/JSTQE.2005.862943 (cit. on p. 4).

[36] Ivan S. Grudinin and Lute Maleki. "Ultralow-threshold Raman lasing with $CaF_2$ resonators". In: *Opt. Lett.* 32.2 (2007), p. 166. DOI: 10.1364/OL.32.000166 (cit. on p. 5).

[37] Ivan S. Grudinin and Lute Maleki. "Efficient Raman laser based on a $CaF_2$ resonator". In: *J. Opt. Soc. Am. B-Optical Phys.* 25.4 (2008), pp. 594–598. DOI: Doi10.1364/Josab.25.000594 (cit. on p. 5).

[38] P. Del'Haye, O. Arcizet, A. Schliesser, R. Holzwarth, and T. J. Kippenberg. "Full stabilization of a microresonator-based optical frequency comb". In: *Phys. Rev. Lett.* 101.5 (2008), pp. 1–4. DOI: 10.1103/PhysRevLett.101.053903 (cit. on p. 5).

[39] Takumi Kato et al. "Transverse mode interaction via stimulated Raman scattering comb in a silica microcavity". In: *Opt. Express* 25.2 (2017), p. 857. DOI: 10.1364/OE.25.000857 (cit. on p. 5).

[40] T. Herr et al. "Temporal solitons in optical microresonators". In: *Nat. Photonics* 8.2 (2014), pp. 145–152. DOI: 10.1038/nphoton.2013.343 (cit. on p. 5).

[41] Joshua T. Karpel, David C. Gold, and Deniz D. Yavuz. "Prospects for continuous-wave molecular modulation in Raman-active microresonators". In: *Opt. Express* 27.23 (2019), p. 34154. DOI: 10.1364/OE.27.034154 (cit. on p. 5).

[42] Robert W. Boyd. *Nonlinear Optics*. 3rd. Academic Press, 2008 (cit. on p. 5).

[43] John David Jackson. *Classical Electrodynamics*. 1962. DOI: 10.1119/1.19136 (cit. on pp. 6, 58).

[44] J. J. Weber. "Continuous-Wave Light Modulation Using Stimulated Raman Scattering". PhD thesis. University of Wisconsin-Madison, 2014 (cit. on p. 9).

[45] K. S. Repasky, J. K. Brasseur, L. Meng, and J. L. Carlsten. "Performance and design of an off-resonant continuous-wave Raman laser". In: *J. Opt. Soc. Am. B* 15.6 (1998), p. 1667. DOI: 10.1364/JOSAB.15.001667 (cit. on p. 26).

[46] J. C. Knight, G. Cheung, F. Jacques, and T. A. Birks. "Phase-matched excitation of whispering-gallery-mode resonances by a fiber taper". In: *Opt. Lett.* 22.15 (1997), p. 1129. DOI: 10.1364/OL.22.001129 (cit. on p. 30).

[47] S. M. Spillane, T. J. Kippenberg, O. J. Painter, and K. J. Vahala. "Ideality in a Fiber-Taper-Coupled Microresonator System for Application to Cavity Quantum Electrodynamics". In: *Phys. Rev. Lett.* 91.4 (2003), pp. 2–5. DOI: 10.1103/PhysRevLett.91.043902 (cit. on pp. 30, 31).

[48] M. L. Gorodetsky, A. A. Savchenkov, and V. S. Ilchenko. "Ultimate Q of optical microsphere resonators". In: *Opt. Lett.* 21.7 (1996), p. 453. DOI: 10.1364/OL.21.000453 (cit. on p. 31).

[49] Michael L. Gorodetsky and Vladimir S. Ilchenko. "Optical microsphere resonators: optimal coupling to high-Q whispering-gallery modes". In: *J. Opt. Soc. Am. B* 16.1 (1999), pp. 147–154. DOI: 10.1364/JOSAB.16.000147 (cit. on pp. 31, 36, 41).

[50] Hermann A. Haus. *Waves and Fields in Optoelectronics*. Prentice-Hall, 1984 (cit. on pp. 31, 34, 36).

[51] G. C. Righini et al. "Whispering Gallery Mode microresonators: Fundamentals and applications". In: *Riv. del Nuovo Cim.* 34.7 (2011), pp. 435–488. DOI: 10.1393/ncr/i2011-10067-2 (cit. on pp. 36, 38, 41, 42, 49).

[52] Dawn Hollenbeck and Cyrus D Cantrell. "Multiple-vibrational-mode model for fiber-optic Raman gain spectrum and response function". In: *J. Opt. Soc. Am. B* 19.12 (2002), pp. 2886–2892 (cit. on p. 41).

[53] Ming Cai, Guido Hunziker, and Kerry Vahala. "Fiber-optic add-drop device based on a silica microsphere-whispering gallery mode system". In: *IEEE Photonics Technol. Lett.* 11.6 (1999), pp. 686–687. DOI: 10.1109/68.766785 (cit. on p. 41).

[54] Yongchao Dong, Keyi Wang, and Xueying Jin. "Package of a dual-tapered-fiber coupled microsphere resonator with high Q factor". In: *Opt. Commun.* 350 (2015), pp. 230–234. DOI: 10.1016/j.optcom.2015.03.074 (cit. on p. 41).

[55] Mark Sadgrove, Ramachandrarao Yalla, Kali P. Nayak, and Kohzo Hakuta. "Photonic crystal nanofiber using an external grating". In: *Opt. Lett.* 38.14 (2013), p. 2542. DOI: 10.1364/ol.38.002542 (cit. on p. 41).

[56] Stéphane Balac. "WGMode: A Matlab toolbox for whispering gallery modes volume computation in spherical optical micro-resonators". In: *Comput. Phys. Commun.* 243 (2019), pp. 121–134. DOI: 10.1016/j.cpc.2019.05.002 (cit. on p. 42).

[57] Andrew Lee, Helen M. Pask, and D. J. Spence. "Control of cascading in multiple-order Raman lasers". In: *Opt. Lett.* 37.18 (2012), p. 3840. DOI: 10.1364/ol.37.003840 (cit. on p. 42).

[58] S M Spillane, T J Kippenberg, and K J Vahala. "Ultralow-threshold Raman laser using a spherical dielectric microcavity". In: *Nature* (2002), pp. 621–623 (cit. on p. 42).

[59] T. J. Kippenberg, S. M. Spillane, Bumki Min, and K. J. Vahala. "Theoretical and experimental study of stimulated and cascaded Raman scattering in ultrahigh-Q optical microcavities". In: *IEEE J. Sel. Top. Quantum Electron.* 10.5 (2004), pp. 1219–1228. DOI: 10.1109/JSTQE.2004.837203 (cit. on pp. 42, 48).

[60] Bumki Min, Tobias J Kippenberg, and Kerry J Vahala. "Compact, fiber-compatible, cascaded Raman laser". In: *Opt. Lett.* 28.17 (2003), pp. 1507–1509. DOI: 10.1364/OL.28.001507 (cit. on pp. 48, 167).

[61] Hongchun Gao et al. "Investigation on the thermo-optic coefficient of silica fiber within a wide temperature range". In: *J. Light. Technol.* 36.24 (2018), pp. 5881–5886. DOI: 10.1109/JLT.2018.2875941 (cit. on p. 49).

[62] I. H. Malitson. "Interspecimen Comparison of the Refractive Index of Fused Silica". In: *J. Opt. Soc. Am.* 55.10 (1965), p. 1205. DOI: 10.1364/JOSA.55.001205 (cit. on p. 50).

[63] K. Gardner et al. "Whispering gallery mode structure in polymer-coated lasing microspheres". In: *J. Opt. Soc. Am. B* 34.10 (2017), p. 2140. DOI: 10.1364/josab.34.002140 (cit. on p. 50).

[64] D. D. Yavuz. "Toward Synthesis of Arbitrary Optical Waveforms". In: *Science* 331.6021 (2011), pp. 1142–1143. DOI: 10.1126/science.1203018 (cit. on pp. 54, 56).

[65] R. A. Lewis. "A review of terahertz sources". In: *J. Phys. D. Appl. Phys.* 47.37 (2014). DOI: 10.1088/0022-3727/47/37/374001 (cit. on p. 54).

[66] D. D. Yavuz and J. J. Weber. "Tunable source of terahertz radiation using molecular modulation". In: *Opt. Lett.* 37.20 (2012), p. 4191. DOI: 10.1364/OL.37.004191 (cit. on p. 54).

[67] Thomas Gaumnitz et al. "Streaking of 43-attosecond soft-X-ray pulses generated by a passively CEP-stable mid-infrared driver". In: *Opt. Express* 25.22 (2017), p. 27506. DOI: 10.1364/oe.25.027506 (cit. on p. 56).

[68] Ferenc Krausz and Misha Ivanov. "Attosecond physics". In: *Rev. Mod. Phys.* 81.1 (2009), pp. 163–234. DOI: 10.1103/RevModPhys.81.163 (cit. on pp. 56, 161).

[69] Ferenc Krausz. "From quantum transitions to electronic motions". In: *Appl. Phys. B* 123.1 (2017), p. 7. DOI: 10.1007/s00340-016-6580-z (cit. on p. 56).

[70] D. D. Yavuz. "A Raman Approach for Generating Ultrashort Pulses". PhD thesis. Stanford, 2003, p. 144 (cit. on p. 56).

[71] J J. Weber and D. D. Yavuz. "Broadband spectrum generation using continuous-wave Raman scattering". In: *Opt. Lett.* 38.14 (2013), p. 2449. DOI: 10.1364/OL.38.002449 (cit. on p. 56).

[72] C J Joachain, N J Klystra, and R M Potvliege. *Atoms in Intense Laser Fields*. Cambridge University Press, 2012 (cit. on pp. 57, 79, 87, 120, 175).

[73] Joshua T. Karpel and Deniz D. Yavuz. "Phase-dependent ionization of hydrogen by intense sub-cycle pulses". In: *Opt. Lett.* 43.11 (2018), p. 2583. DOI: 10.1364/OL.43.002583 (cit. on pp. 57, 133, 142).

[74] H. R. Reiss. "Frequency Effects and Classical Paths in Strong-Field Ionization". In: *J. Nonlinear Opt. Phys. Mater.* 04.03 (1995), pp. 687–700. DOI: 10.1142/S0218863595000306 (cit. on p. 60).

[75] H. R. Reiss. "Foundation of Strong-Field Physics". In: *Lect. Ultrafast Intense Laser Sci. 1*. Ed. by K. Yamanouchi. Springer Berlin Heidelberg, 2010, pp. 41–84 (cit. on p. 60).

[76] H. R. Reiss. "Unsuitability of the Keldysh parameter for laser fields". In: *Phys. Rev. A - At. Mol. Opt. Phys.* 82.2 (2010). DOI: 10.1103/PhysRevA.82.023418 (cit. on pp. 60, 82).

[77] H. R. Reiss. "Properties of the Strong-Field Approximation". In: (2018), pp. 1–36 (cit. on pp. 60, 82).

[78] H. R. Reiss. "Ascendancy of potentials over fields in electrodynamics". In: (2018), pp. 1–29 (cit. on pp. 60, 82).

[79] J. J. Sakurai and Jim Napolitano. *Modern Quantum Mechanics*. 2010, p. 550. DOI: 10.1119/1.14491 (cit. on p. 80).

[80] K. J. Schafer, M. B. Gaarde, K. C. Kulander, B. Sheehy, and L. F. DiMauro. "Calculations of strong field multiphoton processes in alkali metal atoms". In: *AIP Conf. Proc.* 8.1 (2000), pp. 45–58. DOI: 10.1063/1.1291925 (cit. on pp. 103, 177, 179).

[81] Kenneth J. Schafer. "Numerical methods in strong field physics". In: *Strong F. Laser Phys.* T. Brabec, Ed. (Springer Science + Media Business, New York), 2008 (cit. on pp. 103, 107, 175–177, 182).

[82] Diego G Arbó et al. "Coulomb-Volkov approximation for near-threshold ionization by short laser pulses". In: (2008). DOI: 10.1103/PhysRevA.77.013401 (cit. on p. 114).

[83] Philipp Bader, Sergio Blanes, and Fernando Casas. "Solving the Schrödinger eigenvalue problem by the imaginary time propagation technique using splitting methods with complex coefficients". In: *J. Chem. Phys.* 139.12 (2013), pp. 124–117. DOI: 10.1063/1.4821126 (cit. on p. 116).

[84] R. B. Lehoucq, D. C. Sorensen, and C. Yang. *ARPACK Users' Guide*. Philadelphia, PA: Society for Industrial and Applied Mathematics, 1998. DOI: 10.1137/1.9780898719628 (cit. on p. 117).

[85] E. A. Volkova, V. V. Gridchin, A. M. Popov, and O. V. Tikhonova. "Tunneling ionization of a hydrogen atom in short and ultrashort laser pulses". In: *J. Exp. Theor. Phys.* 102.1 (2006), pp. 40–52. DOI: 10.1134/S1063776106010055 (cit. on p. 117).

[86] Maciej Lewenstein, J Mostowski, and M Trippenbach. "Multichannel decay and continuum-continuum transitions in above-threshold ionisation". In: *J. Phys. B* 18.14 (1985), pp. L461–L466. DOI: 10.1088/0022-3700/18/24/520 (cit. on p. 121).

[87] J Grochmalicki Lewenstein, J R Kuklinski, and M. "Above-threshold ionisation and electron scattering in intense laser fields". In: *J. Phys. B* 19.22 (1986), p. 3649. DOI: 10.1088/0022-3700/19/22/010 (cit. on p. 121).

[88] M. Lewenstein et al. "Theory of high-harmonic generation by low-frequency laser fields". In: *Phys. Rev. A* 49.3 (1994), pp. 2117–2132. DOI: 10.1103/PhysRevA.49.2117 (cit. on p. 121).

[89] M. Lewenstein, K. C. Kulander, K. J. Schafer, and P. H. Bucksbaum. "Rings in above-threshold ionization: A quasiclassical analysis". In: *Phys. Rev. A* 51.2 (1995), pp. 1495–1507. DOI: 10.1103/PhysRevA.51.1495 (cit. on p. 121).

[90] Noslen Suárez, Alexis Chacón, Marcelo F. Ciappina, Jens Biegert, and Maciej Lewenstein. "Above-threshold ionization and photoelectron spectra in atomic systems driven by strong laser fields". In: *Phys. Rev. A* 92.6 (2015), p. 063421. DOI: 10.1103/PhysRevA.92.063421 (cit. on pp. 121, 142, 143).

[91] Claudio A. Gelmi and Héctor Jorquera. "IDSOLVER: A general purpose solver for nth-order integro-differential equations". In: *Comput. Phys. Commun.* 185.1 (2014), pp. 392–397. DOI: 10.1016/j.cpc.2013.09.008 (cit. on pp. 122, 182).

[92] William H Press, Saul A Teukolsky, William T Vetterling, and Brian P Flannery. *Numerical Recipes in C: The Art of Scientific Computing*. 2nd. Cambridge University Press, 1992 (cit. on pp. 122, 132, 162).

[93] W. Becker et al. "Above-Threshold Ionization: From Classical Features to Quantum Effects". In: *Adv. At. Mol. Opt. Phys.* Ed. by Benjamin Bederson and Herbert Walther. Vol. 48. Academic Press, 2002, pp. 35–98. DOI: 10.1016/S1049-250X(02)80006-4 (cit. on pp. 124, 127).

[94] M. Protopapas, C. H. Keitel, and P. L. Knight. "Atomic physics with super-high intensity lasers". In: *Reports Prog. Phys.* 60.4 (1997), pp. 389–486. DOI: 10.1088/0034-4885/60/4/001 (cit. on p. 127).

[95] D. Bahuguna, A. Ujlayan, and D.N. Pandey. "A comparative study of numerical methods for solving an integro-differential equation". In: *Comput. Math. with Appl.* 57.9 (2009), pp. 1485–1493. DOI: 10.1016/j.camwa.2008.10.097 (cit. on p. 132).

[96] D. Bauer and P. Mulser. "Exact field ionization rates in the barrier-suppression regime from numerical time-dependent Schrödinger-equation calculations". In: *Phys. Rev. A* 59.1 (1999), pp. 569–577. DOI: 10.1103/PhysRevA.59.569 (cit. on pp. 151, 154, 156, 157).

[97] Jarosław H Bauer. "Search for the best analytical formula in the tunneling and the barrier-suppression ionization regimes". In: *J. Phys. B At. Mol. Opt. Phys* 085601.50 (2017). DOI: 10.1088/1361-6455/aa65ae (cit. on p. 154).

[98] J. H. Bauer. "Keldysh theory re-examined". In: *J. Phys. B* 49.14 (2016), p. 145601. DOI: 10.1088/0953-4075/49/14/145601 (cit. on p. 154).

[99] *NIST Digital Library of Mathematical Functions*. http://dlmf.nist.gov/, Release 1.0.11 of 2016-06-08 (cit. on p. 163).

[100] Taweetham Limpanuparb and Josh Milthorpe. "Associated Legendre Polynomials and Spherical Harmonics Computation for Chemistry Applications". In: *arXiv* (2014), pp. 1–12 (cit. on p. 169).